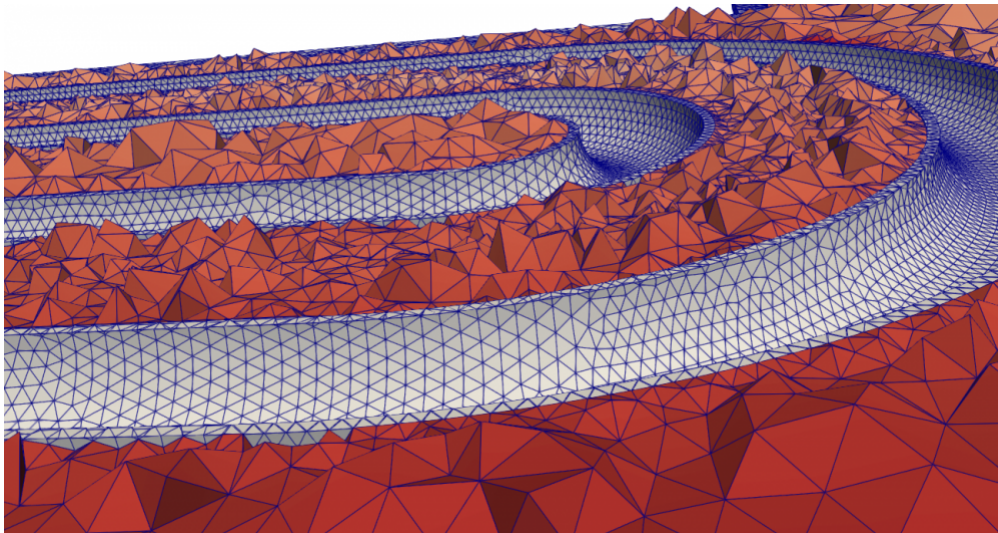


Validating results from the Molten Salt Reactor Experiment by use of turbulent CFD simulations

*A study of a modified U-tube shell-and-tube primary heat exchanger and
radiator with molten salts*



Malcolm Akner

**Space Engineering, master's level
2021**

Luleå University of Technology
Department of Computer Science, Electrical and Space Engineering

PREFACE

This thesis is produced as part of the graduating work for my Space Engineering master's degree, with a profile in aerospace and mathematical modelling, at Luleå University of Technology (LTU). It has been produced in collaboration with Copenhagen Atomics, situated in Copenhagen, Denmark, where I spent the entirety of the project. The project spanned the duration from September 2020 to April 2021, under the supervision of Aslak Stubsgaard (CTO of Copenhagen Atomics) and Robin Andersson (Postdoc at LTU).

I have always been interested in energy and electricity generation and have had a special interest in nuclear energy for many years. During my university studies I came across Kirk Sorensen and his work in molten salt reactors. His strong arguments and well-reasoned points, backed up by the successful operation of the Molten Salt Reactor Experiment, conducted in the U.S.A. in the 1960s, convinced me that the MSR technology might be a solution to the energy crisis the world is currently facing. This is a problem that must be solved, with scalable, cost efficient, energy efficient and robust solutions.

In this thesis, the fluid dynamic aspects of reactor components from the MSRE were studied and modelled, with the intent to improve our understanding of the functionality and behaviour of high temperature, molten salt environments.

ACKNOWLEDGEMENT

This project could not have been done without the generous help and contributions from many people.

I would like to first and foremost thank my on-site supervisor Aslak Stubsgaard, without whom this project would not have been possible. Through encouragement and a wealth of knowledge he has guided me through the project and have been ready to supply ideas and feedback whenever I needed.

Thank you also to Robin Andersson, my other supervisor situated at LTU, for proofreading and guiding me through the challenging world of CFD, providing great advice and ideas on how to proceed with my work.

My father, Gunnar, has been a rock in stormy seas, upon whom I have always been able to depend. Even though he lacks understanding of this specific field, he has painstakingly proofread every word of my documents and findings and helped me formulate my thoughts and structure my arguments in a professional yet living tone.

My mother, Cheryl, always ready with interesting and encouraging conversations, drawing from her unique aesthetic background and reminding me to keep my writing relevant and meaningful.

My sister, Corina for helping me through the difficult times when it felt like nothing went my way, always being able to make me laugh and summon the strength to go on. She has been a great catalyst through my university studies, for which I will forever be thankful.

My partner and love, Marit, who never doubted in me and could help me get perspective through her own, recent experience going through a university examination process. With her intelligence and wit, she gives me continuous support while keeping me realistic and focused on the goal.

Last, but not least, I would like to thank Copenhagen Atomics and my colleagues, inviting me into a professional and competent atmosphere to work in, something that I have not experienced before. This project would have been a very different experience writing alone in a temporary cubicle at my university, and I am very glad that I went to Copenhagen for this thesis work.

ABSTRACT

Background

Nuclear reactors utilizing molten fuels rather than solid fuels show a massive advantage in energy yield, waste handling and safety features. The only successful reactor utilizing a molten fuel was called the ‘Molten Salt Reactor Experiment’ (MSRE), built and operated in the Oak Ridge national laboratory (ORNL) in Tennessee, U.S.A. during the 1960s. The molten salts in question are fluoride compounds under the name of “FLiBe”.

In this thesis, the heat exchangers of the MSRE are modelled and simulated, with the aim to test whether current computational fluid dynamics (CFD) software and mathematical models can accurately predict molten salt heat transfer behaviour.

Methods

All programs used are open-source and/or free-access to facilitate open collaboration between researchers in this growing field. All models and findings produced in this thesis are free to use for future research.

- The program Onshape was used to draw CAD-models based on hand-drawn technical documents released by ORNL.
- Several programs, e.g., Simscale and Salome, were used to create high detailed meshes of the heat exchangers.
- The CFD software Simscale and OpenFOAM have been used to simulate the heat exchangers, using the $k - \omega SST$ Reynolds averaged Navier-Stokes (RANS) turbulence model to perform a multiregion conjugate heat transfer (CHT) analysis.
- The program Paraview has been used for all post-processing on the large datasets.

Results

- A working toolchain with open-source programs for CFD has been identified.
- Highly detailed, full-scale and accurate CAD-drawings of the two heat exchangers have been produced.
- Models have been finely meshed, containing tens of millions of cells, with good quality measures.
- The simulations produced physically sound and valuable data:
 - Great heat transfer predictive capability with high accuracy to the data presented by ORNL.
 - Pressure data showed a consistent over-prediction with a factor of ~ 2 . Possibility of error within the MSRE measurement.

Conclusions

- CHT using modern turbulence methods work well for the intended purpose and can be used by industry to simulate molten salt heat transfer.
- Open-source programs perform well and can be used by researchers to share ideas and progress.
- Doubts around certain measurements from the MSRE, showing large uncertainties.
- Future projects have been outlined to continue the work performed in this thesis.

Molten salt reactors show fantastic promise as an energy generation method and should be seriously considered for the future of clean, reliable energy.

TABLE OF CONTENTS

1	INTRODUCTION AND BACKGROUND.....	1
1.1	PROBLEM FORMULATION OF THE PROJECT	1
1.2	COMPUTATIONAL FLUID DYNAMICS	2
1.3	A BRIEF OVERVIEW OF THE ROLE OF NUCLEAR FISSION IN TODAY’S SOCIETY	3
1.4	BASICS OF HOW NUCLEAR FISSION OPERATES	8
1.5	LEADING UP TO THE MSRE	13
1.6	THE MSRE	16
1.6.1	<i>Plant design of the MSRE.....</i>	<i>18</i>
1.6.2	<i>MSRE reactor core.....</i>	<i>19</i>
1.6.3	<i>MSRE primary heat exchanger</i>	<i>20</i>
1.6.4	<i>MSRE radiator</i>	<i>23</i>
2	THEORY AND MATHEMATICAL MODELS	26
2.1	BASIC PHYSICAL CONCEPTS OF FLUID MECHANICS	26
2.1.1	<i>Reynolds number.....</i>	<i>26</i>
2.1.2	<i>Turbulence and eddy currents</i>	<i>28</i>
2.1.2.1	<i>The energy cascade.....</i>	<i>30</i>
2.2	NAVIER-STOKES (N-S)	33
2.3	REYNOLDS AVERAGED NAVIER-STOKES (RANS)	37
2.3.1	<i>Boussinesq approximation</i>	<i>38</i>
2.3.2	<i>k – ϵ model.....</i>	<i>40</i>
2.3.3	<i>k – ω model.....</i>	<i>42</i>
2.3.4	<i>k – ω SST model</i>	<i>43</i>
2.4	MODELLING PARAMETERS	46
2.4.1	<i>Courant number</i>	<i>46</i>
2.4.2	<i>Wall functions: y + and u +</i>	<i>47</i>
2.5	MESHING PARAMETERS	51
2.5.1	<i>Non-orthogonality.....</i>	<i>51</i>
2.5.2	<i>Skewness</i>	<i>52</i>
2.5.3	<i>Aspect ratio</i>	<i>53</i>
2.6	SALTS AND HASTELLOY-N	54
2.7	OVERALL HEAT TRANSFER COEFFICIENT	57
3	METHOD	58
3.1	TOOLCHAIN	58
3.1.1	<i>Flowchart of tool chain.....</i>	<i>60</i>
4	CAD RESULTS	61
4.1	PRIMARY HEAT EXCHANGER	61
4.1.1	<i>Construction of the model</i>	<i>62</i>
4.1.2	<i>Tube sheet.....</i>	<i>63</i>
4.1.3	<i>Barrier- and baffle plates.....</i>	<i>65</i>
4.1.4	<i>Shell.....</i>	<i>67</i>
4.1.5	<i>Tubes.....</i>	<i>68</i>
4.1.6	<i>Inlets and outlets.....</i>	<i>70</i>
4.1.6.1	<i>Shell-side (Fuel).....</i>	<i>70</i>
4.1.6.2	<i>Tube-side (Coolant).....</i>	<i>71</i>
4.1.7	<i>Deviations from the PHeX technical drawings</i>	<i>71</i>
4.2	RADIATOR.....	74
4.2.1	<i>Construction of the model</i>	<i>75</i>
4.2.2	<i>Main-headers</i>	<i>76</i>
4.2.3	<i>Sub-headers.....</i>	<i>77</i>
4.2.4	<i>Tubes and tube configuration.....</i>	<i>78</i>
4.2.5	<i>Radiator enclosure</i>	<i>79</i>
4.2.6	<i>Deviations from the technical drawings</i>	<i>80</i>
4.3	HEAT EXCHANGER TEST MODEL	81
5	MESHING RESULTS	82
5.1	MESHING WITH SIMSCALE.....	83
5.1.1	<i>Simscale mesh results: PHeX</i>	<i>83</i>
5.1.2	<i>Simscale mesh results: Radiator</i>	<i>86</i>
5.2	MESHING WITH SALOME	89
5.2.1	<i>Salome mesh results: PHeX.....</i>	<i>89</i>
5.2.2	<i>Salome mesh results: Radiator</i>	<i>92</i>
5.2.3	<i>Salome mesh results: Heat exchanger test model</i>	<i>95</i>
5.3	IDEASUNVTOFOAM PROGRAM.....	97
5.4	SNAPPYHEXMESH	99
6	SIMULATION RESULTS AND MSRE DATA	100
6.1	DATA FROM THE MSRE.....	100
6.1.1	<i>PHeX operational data</i>	<i>101</i>

6.1.1.1	Water tests	101
6.1.2	<i>Radiator operational data</i>	102
6.2	RESULTS FROM SIMULATIONS	103
6.2.1	<i>Reynolds number (Re) analysis</i>	103
6.2.2	<i>Simscale</i>	104
6.2.2.1	Simscale simulation results: PHeX	104
6.2.2.1.1	Water simulation	104
6.2.2.1.2	Salt simulation	106
6.2.2.2	Simscale simulation results: Radiator	108
6.2.3	<i>OpenFOAM</i>	110
6.2.3.1	Initial conditions for turbulence properties	110
6.2.3.2	OpenFOAM simulation results: PHeX	111
6.2.3.3	OpenFOAM simulation results: Radiator	111
7	DISCUSSION	112
7.1	COMPARISON BETWEEN SIMULATIONS AND MSRE DATA	112
7.1.1	<i>PHeX data comparison</i>	112
7.1.1.1	Water simulation comparison to MSRE data	112
7.1.1.2	Salt simulation comparison to MSRE data	113
7.1.1.3	Heat transfer coefficient	114
7.1.2	<i>Radiator data comparison</i>	116
7.2	DATA ACCURACY	118
7.2.1	<i>Accuracy of simulated data</i>	118
7.2.1.1	Temperature	118
7.2.1.2	Pressure	118
7.2.1.3	Temperature dependence	120
7.3	ACCURACY OF MSRE DATA	121
7.3.1	<i>Internal comments from personnel in MSRE</i>	124
7.3.2	<i>Uncertainties in measurements</i>	125
7.4	MODELS	126
7.4.1	<i>CAD-models</i>	126
7.4.1.1	PHeX design suggestions	126
7.4.1.2	Radiator design suggestions	127
7.4.2	<i>Validity of $k - \omega$ SST model</i>	128
7.5	EXPERIENCE WITH THE SOFTWARE UTILIZED	129
7.5.1	<i>Onshape</i>	129
7.5.2	<i>Simscale</i>	129
7.5.3	<i>Salome</i>	129
7.5.4	<i>ideasUnvToFoam</i>	130
7.5.5	<i>OpenFOAM</i>	130
7.5.6	<i>Paraview</i>	131
7.5.7	<i>Atom</i>	131
8	CONCLUSIONS AND FUTURE PROJECTS	132
8.1	CONCLUSIONS	132
8.1.1	<i>Revisiting the problem formulation</i>	132
8.1.2	<i>CAD</i>	132
8.1.3	<i>Mesh</i>	132
8.1.4	<i>Simulations</i>	133
8.2	FUTURE IMPLICATIONS AND PROJECTS	134
8.2.1	<i>Radiator simulations</i>	134
8.2.2	<i>Comparative studies</i>	134
8.2.2.1	Turbulence models	134
8.2.2.2	Other heat exchangers	135
8.2.2.3	Energy generation to demonstrate MSR feasibility	135
8.2.3	<i>Accessibility</i>	135
8.2.3.1	Declassification of test memo-data from ORNL	135
8.2.3.2	Developing MSR-archive	136
8.2.3.3	Further toolchain development	136
8.3	FREEDOM AND THE NECESSITY OF OPEN-SOURCE	137
9	APPENDIX I: TENSOR NOTATION	139
10	APPENDIX II: MODELS AND CASE SET-UP ACCESS	140
10.1	SIMSCALE:	140
10.2	ONSHAPE:	140
11	APPENDIX III: SALOME SET UP AND MESH GUIDE	141
12	APPENDIX IV: CODE	149
12.1	SALOME SCRIPT - MESH QUALITY	149
12.2	OCTAVE SCRIPTS	150
12.2.1	<i>ideasUnvToFoam - cell count vs execution time for meshes of different size</i>	150
12.2.2	<i>Water tests for the primary heat exchanger</i>	151
13	REFERENCES	152

LIST OF FIGURES

FIGURE 1.1 TES AND TEP AS OF 2018 BROKEN DOWN BY SOURCE. LEFT: WORLD TOTAL ENERGY SUPPLY (IEA, 2020), RIGHT: WORLD TOTAL ELECTRICITY PRODUCTION (WORLD NUCLEAR ASSOCIATION, 2020).....	4
FIGURE 1.2 LIFE-TIME GREENHOUSE GAS EMISSIONS FOR CONTEMPORARY ELECTRICITY PRODUCTION MEANS, TOGETHER WITH DEATH RATES PER TWh OF ENERGY PRODUCED (RITCHIE, 2020).	5
FIGURE 1.3 LAND REQUIREMENT FOR NUCLEAR, WIND AND SOLAR TECHNOLOGIES PER 1 GW OF CAPACITY (IAEA, 2016).....	5
FIGURE 1.4 NET INSTALLED NUCLEAR CAPACITY, PROJECTED AS 'HIGH'-CASE AND 'LOW'-CASE TO 2050 (IAEA, 2017).	6
FIGURE 1.5 CHICAGO PILE-1. LEFT: IN FULL OPERATION (U.S. DEPARTMENT OF ENERGY, 1982), RIGHT: ARTISTS RENDITION (SHEEHAN, 1957).....	7
FIGURE 1.6 SCHEMATIC OF A PRESSURIZED WATER REACTOR. GRAPHICS BY SARAH HARMAN, U.S. DEPARTMENT OF ENERGY (ENERGY.GOV, 2021).....	8
FIGURE 1.7 FISSION PRODUCTS FROM ^{233}U (GREEN CURVE), ^{239}Pu (BLUE CURVE) AND ^{235}U (RED CURVE). X -AXIS: NUMBER OF PARTICLES IN NUCLEUS OF THE FISSION PRODUCT, Y -AXIS: FISSION PRODUCT YIELD IN % (DAYMAN, BIEGALSKI, & HAAS, 2014).	9
FIGURE 1.8 STANDARD ISOTOPE CHART AND NUCLEAR DECAY MODES.....	9
FIGURE 1.9 FISSIONING OF ^{235}U	10
FIGURE 1.10 NUCLEAR CHAIN REACTION OF ^{235}U	10
FIGURE 1.11 NEUTRON YIELD VERSUS ENERGY SPECTRUM OF NEUTRON IN ^{233}U , ^{235}U AND ^{239}Pu (WALTAR, TODD, & TSVETKOV, 2012). ...	11
FIGURE 1.12 CROSS SECTION (INTERACTION PROBABILITY) OF Th , Pa , ^{233}U , ^{235}U , ^{238}U AND ^{239}Pu IN THERMAL, INTERMEDIATE AND FAST SPECTRUM OF INCIDENT NEUTRON (WALTAR, TODD, & TSVETKOV, 2012).	12
FIGURE 1.13 BUILDING 7503 AT THE OAK RIDGE NATIONAL LABORATORY, OAK RIDGE, TENNESSEE, MSRE HEADQUARTERS (ORNL-2465, 1960).	16
FIGURE 1.14 TOP: MSRE ACTIVITIES LEADING UP TO POWER TESTING, FROM SUMMER 1964 TO END OF 1965.....	17
FIGURE 1.15 MOLTEN SALT REACTOR EXPERIMENT PLANT DESIGN, SHOWING THE MAJOR COMPONENTS AND THE TWO PRIMARY SALT LOOPS, RED AND YELLOW (GONÇALVES, MAIORINO, MONTEIRO, & ROSSI, 2019).	18
FIGURE 1.16 THE MSRE REACTOR CORE (POWERS, 2019). LEFT: SECTION VIEW OF TECHNICAL DRAWING FROM ORNL, RIGHT: HALFWAY COMPLETED GRAPHITE ROD ASSEMBLY OF CORE.....	19
FIGURE 1.17 TYPICAL GRAPHITE BAR ARRANGEMENT. LEFT: LENGTHWISE SECTION VIEW CONFIGURATION, RIGHT: SECTION VIEW OF GRAPHITE BARS ACROSS CENTRELINE OF THE REACTOR (SHEN, FRATONI, AUFIERO, & BIDAUD, 2018).	20
FIGURE 1.18 EARLIER ITERATION OF THE PRIMARY HEAT EXCHANGER MADE BY THE TEAM AT ORNL (THORIUM ENERGY ALLIANCE, 2020).	21
FIGURE 1.19 TUBE BUNDLE OF COMPLETED, MODIFIED PHEX (ORNL-TM-1023, 1965). HIGH QUALITY IMAGE COURTESY OF DAVID E. HOLCOMB, SENIOR TECHNICAL ADVISOR WORKING CURRENTLY AT ORNL.	22
FIGURE 1.20 STAINLESS STEEL SHELL WITH 16 VIEWING WINDOWS, DESIGNED TO FIND THE CAUSE OF THE RATTLING SOUND (ORNL-TM-2098, 1968).	23
FIGURE 1.21 RADIATOR USED IN THE MSRE, WITH ORNL TECHNICIANS (THORIUM ENERGY ALLIANCE, 2020).....	24
FIGURE 1.22 MAIN BLOWER FOR MSRE COOLANT SYSTEM (ORNL-3708, 1964).....	25
FIGURE 1.23 LEFT: SCHEMATIC OF THE RADIATOR IN THE MSRE, RIGHT: DRAWING OF THE RADIATOR (ORNL-3014, 1960).....	25
FIGURE 2.1 ILLUSTRATION OF SMALL RE (TOP) AND LARGE RE (BOTTOM) (NUCLEAR-POWER, 2021).	27
FIGURE 2.2 ILLUSTRATION OF TURBULENCE. TURBULENT JET OF WATER CONTAINING FLUORESCENT DYE EMERGING INTO A TANK OF STILL WATER, ILLUMINATED WITH A SHEET OF LIGHT (SREENIVASAN, 1999).	29
FIGURE 2.3 ENERGY DISTRIBUTION IN THE EDDIES OF A TURBULENT FLOW. AS TURBULENT KINETIC ENERGY INCREASES (k , x -AXIS), TOTAL ENERGY (E , y -AXIS) TENDS TO DECREASE (MODIR-KHAZENI & TRELLES, 2015).....	30
FIGURE 2.4 STRESS COMPONENTS OF A FLUID ELEMENT SUBJECTED TO FORCES (IOWA STATE UNIVERSITY, 2016). THIS FIGURE IS REUSED WITH PERMISSION FROM, ©IOWA STATE UNIVERSITY CENTER FOR NON-DESTRUCTIVE EVALUATION. (CNDE).	33
FIGURE 2.5 AVERAGE PART ui (SMOOTH LINE) AND FLUCTUATING PART $u'i$ (WIGGLY AND CHAOTIC LINE) (HAZRA, 2020).	37
FIGURE 2.6 LARGEST EDDIES PERMISSIBLE BY THE PROXIMITY TO THE WALL.	39
FIGURE 2.7 WALL FUNCTION $F1$, WHERE $arg1$ IS $\xi1$ IN EQ. 31.....	43
FIGURE 2.8 TIMELINE SHOWING WHEN TURBULENCE MODELS AND THEIR VERSIONS WERE DEVELOPED.	45
FIGURE 2.9 VISUALIZATION OF COURANT NUMBER. LEFT: $Co < 1$, RIGHT: $Co > 1$	46
FIGURE 2.10 VELOCITY REPRESENTATION FOR AN ARBITRARY CELL.....	47
FIGURE 2.11 y^+ VS u^+ FOR BOUNDARY LAYER FLOW, SHOWING VISCOUS SUBLAYER, TRANSITION LAYER AND LOG LAYER. GREEN LINE IS A DNS SOLUTION FOR FLOW OVER A FLAT PLATE (NASA, 2020). DASHED LINES ARE WALL FUNCTIONS (NOTE THE LOG-SCALE ON x -AXIS). $\kappa = 0.41$ AND $C = 5.1$	48
FIGURE 2.12 ONSET OF TURBULENCE OVER A FLAT PLATE, SHOWING THE VISCOUS SUBLAYER AND THE BUFFER LAYER (BANIHANI & ASSAD, 2018)....	49

FIGURE 2.13 NON-ORTHOGONALITY VISUALIZED WITH A 2D EXAMPLE (IMAGE SOURCE: AIDAN WIMSHURST, FLUID MECHANICS 101). LEFT: DEFINING THE NON-ORTHOGONALITY ANGLE θ , RIGHT: INTRODUCING k AS THE DEVIATION FROM PARALLEL PROJECTION.	51
FIGURE 2.14 SKEWNESS INDICATION FOR 2D CELLS.	52
FIGURE 2.15 ASPECT RATIO INDICATION OF TRIANGLE AND QUADRANGLE.	53
FIGURE 2.16 MOLTEN AND SOLID <i>FLiBe</i> (OAK RIDGE NATIONAL LABORATORY, 2017).	54
FIGURE 3.1 FLOWCHART SHOWING PATHWAYS OF DIFFERENT PROGRAMS USED IN THIS THESIS.	60
FIGURE 4.1 ONSHAPE RECONSTRUCTION OF PHeX. GREEN INDICATES FUEL- AND BLUE COOLANT SALT. TOP: FULL MODEL, BOTTOM: SECTION VIEW.	61
FIGURE 4.2 SECTION VIEW OF THE TUBE SHEET. LEFT: TECHNICAL DRAWING (ORNL-TM-2098, 1968), RIGHT: ONSHAPE RECONSTRUCTION.	63
FIGURE 4.3 TUBE SHEET. LEFT: MSRE, MANUFACTURED PART (ORNL-3500, 1963), RIGHT: ONSHAPE RECONSTRUCTION WITH GUIDES FOR TUBE HOLES.	64
FIGURE 4.4 TUBE ARRANGEMENT PATTERN. LEFT: TECHNICAL DRAWING (ORNL-TM-2098, 1968). RIGHT: ONSHAPE RECONSTRUCTION.	64
FIGURE 4.5 TECHNICAL DRAWING OF THE BAFFLE PLATES (ORNL-TM-2098, 1968). TOP LEFT: "A", TOP RIGHT: "B", BOTTOM: "C".	65
FIGURE 4.6 PHeX WITH ALL THE BAFFLE PLATES IN PLACE, SPACED APART BY THE SPACER RODS AS BUILT (ORNL-3500, 1963).	66
FIGURE 4.7 ONSHAPE RECONSTRUCTION OF THE BAFFLE PLATES "A", "B", "C" AND THE BARRIER PLATE.	66
FIGURE 4.8 TECHNICAL DRAWING OF THE IMPINGEMENT BAFFLE AT FUEL INLET (ORNL-TM-2098). LEFT: LOCATION IN THE PHeX (FUEL INLET), RIGHT: IMPINGEMENT BAFFLE HOLE ARRANGEMENT.	67
FIGURE 4.9 SECTION VIEW OF ONSHAPE IMPINGEMENT BAFFLE RECONSTRUCTION.	67
FIGURE 4.10 PHeX SHELL, SIDE VIEW. TOP: TECHNICAL DRAWING (ORNL-TM-2098, 1968), BOTTOM: ONSHAPE RECONSTRUCTION.	68
FIGURE 4.11 PHeX TUBE, SIDE VIEW. TOP: TECHNICAL DRAWING, NOT TO SCALE (ORNL-TM-2098, 1968), BOTTOM: ONSHAPE RECONSTRUCTION.	69
FIGURE 4.12 PHeX TUBE BUNDLE. LEFT: BUNDLE MANUFACTURED AT ORNL (ORNL-3500, 1963), RIGHT: ONSHAPE RECONSTRUCTION.	69
FIGURE 4.13 FUEL INLET. LEFT: TECHNICAL DRAWING (ORNL-TM-2098, 1968), RIGHT: ONSHAPE RECONSTRUCTION.	70
FIGURE 4.14 FUEL OUTLET. LEFT: TECHNICAL DRAWING OF FUEL OUTLET (ORNL-TM-2098, 1968), RIGHT: ONSHAPE RECONSTRUCTION OF FUEL OUTLET.	71
FIGURE 4.15 COOLANT INLET AND OUTLET. LEFT: TECHNICAL DRAWING (ORNL-TM-2098, 1968), RIGHT: ONSHAPE RECONSTRUCTION.	71
FIGURE 4.16 ONSHAPE RECONSTRUCTION OF THE RADIATOR. TOP: FULL MODEL, BOTTOM: SECTION VIEW.	74
FIGURE 4.17 MAIN-HEADER FOR THE RADIATOR. TOP: TECHNICAL DRAWING (ORNL-TM-4174, 1972), BOTTOM LEFT: MANUFACTURED PART AT ORNL (ORNL-3708, 1964), BOTTOM RIGHT: ONSHAPE RECONSTRUCTION.	76
FIGURE 4.18 SUB-HEADER CONFIGURATION. TOP: TECHNICAL DRAWING (ORNL-TM-4174, 1972), BOTTOM LEFT: MANUFACTURED PART AT ORNL (ORNL-3708, 1964), BOTTOM RIGHT: ONSHAPE RECONSTRUCTION.	77
FIGURE 4.19 TUBE CONFIGURATION IN THE MSRE RADIATOR. LEFT: TECHNICAL DRAWING (ORNL-3122, 1961), RIGHT: ONSHAPE RECONSTRUCTION.	78
FIGURE 4.20 RADIATOR TUBES, FULL CONFIGURATION. TOP: MANUFACTURED PART (ORNL-3708, 1964), BOTTOM LEFT: TECHNICAL DRAWING (ORNL-3014, 1960), BOTTOM RIGHT: ONSHAPE RECONSTRUCTION.	79
FIGURE 4.21 RADIATOR ENCLOSURE. TOP: TECHNICAL DRAWING (ORNL-3215, 1961), BOTTOM LEFT: MANUFACTURED PART (ORNL-3369, 1962), BOTTOM RIGHT: ONSHAPE RECONSTRUCTION.	80
FIGURE 4.22 TEST MODEL FOR MESHING AND SIMULATION SETUP PURPOSES. LEFT: TRANSLUCENT FULL VIEW, RIGHT: SECTION VIEW SHOWING ALL THREE REGIONS: SHELL (ORANGE), TUBE (GREY) AND SOLID (BLUE).	81
FIGURE 5.1 SIMSCALE MESHING OF TYPICAL INLET AND OUTLET IN THE PHeX, SHOWING BOUNDARY LAYERS.	83
FIGURE 5.2 SIMSCALE MESHING OF A TYPICAL SECTION OF THE PHeX TUBES. TOP: OUTSIDE OF TUBES, BOTTOM: INSIDE OF TUBES, SHOWING BOUNDARY LAYERS.	83
FIGURE 5.3 SIMSCALE MESHING, SECTION VIEW OF THE PHeX, SHOWING BOUNDARY LAYERS FOR BOTH TUBE-SIDE (BLUE) AND SHELL-REGION (RED).	84
FIGURE 5.4 SIMSCALE MESHING, SECTION VIEW OF THE MESHING OF REGIONS BETWEEN PHeX TUBES, SHOWING BOUNDARY LAYERS IN THE SHELL-SIDE.	84
FIGURE 5.5 SIMSCALE MESHING OF PHeX COOLANT BOTTOM CHANNEL, WITH INLET (TOP RIGHT) AND OUTLET (BOTTOM LEFT).	85
FIGURE 5.6 SIMSCALE MESHING OF THE TUBE SHEET WHERE ALL THE TUBES ARE ATTACHED IN THE PHeX.	85
FIGURE 5.7 SIMSCALE MESHING OF AIR INLET FOR THE RADIATOR, WITH BOUNDARY LAYERS.	86
FIGURE 5.8 SIMSCALE MESHING OF SALT INLET FOR THE RADIATOR, WITH BOUNDARY LAYERS.	87
FIGURE 5.9 SIMSCALE MESHING OF TYPICAL SEGMENT OF RADIATOR TUBE, TOP: OUTSIDE OF TUBE, BOTTOM: INSIDE OF TUBE, SHOWING BOUNDARY LAYERS.	87
FIGURE 5.10 SIMSCALE MESHING OF TYPICAL SECTION OF MESHED RADIATOR TUBE AND SURROUNDING SHELL, SHOWING BOUNDARY LAYERS IN BOTH REGIONS.	88
FIGURE 5.11 SIMSCALE MESHING OF ONE OF THE MAIN RADIATOR HEADERS WITH CONNECTED SUB-HEADERS AND TUBES.	88

FIGURE 5.12	SALOME MESHING OF TYPICAL IN- AND OUTLET OF THE PHeX.	89
FIGURE 5.13	SALOME MESHING OF A TYPICAL SEGMENT OF THE PHeX TUBE. TOP: OUTSIDE OF TUBE, BOTTOM: INSIDE OF TUBE.	90
FIGURE 5.14	SALOME MESHING, SECTION VIEW OF A TYPICAL MESHING IN-BETWEEN TUBES.	90
FIGURE 5.15	SALOME MESHING OF THE TUBE SHEET, WHERE ALL THE TUBES ARE ATTACHED IN THE PHeX.	91
FIGURE 5.16	SALOME MESH OF RADIATOR AIR INLET.	92
FIGURE 5.17	SALOME MESH OF RADIATOR SALT INLET.	93
FIGURE 5.18	SALOME MESH OF RADIATOR TUBES. TOP: OUTSIDE OF TUBES. BOTTOM: INSIDE OF TUBES.	93
FIGURE 5.19	SECTION VIEW OF SALOME MESH OF AIR REGION IN BETWEEN TUBES.	94
FIGURE 5.20	SECTION VIEW OF SALOME MESH SHOWING THE ENTIRE RADIATOR.	94
FIGURE 5.21	SALOME MESHING, SHOWING TYPICAL INLET AND OUTLET FOR THE TEST MODEL. GRAY IS THE SOLID MATERIAL.	95
FIGURE 5.22	SALOME MESHING OF TYPICAL TUBE SECTION, SHOWING INSIDE OF TUBE IN TEST MODEL. GREY IS THE SOLID MATERIAL.	95
FIGURE 5.23	SALOME MESHING OF TYPICAL SECTION OF MESHED TUBE AND SURROUNDING SHELL OF TEST MODEL.	96
FIGURE 5.24	SALOME MESHING OF HEAT EXCHANGER TEST MODEL, SHOWING SECTION VIEW OF SHELL-SIDE WITH PROTRUDING TUBES.	96
FIGURE 5.25	LOG-LOG DATA FIT FOR EXECUTION TIME OF IDEASUnvToFoam OF MESHES OF DIFFERENT CELL COUNTS. DATA FIT ONTO EQUATION OF FORM: $t = Anb$, WITH AN ESTIMATION OF $b = 1.55$, AND $A = e - 16.25$.	97
FIGURE 5.26	HTOP MONITORING SOFTWARE SHOWING SYSTEM USAGE WHEN RUNNING SNAPPYHexMesh ON THE FULL PHeX MODEL.	99
FIGURE 6.1	RELATIONSHIP BETWEEN FLOW RATE AND PRESSURE DROP FOR THE PHeX. THIS TEST WAS CONDUCTED AT ORNL WITH WATER (ORNL-TM-2098, 1968).	101
FIGURE 6.2	VELOCITY PLOT IN A TYPICAL RUN OF THE PHeX, SHOWING FLOW PATHS COLOURED AS VELOCITY AS A Re NUMBER INDICATOR. TOP: TUBES, BOTTOM: SHELL.	104
FIGURE 6.3	SIMSCALE RESULTS WITH WATER PARAMETERS FOR PRESSURE DROP VERSUS DIFFERENT FLOW RATES. DATA MANIPULATED TO FIT MSRE DATA; ALL SHELL-SIDE DATA POINTS (BLUE CURVE) HAVE BEEN DIVIDED BY 2 (SEE DISCUSSION IN CHAPTER 7), GPM: GALLON PER MINUTE, FT WATER: FEET OF WATER COLUMN.	105
FIGURE 6.4	FLOW PATHS OF THE SALT IN THE SHELL-SIDE, COLOURED WITH TEMPERATURE.	106
FIGURE 6.5	FLOW PATHS OF THE SALT IN THE TUBE-SIDE, TOP: COLOURED AS TEMPERATURE, BOTTOM: COLOURED AS PRESSURE.	107
FIGURE 6.6	THERMAL BARRIER IN THE SHELL-SIDE, PROTECTING THE TUBE SHEET FROM EXCESSIVE THERMAL CYCLING.	108
FIGURE 6.7	FLOW PATHS OF AIR ACROSS THE RADIATOR AIR-SIDE, FROM LEFT TO RIGHT, COLOURED BY TEMPERATURE.	109
FIGURE 6.8	FLOW PATHS OF SALT THROUGH TUBES FROM TOP TO BOTTOM IN THE RADIATOR, COLOURED BY TEMPERATURE.	109
FIGURE 7.1	DENSITY AND VISCOSITY VARIATIONS OVER TEMPERATURE FOR MOLTEN FLiBe SALT (SOHAL, EBNER, SABHARWALL, & SHARPE, 2010). INSERTED LINES SHOW MAX- AND MIN TEMPERATURE OF THE SALTS IN THE PHeX.	120
FIGURE 7.2	TIMELINE OF REACTOR POWER AND CONDUCTED TESTS (ORNL-TM-3039, 1973).	121
FIGURE 7.3	TEMPERATURE GRADIENT IN SHELL-SIDE OUTLET OF THE PHeX.	126
FIGURE 7.4	FLOW PATHS IN THE PHeX TUBE-SIDE, COLOURED AS VORTICITY, INDICATING TURBULENCE.	127
FIGURE 7.5	OUTLET, MAIN- AND SUB-HEADER OF RADIATOR WITH CONNECTING TUBES. EXAMPLE OF EXCESSIVE USE OF 90 DEGREE BENDS.	127
FIGURE 7.6	GEOMETRY EXAMPLES OF LIMITATIONS WITHIN THE $k - \omega SST$ MODEL. RED ARROWS INDICATE VELOCITY PROFILES OR FLOW PATHS.	128
FIGURE 9.1	DOUBLE INDEX CONVENTION OF TENSORS.	139
FIGURE 11.1	INTERACTION STYLE SWITCH IN SALOME, TO ACTIVATE MODEL CONTROL BY MOUSE MOVEMENT.	141
FIGURE 11.2	OBJECT BROWSER AFTER ALL GROUPS ON GEOMETRY HAVE BEEN CREATED.	143
FIGURE 11.3	MESH GROUP CREATION, INLETShell AS EXAMPLE.	144
FIGURE 11.4	GROUPS OF FACES AND GROUPS OF VOLUMES IN THE OBJECT BROWSER .	145
FIGURE 11.5	SUB-MESH CREATION.	146
FIGURE 11.6	SECTION VIEW OF SUB-MESH COMPUTED FOR THE SOLID REGION.	146
FIGURE 11.7	SECTION VIEW OF MESHED BOUNDARY LAYERS IN TEST MODEL.	147
FIGURE 11.8	SECTION VIEW OF TEST MODEL, FULLY MESHED WITH THE PROCEDURES OUTLINED IN THIS APPENDIX.	148

LIST OF TABLES

TABLE 2.1	CONSTANTS FOR THE $k - \varepsilon$ MODEL	41
TABLE 2.2	CONSTANTS FOR THE $k - \omega$ MODEL	42
TABLE 2.3	CONSTANTS FOR THE $k - \omega SST$ MODEL	45
TABLE 2.4	TABLE INDICATING VALUES USED FOR EVALUATING CELL SKEWNESS (ANSYS, 2008).....	52
TABLE 2.5	COMPOSITION OF FUEL AND COOLANT SALT (ORNL-TM-2098, 1968).....	54
TABLE 2.6	PHYSICAL PROPERTIES OF COOLANT AND FUEL SALT USED IN THE MSRE (ORNL-TM-3039, 1973).....	55
TABLE 2.7	PHYSICAL PROPERTIES OF HASTELLOY-N USED IN THE MSRE (ORNL-TM-2098, 1968).....	55
TABLE 2.8	COMPOSITION OF HASTELLOY-N AND INCONEL-600 (ORNL-TM-2098), (INOR-8 STORY).....	56
TABLE 5.1	QUALITY OF SIMSCALE PHEX MESH	83
TABLE 5.2	QUALITY OF SIMSCALE RADIATOR MESH.	86
TABLE 5.3	QUALITY OF SALOME PHEX MESH.	89
TABLE 5.4	QUALITY OF SALOME RADIATOR MESH.	92
TABLE 5.5	QUALITY OF SALOME HEAT EXCHANGER TEST MODEL MESH.	95
TABLE 6.1	RESULTS AND SALT PARAMETERS FROM THE PHEX, INSTALLED AND OPERATED AT ORNL IN THE MSRE.	101
TABLE 6.2	RESULTS AND PARAMETERS FOR THE RADIATOR, INSTALLED AND OPERATED AT ORNL IN THE MSRE.	102
TABLE 6.3	TEMPERATURE AND PRESSURE DATA FOR THE PHEX, SIMSCALE SIMULATIONS.....	106
TABLE 6.4	TEMPERATURE AND PRESSURE DATA FOR THE RADIATOR, SIMSCALE SIMULATIONS.....	108
TABLE 6.5	ESTIMATES FOR INITIAL VALUES OF TURBULENCE COEFFICIENTS FOR THE OPENFOAM SOLVER ‘CHTMultiRegionFoam’	110
TABLE 6.6	TEMPERATURE AND PRESSURE DATA FOR THE PHEX, OPENFOAM SIMULATION.	111
TABLE 7.1	COMPARISON OF SLOPES OF GRAPHS IN WATER SIMULATION TEST VS. MSRE WATER TEST.	112
TABLE 7.2	DIFFERENCE FOR TEMPERATURE AND PRESSURE ACROSS THE PHEX, MSRE RESULTS.	113
TABLE 7.3	TEMPERATURE AND PRESSURE COMPARISON BETWEEN SIMULATIONS AND MSRE DATA.....	113
TABLE 7.4	INLET- AND OUTLET TEMPERATURE DEFINITION FOR LMTD CALCULATION.....	114
TABLE 7.5	OVERALL HEAT TRANSFER COEFFICIENT PARAMETERS FOR THE PHEX.	114
TABLE 7.6	EXPECTED DIFFERENCE FOR TEMPERATURE AND PRESSURE ACROSS THE RADIATOR, MSRE RESULTS.....	116
TABLE 7.7	TEMPERATURE AND PRESSURE COMPARISON BETWEEN SIMULATION AND MSRE DATA	116
TABLE 7.8	UNCERTAINTIES IN MEASURED PARAMETERS OF FUEL AND COOLANT SALT OF THE MSRE.....	125

SYMBOLS AND ABBREVIATIONS

Abbreviation	Meaning
MSR	Molten Salt Reactor
PWR	Pressurized Water Reactor
BWR	Boiling Water Reactor
LMR	Liquid Metal Reactor
MSRE	Molten Salt Reactor Experiment
ARE	Aircraft Reactor Experiment
ART	Aircraft Reactor Test
ORNL	Oak Ridge National Laboratory
PHeX	Primary Heat Exchanger
IAEA	International Atomic Energy Agency
IEA	International Energy Agency
AEC	Atomic Energy Commission
PDE	Partial Differential Equation
N-S	Navier-Stokes
RANS	Reynolds Averaged Navier-Stokes
GUI	Graphical User Interface
RAM	Random Access Memory
CAD	Computer Aided Design
CAE	Computer Aided Engineering
CFD	Computational Fluid Dynamics
CHT	Conjugate Heat Transfer
LES	Large Eddy Simulation
DNS	Direct Numerical Simulation
1D	One dimension
2D	Two dimensions
3D	Three dimensions
GHG	Green House Gas

Symbol	Meaning
k	Turbulent kinetic energy
ε	Turbulent kinetic energy dissipation rate
ω	Specific turbulence dissipation rate
T	Temperature
p	Pressure
Pa	Pascal
ρ	Density
U	Velocity vector
u	Velocity in x -dir
v	Velocity in y -dir
w	Velocity in z -dir
g	Gravity
e	Internal energy
k_{th}	Thermal diffusion coefficient
E	Total Energy
K	Kinetic Energy
σ	Normal stress
τ	Shear stress
c_p	Specific heat
k	Thermal conductivity
η	Kolmogorov length scale
τ_η	Kolmogorov time scale
u_η	Kolmogorov velocity scale
μ_t	Turbulent viscosity
μ	Dynamic viscosity
ν	Kinematic viscosity
Pr	Prandtl number
\bar{u}_i	Averaged velocity
u'_i	Fluctuating velocity
I	Turbulent intensity
P_k	Production of turbulent kinetic energy
D_ε	Destruction of turbulent kinetic energy
y	Absolute wall distance
y^+	Dimensionless wall distance
u^+	Dimensionless velocity
θ	Non-orthogonality Angle
k	Deviation from orthogonal line
∇	Nabla
∇^2	Laplacian
\cdot	Dot-product
δ_{ij}	Kronecker delta

1 Introduction and background

1.1 Problem formulation of the project

The goal of this thesis is to assess whether the computational fluid dynamics (CFD) platform Simscale, and the open-source CFD-program OpenFOAM, can be used to accurately predict molten salt heat exchanger behaviour. Parameters such as heat transfer and pressure loss will be simulated using a conjugate heat transfer (CHT) simulation using the $k - \omega SST$ turbulence model. Data gathered from the Molten Salt Reactor Experiment (MSRE) reports written in the 1960s and 1970s will be used as validation, and the accuracy of the data gathered in the reports will be analysed and commented upon.

Other papers have been written on fluid dynamics for Molten Salt Reactors (MSRs), but those that have been found are a combination of CFD and neutronics (the physics of radioactivity) (Lecce, 2018). Since most neutronics software have been developed to fit the needs of the current industry, they are based on modelling solid fuel particle interactions and burnup, thus not directly applicable for fluid fuel behaviour (Okui & Sekimoto, 2009). Vasconcelos et. al. has written an article about a proof-of-concept to bridge this gap, but currently no such software exists (Vasconcelos, Santos, Campolina, Theler, & Pereira, 2018). Thus, fluid simulations of radioactive systems tend to simplify the model to make the use of existing neutronics software possible. However, the systems modelled in this thesis does not concern the neutronics of the reactor core, and therefore the neutronics are neglected completely, allowing for a much more finely detailed model and CHT.

The two components of the MSRE that will be modelled and simulated in this thesis are the molten-salt-to-molten-salt U-tube shell-and-tube primary heat exchanger (referred to as the 'PHeX' throughout the thesis), and the molten-salt-to-air radiator, both shown in great detail in Chapter 4. Modelling these two rather complex components and validating the simulations to the experimental data will give great insight into the feasibility of using CFD-software in more general molten salt environments. Not many articles have been found on full CFD simulations of shell-and-tube heat exchangers, and those that have been found usually involve much smaller and simpler models (Pal, Kumar, Joshi, & Maheshwari, 2016).

Since most of the software available for computer aided design (CAD), meshing algorithms and fluid simulations are expensive and mostly non open-source, it is difficult sharing ideas between companies, students or researchers. Therefore, all the programs used for this project will be open-source so that anyone can access and simulate these results for themselves to develop these models further. The exciting field of MSRs is in its naissance, and therefore collaborations between the people developing this technology is going to be crucial to bring it into fruition.

1.2 Computational Fluid Dynamics

Computers have grown more and more powerful over the last few decades and with that, increasingly complex systems can be modelled and analysed. This is of particular interest when analytical or theoretical results cannot be obtained, for example when the model of interest is too complex. Simulation of the model is often the only way forward, and a multitude of tools exist for this purpose. In the world of fluid mechanics, an indispensable tool is Computational Fluid Dynamics (CFD).

One of the many aspects of fluid flow that makes it so difficult to model is the inherent property of fluids to exhibit turbulent behaviour; a highly disorganized and diffusive behaviour of fluids that is particularly difficult to simulate.

The Navier-Stokes (N-S) equations, which are a set of non-linear, second order partial differential equations (PDEs), describe fluid flow and underpin every CFD-software available. Only a handful of analytical solutions for some very special cases exist, where for example the geometry is defined in such a way to eliminate the non-linear terms. Thus, in general, analytical solutions to the N-S equations cannot be reached, and a numerical, CFD-approach is the only viable method of obtaining useful results. The first use of CFD in practice is credited to Hess & Smith as early as 1967 (Hess & Smith, 1967). Since then, CFD has been used to model heat- and fluid flow for most situations imaginable and is indispensable for industries and researchers alike.

CFD-based code involves a solution of conservation of mass, momentum and energy over the defined region. The equations can be approximated for a mesh element, where the flux of the just mentioned quantities moving in and out of the element is considered with suitable boundary conditions.

Breaking down complex geometries in what is known as a mesh and solving fluid- and/or heat equations over the many volumes and surfaces of the mesh-elements (which for this project ranges to tens of millions of mesh-elements) is a powerful technique to solve fluid flows and heat transfer for any geometry that can be modelled. The complexity or resolution of the mesh, meaning the

number of mesh-cells and boundaries, puts a practical limit on what computers can calculate within a reasonable time. However, more accurate results are usually reached when the resolution of the mesh is increased. The cost-benefit of a more highly resolved mesh and thereby longer solving time is something that everyone that uses CFD must keep in mind.

To deal with the aforementioned complexities of a fluid's turbulent behaviour, there exists a multitude of different CFD approximations and methods. Those utilized for this project are called $k - \varepsilon$ and $k - \omega SST$ (Shear Stress Transport), both will be explained in Chapter 2.

1.3 A brief overview of the role of nuclear fission in today's society

Since 1980 the world's electricity generation and demand has more than doubled (IAEA, 2007). As the power demand of the world increases, there is a need for new and innovative solutions to power generation. Many methods of power generation are readily available, and the last decade has seen an unprecedented development in solar and wind around the world (Manzano-Agugliaro, Alcayde, Montoya, Zapata-Sierra, & Gil, 2013), (Best & Burke, 2018).

However, these sources cannot function as base load for power generation in our societies, since they are inherently intermittent, meaning that they are not predictable and cannot produce a stable output of power. Lacking sufficient energy storage, backup power is needed to provide a stable output, meaning that other power generation methods must be utilized.

When talking about energy it is crucial to be clear about the units. There is an important distinction between power and energy. Power is measured in watts (W), which has units of J/s , or unit of energy per unit of time. Energy is measured in watt-hours (Wh), which has units of J . Running one watt for one hour generates one Wh of energy. This means that installed capacity is expressed in terms of power (W) but energy produced is expressed in terms of energy (Wh or, equivalently, J).

Among the many ways we have of generating useful energy, six major types dominate the electricity market, namely:

- Oil
- Coal
- Natural gas
- Hydropower
- Nuclear
- Renewables (solar, wind, geothermal, tidal, etc.)

These production means are broken down and shown as world Total Energy Supply, TES and world Total Electricity Production, TEP seen in Figure 1.1 (Data from International Energy Agency, IEA).

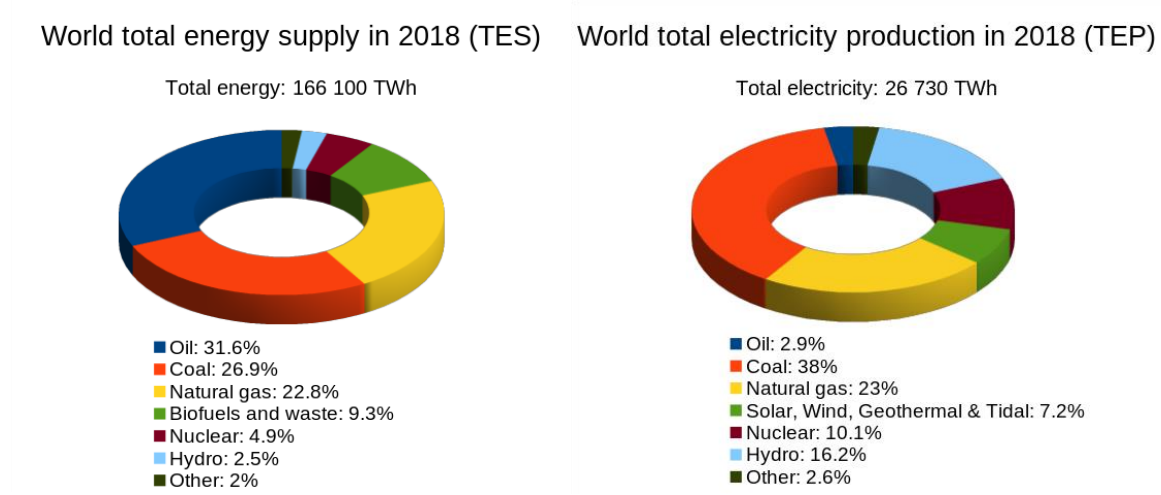


*Figure 1.1 TES and TEP as of 2018 broken down by source.
Left: World total energy supply (IEA, 2020),
Right: World total electricity production (World Nuclear Association, 2020).*

The right diagram in Figure 1.1 shows only electricity production where, for example, oil is a rather insubstantial candidate at only 2.9% (about 775 TWh). However, in the left diagram heat production and transportation is also included as energy usage, where oil shows up as the biggest contributor at 31.6% (about 52 500 TWh), showing clearly how dependent the world still is on oil as an energy source.

In contrast, the right diagram in Figure 1.1 shows that nuclear energy accounts for about 10% of the world's total electricity production, which is about 2 670 TWh.

The TES in the left diagram is estimated to roughly 166 100 TWh, which is about 6 times as much as the 26 730 TWh of electricity production, clearly showing that electricity production is a minority when looking at energy usage in society.

Coal-fired power capacity has doubled between the years 2000 – 2019, to around 2 045 gigawatts (GW) of power (Carbon Brief Ltd., 2020) which poses many problems, e.g. ecologically and environmentally. The International Atomic Energy Agency (IAEA) have made an extensive review of the entire life-time greenhouse gas (GHG) emissions for the major energy sources listed previously (IAEA, 2016) and the results are shown in Figure 1.2. It is clear that we need to move away as quickly as possible from fossil fuels to limit our GHG emissions. It is also clear that nuclear energy has very low GHG emissions and is therefore a prime candidate for clean energy generation, especially considering its scalability and reliability.

What are the **safest** and **cleanest** sources of energy?

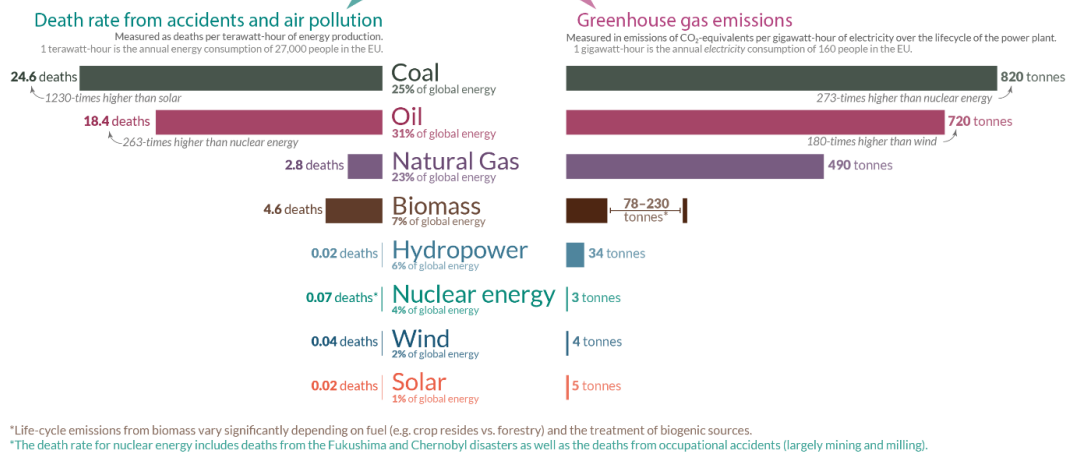


Figure 1.2 Life-time greenhouse gas emissions for contemporary electricity production means, together with death rates per TWh of energy produced (Ritchie, 2020).

To make the case for nuclear even stronger, the International Atomic Energy Agency (IAEA) has made a comparison of land requirement per GW of capacity between nuclear, wind and solar energy, shown in Figure 1.3.

As seen, nuclear is vastly more land efficient for the same power output, which is one of the many positive aspects surrounding nuclear energy.

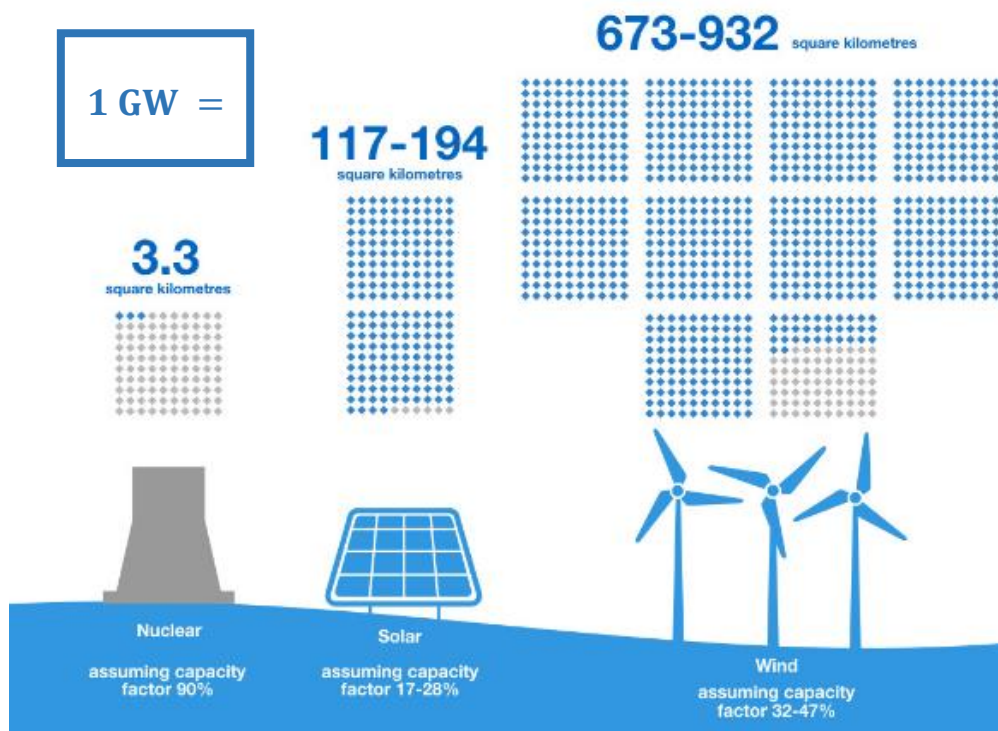


Figure 1.3 Land requirement for nuclear, wind and solar technologies per 1 GW of capacity (IAEA, 2016).

In 2019, 450 nuclear power reactors were in operation worldwide, totalling around 400 *GW* of net installed capacity, according to IAEA (IAEA, 2020). In the paper “International status and prospects for nuclear power”, published in 2017 by the IAEA, a projection of the future of nuclear energy into the 2050s is carried out for two scenarios, called ‘high’ and ‘low’ in the report, shown in Figure 1.4 (IAEA, 2017). The ‘low’ case assumes that nuclear power will slowly reduce in total world capacity up until the 2050s. In the ‘high’ case, approximately 30 – 35 additional reactors must be connected to the electricity grid every year, starting in 2025. This rate of connection of nuclear fission was last seen in 1984 when 33 new reactors were connected to the grid.

No emphasis is put on which of these scenarios is the most likely, since this depends on many factors, most notably public and political acceptance of nuclear energy, which is a hot topic all over the world. The significance of this is to highlight the fact that even if the ‘high’ case were to be implemented, the total share of energy coming from nuclear fission would not increase by much.

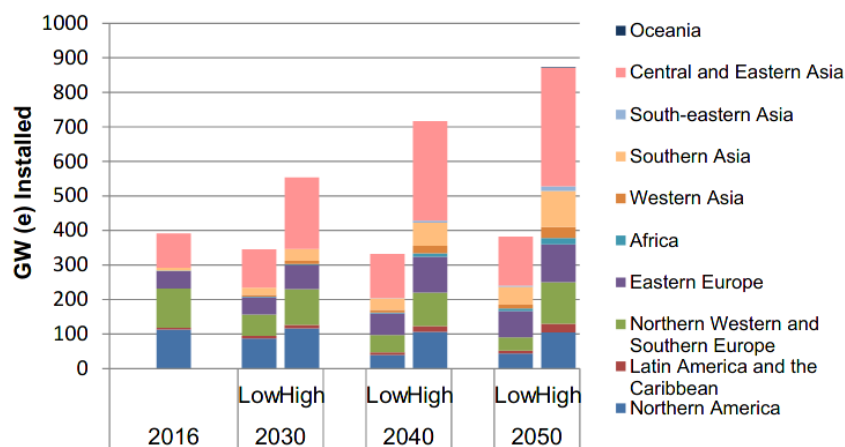


Figure 1.4 Net installed nuclear capacity, projected as ‘high’-case and ‘low’-case to 2050 (IAEA, 2017).

Nuclear energy production varies hugely from country to country. One of the more notable examples is France, who’s current electricity profile is primarily made up of nuclear fission of around 80% of the total energy generated, averaging around 32 *g/kWh* of *CO*₂ equivalent GHGs, which is one of the lowest in Europe. (World-Nuclear, 2021). Contrasting this with Poland, which has an electricity production profile of about 50% coal (GUS, 2019) and an average of 650 *g/kWh* of *CO*₂ equivalent GHGs. Comparing these two countries, it is clear that nuclear energy can be of great use to limit a country’s total GHG emission. The webpage ‘electricitymap’ (Electricitymap.org, 2021) is a fantastic resource for real-time updates of GHG emission and electricity production breakdown around the world.

If we intend to continue our expansion of civilization, with ever increasing power demands and electrification of goods and services, effective and scalable energy solutions must be found with little to no environmental impact. Nuclear fission is most probably going to be one of the solutions to provide a stable, predictable and scalable base load (Buongiorno, Corradini, Parsons, & Petti, 2019). Since the 1940s, nuclear power has often been regarded as the future of energy; the harnessing of the power of the atom being arguably one of mankind's greatest achievements. The first sustained criticality of a nuclear reactor was achieved on the 2nd of December 1942 underneath University of Chicago's Stagg Field football stadium. The reactor was named "Chicago Pile-1", led by the infamous physicist Enrico Fermi (U.S. Department of Energy, 1982).



*Figure 1.5 Chicago Pile-1.
Left: In full operation (U.S. Department of Energy, 1982),
Right: Artists rendition (Sheehan, 1957).*

Since then, a catalogue of different reactors has been designed and realized, such as the boiling water reactor (BWR), pressurized water reactor (PWR), liquid metal reactor (LMR) and molten salt reactor (MSR) to name just a few.

1.4 Basics of how nuclear fission operates

Today, the most commonly used reactor is the Pressurized Water Reactor (PWR), comprising about 60% of the world's operational reactors (World-Nuclear, 2020). It operates with two closed water loops, one primary loop going through the reactor core and one secondary loop through a steam turbine. A third, open loop connected to a nearby water supply is utilized to condense the secondary loop after it has gone through the steam turbine. In Figure 1.6 a schematic of a PWR is shown.

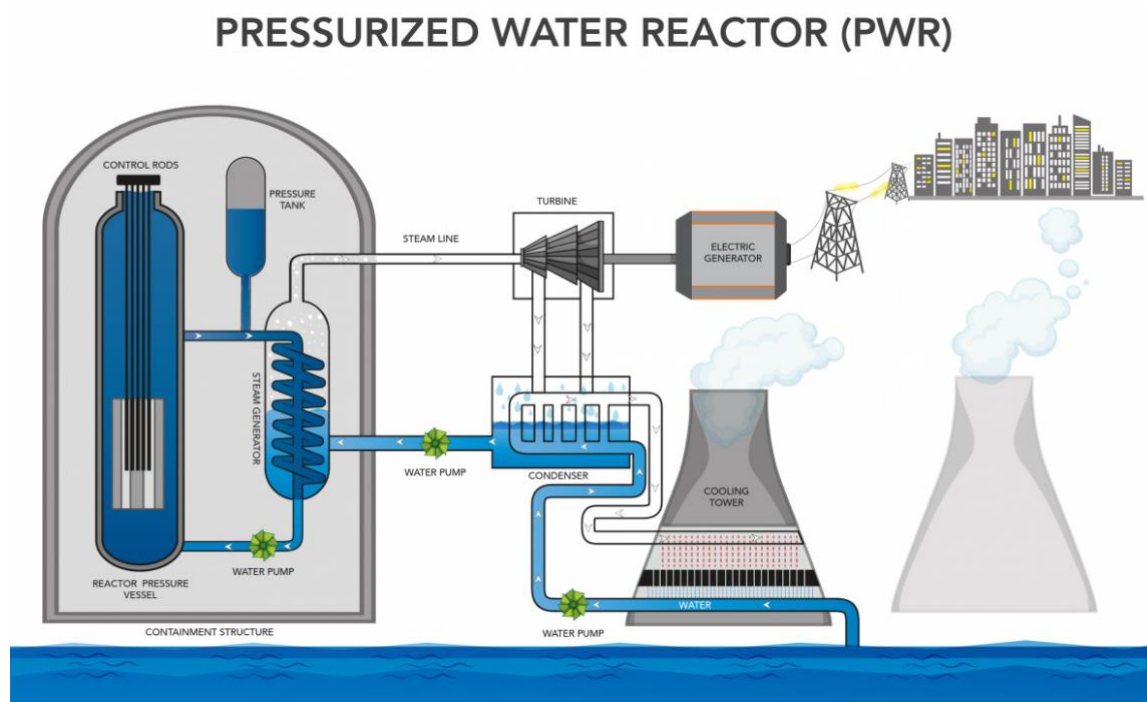


Figure 1.6 Schematic of a pressurized water reactor.
Graphics by Sarah Harman, U.S. Department of Energy (Energy.gov, 2021).

The primary loop that goes through the core is pressurised to about 150 atm, keeping the water in its liquid state as the temperature rises to about 300 degrees C as it absorbs heat from the fission process in the core. This heat is then transferred to the secondary, unpressurised loop, through a heat exchanger, and the water in the secondary loop is turned to steam to drive a steam turbine, generating the power. The steam is then cooled, condensed and sent back into the heat exchanger. The water in the primary loop acts as coolant to the core as well as a moderator, slowing down neutrons, which facilitates more fission reactions, maintaining the chain reaction inside the core. The heat in the core comes from the fissioning of ^{235}U in the core, which releases vast amounts of energy, splitting each fissioned atom of ^{235}U into lighter elements (called the 'fission products' or

‘fission yields’), which in turn decay a number of times until they reach a stable element, usually lead (*Pb*) or iron (*Fe*). For quantum mechanical reasons, exactly which elements that a particular ^{235}U atom will fission to is undefinable, but for a large number of fission events the distribution is well known and is shown in Figure 1.7.

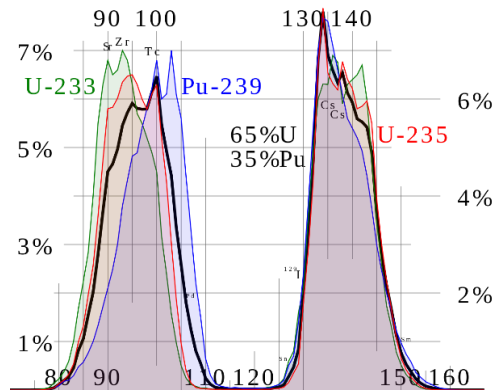


Figure 1.7 Fission products from ^{233}U (green curve), ^{239}Pu (blue curve) and ^{235}U (red curve).
X-axis: number of particles in nucleus of the fission product,
Y-axis: fission product yield in % (Dayman, Biegalski, & Haas, 2014).

The reason that the fission products decay is that the number of neutrons in the nucleus of each fission product will be high compared to the stable isotopes of the same element. This is clearly seen from the Figure 1.8, showing that stable elements (black in the graph) contain more neutrons than protons as we go up in atomic number.

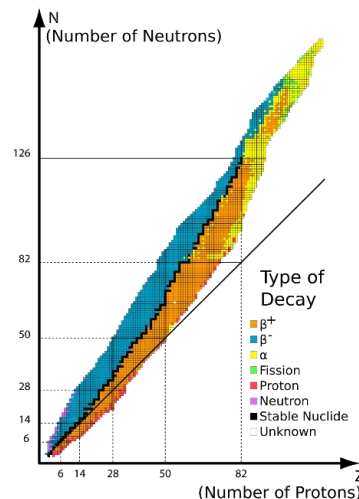


Figure 1.8 Standard isotope chart and nuclear decay modes.

^{235}U (with 92 protons) has $235 - 92 = 143$ neutrons, and when this element is split into 2 smaller nuclei, the ratio of neutrons to protons will put that fission product well off the black line of stable elements in Figure 1.8. Thus, it will be very unstable and decay a number of times until it reaches a

stable element. The radiation released by this decay is the main reason why spent nuclear fuel is so harmful and needs to be confined for a long time.

For the ^{235}U atom to actually undergo a fission event it needs to be struck by a neutron to turn into ^{236}U which has a very short half-life, meaning that it is highly unstable. Graphical depiction of fission shown in Figure 1.9

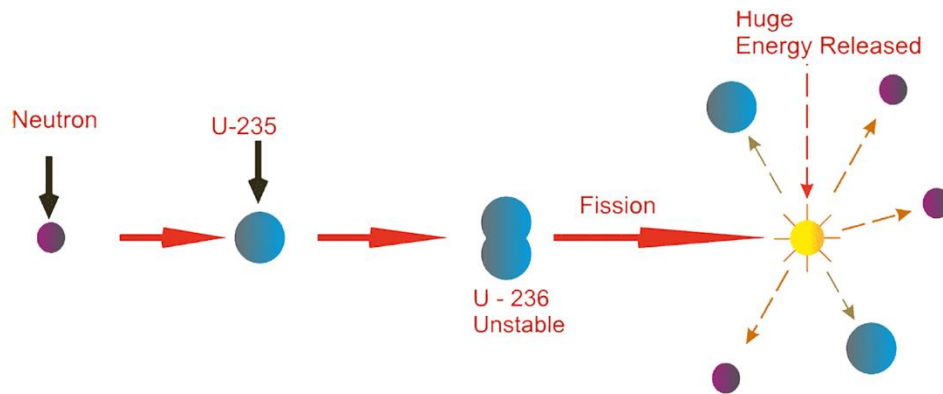


Figure 1.9 Fissioning of ^{235}U .

The fissioning event releases further neutrons, which in turn causes more ^{235}U to undergo fissioning events. This is the underlying basis of the chain reaction of nuclear fuel that all nuclear reactors are based upon. Schematic of the chain reaction shown in Figure 1.10.

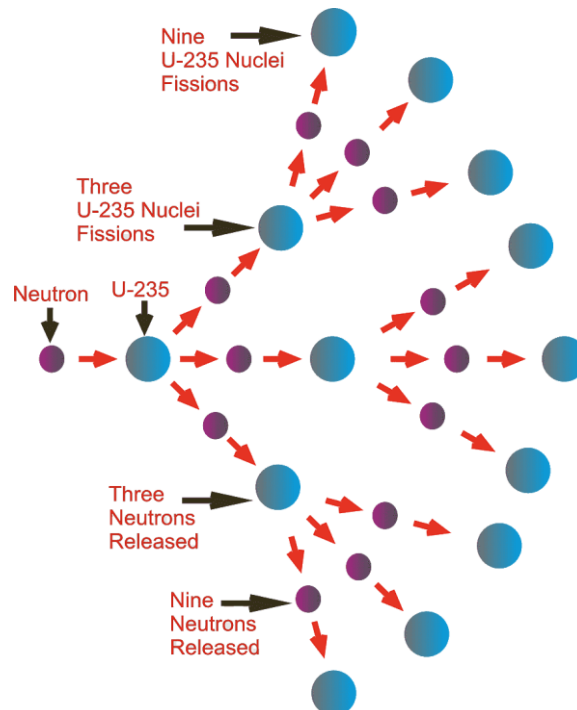


Figure 1.10 Nuclear chain reaction of ^{235}U

The energy of the neutrons that are released from the fissioning of ^{235}U is too high initially, and without any modification of the physical system the chance of one of these neutrons striking the nucleus of another ^{235}U atom is very low. To solve this a moderator needs to be introduced, to slow the neutrons down sufficiently to increase the probability (also known as ‘cross section’) of the neutrons being absorbed by the ^{235}U . There are many different moderators, and as stated, the conventional PWR uses the water that passes through the core for this purpose.

In Figure 1.11, a chart over neutron yield (y-axis) versus log of neutron energy spectrum (x-axis) is shown. Kirk Sorensen, a great proponent of MSRs and the person that sparked my own interest in this subject, says when talking about the contents of Figure 1.11 that:

“I think you can probably tell the entire history of the development of nuclear energy in this one graph.”

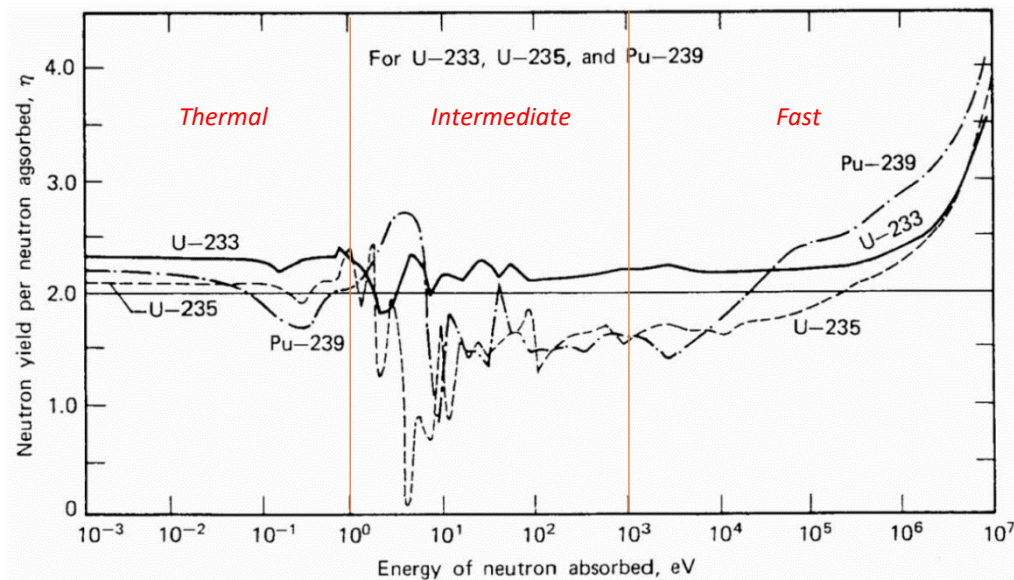


Figure 1.11 Neutron yield versus energy spectrum of neutron in ^{233}U , ^{235}U and ^{239}Pu (Waltar, Todd, & Tsvetkov, 2012).

Figure 1.11 shows the number of neutrons ejected from the nucleus of a given species depending on the incident energy of the neutron. This figure can be broadly thought of as three regions; thermal ($10^{-3} - 10^0 \text{ eV}$), intermediate ($10^0 - 10^3 \text{ eV}$), and fast ($10^3 - 10^7 \text{ eV}$) (Waltar, Todd, & Tsvetkov, 2012). The number of neutrons that get ejected is the important parameter in Figure 1.11, since it determines what kind of reactor in what kind of physical environment can be used for different fuels.

In conjunction with Figure 1.11, another diagram needs to be shown, namely that of the cross sections of these different regions. Such a diagram is shown in Figure 1.12.

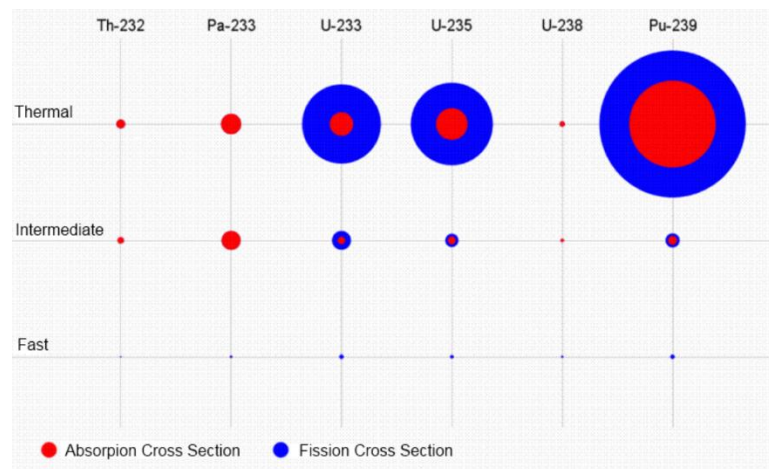


Figure 1.12 Cross section (interaction probability) of Th, Pa, ^{233}U , ^{235}U , ^{238}U and ^{239}Pu in thermal, intermediate and fast spectrum of incident neutron (Waltar, Todd, & Tsvetkov, 2012).

The red cross section corresponds to the probability of a neutron being absorbed but not leading to a fissioning event. The blue cross section corresponds to the probability of a neutron being absorbed and then followed by a fissioning event of the created isotope. The size of these cross sections is analogous to the probability of such an event occurring, and the main takeaway from Figure 1.12 is that as the energy of the incident neutron increases, the probability of an interaction with the nucleus of the target atom decreases.

Thus, to make a fast spectrum reactor, the neutron density needs to be much higher to keep the core critical so that the reactor can produce energy. The upside is that these types of reactors are not very dependent on an efficient moderator since the neutrons do not need to be slowed down. For a thermal spectrum reactor, a lower neutron density is needed to keep the core critical, but it is dependent on an efficient moderator to slow the neutrons down to the desirable ranges of energy. I will not go into any more detail about this since this is outside of the scope of the current project. For more information about this, see Kirk Sorensen's talks on YouTube as well as the textbook by Alan E. Waltar et. al. (Waltar, Todd, & Tsvetkov, 2012).

For a comprehensive analysis of the PWR see the following reference (Durmaz & Yavuz, 2001)

As stated, the PWR is only one of many nuclear power plant designs. The primary reason why this is the most commonly used reactor worldwide is the know-how and existing infrastructure combined with mining operations surrounding everything from manufacturing to operating the power plant.

However, many problems exist with the PWR, most notably the reliance on high pressure keeping the superheated water that runs through the core in its liquid state. In the event of sudden, radical pressure loss, for example a double ended pipe-break, the water instantly vaporizes, increasing in volume by a factor of about 1000. This is one of the main reasons that PWRs have large containment buildings; to keep the radioactive, vaporized water contained in the event of one of these decompressions. Since the water going through the core serves two critically important roles, namely that of coolant and that of moderator, the loss of this water due to vaporization means that the reactor can go through a critical meltdown process. This must be circumvented, and a myriad of safety measures are included in the design of PWRs to shut down the reactor in the case of such an event.

Switching from using water as a coolant, thereby avoiding the need to have it pressurized, would solve many of the existing problems with today's nuclear fission. This is where the Molten Salt Reactor becomes appealing.

The focus of the current report is on MSRs, specifically the reactor built and operated at Oak Ridge National Laboratories (ORNL) in Tennessee, United States of America in the 1960s, referred to as the Molten Salt Reactor Experiment (MSRE).

1.5 Leading up to the MSRE

In the 1940s the US started working on nuclear marine propulsion. The first submarine to use nuclear propulsion was the USS Nautilus and was put to sea in 1955 (World-nuclear, 2021). In conjunction with the successful incorporation of nuclear fission reactors as a power source for the United States navy's submarines, the U.S. air force wanted to experiment with nuclear powered aircrafts to overcome range limitations of jet-fuelled aircrafts at that time. Since water cooling was impractical in an aircraft, in what had to be a lightweight, small and resilient system, other nuclear power generation options were researched.

Research into molten salt technology began in 1947 at ORNL under the direction of the American scientist Alvin Martin Weinberg, as part of the US program the 'Aircraft Reactor Experiment' (ARE), wherein research into a nuclear powered aircraft was the main objective (Rosenthal, Kasten, & Briggs, 1969) (Bettis, et al., 1957). The idea of an MSR was developed by Ed Bettis and Ray Briant in this project (MacPherson, 1985), and around 25% of the entire funding at ORNL went into the ARE (Gonçalves, Maiorino, Monteiro, & Rossi, 2019).

The reactor in the ARE, developed for testing purposes, was a rather complicated machine, pumped

with a molten salt fuel mixture of sodium fluoride (NaF), zirconium fluoride (ZrF_4) and uranium fluoride (UF_4) through Inconel-600 tubes at a temperature of 870 C. Inconel-600 is a superalloy, composed of primarily of nickel (Ni) and chromium (Cr), with great thermal and corrosion resistance (McCoy, 1969). The reactor achieved criticality in November 1954 and operated for 221 hours before being dismantled for examination.

Much of the complication surrounding the ARE was the use of beryllium oxide (BeO) as a moderator. The beryllium would dissolve into the fuel salt and degrade it, and to circumvent this, pipes of Inconel-600 was used to let the fuel salt flow through the moderator.

The ARE was shut down the 12th of November 1954, after testing was successful and reactor criticality was achieved, and was followed by the Aircraft Reactor Test (ART). This test was discontinued in 1957, but the high promise of MSR technology for achieving low electric power generating costs led ORNL to continue the program in other avenues, mainly into the MSRE.

The researchers at ORNL summarized the *advantages* of MSR technology as follows (ORNL-TM-0728, 1965):

1. The fuel is fluid at reactor temperatures, thus eliminating extra cost for fabrication, handling and reprocessing of solid fuel elements.
2. Burnup of fuel is not limited by radiation damage or reactivity loss.
3. The fuel can be reprocessed continuously in a side stream for removal of fission products and new fissionable material can be added while the reactor is in operation.
4. MSRs operate at high temperature and produce high pressure, superheated steam to achieve thermal efficiencies in the heat-power cycle equal to the best [contemporary] fossil fuel fired plants.
5. Low vapor pressure of the salts permits use of low-pressure containers and piping.
6. Negative temperature coefficients of the reactor (a self-stabilizing feature of MSRs) leads to nuclear safety that is not dependent on fast acting control rods.
7. The fuel salt has a low cross section (interaction probability) for the parasitic absorption of neutrons. This leads MSRs to be efficient converters and breeders on the $Th-^{233}U$ cycle.
8. The fluoride salts used as the fluid fuel mixture have good thermal and radiation stability and do not undergo violent chemical reactions with water or air. Volumetric heat capacity, viscosity, thermal conductivity and other properties all lie within desirable ranges.
9. Use of high circulation rates and large temperature differences results in high mean power density, high specific power and low fuel inventory.

These points, among many others, led the people at ORNL to conceive and develop new reactor concepts to further the MSR design.

Some of the *disadvantages* that ORNL has identified with MSR technology are (ORNL-TM-0728, 1965):

1. The fuel salt melts at 450 C, so all salt-containing portions of the reactor must be kept above this temperature.
2. Fluoride salts react with oxygen and can potentially precipitate fuel constituents as oxides. Zirconium is added in the fuel salt to remedy this, but care must be taken to prevent the fuel from being contaminated with air, water or other oxygen containing materials.
3. The radioactivity in any fluid fuel system is in a mobile form, so special provisions must be taken for containment and maintenance.

Overall, the promising results of the ARE and ART paved the way for a reactor concept that could become a real contender with contemporary means of generating power. In 1956, the interest in nuclear powered aircraft began to fall off, and Alvin Weinberg wished to see whether the molten fluoride fuel technology could be adapted for civilian use (MacPherson , 1985).

1.6 The MSRE

After the ART was decommissioned in 1957 design of the MSRE was started in the same building, building 7503 in the summer of 1960, shown in Figure 1.13. This was done after the Atomic Energy Commission (AEC) put together a task force called ‘the Fluid Fuels Reactor Task Force’. In 1959 they wrote a report, in which the first sentence of the summary reads “The Molten Salt Reactor has the highest probability of achieving technical feasibility” (Atomic Energy Commission , 1959).

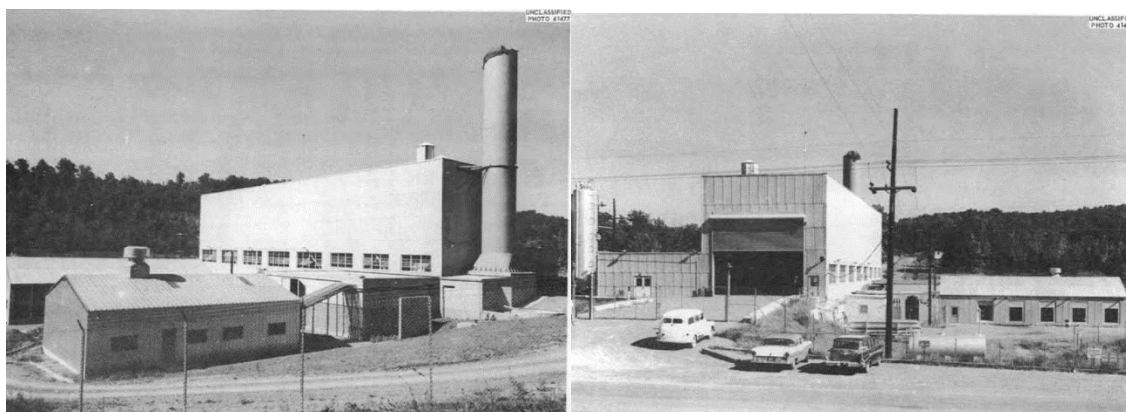


Figure 1.13 Building 7503 at the Oak Ridge National Laboratory, Oak Ridge, Tennessee, MSRE headquarters (ORNL-2465, 1960).

*Left: View from Southwest,
Right: View from Northwest.*

Research went on to provide the first large scale, long term, high temperature tests in a reactor environment of the fuel salt, graphite moderator and alloy capable of withstanding the physical environment. Discoveries that graphite and the fuel salt used in the MSRE were physically compatible made the construction of the core much simpler.

The hope was that data from the MSRE could provide important information regarding the feasibility of large-scale molten salt reactors, and thus serve as a proof of concept. The main objective was to demonstrate the safety, dependability and serviceability of an MSR, as well as validating the use of graphite as a moderator in an operating power reactor (MacPherson , 1985).

The MSRE was a 7.4 MW molten salt fueled, graphite moderated, single region reactor. Initially, this reactor was designed to output 10 MW of power, but due to errors in calculations of the effectiveness of the heat exchangers the full plant could only output 7.4 MW. This error will be revisited in Chapter 7.

One of the unique aspects with this reactor concept is that the power is generated in circulating fluid fuel, rather than stationary solid fuel elements as in contemporary PWRs. This allows fission products to be extracted from the solution, while more fuel salt can be added during ongoing

operation. It can be shown that most fission products will at some point decay through a gaseous phase, which can be exploited for safe removal (MacPherson , 1985).

A special metal alloy had to be invented that could withstand the temperature and corrosion of the salt (McCoy, 1969) (Haubenreich & Engel, 1970). Previously used Inconel-600 was not corrosive resistant enough, and the researchers at ORNL wanted the MSRE to be able to run for extended periods of time. Thus, research went into superalloys capable of withstanding the physical environment and Hastelloy-N (also known as INOR-8) was developed and produced in 1956 at ORNL (McCoy, 1969), having much better corrosion resistance due to a lower concentration of chromium in its constituents, which will be displayed in Chapter 2. Every metal component in contact with the salt of the MSRE was built using Hastelloy-N.

The MSRE operated at a nominal temperature of 650 C and first went critical on 1st of June 1965. Its operation was terminated on 12th of September 1969, after it had completed 17,655 hours of criticality (ORNL-TM-3229, 1970). Figure 1.14 is a timeline for activities leading up to power operation for the MSRE as well as a table showing important milestones of the MSRE.

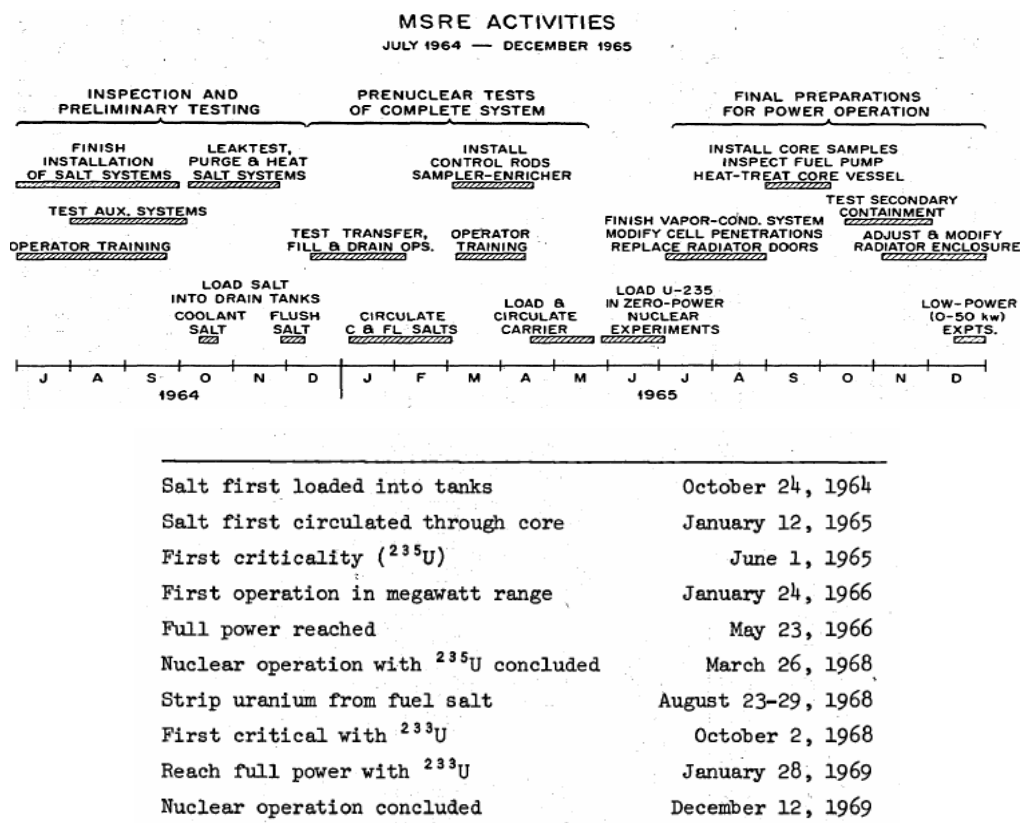


Figure 1.14 Top: MSRE activities leading up to power testing, from summer 1964 to end of 1965. Bottom: Important milestones for the MSREs full lifetime (ORNL-TM-3039).

1.6.1 Plant design of the MSRE

The major components of the MSRE are listed below in Figure 1.15. The ones concerning this project are number 2 (the primary heat exchanger), and number 7 (the radiator).

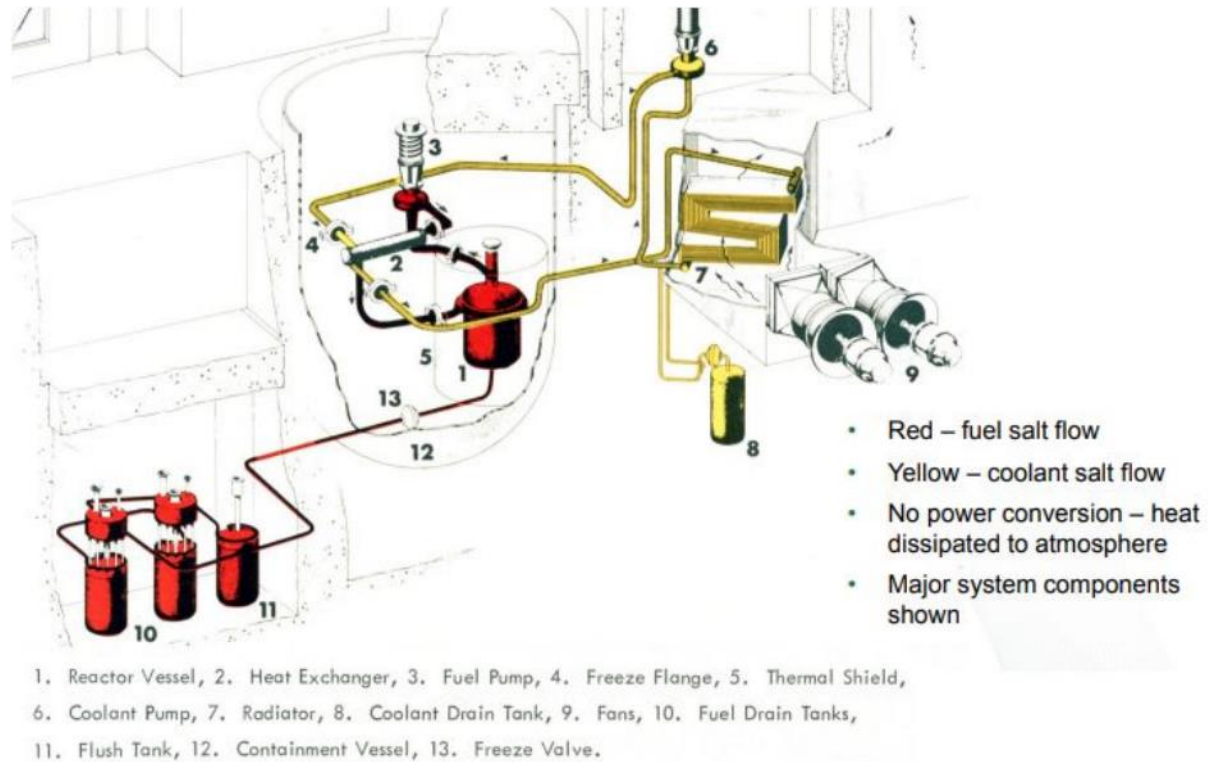
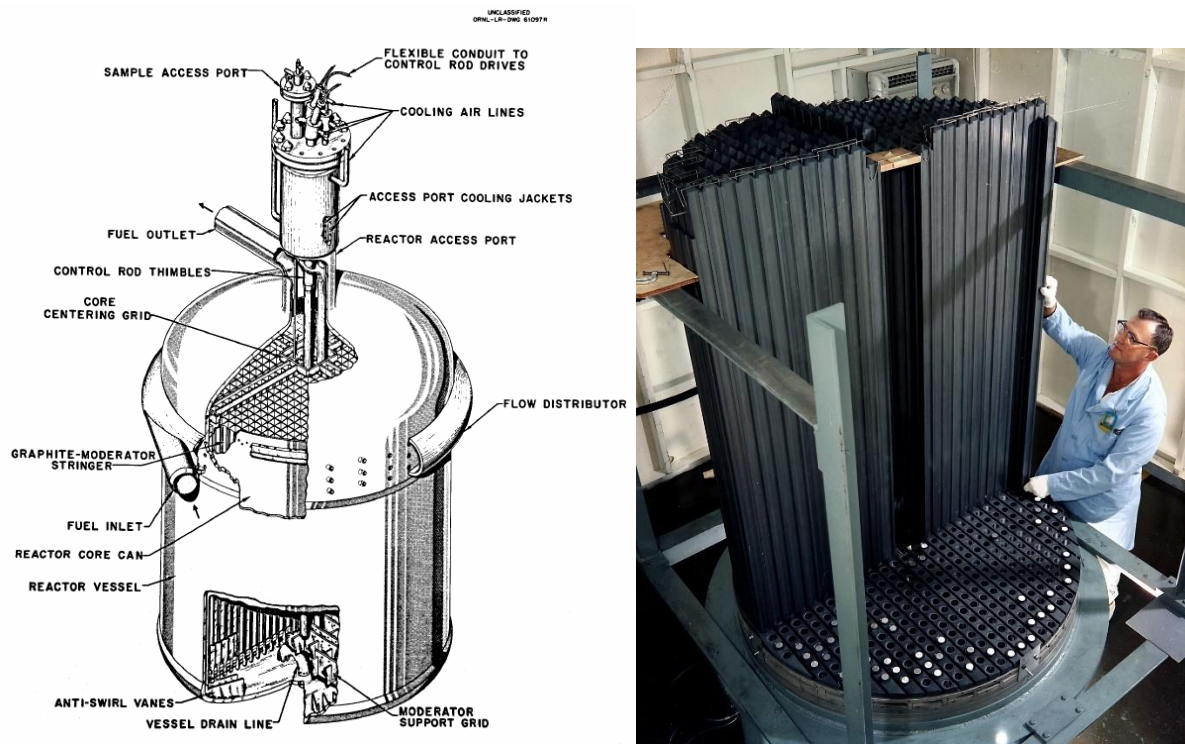


Figure 1.15 Molten Salt Reactor Experiment plant design, showing the major components and the two primary salt loops, red and yellow (Gonçalves, Maiorino, Monteiro, & Rossi, 2019).

The fuel salt circulating system (red in Figure 1.15) is the reactor primary system. It consists of the reactor vessel (1) where the nuclear heat is generated, the primary heat exchanger (2) in which heat is transferred from fuel to coolant, the fuel circulating pump (3), and the interconnecting piping.

The coolant system (yellow in Figure 1.15) is the reactor secondary system. It consists of the coolant pump (6), the radiator (7) in which heat is transferred from coolant salt to air, the primary heat exchanger (2) and the interconnecting piping. When the circulating systems are not in operation the fuel is contained in the drain tank system (10) (ORNL-TM-0728, 1965).

1.6.2 MSRE reactor core



*Figure 1.16 The MSRE reactor core (Powers, 2019).
Left: Section view of technical drawing from ORNL,
Right: Halfway completed graphite rod assembly of core.*

The reactor vessel is a 1.5 m diameter by 2.4 m high tank, that contains the 1.4 m diameter by 1.6 m high graphite core structure seen to the right in Figure 1.16.

Grooves were machined in each side of the 4-sided square graphite bars, such that when they were put together, the grooves formed channels that the fuel salt could flow through. A typical arrangement of graphite bars can be seen in Figure 1.17.

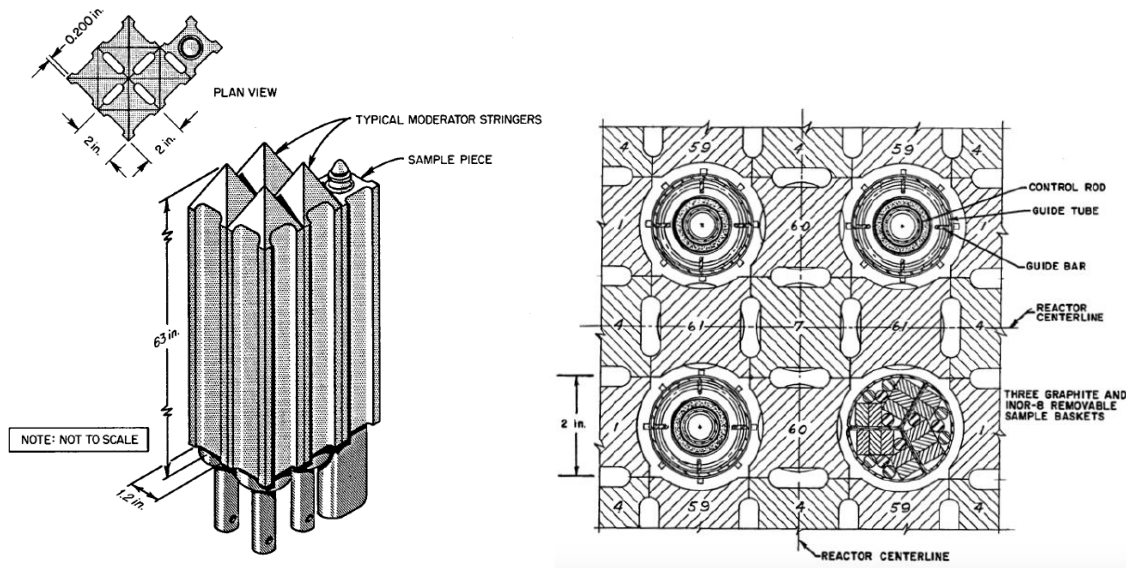


Figure 1.17 Typical graphite bar arrangement.

Left: Lengthwise section view configuration,

Right: Section view of graphite bars across centreline of the reactor (Shen, Fratoni, Aufiero , & Bidaud, 2018).

The fuel would enter the top of the vessel at 635 C , at around 140 kPa difference to the atmosphere, at a flow rate of about 4.54 m^3/min . The fuel is distributed evenly around the circumference of the vessel and then flows turbulently downward in a spiral path through a 2.54 cm annulus between the vessel wall and the core can. At the bottom of the lower plenum of the reactor vessel the salt loses its rotational motion when flowing past straightening vanes, and then flows up, through the machined channels in the graphite bars. While the salt is flowing through the graphite bars, fissioning of the uranium occurs and raises the temperature of the salt. As the salt exits the core at the top of the reactor vessel (seen in Figure 1.16) its temperature is around 663 C (Shen, Fratoni, Aufiero , & Bidaud, 2018).

1.6.3 MSRE primary heat exchanger

One of the main components in the MSRE is the primary heat exchanger (referred to throughout this document as the PHeX, for short). It fulfils a simple function; to transfer heat from the fuel salt to the coolant salt at a sufficiently high rate.

The design of the PHeX for the MSRE was a conventional U-tube shell-and-tube heat exchanger with cross baffles, used extensively in industry (Annaratone, 2010), (Mohanty & Arora, 2020). The baffles (seen in the upper right of Figure 1.18, going across the tubes at various lengths) force the fluid in the shell-side to change direction multiple times along its path, which creates a counter flow across

the tubes, rather than just along them had the baffles not been there. This greatly increases the heat transfer capability of the heat exchanger by making the fluid very turbulent in the entire region. This design was chosen by the team at ORNL since there were a lot of experience of building and operating these heat exchangers available, as well as being one of the more efficient heat exchangers on the market at the time.

The primary salt contains the fissionable material and is never in direct, chemical contact with the secondary salt; they only exchange heat through contact with joined Hastelloy-N surfaces. Molten salt flows through the shell-side of the PHeX at $4.54 \text{ m}^3/\text{min}$, cooling it from 663 C to 635 C . Coolant salt circulates through the tubes at $3.22 \text{ m}^3/\text{min}$, heating it from 552 C to 593 C (ORNL-TM-2098, 1968).

An early version of the completed PHeX for the MSRE can be seen in Figure 1.18, and the completed tube bundle is shown in Figure 1.19.



Figure 1.18 Earlier iteration of the primary heat exchanger made by the team at ORNL (Thorium Energy Alliance, 2020).

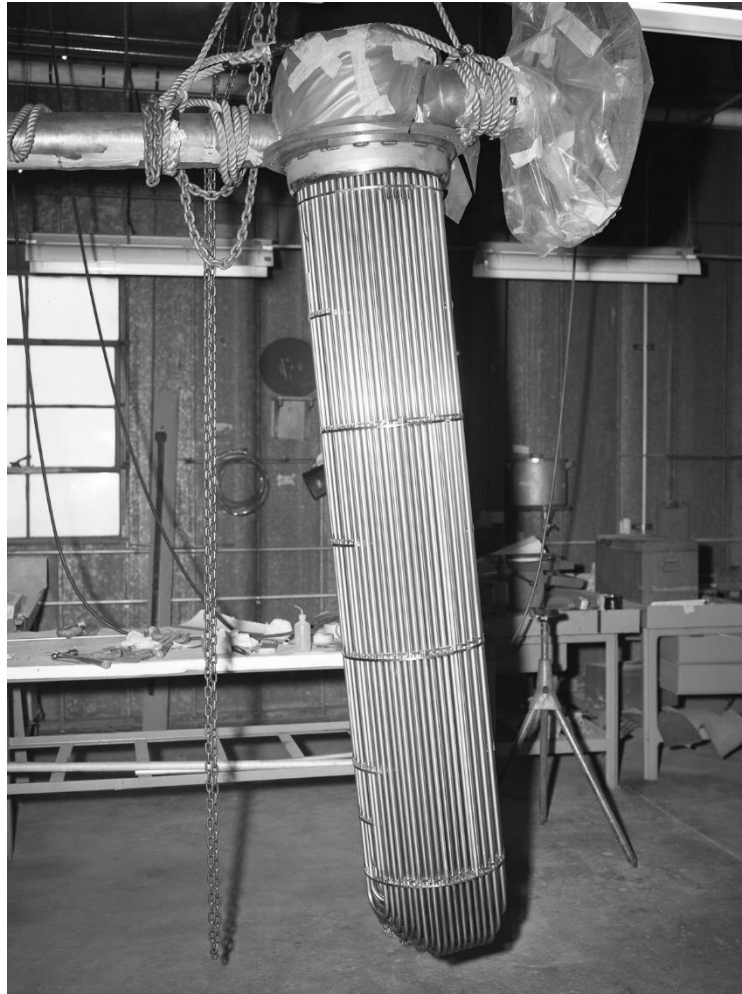


*Figure 1.19 Tube bundle of completed, modified PHeX (ORNL-TM-1023, 1965).
High quality image courtesy of David E. Holcomb, senior technical advisor working currently at ORNL.*

The PHeX was designed in 1961 and fabrication completed in 1963. In the winter of 1963 – 64 flow tests with water were conducted to research previously reported tube vibration. Excessive and audible rattling as well as higher than expected pressure drops were found, and the source of these were crucial to find and eliminate. One of the first theories was that cavitation bubbles within the system was the cause of the audible rattling, which could induce vibrations in the tubes. To test this theory, the back pressure was increased to 380 kPa difference at $0.063\ m^3/s$, but no obvious change to the noise could be detected. This meant that cavitation bubbles most probably were not the cause, and other measures had to be taken. To further investigate the noise, a modified shell was installed, constructed out of stainless steel and with 16 viewing windows, to facilitate visual information and confirmation that the tubes were indeed vibrating (ORNL-TM-2098, 1968). Figure 1.20 shows the stainless-steel shell that was used.

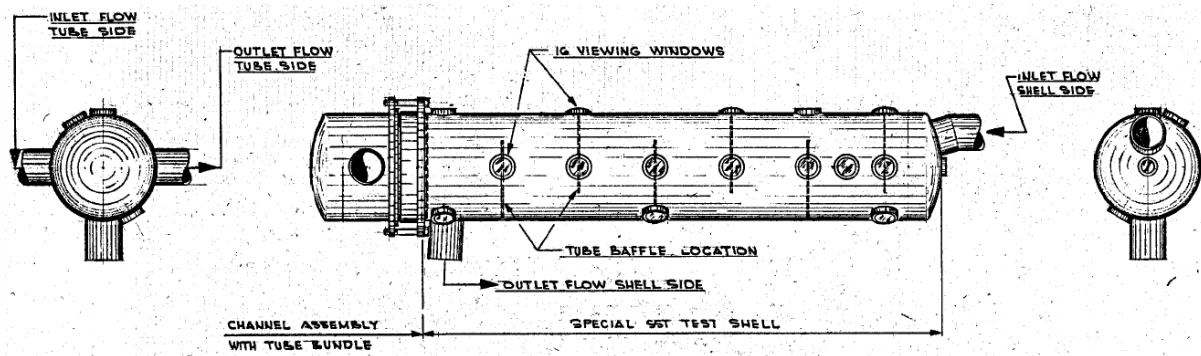


Figure 1.20 Stainless steel shell with 16 viewing windows, designed to find the cause of the rattling sound (ORNL-TM-2098, 1968).

With this new installation the cause of the rattling sound could clearly be traced to vibrations of the tubes and modifications to the PHeX was proposed to remedy this. The modifications to the PHeX were installed and completed in spring 1964. After installation, more water tests were conducted, and the tube vibration problem had been completely mitigated. All of the modifications will be laid out in detail in Chapter 4.

The heat exchanger that was used operated successfully between January 1965 to November 1967 for about 14 000 hours with molten salts in the temperature range 538 — 663 C, without indications of leakage or change in performance (ORNL-TM-2098, 1968).

The PHeX is one of the many bottlenecks of the MSRE, since the total heat transfer capability of the PHeX puts a limit on how much heat can be extracted from the fuel that passes through the reactor core.

1.6.4 MSRE radiator

The MSRE was not built to actually generate power, but as a proof of concept and viability of an MSR in action. Thus, there was no electricity generated from its many hours of operation. Instead, the excess heat that would have been used to drive a turbine of some sort, was dumped to the atmosphere through a radiator, consisting of 120 Hastelloy-N pipes carrying the coolant salt, and two powerful blow-fans, regulated by two shutter doors to avoid freezing of the salt in the pipes. (ORNL-3122, 1971) (ORNL-3014, 1960). The radiator that was used and operated is shown in Figure 1.21.

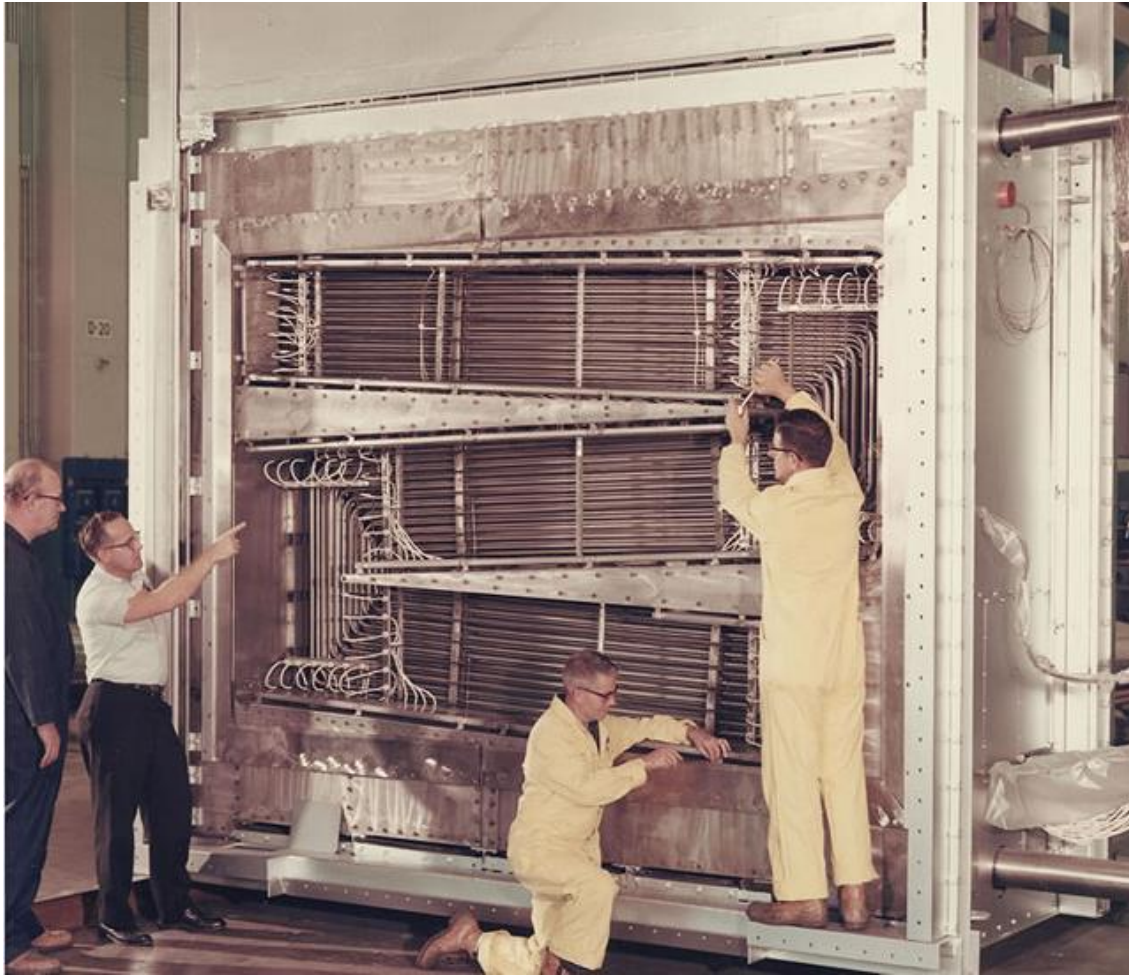


Figure 1.21 Radiator used in the MSRE, with ORNL technicians (Thorium Energy Alliance, 2020).

The design was chosen based on pre-existing equipment and facilities present in the building that was left over from the Aircraft Reactor Test (ART). Blowers, motors, ducting and a stack for discharge of air to the atmosphere was already installed when the MSRE took over the ART building (ORNL-CF-60-11-108, 1960).

The coolant salt, which comes directly from the PHeX, enters at the top and is then pumped through the radiator at a rate of $0.054 \text{ m}^3/\text{s}$. The coolant salt first enters the 22.9 cm main-header and then flows through 10 attached 6.35 cm sub-header manifolds. Each of the 10 sub-headers have 12 tubes attached to it, making a total of 120 tubes, each about 9.1 m long. The coolant salt flows through the S-shaped radiator, exiting at the bottom outlet, with the same structure as the inlet. The shape and length of tubes was somewhat arbitrarily chosen, so long as the overall heat transfer coefficient would be sufficient for the heat removal that was needed for operation (ORNL-CF-60-11-108, 1960).

The cooling provided to the radiator is provided by two blow fans, one of which is seen in Figure 1.22. These blow fans were left behind after the ART and could be installed for the purpose of cooling the radiator, dumping the heat to the atmosphere. The blow fans are each capable of delivering $77.4 \text{ m}^3/\text{s}$ of air across the radiator, each having a power of 250 horsepower. To limit the cooling power and avoid freezing of the coolant salt in the tubes, shutter doors could be opened and closed to control the temperature of the coolant salt within the tubes. The two shutter doors mounted at the inlet and outlet of the radiator is seen in Figure 1.23.

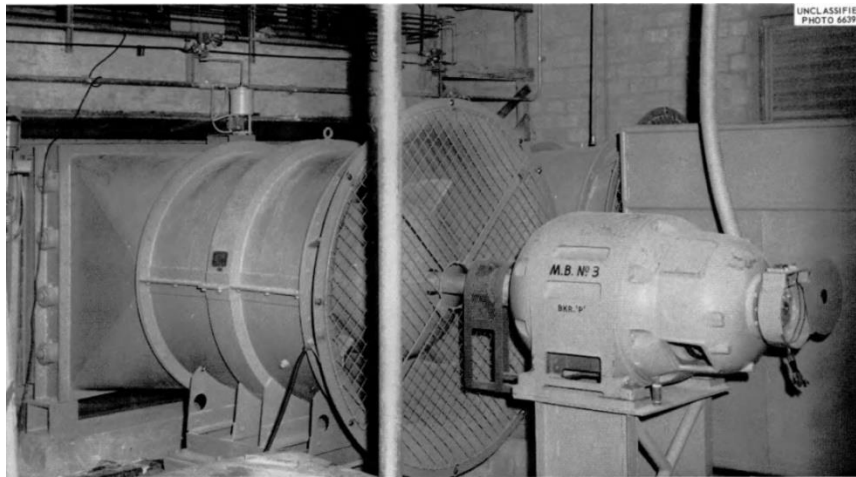


Figure 1.22 Main blower for MSRE coolant system (ORNL-3708, 1964).

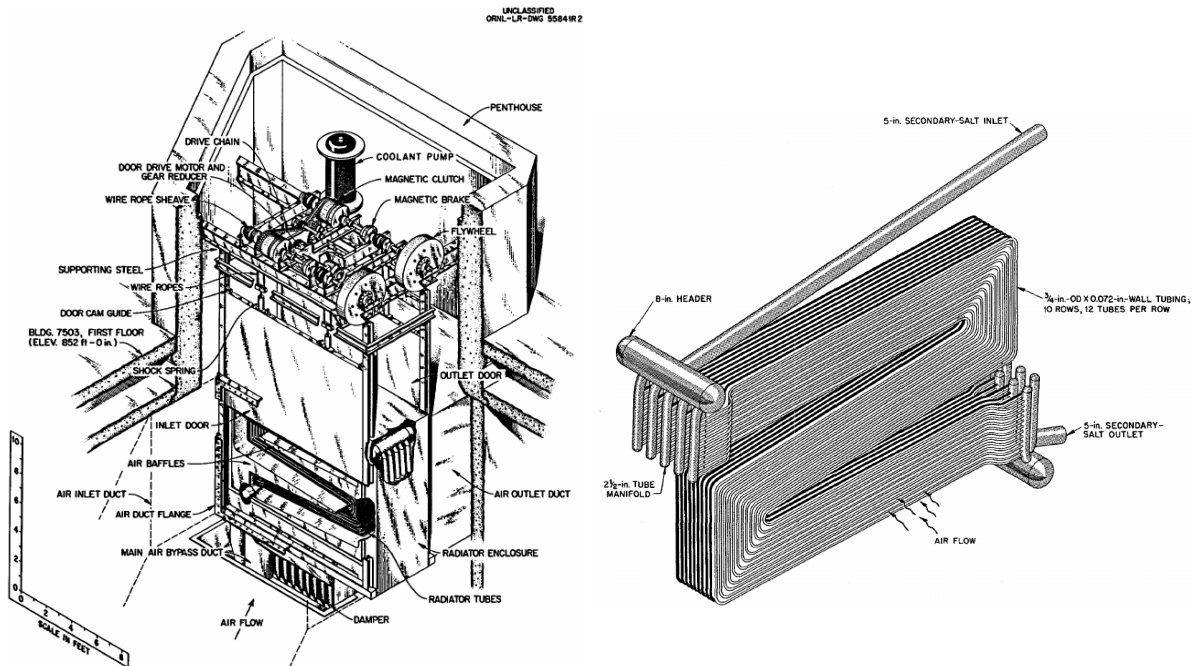


Figure 1.23 Left: schematic of the radiator in the MSRE, Right: Drawing of the radiator (ORNL-3014, 1960).

2 Theory and mathematical models

2.1 Basic physical concepts of fluid mechanics

In this chapter, the governing equations solved by the CFD-platform Simscale and OpenFOAM, and the turbulence models used for this simulation are briefly explained. Since this thesis is a validation rather than a mathematical excursion, a deep dive into the derivations and resulting tensor analysis of the equations used will not be performed. There are many sources where all of the theory is thoroughly explained and expanded upon (Anderson, 2009). However, since the language of tensors is ubiquitous throughout fluid mechanics, most of the equations will be written with either tensor notation for its compactness or vector notation for its clarity. If the reader is not familiar with the tensor notational system, they are directed to Appendix I of this report.

What will be covered are the Navier-Stokes (N-S) equations, how they get transformed to the Reynolds Averaged Navier-Stokes (RANS) equations, together with methods to deal with the new term that appears in the RANS equations; the Reynolds Stress term. The methods are the Boussinesq approximation, $k - \varepsilon$ model, $k - \omega$ model, and the $k - \omega SST$ model. The solvers and discretization schemes that OpenFOAM uses are industry standards and will not be expanded upon. If the reader is interested, they are directed to OpenFOAM's documentation (Greenshields, 2015) (OpenFOAM, 2004).

2.1.1 Reynolds number

One very important number in any fluid flow situation is the Reynolds number, which is the ratio of inertial forces to viscous forces, shown in Eq. 1. It was proposed by Osborne Reynolds in 1883, and his original papers can be found in the reference for the interested reader (Jackson & Launder, 2006).

$$Re = \frac{\text{Inertial forces}}{\text{Viscous forces}} = \frac{\rho UL}{\mu} = \frac{UL}{\nu} \quad \text{Eq. 1}$$

with μ being dynamic viscosity, ρ being density, $\nu = \mu/\rho$ being the kinematic viscosity, U being a characteristic velocity and L being a characteristic length scale of the specific flow set up (Zuck, 1971).

Performing a dimensional analysis on this number one finds that it is dimensionless, meaning that it speaks about something more fundamental about the flow, rather than specific setups.

If Re is large ($> 10^4$), inertial forces dominate, and turbulence will be present in the flow setup. If Re is small ($< 10^2$), viscous forces dominate, and the flow setup will exhibit laminar properties. By taking the same flow setup and changing one of the variables in Eq. 1, e.g., the velocity of the flow, one can change the Re for that particular set up. This number essentially encapsulates how turbulent the flow is, and its magnitude determines what kind of flow will develop.

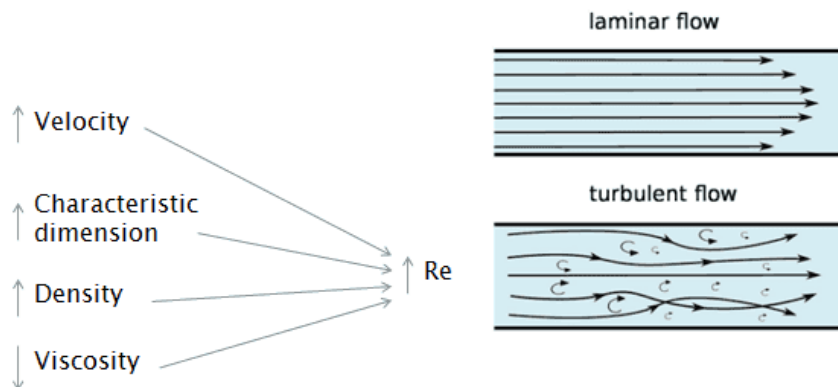


Figure 2.1 Illustration of small Re (top) and large Re (bottom) (Nuclear-Power, 2021).

A person swimming in water is in an inertial situation, with Re in the order of 10^4 . In contrast, an *E. coli* bacterium moving in water has a Re of approximately 10^{-5} , meaning that inertial forces are hardly present from its point of view and the viscous forces dominate. If we would like to know what the *E. coli* bacteria is experiencing, we would have to modify the flow situation for the person, by, for example, changing the fluid from water to something much more viscous, e.g., black tar and limiting the speed at which we can move. Standard swimming techniques will be useless in this scenario.

The world of low Re is a very different world from the one we are used to, which E. M. Purcell expands upon in his short, lovely paper “Life at low Reynolds number” (Purcell, 1976).

In a more practical view, the Re is actually a field of values throughout the flow domain, where it changes as the characteristic lengths and velocities differ. Since viscosity and density usually are set as constant, as they are in this thesis, they cannot be changed. For this thesis, the Re is often well above 10^4 and the flow is highly turbulent.

2.1.2 Turbulence and eddy currents

Fluid flow is often highly chaotic, exhibiting behaviour that is extremely sensitive to initial- and boundary conditions to obtain exact, analytical mathematical solutions. Interchangeably, in fluid dynamics this is referred to as turbulence, in contrast to the ‘well behaved’ dynamics of laminar flow. In essence, turbulence in fluids is the behaviour of so-called eddy-currents within the fluid, which are local regions where the direction of velocity differs to that of the general direction of the fluid. Eddy currents are most notably recognized for their characteristic vortex patterns, e.g., as shown in Figure 2.2. These local regions can span scales from the largest permissible by the geometry down to the scale where viscosity dominates and turbulent kinetic energy dissipates directly into random motions of the molecules, i.e., heat. This smallest resolution is known as the Kolmogorov microscale (George, 2013).

Larger eddies break apart and cascade down into smaller eddies, converting their energy to smaller length scales until it dissipates as heat. However, it can be shown that the majority of the energy in a turbulent fluid is located in the largest eddies, even though the small eddies vastly outnumber the larger ones, as seen in Figure 2.2. Computationally, this would mean that the vast majority of computing power would be spent at resolving and calculating the small eddies, which contribute very little to the overall behaviour of the fluid.



Figure 2.2 Illustration of turbulence. Turbulent jet of water containing fluorescent dye emerging into a tank of still water, illuminated with a sheet of light (Sreenivasan, 1999).

In addition to the Kolmogorov *length* scales there are the Kolmogorov *time* scales and Kolmogorov *velocity* scales, used to resolve the time evolution of the smallest eddies. These time and velocity scales are vastly shorter than for the larger eddies, which adds even more computational strain. The number of grid points required to resolve a turbulent flow down to the Kolmogorov scales is proportional to $Re^{9/4}$, which for a $Re \sim 10^3$ would be roughly one billion cells (AMS, 2012). Mathematically, the Kolmogorov length, time and velocity scales are expressed as follows, respectively:

$$\text{Kolmogorov length scale: } \eta = (\nu^3/\varepsilon)^{1/4} \quad \text{Eq. 2}$$

$$\text{Kolmogorov time scale: } \tau_\eta = (\nu/\varepsilon)^{1/2} \quad \text{Eq. 3}$$

$$\text{Kolmogorov velocity scale: } u_\eta = (\nu\varepsilon)^{1/4} \quad \text{Eq. 4}$$

where ν is the kinematic viscosity with dimensions $[L^2T^{-1}]$ and ε is the average rate of dissipation of turbulent kinetic energy per unit mass with dimensions $[L^2T^{-3}]$ (George, 2013).

2.1.2.1 The energy cascade

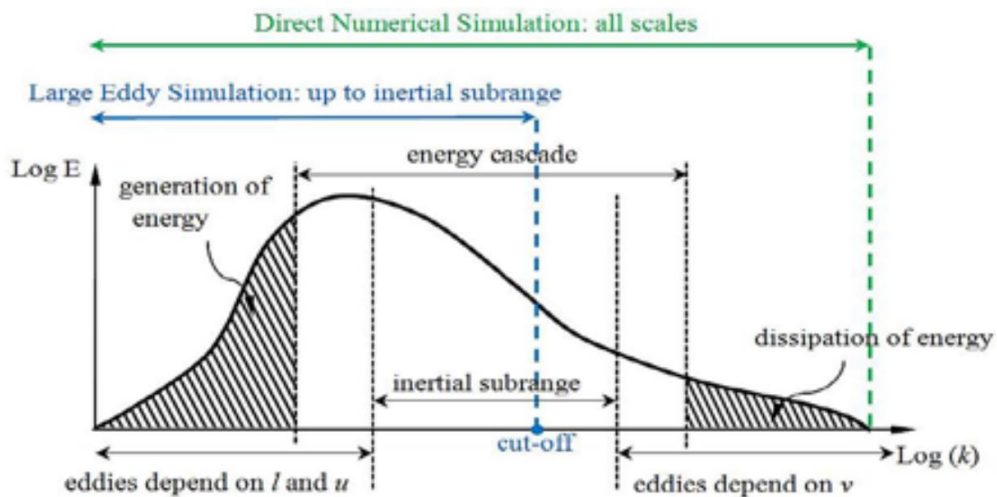


Figure 2.3 Energy distribution in the eddies of a turbulent flow. As turbulent kinetic energy increases (k , x -axis), total energy (E , y -axis) tends to decrease (Modir-Khazeni & Trelles, 2015).

Figure 2.3 is important when considering the distribution of energy in a turbulent fluid. It can be thought of as three distinct regions: turbulence generation, energy cascade and dissipation.

As the turbulent kinetic energy, k , increases, the eddies first depend on the characteristic length scales of the geometry, l , and the characteristic speed of the fluid, u . The total energy in these eddies is large and growing, and the sizes of the eddies are also large.

As k further increases, the energy cascade region is entered, where the bulk of the total energy of the fluid is contained. Here larger eddies feed their energy into smaller and smaller eddies, known as the energy cascade, dumping their total energy in the process to the surrounding fluid.

At the tail end of the graph, for the highest k , the dissipation region is entered. Here, the turbulent movement of the fluid is contained in the smallest eddies (now depending on ν), that dissipate their energy directly into random thermal motion, i.e., heat. The number of these smallest eddies is vast, but the total energy contained in all of them is very low, as seen in Figure 2.3.

When modelling and meshing a fluid, the behaviour of the turbulence has to be considered for each case. For highly detailed transient solutions it might be of importance to accurately model the eddies on small length scales. This can be done with e.g., a Direct Numerical Simulation (DNS) or a Large Eddy Simulation (LES).

A DNS solves the N-S equations directly and relies on a well meshed geometry to accurately model the eddies to a sufficiently small scale (Moin & Mahesh, 1998).

In a LES the contribution of the large, energy-carrying eddies is computed exactly (as in a DNS), and only the effect of the smallest scales of turbulence is modelled. Small length scales are usually more homogenous and independent of the boundary conditions, and the assumption underlying LES is that the modelling of the smallest eddies is simple and requires few adjustments to the model (Piomelli, 1999).

In the case of the simulations of this thesis, only steady states are sought after, and thus exact simulation of the eddies is of no importance. However, the energy contained in the eddies still has to be resolved to some extent to correctly estimate and account for the total energy of the fluid. There exists a multitude of techniques to average and estimate this energy without going through the computationally heavy task of modelling and meshing the fluid to encompass all the eddies. One such approach is the Reynolds Averaged Navier Stokes equations, also known as the “RANS” equations.

Since the world of turbulence is one of the more aesthetic parts of science, a couple of poems seemed fitting.

L.F. Richardson summarized the peculiar eddy-behaviour in this often-cited verse (Richardson, 1922):

*“Big whirls have little whirls
Which feed on their velocity;
And little whirls have lesser whirls,
And so on to viscosity”*

A more obscure, but beautiful sonnet about turbulence was written by the John Hopkins researcher and professor S. Corrsin to honour his Ph.D. dissertation adviser Hans Liepmann’s 70s birthday, which goes like this (George, 2013):

*“Shall we compare you to a laminar flow?
You are more lovely and more sinuous.
Rough winter winds shake branches free of snow,
And summer’s plumes churn up in cumulus.*

*How do we perceive you? Let me count the ways.
A random vortex field with strain entwined.
Fractal? Big and small swirls in the maze
May give us paradigms of flows to find.*

*Orthonormal forms non-linearly renew
Intricate flows with many free degrees
Or, in the latest fashion, merely few -
As strange attractor. In fact, we need Cray 3’s*.*

*Experiment and theory, unforgiving:
For serious searcher, fun ... and it’s a living!”*

**Cray 2 was the world’s most powerful supercomputer at the time.*

2.2 Navier-Stokes (N-S)

Fluid dynamics in general sets out to solve the difficult problem of getting real world fluid flow codified into a numerical domain with the end goal of making useful simulations. A variety of different fluid properties that are of importance need to be considered simultaneously in order to describe the behaviour of a fluid. These are velocities in 3 dimensions ($U = [u, v, w]$), pressure (p), temperature (T), density (ρ) and dynamic viscosity (μ). How these properties evolve within a fluid volume is the central question, and the relationships used to describe these changes were formulated by Claude-Louis Navier (1827) and Sir George Stokes (1845) in what is now known as the Navier-Stokes equations (Pope, 2000). The N-S equations rest upon the fundamental physical principles of:

1. Conservation of mass
2. Conservation of momentum
3. Conservation of energy

A common approach to derive the N-S equations is to perform an analysis with these three principles on a force applied on an infinitesimal fluid volume, where stresses in all directions are expressed, as shown in Figure 2.4.

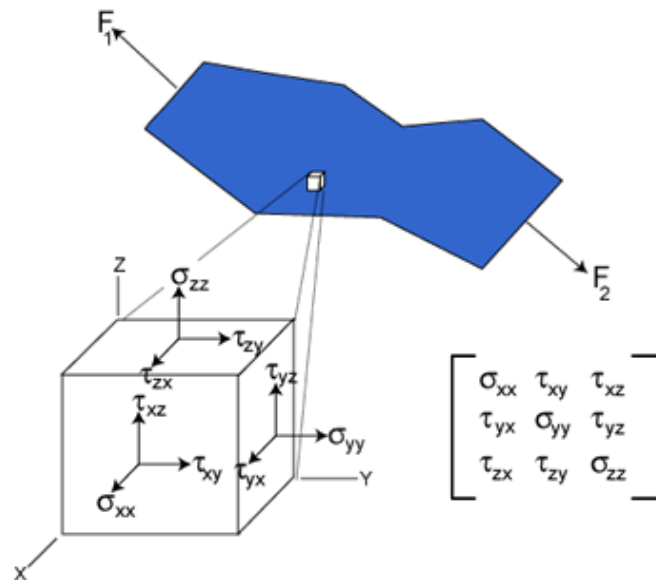


Figure 2.4 Stress components of a fluid element subjected to forces (Iowa State University, 2016).
This figure is reused with permission from, ©Iowa State University Center for Non-destructive Evaluation. (CNDE).

The stresses and resulting strains (deformations) in Figure 2.4 are unknowns prior to any assumptions. How these unknowns get resolved rely heavily on the application. In the case of the present thesis, as with the most common applications of N-S, the fluid in questions is a Newtonian fluid, meaning that stresses and the resulting deformations are linearly related. For such a fluid, Stokes obtained the relationship shown in Eq. 5, (Henningson & Berggren, 2005)

$$\tau_{ij} = \mu \left(\frac{\partial u_i}{\partial x_j} + \frac{\partial u_j}{\partial x_i} \right) + \lambda \frac{\partial u_k}{\partial x_k} \delta_{ij} \quad \text{Eq. 5}$$

where μ is the molecular dynamic viscosity coefficient and λ is the bulk viscosity coefficient. The quantity u_i contains the velocities u_1, u_2 and u_3 which are velocities in x -, y - and z -direction, respectively. Stokes made the hypothesis that

$$\lambda = -\frac{2}{3}\mu, \quad \text{Eq. 6}$$

which is frequently used to this day, even though it has not been definitely confirmed yet (Anderson, 2009).

Using the assumption of Newtonian fluids all of the strains are expressible through the velocity of the fluid and hence are no longer independent unknowns.

The fluid is treated as isothermal, meaning that there is no preferred thermal direction for the heat to travel, further reducing the number of unknowns. Together with the assumption of incompressibility, which works for the salts in this thesis, the density and viscosity are also assumed constant. These assumptions bring the total unknowns down to 5;

- The velocities in x , y and z , comprising a velocity vector field,
- A pressure scalar field,
- A temperature scalar field.

Together with the fundamental physical principles outlined above, this derivation leads to the well-known N-S equations for incompressible, Newtonian fluids expressed in tensor notation (Henningson & Berggren, 2005):

Conservation of mass:

$$\frac{\partial u_i}{\partial x_i} = 0 \quad \text{Eq. 7}$$

Conservation of momentum:

$$\rho \frac{Du_i}{Dt} = -\frac{\partial p}{\partial x_i} + \mu \frac{\partial^2 u_i}{\partial x_j \partial x_j} + \rho F_i \quad \text{Eq. 8}$$

Conservation of Energy:

$$\rho \frac{Dh}{Dt} = \frac{Dp}{Dt} + 2\mu \left(e_{ij} - \frac{1}{3} \frac{\partial u_k}{\partial x_k} \delta_{ij} \right)^2 + \kappa \frac{\partial}{\partial x_i} \left(\frac{\partial T}{\partial x_i} \right) \quad \text{Eq. 9}$$

Where $\frac{D}{Dt} = \left(\frac{\partial}{\partial t} + u_i \frac{\partial}{\partial x_i} \right)$ is the material derivative, commonly used in CFD. i, j and k take on values of 1, 2, 3 and the Einstein summation convention is used.

F_i are external forces (usually gravity), $h = e + p/\rho$ is the enthalpy where e is the internal energy. e_{ij} is the deformation rate tensor which are related to the velocities, $\kappa = 0.41$ is the von Kármán constant and T is the temperature.

For a full derivation of the N-S equations, see (Coleman, 2010), (Henningson & Berggren, 2005).

The N-S equations can be written in many ways, Eq. 7 through Eq. 9 are one of the more common forms of writing them, but for specific solvers, e.g. those used in the CFD program OpenFOAM used in this thesis, the N-S equations can show up with slight variations depending on the model application.

The three specified N-S equations together with the conservation of mass and conservation of energy provide 5 equations, and thus the system can be closed with these assumptions.

However, to use these equations straight away, a Direct Numerical Simulation (DNS) has to be utilized, where the turbulent eddies must be resolved down to the smallest scales to give an accurate description of the flow. The length-, time and velocity scales required for a fully resolved DNS are the previous mentioned Kolmogorov scales. To adequately mesh the complex geometries of this thesis to perform a DNS requires an unfeasible number of mesh-elements, for which the computational power required currently does not exist.

However, DNS for other applications, e.g., smaller models or for laminar flows or specific turbulent analyses, have been indispensable for developing theory and other methods of modelling. For this thesis, a lower resolution model is therefore desirable, capable of fairly accurately predicting molten salt heat transfer. The difficulty of the CFD is then to model and predict what happens near the walls, since this is where the intricacies of turbulence show up the most, where turbulence quickly must dissipate its energy down to heat. For most CFD-setups a 'no-slip' condition is attributed to the walls, meaning that the velocity of the fluid right next to the wall is zero. The velocity profile from the wall must then quickly ramp up, and it has some characteristic behaviours that modern CFD-solvers and algorithms are capable of solving. This characteristic behaviour is expanded upon later in this chapter.

2.3 Reynolds averaged Navier-Stokes (RANS)

A powerful technique in modelling a fluid is to consider the velocity in each direction to be primarily composed of two parts, namely an average part \bar{u}_i and a fluctuating part u'_i , as depicted graphically in Figure 2.5. This is known as a Reynolds decomposition. The method of averaging is shown in Eq. 10.

$$u_i = \bar{u}_i + u'_i \quad \text{Eq. 10}$$

where $\bar{u}_i = \frac{1}{\Delta T} \int_{T_0}^{T_0+T_1} u_i dt$ and $u'_i = u_i - \bar{u}_i$.

Here, ΔT is the time interval being averaged, T_0 and T_1 are time interval bounds for averaging. The pressure is decomposed in a similar manner. This RANS method of averaging the N-S equations will be used in this thesis, since what is being sought after is an averaged steady state solution, where the transient behaviour of turbulence is not of interest. The averaged quantity of e.g., velocity is easier to compute, which leaves the fluctuating part to be mathematically modelled, thus relaxing the necessity of having a highly refined mesh to fully resolve the turbulent behaviour (Hazra , 2020).

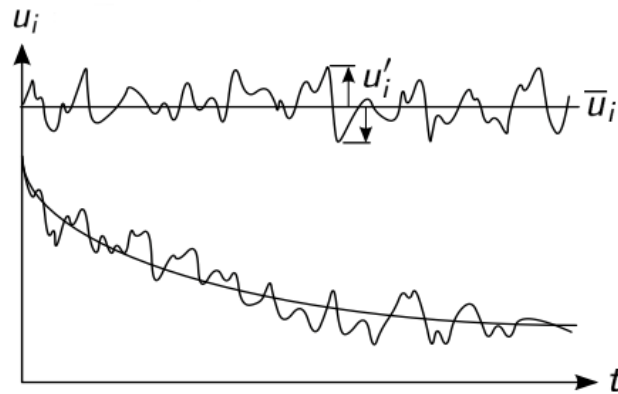


Figure 2.5 Average part \bar{u}_i (smooth line) and fluctuating part u'_i (wiggly and chaotic line) (Hazra , 2020).

A parameter denoted I is used to indicate the ratio of the fluctuating part to the averaged part, and this is referred to as turbulent intensity, shown in Eq. 11.

$$I = \frac{u'_i}{\bar{u}_i} \quad \text{Eq. 11}$$

For a highly turbulent situation in complex geometries, as in heat exchangers or engines, I is usually in the range of 5 – 20% (Simscale, 2020).

Inserting the Reynolds decomposed velocities in the previously defined N-S equations (Eq. 7 through Eq. 9), they can be rewritten and compressed in a new form, expressed in terms of averaged and fluctuating parts, shown in Eq. 12. These are the RANS equations.

$$\rho u_j \frac{\partial u_i}{\partial x_j} = \rho g_i + \frac{\partial}{\partial x_j} \left[-p \delta_{ij} + \mu \left(\frac{\partial u_i}{\partial x_j} + \frac{\partial u_j}{\partial x_i} \right) - \rho u'_i u'_j \right] \quad \text{Eq. 12}$$

In the RANS equations, a new term gets introduced, called the “Reynold’s stress tensor” or the viscous stress term, which is seen in the last term of Eq. 12, namely: $-\rho u'_i u'_j$. How to determine the Reynold’s stress tensor is usually referred to as “the closure problem” and is central to RANS CFD-algorithms and solution schemes (Brennen , 2006).

Closure refers to the system of equations being solvable, meaning that there are an equal number of equations to the number of variables. What needs to be ascertained is how the newly introduced Reynold’s stress term can be modelled, and what assumptions can be made of these fluctuating parts. The first step towards modelling this is using the Boussinesq approximation, proposed by Joseph Valentin Boussinesq in 1877 (Spalding & Launder, 1974).

2.3.1 Boussinesq approximation

Boussinesq relates the turbulence stresses to the mean flow of the system as a method to model the Reynold’s stress terms, shown in Eq. 13 (Brocchini, 2013). This will introduce the new parameter of turbulent viscosity denoted μ_t . The turbulent viscosity (also known as eddy viscosity in the literature) is added to the model in order to account for the behaviour of turbulence to increase the apparent viscosity of the fluid in the turbulent regions.

An important assumption is that μ_t is isotropic, meaning that it behaves the same in all directions and can therefore be treated as a proper scalar. The parameter k is the turbulent kinetic energy and is also treated as isotropic. As seen in Eq. 14 k is composed of the fluctuating velocity field.

$$-\rho u'_i u'_j = \mu_t \left(\frac{\partial u_i}{\partial x_j} + \frac{\partial u_j}{\partial x_i} - \frac{1}{3} \frac{\partial u_k}{\partial x_k} \delta_{ij} \right) - \frac{2}{3} \rho k \delta_{ij} \quad \text{Eq. 13}$$

$$k = \frac{1}{2} u'_i u'_i \quad \text{Eq. 14}$$

$$\delta_{ij} = \begin{cases} 1 & \text{if } i = j \\ 0 & \text{otherwise} \end{cases} \quad \text{Eq. 15}$$

(Wimshurst, 2021), (CFD-Online, 2021)

The parameter μ_t is an introduced parameter which needs to be specified to fully close the system of equations, and a number of methods exists for this purpose. Usually a *mixing length* is introduced, which has to do with the sizes of the eddies permitted by the proximity of the wall from the mesh element (i.e., cell) that is currently being calculated, shown in Figure 2.6. As the wall is approached the sizes of the eddies will have an upper bound and thus the energy of the eddies will tend to decrease closer to the wall. The mixing length was expressed by Prandtl as shown in Eq. 17 (Pope, 2000). An improvement to the Boussinesq approximation to account for this behaviour is to include the effect of viscosity in the viscous sub-layer close to the wall. This was done by Van Driest in 1956 (Driest, 1956) where a damping term was introduced to the mixing length equation, shown in Eq. 18.



Figure 2.6 Largest eddies permissible by the proximity to the wall.

Eddy viscosity model:

$$\mu_t = \rho k^{1/2} l_m$$

Eq. 16

Prandtl's mixing length hypothesis:

$$l_m = \kappa y$$

Eq. 17

Van Driest model, damping close to wall:

$$l_m = \kappa y \left[1 - \exp\left(-\frac{y^+}{A^+}\right) \right]$$

Eq. 18

where $\kappa = 0.41$, $A^+ = 26.0$ and y is the distance to the nearest wall. $y^+ = y u_t / \nu$, is a dimensionless wall distance, and will be covered later in this chapter. So far, the modelling of the fluid has been achieved by introducing simple algebraic relations to deal with the Reynold's stress tensor, introduced in Eq. 12. This, however, is not adequate to accurately describe a fluid, and another approach must be taken, namely that of the two-equation models, $k - \varepsilon$ and $k - \omega$.

2.3.2 $k - \varepsilon$ model

The $k - \varepsilon$ model was developed in 1973, and is considered to be the first modern turbulence model. It is known as a “two equation model” and it builds upon the Boussinesq approximation providing a method of calculating μ_t with the aid of two transport equations that depend on the flow.

Since we know that turbulence is convective and diffuses through the flow, it seems too crude to use a purely algebraic approach (as the Boussinesq approximation uses) to define the eddy viscosity, where the only parameter is proximity to the wall. The distance to the wall is specified by the geometry and not the flow, which would mean that the turbulent viscosity is defined everywhere at the start of the simulation. This is what the $k - \varepsilon$ model sets out to improve upon.

The Boussinesq relation is thus further expanded upon by introducing the parameter ε , which will have units of rate of change of k , capturing the dissipation rate of turbulent kinetic energy.

Physically this means the rate at which turbulent kinetic energy is converted into thermal energy by the action of viscosity, which means that ε acts as a sink to the turbulent kinetic energy.

ε can be written explicitly as shown in Eq. 19, but this form is not useful since it depends on the unknown u'_i , the fluctuating velocity field.

$$\varepsilon = \mu \frac{\partial u'_i}{\partial x_j} \frac{\partial u'_i}{\partial x_j} \quad \text{Eq. 19}$$

To include this convective and diffusive behaviour of turbulence in our model, transport equations relating how the quantities of k and ε change over time has to be solved. These transport equations usually take the form shown in Eq. 20 and Eq. 21 for incompressible flow. The value of ε has to be thought of as a field throughout the model, having different values for each cell depending on the flow environment, but in general it will be large close to walls since that is where the dissipation of turbulence is going to be high.

$$\frac{\partial k}{\partial t} + u_i \frac{\partial k}{\partial x_i} = P_k - D_\varepsilon + \frac{\partial}{\partial x_j} \left[\left(\mu + \frac{\mu_t}{\sigma_k} \right) \frac{\partial k}{\partial x_j} \right] \quad \text{Eq. 20}$$

$$\frac{\partial \varepsilon}{\partial t} + u_i \frac{\partial \varepsilon}{\partial x_i} = C_{1\varepsilon} \frac{\varepsilon}{k} P_k - C_{2\varepsilon} \frac{\varepsilon}{k} D_\varepsilon + \frac{\partial}{\partial x_j} \left[\left(\mu + \frac{\mu_t}{\sigma_\varepsilon} \right) \frac{\partial \varepsilon}{\partial x_j} \right] \quad \text{Eq. 21}$$

where

$$\mu_t = \rho C_\mu \frac{k^2}{\varepsilon} \quad \text{Eq. 22}$$

$$D_\varepsilon = \varepsilon \quad \text{Eq. 23}$$

$$P_k = 2\mu_t E_{ij} E_{ij} \quad \text{Eq. 24}$$

$$E_{ij} = \frac{1}{2} \left(\frac{\partial u_i}{\partial x_j} + \frac{\partial u_j}{\partial x_i} \right) \quad \text{Eq. 25}$$

Table 2.1 Constants for the $k - \varepsilon$ model.

$C_{1\varepsilon}$	1.44
$C_{2\varepsilon}$	1.92
σ_k	1.0
σ_ε	1.3

(Launder & Sharma, 1974), (CFD-Online, 2014)

P_k in Eq. 21 represents production, similarly the D_ε represents destruction of turbulent kinetic energy, which justifies the minus sign. The rest of the constants introduced have been verified experimentally (Spalding & Launder, 1974).

To further improve upon this model certain damping-functions have to be introduced when the cell being calculated is close to the wall, where the dissipation of turbulence is high. These damping terms have to be introduced in order for the $k - \varepsilon$ model to behave correctly and arrive at a physical solution, but when applied to geometries with adverse pressure gradients this is usually not the best method (e.g., enlargement of openings or aerofoil separation locations). These damping functions will not be expanded upon here, but if the reader is interested there are many papers concerning this topic (Jones & Launder, 1972), (Launder & Sharma, 1974).

2.3.3 $k - \omega$ model

A further improvement to our ability to model turbulent flows is the $k - \omega$ model. ω in this model is the specific turbulence dissipation rate having units of s^{-1} . Explicitly, ω is shown in Eq. 26.

$$\omega = \frac{\varepsilon}{C_\mu k} \quad \text{Eq. 26}$$

With Eq. 26 it is seen that both ω and ε essentially represent the same quantity, namely dissipation of turbulent kinetic energy, and with Eq. 26 one can be converted to the other.

Many years of research have proven that the $k - \varepsilon$ model fails to compute flows with adverse pressure gradients and flow separation (Menter, Kuntz, & Langtry, 2003). Thus $k - \omega$ formulation was introduced to be able to predict more general flows, e.g., adverse pressure gradients.

The transport equations for the $k - \omega$ model are shown in Eq. 27 and Eq. 28.

$$\frac{\partial k}{\partial t} + u_j \frac{\partial k}{\partial x_j} = \tau_{ij} \frac{\partial u_i}{\partial x_j} - \beta^* k \omega + \frac{\partial}{\partial x_j} \left[(v + \sigma^* v_T) \frac{\partial k}{\partial x_j} \right] \quad \text{Eq. 27}$$

$$\frac{\partial \omega}{\partial t} + u_j \frac{\partial \omega}{\partial x_j} = \alpha \frac{\omega}{k} \tau_{ij} \frac{\partial u_i}{\partial x_j} - \beta \omega^2 + \frac{\partial}{\partial x_j} \left[(v + \sigma v_T) \frac{\partial \omega}{\partial x_j} \right] \quad \text{Eq. 28}$$

Table 2.2 Constants for the $k - \omega$ model.

α	5/9
β	3/40
β^*	9/100
σ	1/2
σ^*	1/2

(CFD-Online, 2011)

There are different versions for the $k - \omega$ model having different values for the empirical constants α , β , β^* , σ , σ^* .

The main difference between the $k - \varepsilon$ model and the $k - \omega$ model is that the $k - \omega$ model does not need the previously mentioned damping functions when calculating flow parameters close to the wall. However, it is the case that the $k - \omega$ model is sensitive to the freestream turbulent kinetic energy which becomes problematic when calculating separation points and turbulent viscosity (Menter, Kuntz, & Langtry, 2003).

2.3.4 $k - \omega$ SST model

To remedy the issues of the pure $k - \varepsilon$ and $k - \omega$ models, F. R. Menter proposed in 1992 that a blend between $k - \varepsilon$ and $k - \omega$ can be used within a simulation (Menter F. R., 1992). For regions far away from any wall the $k - \varepsilon$ model is used, and for regions close to the wall the $k - \omega$ model is used, with a region of blending in between the two models. This is the basis for the $k - \omega$ SST (Shear Stress Transport) model, and is the model used for this thesis.

By inserting the relation in Eq. 26, rewritten as $\varepsilon = C_\mu \omega k$, in the $k - \omega$ model and performing the derivation, an extra term will appear, namely the last term of Eq. 30, namely:

$2(1 - F_1)\rho\sigma_\omega 2 \frac{1}{\omega} \frac{\partial k}{\partial x_i} \frac{\partial \omega}{\partial x_i}$. The blending function F_1 in Eq. 30 takes on a continuous range of values, but most importantly it acts as a form of shut-off to that last term. When F_1 is 0, i.e., far away from the wall, the last term is at maximum strength, which makes this essentially a $k - \varepsilon$ formulation. When F_1 is 1, i.e., very close to the wall, the last term in Eq. 30 is omitted, which results in a $k - \omega$ formulation. Between these extreme values of F_1 , a smooth blend between the models can occur. F_1 is shown graphically in Figure 2.7.

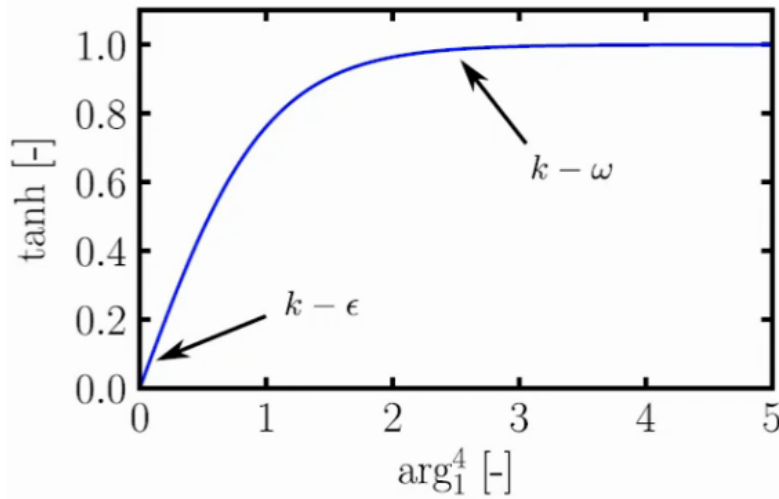


Figure 2.7 Wall function F_1 , where arg_1 is ξ_1 in Eq. 31.

Taken from OpenFOAM's documentation about the $k - \omega$ SST model, the following equations and parameters constitute the basis of the model, developed by Menter (Menter, Kuntz, & Langtry, 2003).

$$\frac{\partial(\rho k)}{\partial t} + \frac{\partial(\rho u_i k)}{\partial x_i} = \tilde{P}_k - \beta^* \rho k \omega + \frac{\partial}{\partial x_i} \left[(\mu + \sigma_k \mu_t) \frac{\partial k}{\partial x_i} \right] \quad \text{Eq. 29}$$

$$\begin{aligned} \frac{\partial(\rho\omega)}{\partial t} + \frac{\partial(\rho u_i \omega)}{\partial x_i} = & \alpha \rho S^2 - \beta \rho \omega^2 + \frac{\partial}{\partial x_i} \left[(\mu + \sigma_\omega \mu_t) \frac{\partial \omega}{\partial x_i} \right] + \\ & + 2(1 - F_1) \rho \sigma_{\omega 2} \frac{1}{\omega} \frac{\partial k}{\partial x_i} \frac{\partial \omega}{\partial x_i}. \end{aligned} \quad \text{Eq. 30}$$

Where the first blending-function F_1 is defined by

$$F_1 = \tanh(\xi_1^4), \quad \text{Eq. 31}$$

with argument $\xi_1 = \min \left[\max \left(\frac{\sqrt{k}}{\beta^* \omega y}, \frac{500\nu}{y^2 \omega} \right), \frac{4\rho \sigma_{\omega 2} k}{CD_{k\omega} y^2} \right]$

where $CD_{k\omega} = \max \left(2\rho \sigma_{\omega 2} \frac{1}{\omega} \frac{\partial k}{\partial x_i} \frac{\partial \omega}{\partial x_i}, 10^{-10} \right)$, and $\nu = \mu/\rho$.

The turbulent kinematic eddy viscosity is then defined:

$$\nu_t = \frac{\mu_t}{\rho} = \frac{a_1 k}{\max(a_1 \omega, SF_2)} \quad \text{Eq. 32}$$

where S is the invariant measure of the strain rate and F_2 is a second blending-function.

$$F_2 = \tanh(\xi_2^2), \quad \text{Eq. 33}$$

with argument $\xi_2 = \max \left(\frac{2\sqrt{k}}{\beta^* \omega y}, \frac{500\nu}{y^2 \omega} \right)$.

Limiting the production of turbulence in stagnant regions, the following correction is made to the production term in Eq. 32:

$$P_k = \mu_t \frac{\partial u_i}{\partial x_i} \left(\frac{\partial u_i}{\partial x_j} + \frac{\partial u_j}{\partial x_i} \right), \quad \text{Eq. 34}$$

making $\tilde{P}_k = \min(P_k, 10\beta^* \rho k \omega)$.

The constants used in the $k - \omega$ SST model is a blend between the constants of the $k - \varepsilon$ and $k - \omega$ models, as shown in Eq. 35.

$$\psi = F_1 \psi_1 + (1 - F_1) \psi_2, \quad \text{Eq. 35}$$

where ψ_1 is the constant of interest from the $k - \omega$ model and ψ_2 is the corresponding constant from the $k - \varepsilon$ model. Thus, explicit values for the constants used in the $k - \omega$ SST model cannot be shown since they vary depending on wall distance and are evaluated as Eq. 35. The underlying constants are shown in Table 2.3.

Table 2.3 Constants for the $k - \omega$ SST model

α_1	5/9
α_2	0.44
a_1	0.31
β_1	3/40
β_2	0.0828
β^*	0.09
σ_{k1}	0.85
σ_{k2}	1

(Menter, Kuntz, & Langtry, 2003), (Menter F. R., Two-equation eddy-viscosity turbulence models for engineering applications , 1994)

With all of this defined, the $k - \omega$ SST model at our disposal is a powerful turbulence model, utilizing the time averaged technique of the RANS formulation, specified in the beginning of this chapter. All of the wall functions and blending regions have been introduced to reduce the dependency on a very fine mesh, which makes it much less computationally intense to do valuable CFD-calculations on real world phenomena. The mesh still has to be quite fine for the results to be physically applicable, but the cells in the boundary layers closest to the walls do not need to be as fine, which will reduce the number of cells by millions for more complex models.

To wrap up the discussion on turbulent formulations, Figure 2.8 shows a timeline for when these models were developed. New and improved models are continuously created by the many people all over the world working with CFD, but the models outlined here still lie at the core of the majority of CFD-analyses.

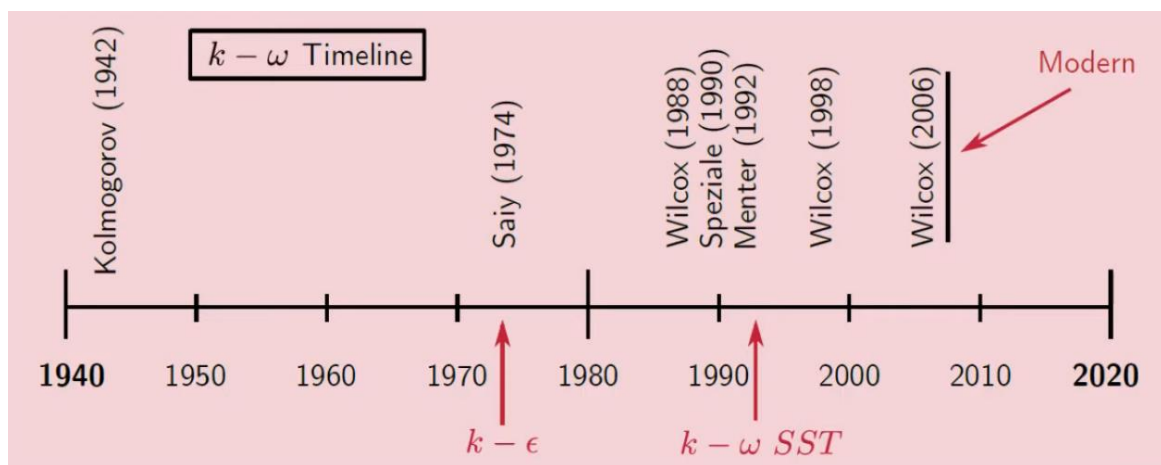


Figure 2.8 Timeline showing when turbulence models and their versions were developed.

2.4 Modelling parameters

2.4.1 Courant number

There are many parts of a simulation setup that will determine the inherent stability (and physicality) of the solution. One of the core concepts within a discretized spatial domain, such as a mesh, is that of the Courant number, also known as the CFL-condition, from the creators Courant, Friedrichs and Lewy who published it in 1956 (Courant, Friedrichs, & Lewy, 1956). Henceforth, the Courant number will be referenced as the Co -number.

For a 1D situation, the Co -number is defined as shown in Eq. 36.

$$Co = \frac{\text{Fluid distance}}{\text{Cell distance}} = \frac{u\Delta t}{\Delta x} \quad \text{Eq. 36}$$

where u is velocity, Δx is the size of the cell and Δt is the time-step.

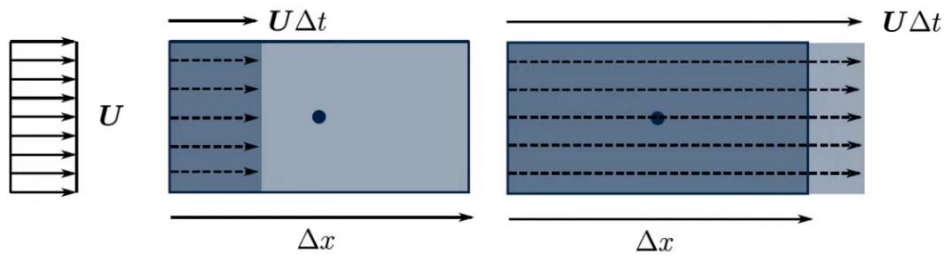


Figure 2.9 Visualization of Courant number.
Left: $Co < 1$,
Right: $Co > 1$.

From the visualization in Figure 2.9 it is clear what the Co -number encapsulates; the distance that the fluid flow traverses during one timestep in relation to the distance of the cell (the mesh element).

To generalize this into 3D a modification to the velocity u must be made, since it can have an arbitrary direction in relationship to the cell size Δx . Furthermore, the cell can have an arbitrary geometry, which means that a general definition for Δx must be made. This is done by formulating the Co -number using the faces of the cell. u is replaced by $1/2|U_f \cdot \hat{n}_f|$, where U_f is the velocity at face f and \hat{n}_f is the unit normal vector of face f , as shown in Figure 2.10. A summation is then carried out over all the faces, and Δx is replaced by the ratio of the area of all the faces to the volume of the entire cell. Eq. 36 is thus modified into Eq. 37 for the 3D case.

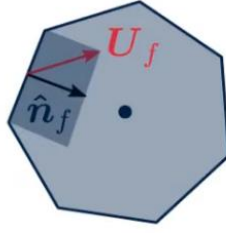


Figure 2.10 Velocity representation for an arbitrary cell.

$$Co = \frac{1}{2} \Delta t \sum_f \frac{|U_f \cdot \hat{n}_f| A_f}{V_{cell}} \quad \text{Eq. 37}$$

Clearly this number will vary throughout the geometry and produce a scalar field, since the:

- Sizes of the cells vary over the geometry,
- Velocity through any particular cell during any particular time-step varies,
- Time-step can, in some simulation setups, also vary.

To find a stable solution, the Co -number must be kept low throughout the entire computational domain, preferably less than 1 everywhere at every time-step, to ensure that convergence can be obtained (Courant, Friedrichs, & Lewy, 196). If the Co -number grows it can seed errors which may propagate and eventually break the simulation, producing unphysical results or halting the program due to internal errors.

If a simulation is seen to have an unstable Co -number, the user can specify to the solver that the time step Δt can vary throughout the solution to always keep the Co -number below some user defined value. This might mean that very small time-steps have to be made, which might cause the solution to take an unreasonable amount of time. Varying parameters and recomputing the mesh to keep the Co -number low can be a time-consuming process, but to ensure that physical results are reached it is vital to keep the Co -number limited. OpenFOAM uses implicit discretization schemes and can therefore still generate useful and physical results for much higher Co -numbers, but it is generally advised to keep it below 1.

2.4.2 Wall functions: y^+ and u^+

To resolve the physics of flow taking place close to the wall there are parameters devised by Nikuradse and Prandtl in 1933 that they named y^+ and u^+ (Colebrook & White, 1937). These parameters are dimensionless height and dimensionless velocity, respectively, and are calculated as shown in Eq. 38 and Eq. 39.

$$y^+ = \frac{yu_t}{\nu} \quad \text{Eq. 38}$$

$$u^+ = \frac{u}{u_t} \quad \text{Eq. 39}$$

where y is the absolute distance to the nearest wall, u_t the frictional velocity close to the wall, ν the kinematic viscosity and u the velocity further away from the wall. u_t is defined as follows.

$$u_t = \sqrt{\frac{\tau_\omega}{\rho}} \quad \text{Eq. 40}$$

$$\tau_\omega = \frac{1}{2} C_f \rho U_\infty^2 \quad \text{Eq. 41}$$

$$C_f = 0.057 Re^{-1/5} \quad \text{Eq. 42}$$

Thus, y^+ is a scalar field with varying values across the geometry, where small values mean that the cell is close to the wall and vice versa (Murad, 2018).

The reason these parameters were introduced was to be able to relate the physics taking place close to the boundary layers across many different flow setups, since the physics close to the wall is very similar. In Figure 2.11, the green curve is a DNS calculated flow velocity over a flat plate in relation to the distance to the wall, the dashed curves are models fitting the DNS data, known as wall functions. Note the log-plot on the x -axis.

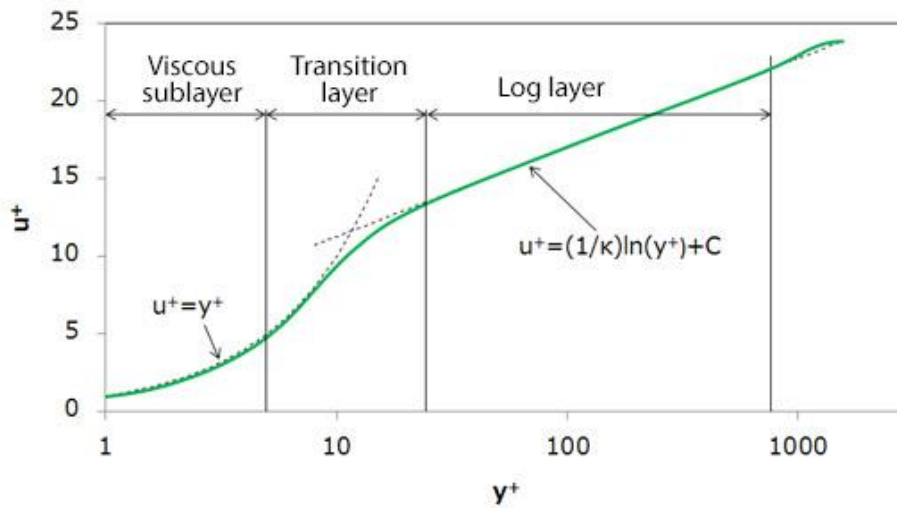


Figure 2.11 y^+ vs u^+ for boundary layer flow, showing viscous sublayer, transition layer and log layer. Green line is a DNS solution for flow over a flat plate (NASA, 2020). Dashed lines are wall functions (note the log-scale on x -axis). $\kappa = 0.41$ and $C = 5.1$.

y^+ . As can be seen in Figure 2.11, these are the:

- Viscous sublayer for $y^+ < 5$
- Transition layer (also called “Buffer layer”) for $5 < y^+ < 30$
- Log layer for $y^+ > 30$

In Figure 2.12, these three regions are shown for the onset of turbulence for flow over a flat plate.

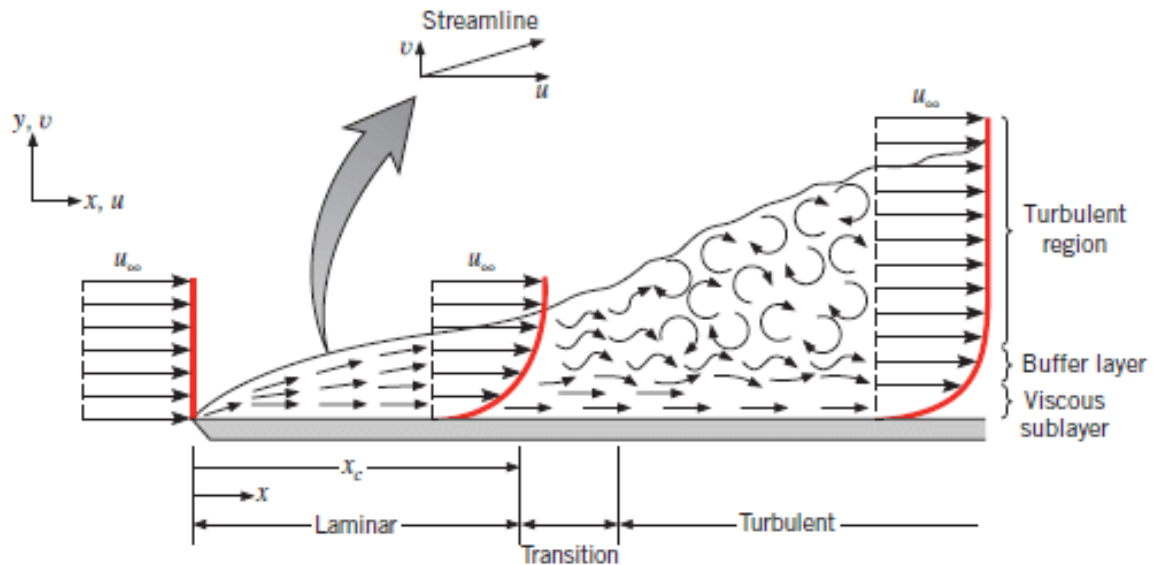


Figure 2.12 Onset of turbulence over a flat plate, showing the viscous sublayer and the buffer layer (Banihani & Assad, 2018).

Since the flow variables in each cell varies linearly piecewise, to capture the steep, non-linear velocity gradient close to the wall requires that the mesh can resolve these changes. This results in a very large number of cells, and thus, methods to model this non-linearity have been introduced to relax the computational need. The two dashed lines of Figure 2.11 are the wall functions, which, in their standard form are expressed as shown in Eq. 43.

$$u^+ = \begin{cases} y^+ & y^+ < 5 \\ 1/\kappa \ln(Ey^+) & y^+ > 30 \end{cases} \quad \text{Eq. 43}$$

where $E = 9.8$, which is an empirically fitted coefficient to the observed DNS data. (Defraeye, Blocken, & Carmeliet, 2011).

There is an awkward region in between these two wall functions, namely the buffer layer $5 < y^+ < 30$, where both wall functions differ substantially from the observed DNS data, as shown in Figure 2.11. Straight forward calculations with this buffer region resolved by the mesh, while using

the specified wall functions, will result in large errors and therefore CFD-codes and user manuals usually suggest not to place any cells in this buffer layer. This results in two different approaches when meshing, either a wall *resolved* mesh which can compute the velocity profile by adding more cells ($y^+ < 5$), or a wall *function* mesh, where the entire non-linear profile is modelled instead of resolved ($y^+ > 30$). The approach in this thesis is to minimize the number of mesh cells and thus, a wall function approach is used since this requires less computation (Liu, 2017).

2.5 Meshing parameters

When evaluating a mesh there are three important parameters that most meshing programs use to estimate an overall quality of the mesh, expressed as one number in the range of 0 to 1. These are:

- Non-orthogonality
- Skewness
- Aspect ratio

These parameters are defined for each cell, giving a range of values for the entire mesh. Below are brief explanations of each of these parameters along with ‘good’ and ‘bad’ values. If these parameters in the mesh are out of bounds it can result in poor solution convergence (Alter, 2004), (Petrock, 2017).

2.5.1 Non-orthogonality

Non-orthogonality is best illustrated with an image, consider Figure 2.13.

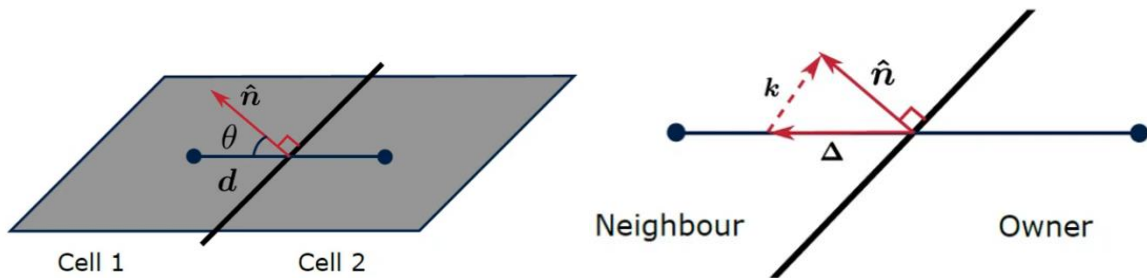


Figure 2.13 Non-orthogonality visualized with a 2D example (Image source: Aidan Wimshurst, Fluid mechanics 101).
Left: Defining the non-orthogonality angle θ ,
Right: Introducing k as the deviation from parallel projection.

The angle θ is the non-orthogonality measure, defined using the common cosine law

$\theta = \cos^{-1} \left(d \cdot \frac{\hat{n}}{|d||\hat{n}|} \right)$, and is usually normalized between 0 and 1. A larger θ will mean a larger k

(not to be confused with turbulent kinetic energy) which introduces the need for corrector loops and under-relaxation factors in the solver to correct the velocity field, resulting in longer computational time and can sometimes break the simulation (Jasak, 1996).

Non-orthogonality measures of $\theta \leq 70$ usually indicate that the mesh will be usable for simulation. Meshes with $70 < \theta < 90$ can still work with most modern solvers, but if problems arise, varying the under-relaxation factors or redoing the mesh will most probably yield better results. $\theta > 90$ is considered unusable in the CFD-community.

2.5.2 Skewness

Skewness is a measure of how much a given cell deviates from an ideal shape (i.e., equilateral or equiangular for 2D cells) as shown in Figure 2.14.

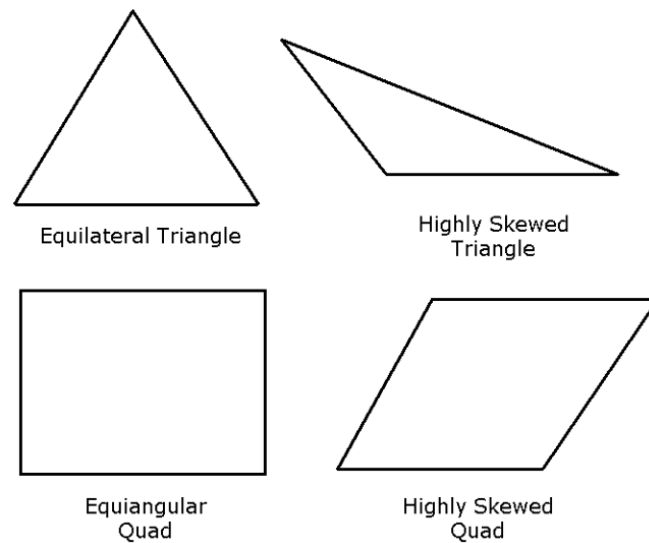


Figure 2.14 Skewness indication for 2D cells.

The values in Table 2.4 are for the CFD suite ANSYS and are normalized according to their method. Different meshing programs show skewness measure in different ranges. In Salome, used in this thesis, the values are normalized between 1 and 100 instead.

Table 2.4 Table indicating values used for evaluating cell skewness (ANSYS, 2008).

Value of skewness	Cell quality
1	<i>Degenerate</i>
$0.9 < 1$	<i>Bad (sliver)</i>
$0.75 - 0.9$	<i>Poor</i>
$0.5 - 0.75$	<i>Fair</i>
$0.25 - 0.5$	<i>Good</i>
$> 0 - 0.25$	<i>Excellent</i>
0	<i>Equilateral</i>

2.5.3 Aspect ratio

Aspect ratio is defined as the ratio of the longest edge to the shortest edge within a cell, as shown in Figure 2.15.

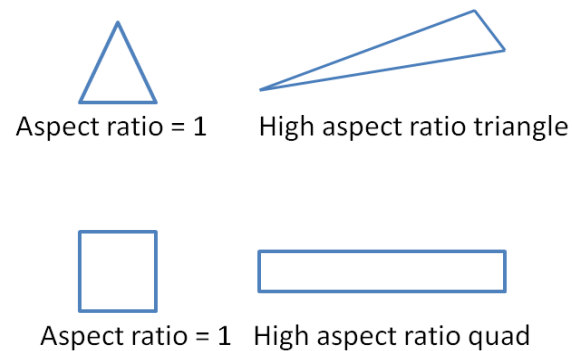


Figure 2.15 Aspect ratio indication of triangle and quadrangle.

There is not a clear guideline in the literature as to what range the aspect ratio should be in, as S. Mittal discusses in his paper “On the performance of high aspect ratio elements for incompressible flows” (Mittal, 2000). In the commercial program ANSYS’ user guide, the recommended maximum values for skewness lie in the low double digits (ANSYS, 2009).

2.6 Salts and Hastelloy-N

The MSRE used two similar salts, both based on the same main ingredients. The fuel salt consisted of uranium fluoride dissolved in a mixture of lithium, beryllium, thorium and zirconium fluorides, while the coolant was a mixture of only lithium and beryllium fluorides. The main constituents of the salts, Lithium Fluoride (LiF) and Beryllium Fluoride (BeF_2) gave rise to the widely used name “*FLiBe*”-salt, which is still in use today. Constituents of *FLiBe* used in the MSRE are shown in Table 2.5, and images of molten and solid *FLiBe* in Figure 2.16.



Figure 2.16 Molten and solid *FLiBe* (Oak Ridge National Laboratory, 2017).

Table 2.5 Composition of fuel and coolant salt (ORNL-TM-2098, 1968).

Fluorides in salt	Fuel Salt composition (mole %)	Coolant salt composition (mole %)
LiF	70	66
BeF_2	23	34
ThF_4	1	—
UF_4	1	—
ZrF_4	5	—

The difference between these two salts shows up quite substantially when comparing their physical properties. What follows in Table 2.6, Table 2.7 and Table 2.8 are the best data accessible through the documents and reports produced by the team at ORNL for the physical properties of the coolant

salt, fuel salt and Hastelloy-N as well as the constituents of Hastelloy-N with a comparison to its predecessor Inconel-600 (ORNL-TM-3039, 1973), (ORNL-TM-2098, 1968).

Table 2.6 Physical properties of coolant and fuel salt used in the MSRE (ORNL-TM-3039, 1973)

Symbol	Physical property	Unit (SI)	Fuel salt (shell-side)	Coolant salt (tube-side)
ρ	Density	$[kg/m^3]$	2261.8	1971.9
μ	Dynamic viscosity	$[kg/(m * s)]$	$7.73e - 3$	$9.756e - 3$
ν	Kinematic viscosity	$[m^2/s]$	$3.42e - 6$	$4.95e - 6$
c_p	Specific heat	$[J/(kg * K)]$	1982.4	2416
k	Thermal conductivity	$[W/(m * K)]$	1.439	1.14
—	Liquidus (melting point)	$[K]$	722	727.4
Pr	Prandtl number	$[-]$	10.65	20.68
—	Mole weight	$[g/mol]$	43.55	33.1

Table 2.7 Physical properties of Hastelloy-N used in the MSRE (ORNL-TM-2098, 1968)

Physical property	Unit (SI)	Hastelloy-N
Density	$[kg/m^3]$	8775
Specific heat	$[J/(kg * K)]$	565
Thermal conductivity	$[W/(m * K)]$	20.267
Melting point	$[C]$	1354 – 1402
Thermal expansion coefficient	$[1/K]$	$1.44e - 5$
Modulus of elasticity	$[Pa]$	$1.71e11$
Mol weight	$[g/mol]$	~65

Table 2.8 Composition of Hastelloy-N and Inconel-600 (ORNL-TM-2098), (Inor-8 story)

Compounds	Hastelloy-N composition (% weight)	Inconel-600 composition (% weight)
Nickel (<i>Ni</i>)	66 – 71	72
Molybdenum (<i>Mo</i>)	15 – 18	–
Chromium (<i>Cr</i>)	6 – 8	14 – 17
Iron (<i>Fe</i>)	5	6 – 10
Carbon (<i>C</i>)	0.04 – 0.08	0.15
Sulphur (<i>S</i>)	0.02	0.015
Manganese (<i>Mn</i>)	–	1
Silicon (<i>Si</i>)	–	0.5

2.7 Overall heat transfer coefficient

The overall heat transfer coefficient is calculated according to Alfa Laval's method (Alfa Laval, 2004).

The equation for overall heat transfer coefficient is expressed as follows:

$$k = \frac{\delta t \, m \, c_p}{LMTD \, A} \quad \text{Eq. 44}$$

Where k is the overall heat transfer coefficient, δt is the temperature difference between inlet and outlet on either shell- or tube-side of the PHeX, m is the mass flow-rate of the salt, c_p is the specific heat capacity of the salt, $LMTD$ is the mean logarithmic temperature difference and A is the heat transfer surface area. $LMTD$ is calculated as follows:

$$LMTD = \frac{\Delta T_1 - \Delta T_2}{\ln \frac{\Delta T_1}{\Delta T_2}} \quad \text{Eq. 45}$$

with $\Delta T_1 = T1 - T4$ and $\Delta T_2 = T2 - T3$, with the following definitions for $T1$ through $T4$:

$T1$	Inlet temperature, shell-side
$T2$	Outlet temperature, shell-side
$T3$	Inlet temperature, tube-side
$T4$	Outlet temperature, tube side

Comparisons between MSRE values and simulated values will be presented in Chapter 7.

3 Method

3.1 Toolchain

In this short chapter the workflow and the programs that are used are shown.

The CAD model of the Primary Heat Exchanger (PHeX) and the radiator was constructed in the online, cloud-based CAD-program Onshape (Onshape, 2014). All models exported from Onshape are in .STEP format.

The full models were initially imported to another online, cloud-based program named Simscale (Simscale, 2013). Simscale is a platform built on OpenFOAM (Open-source Field Operation And Manipulation); an open-source, customizable numerical solver for CFD (OpenFOAM, 2011), (Weller, Tabor, Jasak, & Fureby, 1998). OpenFOAM is very powerful, but lacks a graphical user interface (GUI), and the platform Simscale was created to remedy just that. Some functionality of OpenFOAM is lost in Simscale, but it is a stable and powerful platform for modern CFD. After a completed simulation, exported files from Simscale have the same file-structure as OpenFOAM, and the simulation data is accessible through a .foam file, available from the Simscale download.

Simscale imports models directly from Onshape, which is why these two programs work well together and were chosen for this project. However, Simscale only provided a limited number of simulation core hours (initially 1000, but increased to 3000 through an academic license), which have been used up for this project, so other simulation software had to be employed. OpenFOAM was chosen as a successor.

Since Simscale had the dual function of being both a meshing program as well as a simulation program, a new method of meshing these complex structures was needed. Initially OpenFOAM's inbuilt "snappyHexMesh" application was tried, but due to the size and complexity of the model, unreasonable RAM issues were faced, and another program had to be utilized. After some research into available, open-source meshing solutions, the program Salome was chosen to proceed. Salome is a multi-purpose platform for pre- and post-processing, developed in 2001 by Open Cascade EDF CEA in France (Salome, 2001). For this thesis it is only used for meshing and mesh evaluation. Salome offers a range of meshing algorithms, and the ones used for this thesis were NETGEN 1D-2D, NETGEN 1D-2D-3D and NETGEN 3D. All meshes exported from Salome are in .unv format.

OpenFOAM cannot work with .unv formats directly, so a utility in OpenFOAM called `ideasUnvToFoam` is used to convert between .unv and .foam format for the selected mesh (OpenFOAM, 2006)

After a successful conversion, the .foam mesh is copied to the appropriate OpenFOAM folder and the `chtMultiRegionFoam` solver is used for a conjugate heat transfer solution (OpenFOAMwiki, 2006).

To view the results after completed simulations, the program Paraview was used (Paraview, 2005). Paraview is an open-source application for interactive, scientific visualization of large datasets. From Paraview, flow-fields, temperature and pressure readings as well as mesh evaluation is performed (Ahrens, Geveci, & Law, 2005).

For any other data-plot needed the open-source program Octave has been used, with the necessary code written by the author. Octave is very similar to the commercial software MATLAB but is free to download and use (Eaton, 2002).

3.1.1 Flowchart of tool chain

A flowchart of the full CFD-process is displayed in Figure 3.1, showing all the programs and how they feed into each other, along with pathways that proved fruitful or unresolved.

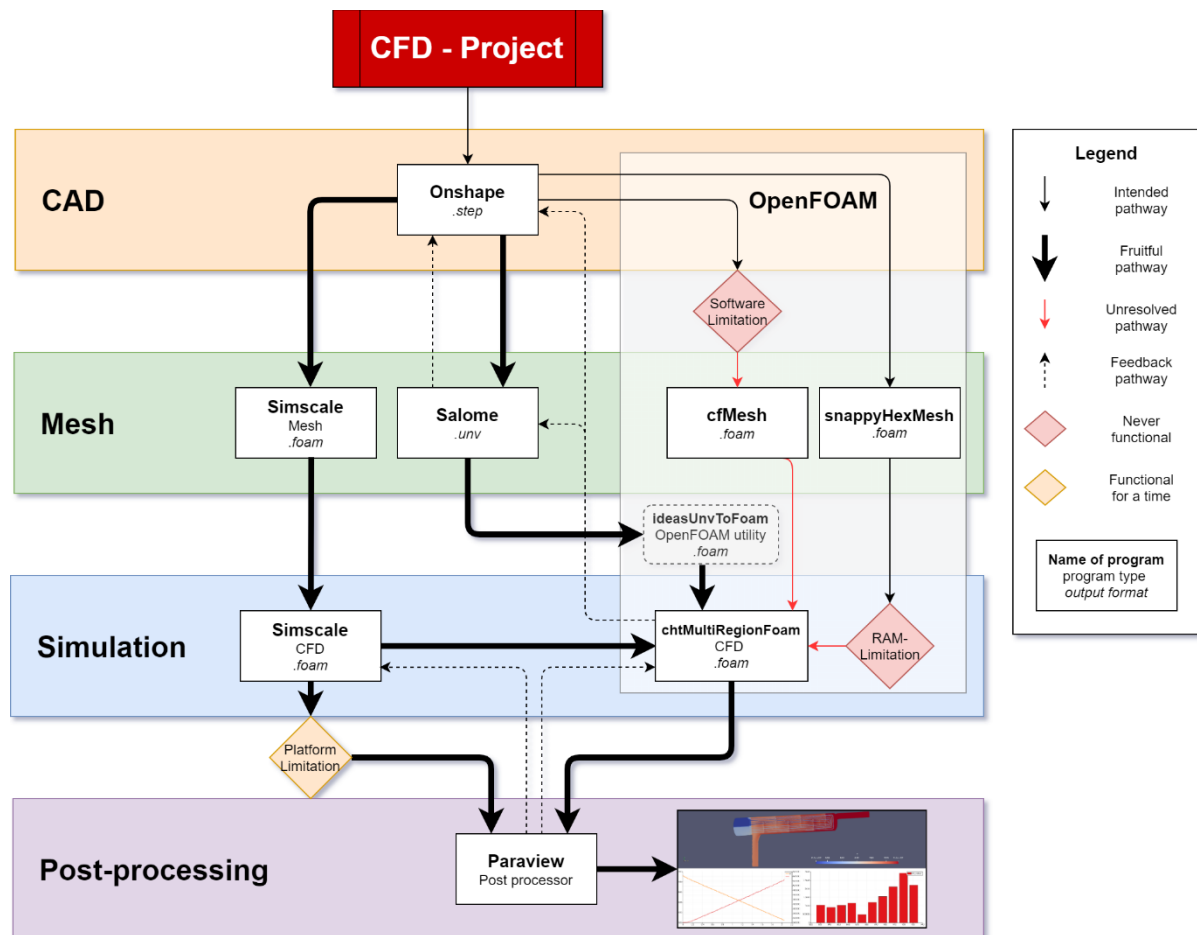


Figure 3.1 Flowchart showing pathways of different programs used in this thesis.

Black thick arrows have proved fruitful, while red arrows indicate pathways that never worked due to some error which is specified in the red diamond boxes. The yellow diamond box indicates that this pathway worked at first but is now unusable since no more core hours are available on Simscale. Dotted lines show the feedback direction, incrementally improving for each iteration until a good enough and physically sound solution is found.

4 CAD results

4.1 Primary heat exchanger

Three distinct regions of the PHeX were defined to handle the simulations; a fluid region for the fuel salt (green), a fluid region for the coolant salt (blue), and a solid region for the metal material (grey) seen at the bottom in Figure 4.1. Top of Figure 4.1 also shows fuel salt inlet and outlet as green, and coolant salt inlet and outlet as blue.

The completed CAD-drawing of the PHeX has been scaled up to include the effect of thermal expansion of Hastelloy-N.

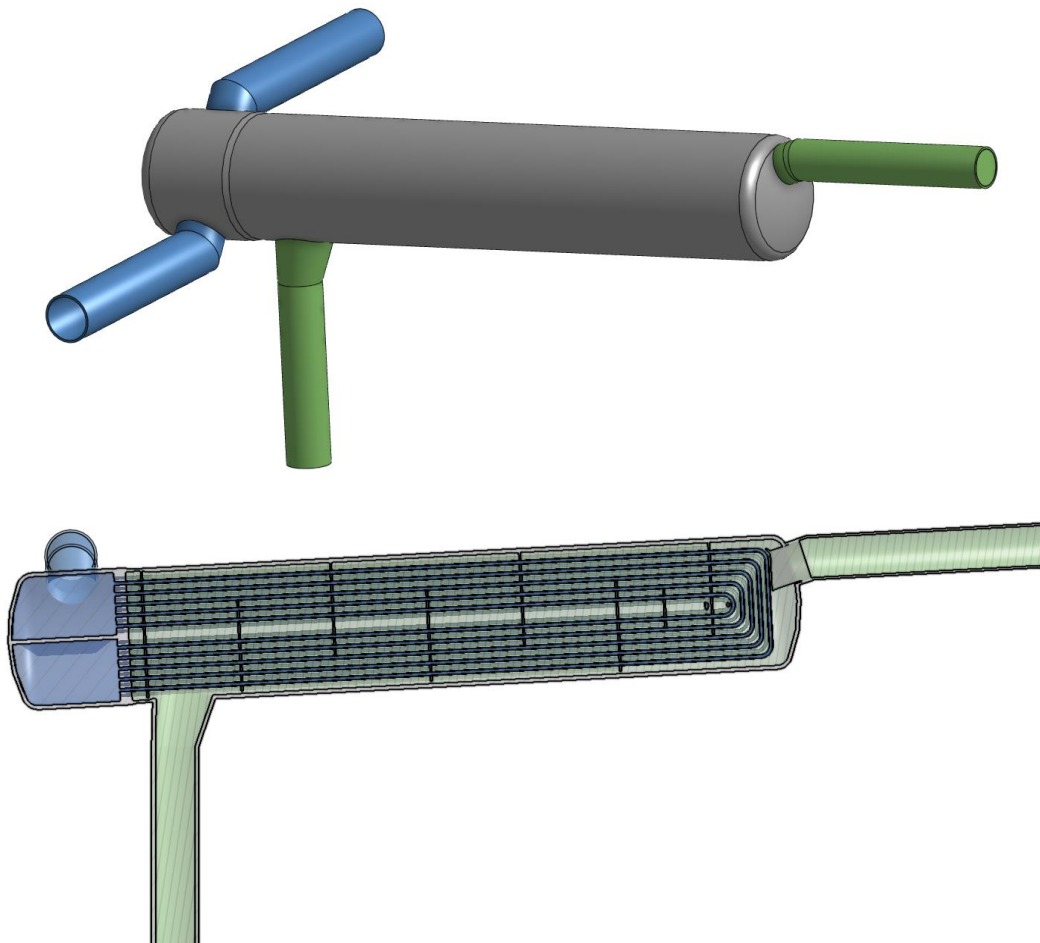


Figure 4.1 Onshape reconstruction of PHeX. Green indicates fuel- and blue coolant salt.
Top: Full model,
Bottom: Section view.

4.1.1 Construction of the model

During the construction of the model of the PHeX, one report in particular has been indispensable, namely ORNL-TM-2098. In that report most of the technical drawings underpinning the extensive design, fabrication and testing of the PHeX can be found. Numerous water tests were performed on the PHeX by the team at ORNL prior to installation, and some modifications were made to alleviate issues they found, mainly relating to tubes vibrating excessively and audibly at certain flow rates. The modifications that the team at ORNL made to the PHeX were successful and are summarized as such (ORNL-TM-2098, 1968), (ORNL-TM-0728, 1965):

1. The four outermost U-tubes were sawed off a couple of centimetres from the barrier plate, and the eight resulting tube stubs were plugged.
2. Thin tie bars laced in a cross-pattern on the downstream side of each baffle plate were put in to stabilize the tubes.
3. Lacing the top of the U-bends in a similar matter, thus making all tubes behave as a single entity.
4. The entire PHeX was lengthened by 2.5 *cm* to allow room for a special impingement baffle at the fuel inlet, spreading the fuel away from the outermost tubes when it enters the shell-side.
5. The former 12.7 *cm* outlet pipe for the fuel was replaced with a 17.8 by 12.7 *cm* conical reducer to reduce the fuel outlet pressure drop.
6. Two spacer rods partially blocking the fuel outlet were removed.

How these changes were incorporated or skipped in the model is detailed in this chapter. Utmost attention to detail was necessary throughout the creation of the CAD model to make sure that the final model would be an adequate reconstruction of the modified PHeX used in the MSRE.

Dimensions have been verified, both visually by superimposing technical drawings upon the model, and numerically by ensuring the lengths and radii were correct where such information was available. Some simplifications were made to the CAD-model which will be outlined below. The modifications listed above do not always appear in the technical drawings and thus, many other documents from ORNL have been examined to make sure that the CAD-model is as true as possible to the one that was actually installed in the MSRE.

The PHeX was completely made out of the heat and corrosion resistant superalloy Hastelloy-N, with a total length of about 2.5 *m*, and an outer diameter of about 0.43 *m*. Inside the shell there are 159 U-shaped tubes (post modifications), each with an outer diameter of 12.7 *mm* and a wall thickness of 1.07 *mm* (ORNL-TM-2098, 1968). Together they spanned an effective heat transfer area of

25.9 m^2 (ORNL-TM-3002, 1970). The completed CAD-model of the PHeX has an effective heat transfer area of 24.5 m^2 which leaves a comparison error of only 5%.

The overall dimensions of the PHeX are 0.4 by 0.7 by 2.4 m .

The two fluid regions will hereby be referred to as the “tube-side” for the coolant region, and the “shell-side” for the fuel region, respectively. What follows is a breakdown of the components in the PHeX, relevant measurements and functionality along with technical drawings provided by ORNL together with images of the reconstructed parts done in Onshape.

4.1.2 Tube sheet

The main separator between the fuel- and coolant salt is the tube sheet, connecting the shell and the bottom side, as well as housing all the tubes. It is a circularly symmetric piece, with an outer diameter of 43.8 cm and a thickness of 3.8 cm . The inner diameter, defining the maximum radius of both fluid volumes, is 41.3 cm , allowing for a 1.3 cm shell. Many of the measurements seen in Figure 4.2 are for construction purposes, allowing for space to weld and fitting parts together (ORNL-TM-2098, 1968).

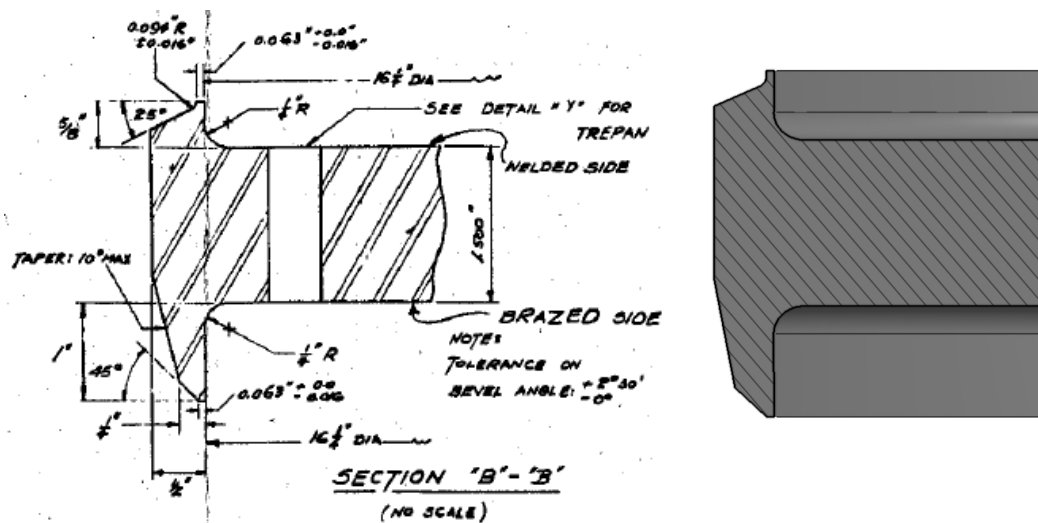


Figure 4.2 Section view of the tube sheet.
Left: Technical drawing (ORNL-TM-2098, 1968),
Right: Onshape reconstruction.

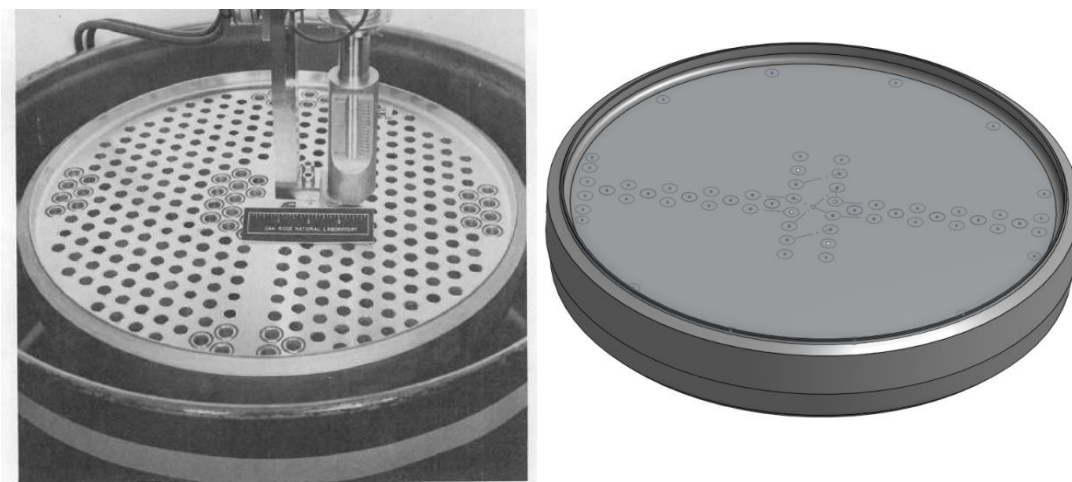


Figure 4.3 Tube sheet.
 Left: MSRE, manufactured part (ORNL-3500, 1963),
 Right: Onshape reconstruction with guides for tube holes.

All the tube holes in the tube sheet and connected baffles are arranged in an equilateral triangular pattern with a side length of 1.97 cm , and a hole diameter of 1.27 cm as shown in Figure 4.4.

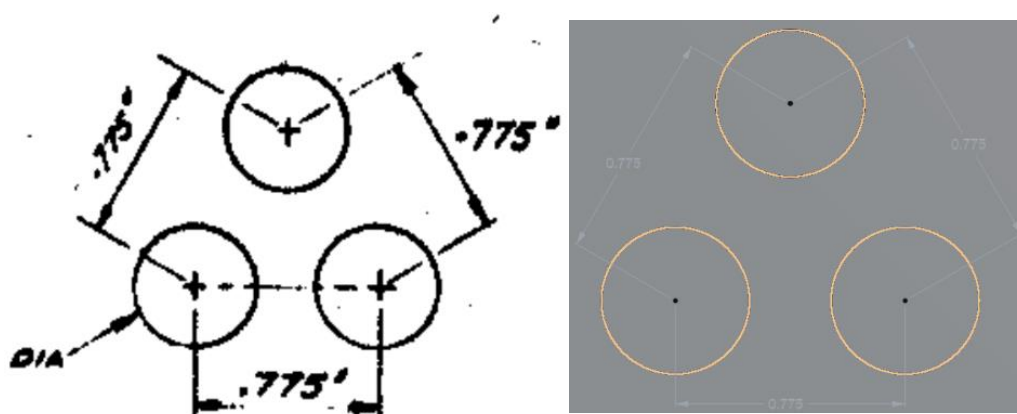


Figure 4.4 Tube arrangement pattern.
 Left: Technical drawing (ORNL-TM-2098, 1968).
 Right: Onshape reconstruction.

4.1.3 Barrier- and baffle plates

The baffle plates are an important addition to the conventional shell-and-tube heat exchanger. They serve two important purposes; 1) fixing the tube spacing and, 2) creating crossflow of the fuel salt over the tubes. The way baffles are oriented, as seen in Figure 4.6, forces the fuel salt to travel along the allowed pathways created by the baffles in the shell-side of the PHeX. The resulting crossflow keeps the salt in a turbulent state, where thermal energies are mixed throughout the flow, ensuring that the temperature gradient across the tube walls are always as large as possible. What limits the heat transfer rate of the PHeX is the thermal conductivity of the Hastelloy-N metal, where the heat physically must travel across the solid metal.

There are 3 types of baffles, referred to as “A”, “B” and “C” seen in Figure 4.5, arranged in the direction shown, screwed and tack welded onto the spacer rods. The “A” and “B” baffles are very similar, except for mirroring around the centreline and a small cutaway section at the bottom of the “A” baffle, allowing for the fuel salt to be passively drained in case the pumps would ever stop. The large cutaway segment is 25% of the diameter on both “A” and “B” baffles. The “C” baffle is only used once between the last two “A” and “B” baffles to provide stability towards the end of the tube bundle. All of the baffles are 0.64 cm thick.

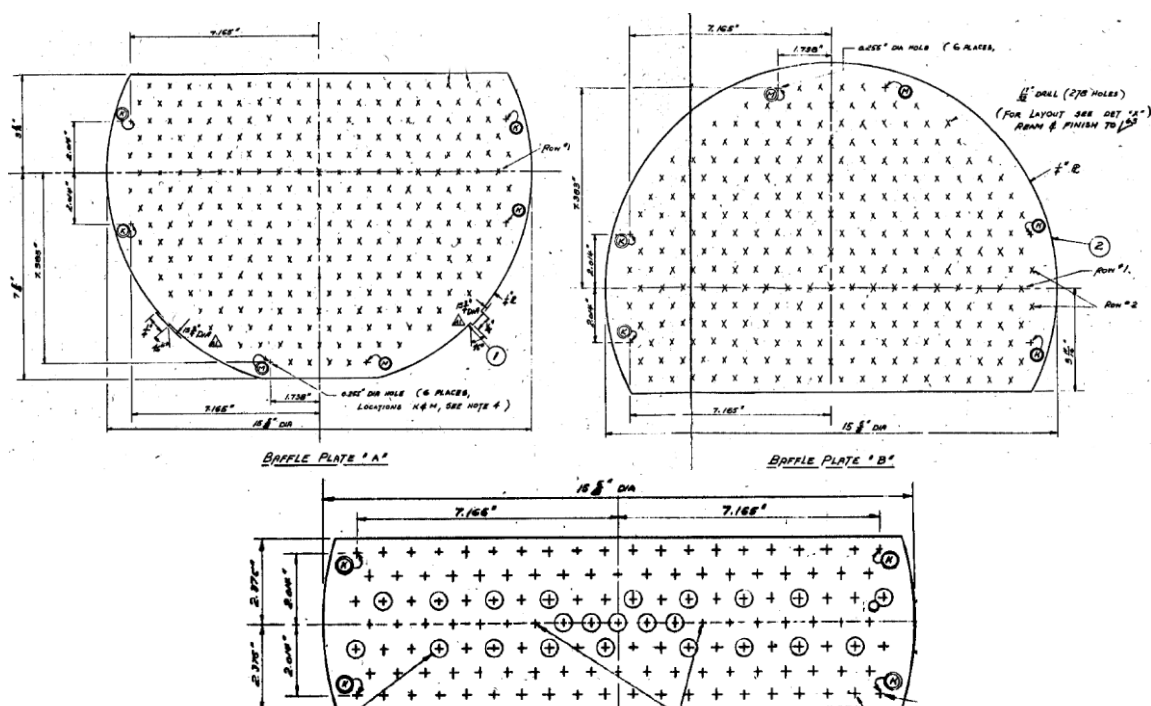


Figure 4.5 Technical drawing of the baffle plates (ORNL-TM-2098, 1968).

Top left: “A”,
Top right: “B”,
Bottom: “C”.

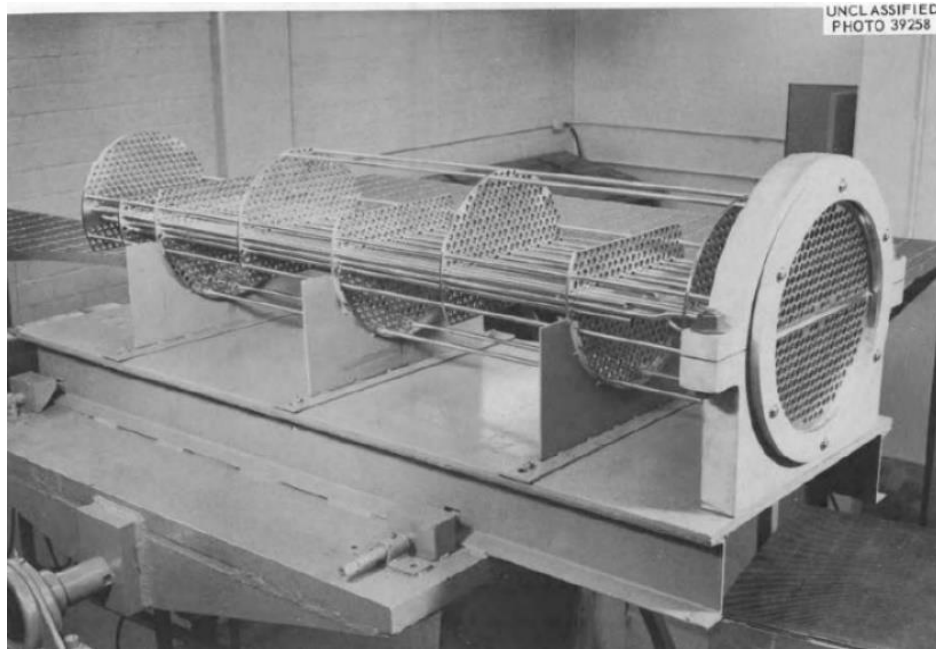


Figure 4.6 PHeX with all the baffle plates in place, spaced apart by the spacer rods as built (ORNL-3500, 1963).

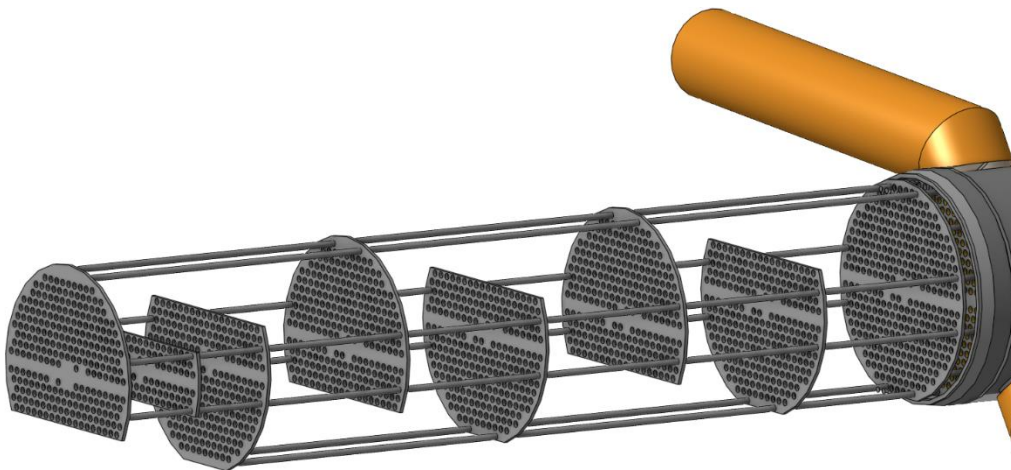


Figure 4.7 Onshape reconstruction of the baffle plates "A", "B", "C" and the barrier plate.

In Figure 4.6 and Figure 4.7 a baffle without any large cutaway segment can be seen closest to the tube sheet. This is the barrier plate, acting as a thermal barrier, keeping a somewhat stagnant layer of fuel salt in between it and the tube sheet to limit the temperature gradient across the tube sheet. It has a small cutaway segment at the bottom to allow for some salt circulation and drainage. As noted in the modifications that the team at ORNL made to the PHeX, a special impingement baffle was added at the fuel inlet to spread the fuel away from the outermost tubes as it enters the shell-side to alleviate tubes vibrating due to the large inlet flow. It was fastened to the fuel inlet nozzle, shown in Figure 4.8 as technical drawings and Figure 4.9 as the Onshape reconstruction.

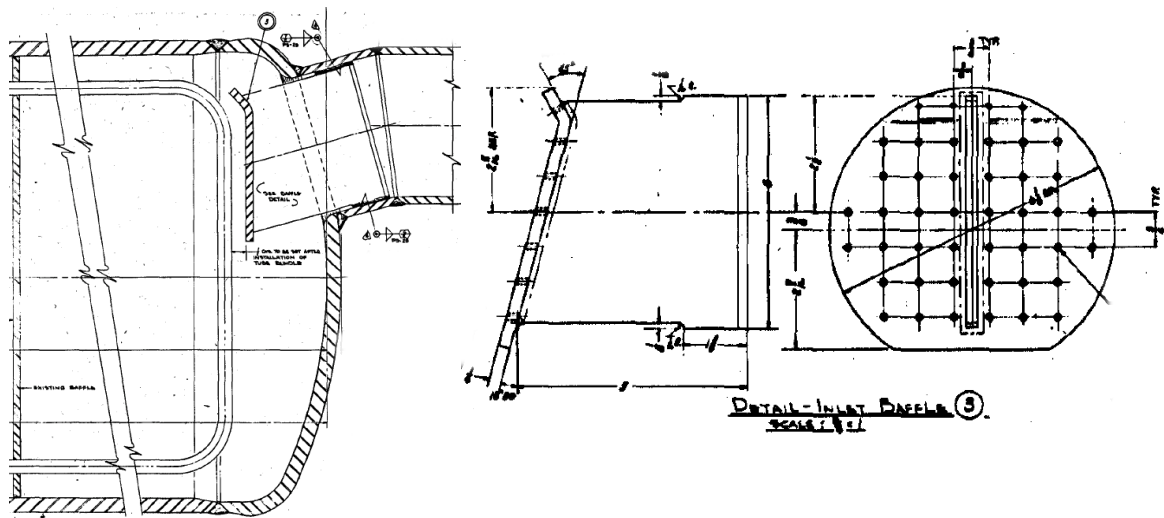


Figure 4.8 Technical drawing of the impingement baffle at fuel inlet (ORNL-TM-2098).

Left: Location in the PHeX (fuel inlet),
Right: Impingement baffle hole arrangement.

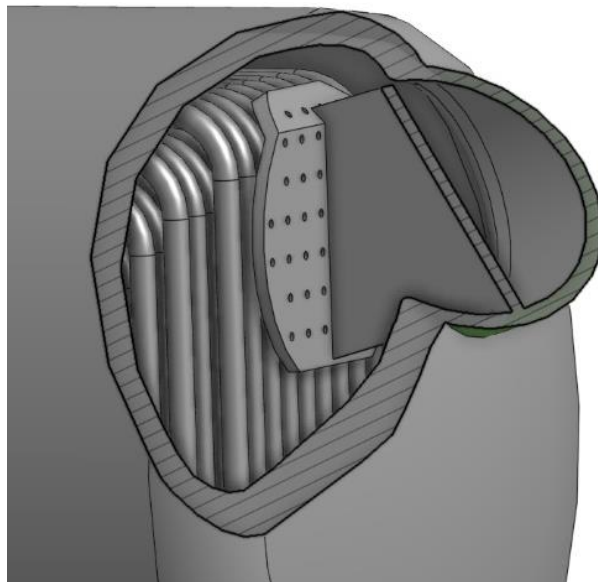


Figure 4.9 Section view of Onshape impingement baffle reconstruction.

4.1.4 Shell

The shell is attached to the tube sheet, with a length of about 2.4 m, and a thickness of 1.3 cm. It has a dished end at both the head (fuel inlet, to the right in Figure 4.10) and the bottom (coolant inlet and outlet, to the left in Figure 4.10). Attached to the shell are the four inlet and outlet nozzles, along with the legs. As can be seen in Figure 4.10, the entire PHeX is rotated towards the outlets to provide passive draining.

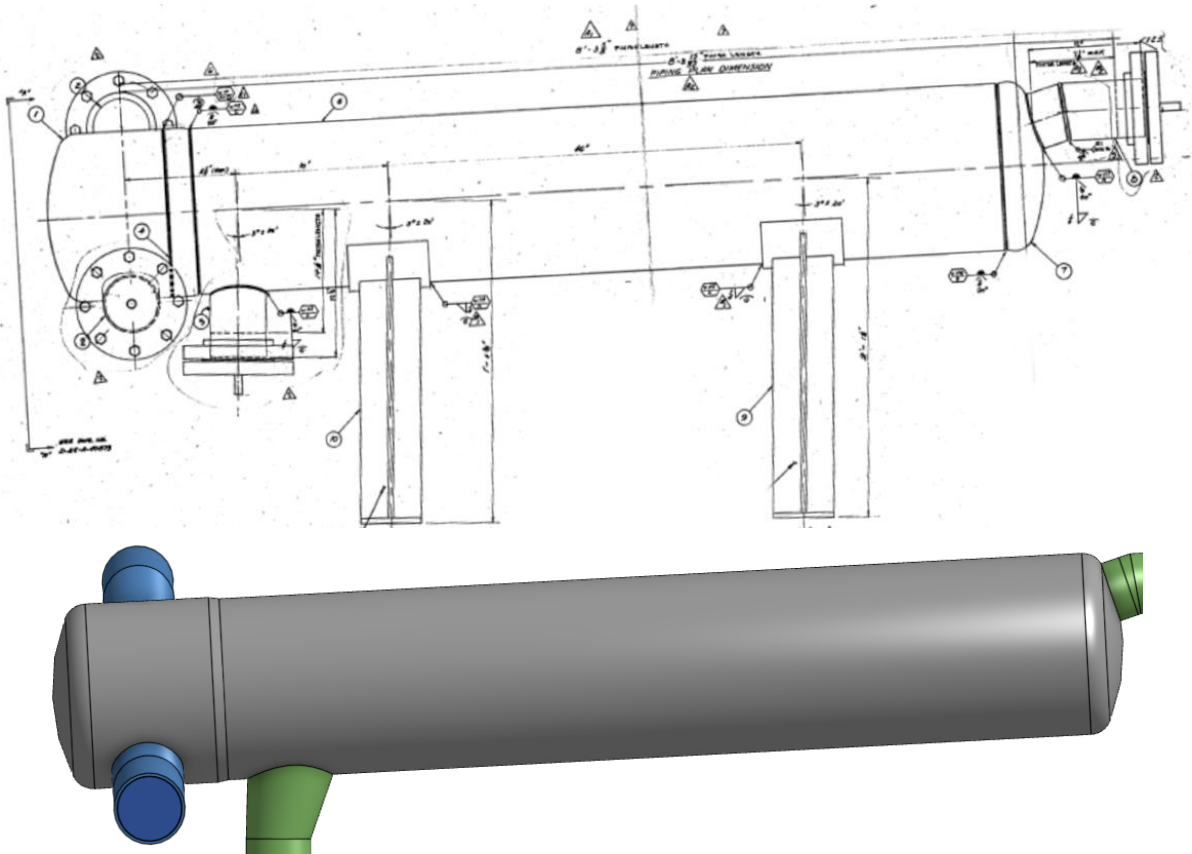


Figure 4.10 PHeX shell, side view.
 Top: Technical drawing (ORNL-TM-2098, 1968),
 Bottom: Onshape reconstruction.

4.1.5 Tubes

All the tubes are housed inside the shell, in the configuration shown in Figure 4.11 and Figure 4.12. The outer diameter of the tubes is 1.3 cm , with a tube wall thickness of 1.07 mm . This thickness was not chosen for pressure-stress consideration, but for welding requirements, where experience had indicated that wall thickness of less than 1.02 mm had more of a tendency to crack at the tube welds (ORNL-TM-0728, 1965).

There are in total 159 tubes after the modifications specified in the ORNL-TM-2098 report (ORNL-TM-2098, 1968). The 4 tubes that were sawed off and plugged are kept in the CAD-model. In addition, there are 12 spacer rods symmetrically distributed, which are solid bars going through various lengths of the PHeX. Their purpose is to provide stability and to hold the baffles in place while spaced apart.

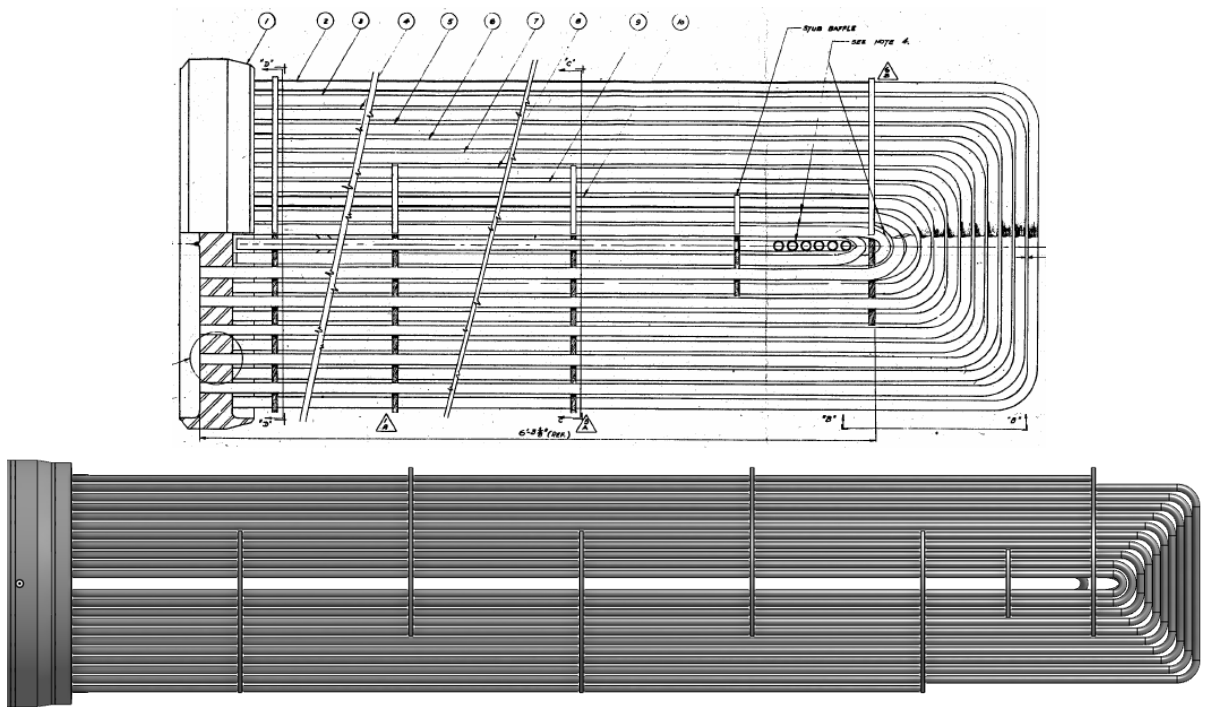


Figure 4.11 PHeX tube, side view.
Top: Technical drawing, not to scale (ORNL-TM-2098, 1968),
Bottom: Onshape reconstruction.

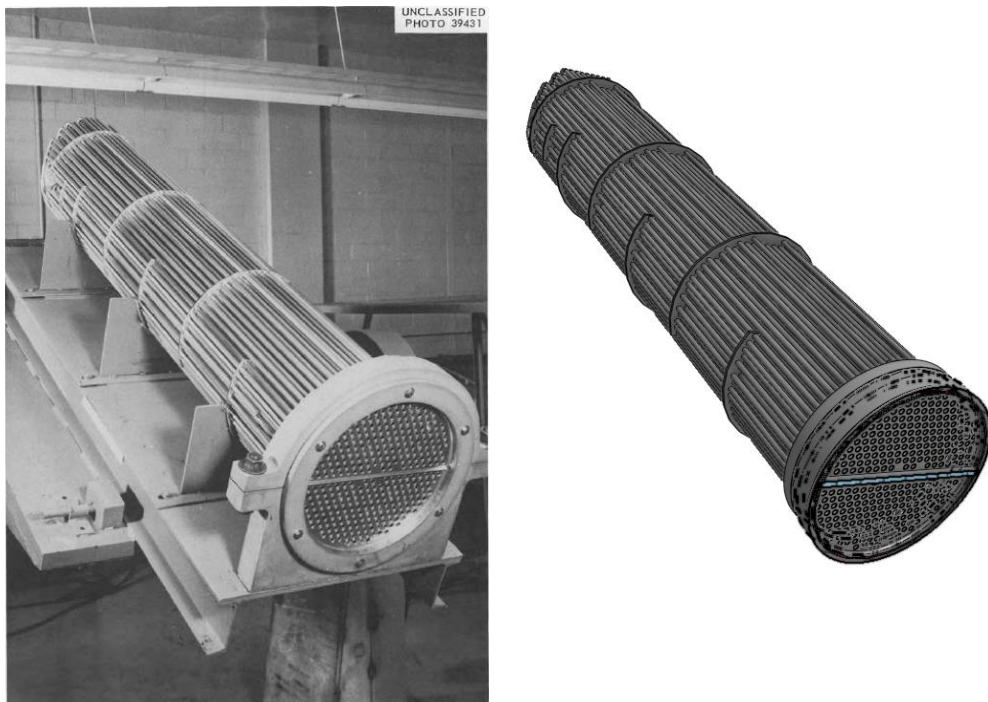


Figure 4.12 PHeX tube bundle.
Left: Bundle manufactured at ORNL (ORNL-3500, 1963),
Right: Onshape reconstruction.

4.1.6 Inlets and outlets

4.1.6.1 Shell-side (Fuel)

The fuel salt inlet and outlet are oriented along the centreline of the PHeX. The inlet is mounted at an angle on the dished end of the shell head, as seen in Figure 4.13 as a technical drawing from ORNL and as the Onshape reconstruction.

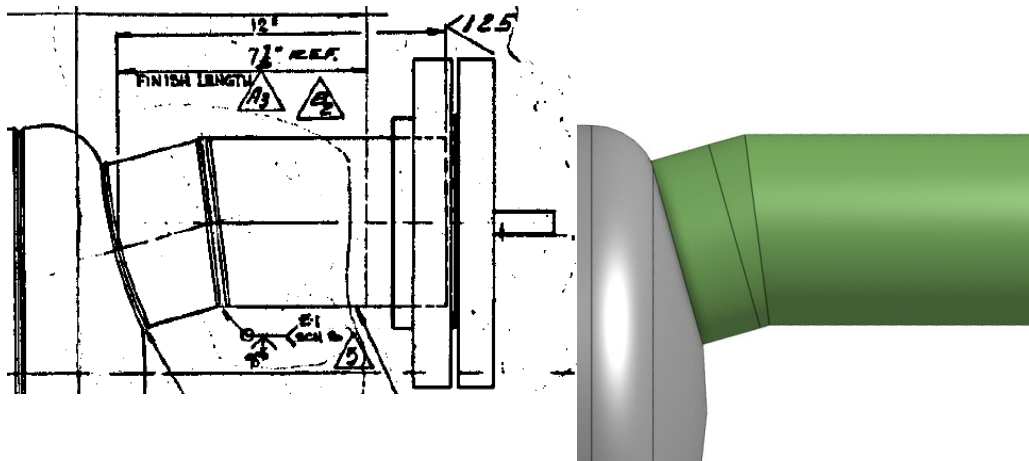
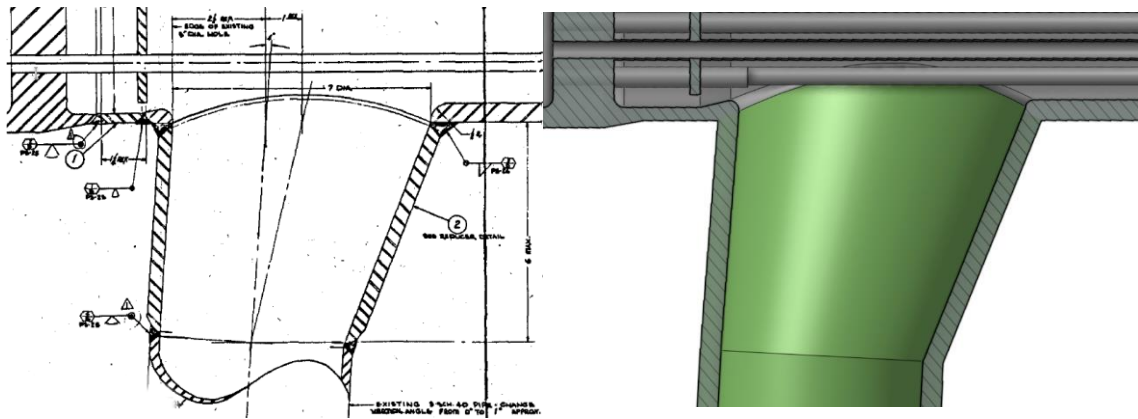


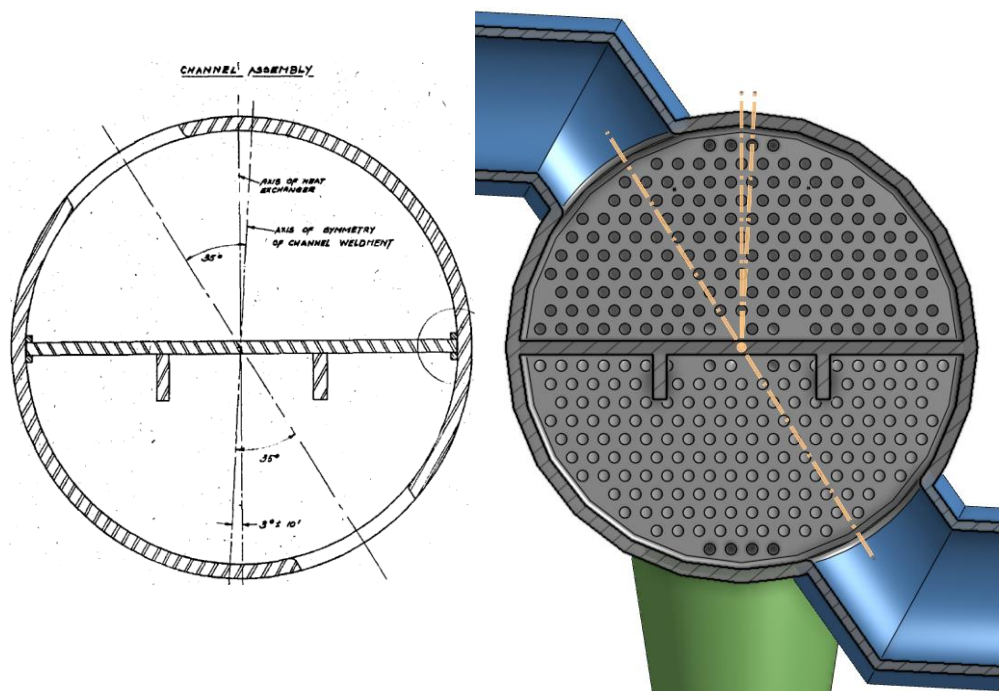
Figure 4.13 Fuel inlet.
Left: Technical drawing (ORNL-TM-2098, 1968),
Right: Onshape reconstruction.

The fuel outlet, as mentioned in the modifications that the team at ORNL made to the PHeX, was switched from a simple 12.7 cm pipe pointing straight down to a slanted conical reducer, with an initial diameter of 17.8 cm, narrowing to 12.7 cm. This was put in to reduce the pressure drop on the shell-side fuel salt. Above in Figure 4.10 this detail cannot be seen and instead, what is shown is the design utilized before they did any modifications to the PHeX. Fuel outlet is seen in Figure 4.14 as technical drawing (post modification) to the left and as Onshape reconstruction to the right.



4.1.6.2 Tube-side (Coolant)

Both the coolant inlet and outlet are mounted symmetrically across the bottom of the PHeX, seen in Figure 4.15. In the right image, the axes of symmetry that the in- and outlets are based upon are highlighted in yellow.



4.1.7 Deviations from the PHeX technical drawings

Some deviations from the specifications made by the team at ORNL were made to limit unnecessary complexity to the CAD-model. The technical documents were put together for construction

purposes, which makes some details unnecessary for CAD work. Deviations from the technical reports are listed below.

- The most significant deviation is the way that the tubes pass through the baffles. In the ORNL specifications, the holes through the baffles are bigger than the tubes, leaving a clearing of 0.8 *mm* around each tube. The reason for the clearance is to allow for thermal expansion of the tubes and to facilitate fabrication of the baffles as specified by the Tubular Exchanger Manufacturers Association (TEMA) standard, followed and upheld by the team at ORNL (TEMA, 2007). Modelling this would not have been difficult, however, the resulting mesh would have significantly increased the mesh-element count as well as the simulation time without adding anything significant to the final result. Instead, the baffles and the tubes were joined together, omitting the clearance altogether.
- The center of the tube bundle seems to have been filled with empty dummy tubes (23 of them according to one reference in (ORNL-TM-3151, 1972)). This was most probably included to make sure that the flow across the tube bundle center would have the same behaviour as across the rest of the bundle, but no references explicitly clarifying this have been found. The difficulty in adequately modelling the center of the tube bundle comes down to missing technical drawings. In ORNL-TM-2098 there are references to a technical drawing titled “DWG No. D-EE-A-40875” where this information seems to have been detailed, but that drawing is missing. Here a choice was needed, and a decision was made to leave the center of the tube bundle empty.
- Any mention of welding procedures and resulting welding material has been omitted for simplicity. The deviations from the smooth surfaces in the model would have added some turbulence but given that the entire system already is highly turbulent, the omission of these details will most probably not alter the final result by any significant amount.
- The lacing bars behind each baffle plate have also been omitted. CFD and CHT are not concerned about mechanical stability, and the inclusion of these bars would only have added unnecessary extra mesh-elements with little to no impact on the final result.

- Both legs were removed for every simulation, since these would not impact either the CFD or CHT and would only have added extra, unnecessary mesh-elements.
- The inlets and outlets have all been lengthened artificially by a couple of pipe diameters. This is standard CFD-practice since we want the incoming and outgoing flows to be as close to fully developed as possible so as to have a well-defined velocity profile at the inlets and outlets.

4.2 Radiator

The radiator was defined with three regions; a fluid region for the coolant salt, a fluid region for the air and a solid region for the metal material, which include the tubes and the surrounding metal enclosure. The fluid regions will hereby be referred to as the “air-side” and the “salt-side”. Figure 4.16 shows the final CAD model of the radiator.

The completed CAD-drawing of the radiator has been scaled up to include the effect of thermal expansion of Hastelloy-N.

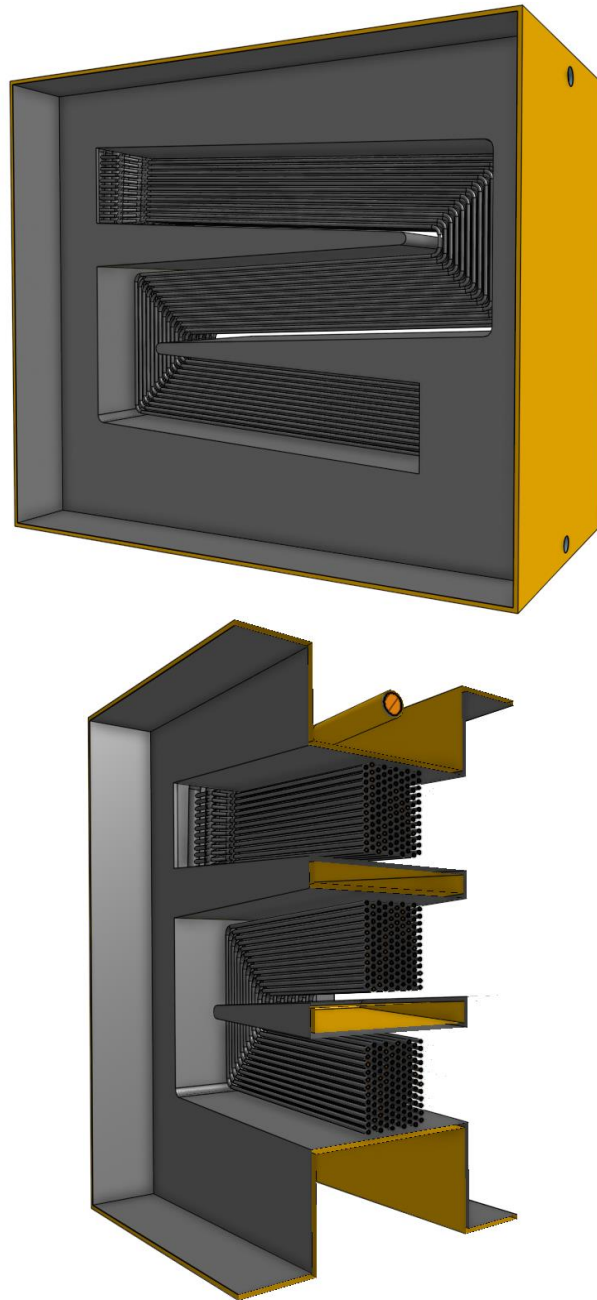


*Figure 4.16 Onshape reconstruction of the radiator.
Top: Full model,
Bottom: Section view.*

4.2.1 Construction of the model

The details necessary to construct the radiator was spread out over multiple documents from ORNL, mainly contained in ORNL-CF-60-11-108, ORNL-TM-4174, and ORNL-3122, -3369, -3708, -4037. In these documents, extensive details of the construction of the radiator can be found (ORNL-CF-60-11-108, 1960), (ORNL-TM-4174, 1972), (ORNL-3122, 1961), (ORNL-3369, 1962), (ORNL-3708, 1964), (ORNL-4037, 1967).

The radiator was also subjected to numerous water tests to make sure that no leakage was present and that all components functioned satisfactorily. Most of the issues were found to be contained in the door mechanism to limit the cooling provided by the air blowers. The door would warp from uneven heating and from thermal cycling during normal operation, and the metal seal was found to leak excessive amounts of air. The team at ORNL included a soft seal around the hard metal seal to remedy this, as well as a reconfiguration of the hard metal seal. Modifications to the door lifting mechanisms were also put in place, preventing slack in the chains and providing an all-around tighter fit around the enclosure. These modifications proved successful, and no more revisions were made. However, the overall heat transfer coefficient never exceeded 66% of the pre calculated value, and the team at ORNL could not precisely identify the source of this discrepancy.

The CAD-model will not contain these modifications since the doors have been completely omitted. That is, all simulations concerning the radiator assume that the doors are fully opened at all times.

Most of the radiator was constructed with structural steel, with parts exposed to high temperatures being made of stainless steel. Every component in direct contact with the molten salt however was constructed out of Hastelloy-N.

The effective heat transfer area of the radiator installed in the MSRE was calculated to be 65.6 m^2 .

The completed CAD-model of the radiator has an effective heat transfer area of 65.3 m^2 which leaves a comparison error of only 0.5%.

The overall dimensions of the radiator are 1.8 by 3.6 by 3.0 *m*

4.2.2 Main-headers

The salt flows in from the top through a long pipe connecting the PHeX and the radiator together. As it enters the radiator it first passes through the main-header. It is a cylindrically shaped part with dished heads at either end, constructed out of Hastelloy-N, with an inner diameter of 20.3 cm and a wall thickness of 1.3 cm. An identical but mirrored main-header is positioned at the outlet as well. From the main-header the salt gets distributed and pumped through the sub-headers. The main-header can be seen as a technical drawing, manufactured part and reconstructed model in Figure 4.17.

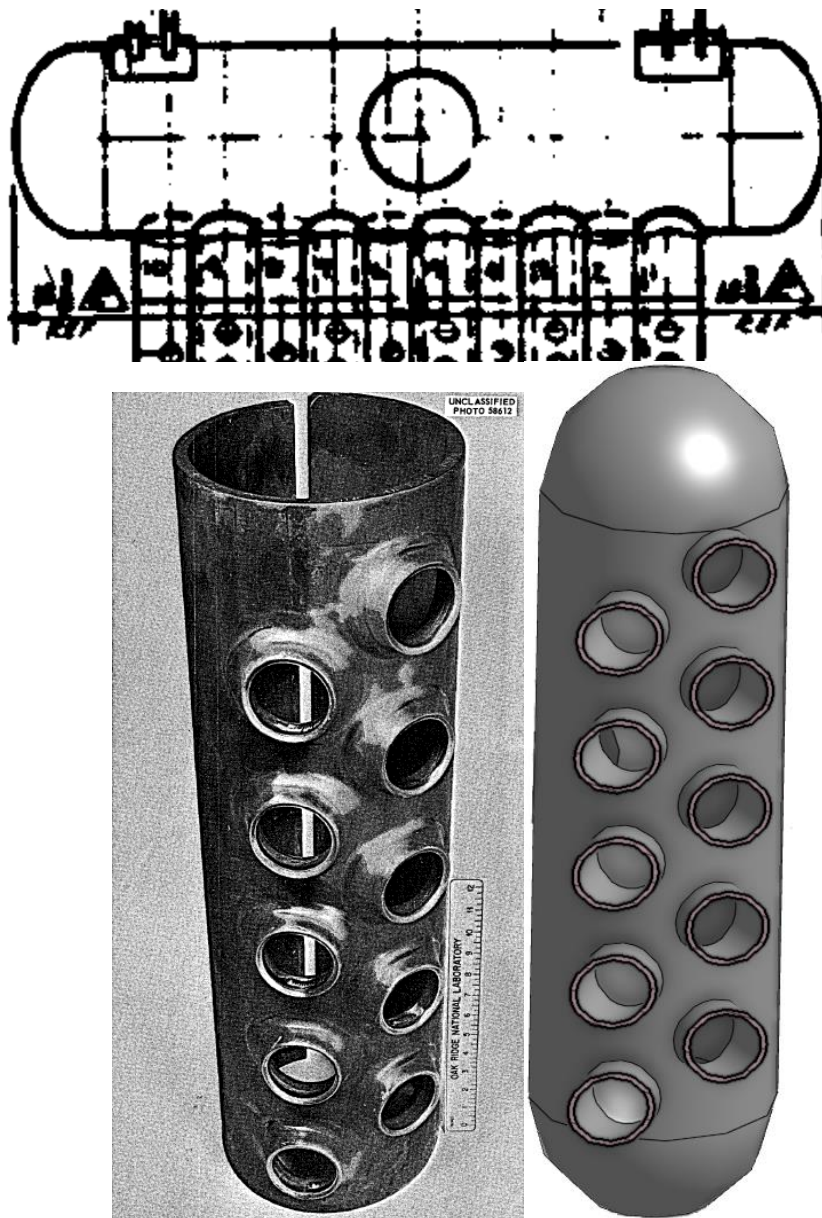


*Figure 4.17 Main-header for the radiator.
Top: Technical drawing (ORNL-TM-4174, 1972),
Bottom left: Manufactured part at ORNL (ORNL-3708, 1964),
Bottom right: Onshape reconstruction.*

4.2.3 Sub-headers

After the salt has passed through the main-headers it gets pumped through the sub-headers, which are smaller pipes attached to the main-header, with the function to distribute the salt equally into smaller tubes to facilitate a better heat transfer. From each main-header there are 10 sub-headers extruding, and from each sub-header 12 tubes are attached, making 120 tubes in total. The sub-headers are each schedule 40 pipes made out of Hastelloy-N, each with an inner diameter of 6.4 cm and a wall thickness of about 1.3 cm. Technical drawing, manufactured part and reconstructed model of the sub-headers can be seen in Figure 4.18.

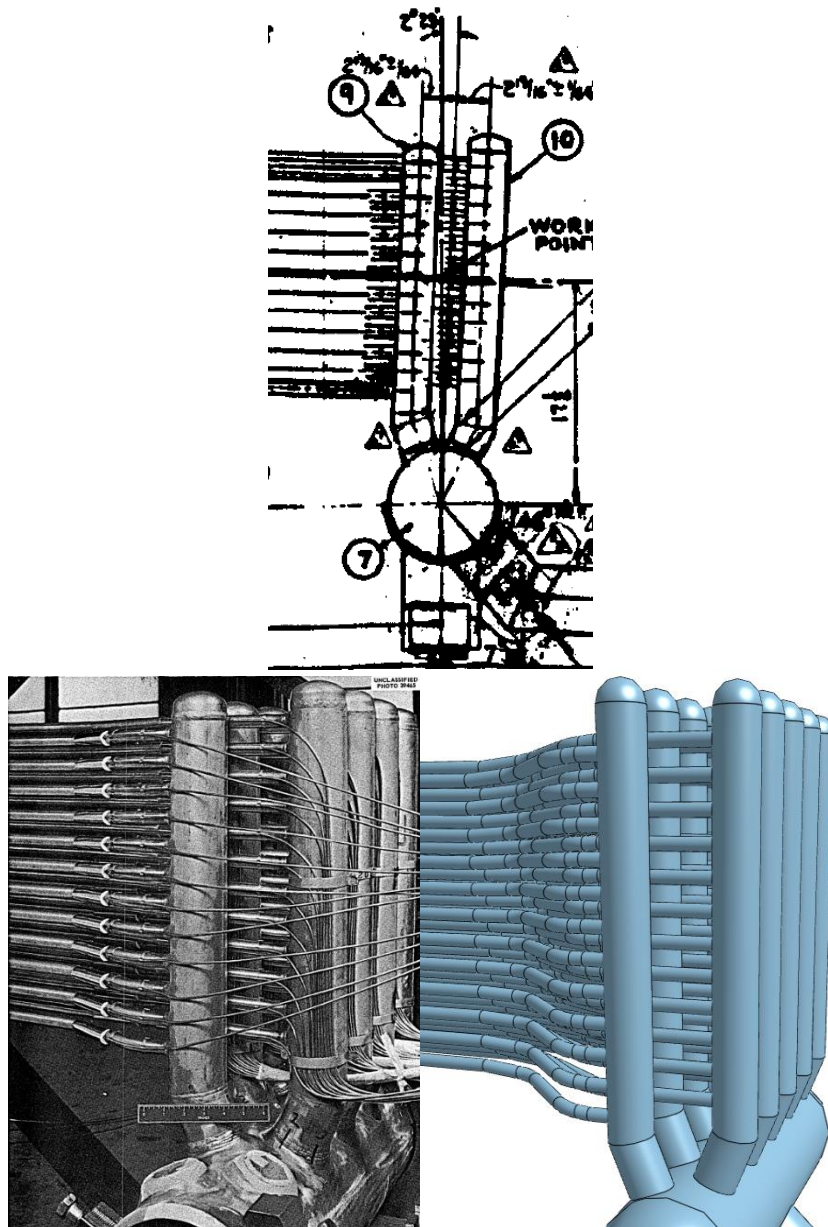


*Figure 4.18 Sub-header configuration.
Top: Technical drawing (ORNL-TM-4174, 1972),
Bottom left: Manufactured part at ORNL (ORNL-3708, 1964),
Bottom right: Onshape reconstruction.*

4.2.4 Tubes and tube configuration

There are 120 tubes in the radiator, each having a diameter of 1.9 cm, a wall thickness of 1.8 mm, and a length of about 9.1 m, providing a total effective heat transfer area of 65.6 m^2 (about the same area as a standard squash court!). A section-view of a segment of the tubes, showing configuration, can be seen in Figure 4.19.

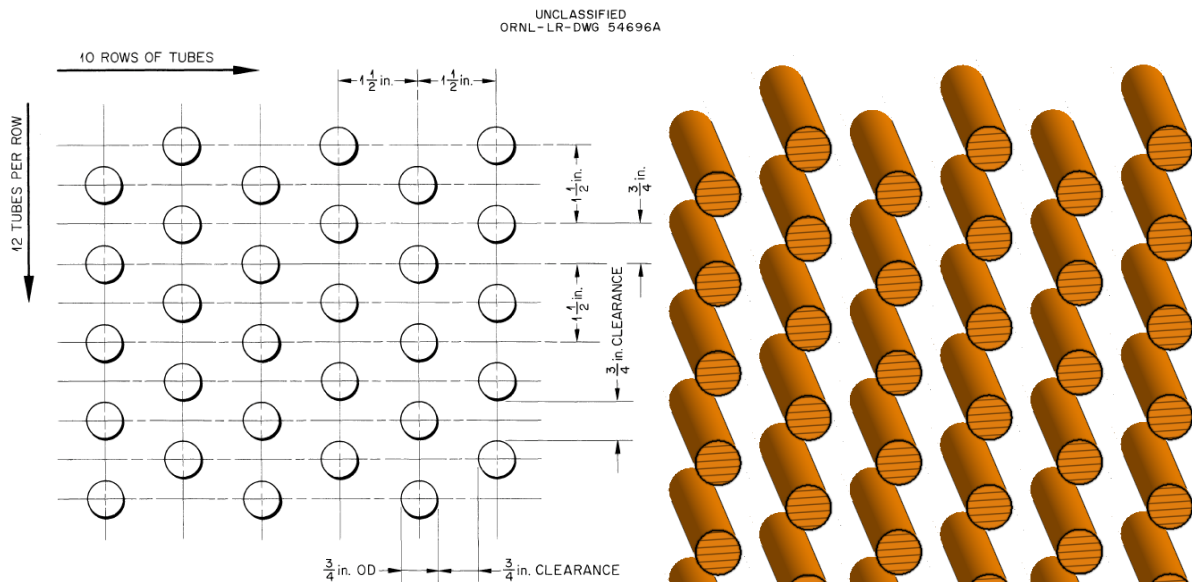
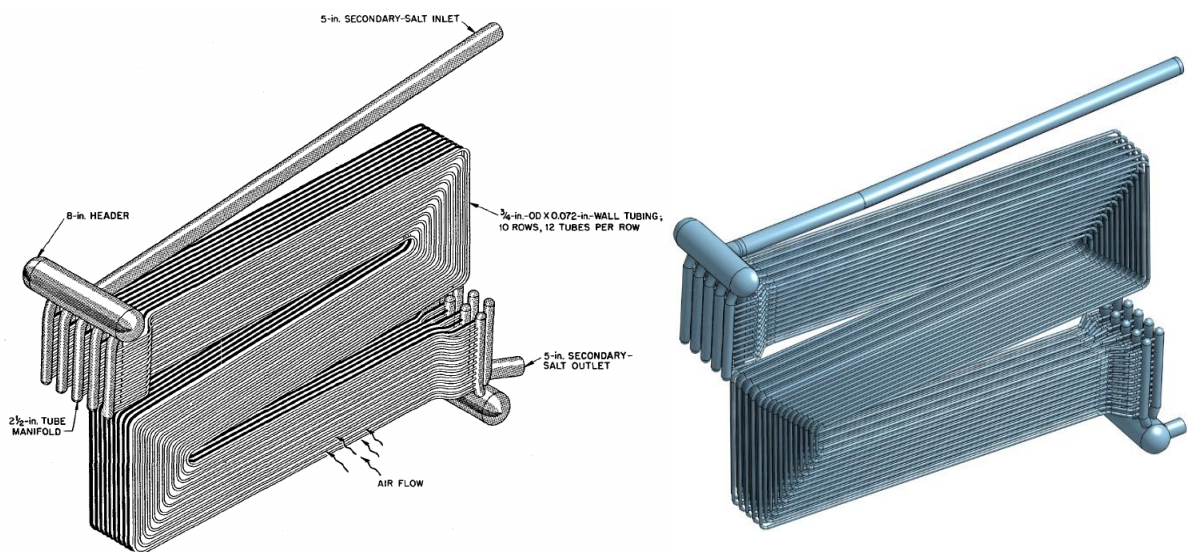
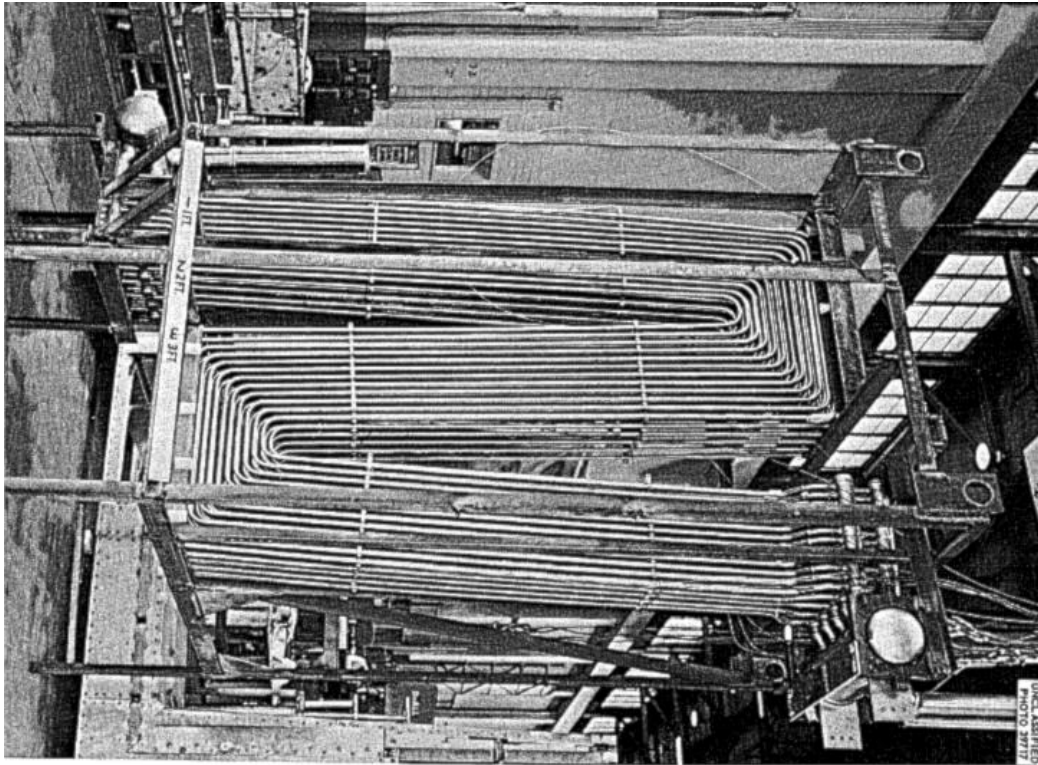


Figure 4.19 Tube configuration in the MSRE radiator.
Left: Technical drawing (ORNL-3122, 1961),
Right: Onshape reconstruction.

The tubes are made out of Hastelloy-N since they will always be in contact with the hot coolant salt. Technical drawing, manufactured part and reconstructed model of the full tube configuration can be seen in Figure 4.20.



*Figure 4.20 Radiator tubes, full configuration.
Top: Manufactured part (ORNL-3708, 1964),
Bottom left: Technical drawing (ORNL-3014, 1960),
Bottom right: Onshape reconstruction.*

4.2.5 Radiator enclosure

The entire radiator had to be enclosed to ensure that the air passed exclusively around the tubes in order to dump the heat to the air. Any air leakage is effectively just another strain on the blow-fans since it will not contribute to the heat transfer. This is where the previously mentioned hard and soft

seals come into play to direct the air further, but they are of no concern when simulating since the air flow is simply set as a boundary condition for the relevant region in the model. The enclosure was mostly made out of structural and stainless steel, since none of it is in direct contact with the coolant salt.

A technical drawing, manufactured part and reconstructed model of the radiator enclosure can be seen in Figure 4.21.

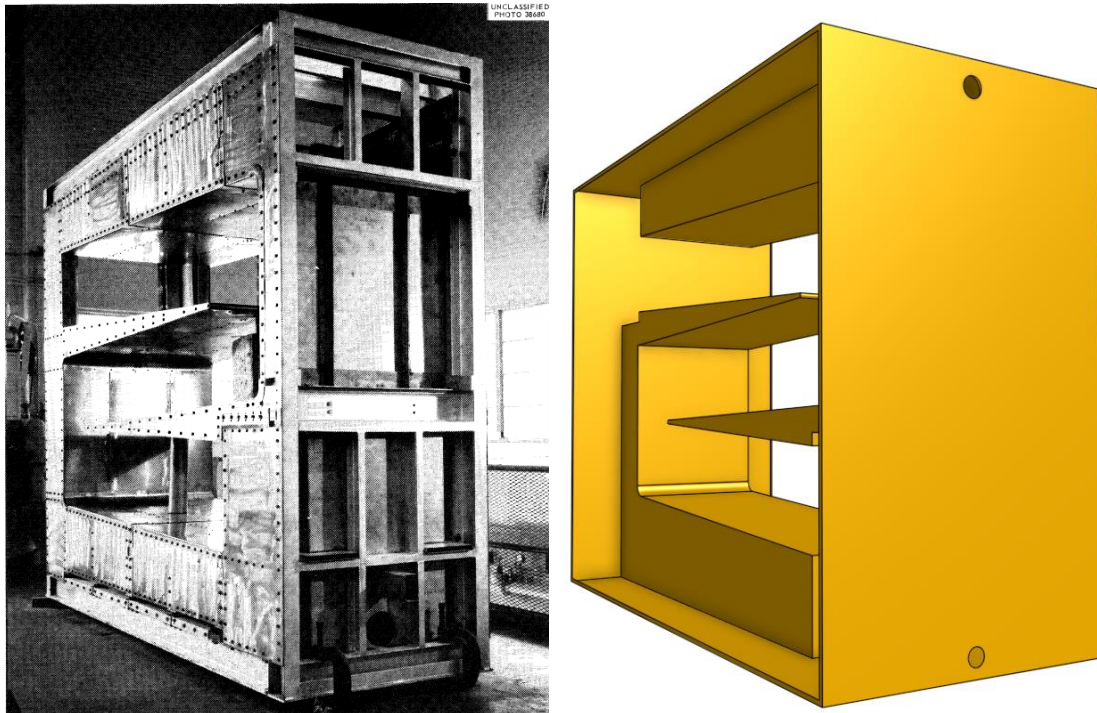


*Figure 4.21 Radiator enclosure.
Top: Technical drawing (ORNL-3215, 1961),
Bottom left: Manufactured part (ORNL-3369, 1962),
Bottom right: Onshape reconstruction.*

4.2.6 Deviations from the technical drawings

Not as many deviations were made for the radiator as were done for the PHeX. Mainly because the information about specifics was very hard to come by, and most of the modifications that were made had to do with components that were not modelled. Some simplifications to the radiator enclosure were made, as can be seen by the side-by-side comparison in Figure 4.21. Such changes will not impact the result at all since they do not concern the Conjugate Heat Transfer (CHT). All the support structures were also omitted since they impact the CHT very little.

4.3 Heat exchanger test model

Since the final model is computationally intensive, it is time consuming to test meshing techniques and initial simulation setup on the full model. For this purpose, a simpler version of the PHeX was created, with essentially the same setup, just much smaller and consisting of only 4 tubes (versus the 159 in the full PHeX model). Tube thickness and configuration is exactly the same as for the PHeX, so that parameters for meshing can be easily translatable between the two models. Figure 4.22 shows a section view and a full translucent view of this test model.

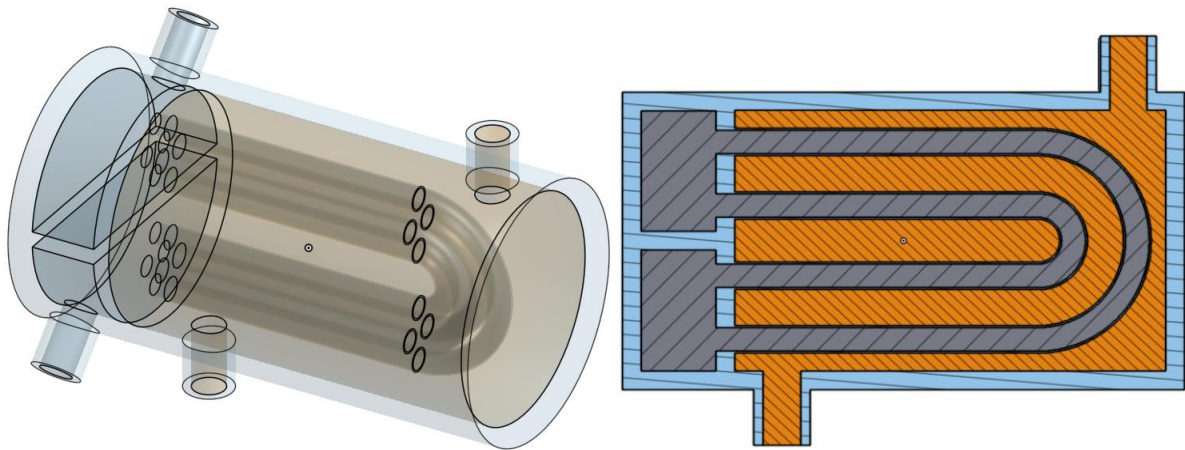


*Figure 4.22 Test model for meshing and simulation setup purposes.
Left: Translucent full view,
Right: Section view showing all three regions: shell (orange), tube (grey) and solid (blue).*

This test model proved to be very useful in designing a workflow with Salome that is scalable to the full PHeX as well as to the radiator, since both models essentially have the same setup. A document has been written by the author, meant to be used as a guide for anyone else that has a big, multiregion CAD model that they wish to mesh with Salome. The document can be found in Appendix III.

5 Meshing results

Two programs were used for meshing. For the first half of the project Simscale was used, when Simscale could provide core hours for usage. When the core hours were used up, Salome was employed instead. The documentation of Simscale is not open and thus, the algorithms employed for meshing are not known. Most probably they used OpenFOAM's application "snappyHexMesh" with some extra functionality added from their side.

In this section the following results are shown:

- Meshing results from Simscale for representative regions
- Similar comparisons from Salome

Many more meshes have been computed for each region, but they have been excluded to not take up unnecessary space. The meshes shown have been used for simulations and underlie the results in Chapter 6. To assess the mesh quality the following parameters will be considered where available:

- The number of mesh-elements (i.e., cells), which serves as an indicator of how well the entire model is meshed, as well as an indicator for the overall solution time
- The number of boundary layers, which indicates how well each boundary is resolved
- Overall quality of the mesh where available
- The three indicators; non-orthogonality, skewness and aspect ratio, introduced in Chapter 2

The overall mesh quality is a measure from Simscale, calculated with an unknown algorithm. This datum will only be shown for the meshes produced by Simscale.

All elements are tetrahedrons, except for the boundary layers. The different shapes seen in the following images comes from truncation caused by cutting planes in the programs used to capture the images.

5.1 Meshing with Simscale

5.1.1 Simscale mesh results: PHeX

Table 5.1 shows a quality breakdown for the PHeX mesh produced by Simscale, followed by figures showing mesh for chosen regions. Figures are produced with Paraview.

Table 5.1 Quality of Simscale PHeX mesh

Quality indicator	Max	Average
Non-orthogonality	89	23.7
Skewness	9.4	0.2
Aspect ratio	51	1.3
Total number of cells	Number of boundary layers included	
38 459 090	3	
		Overall quality
		0.42

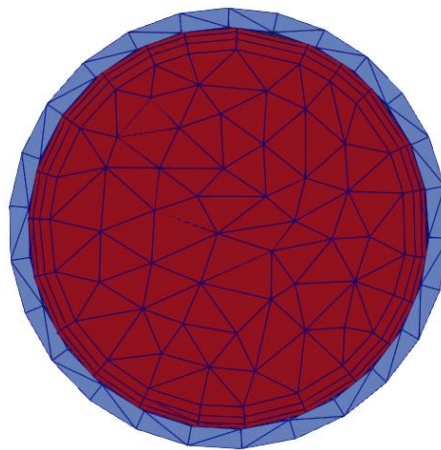


Figure 5.1 Simscale meshing of typical inlet and outlet in the PHeX, showing boundary layers.

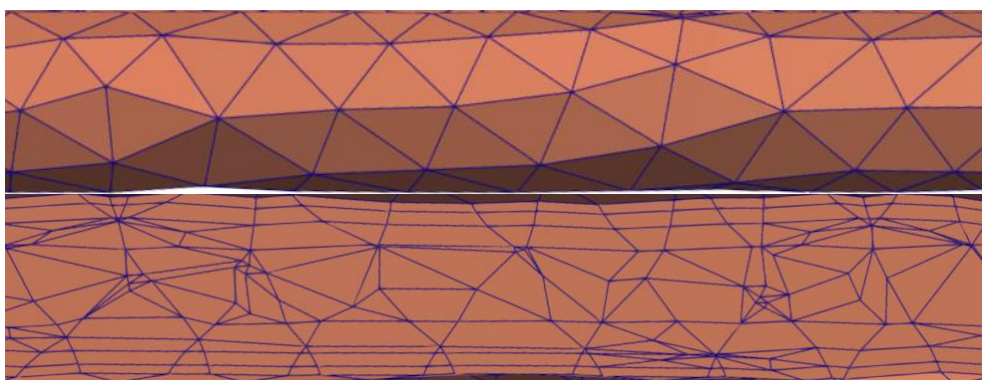


Figure 5.2 Simscale meshing of a typical section of the PHeX tubes.
Top: Outside of tubes,
Bottom: Inside of tubes, showing boundary layers.

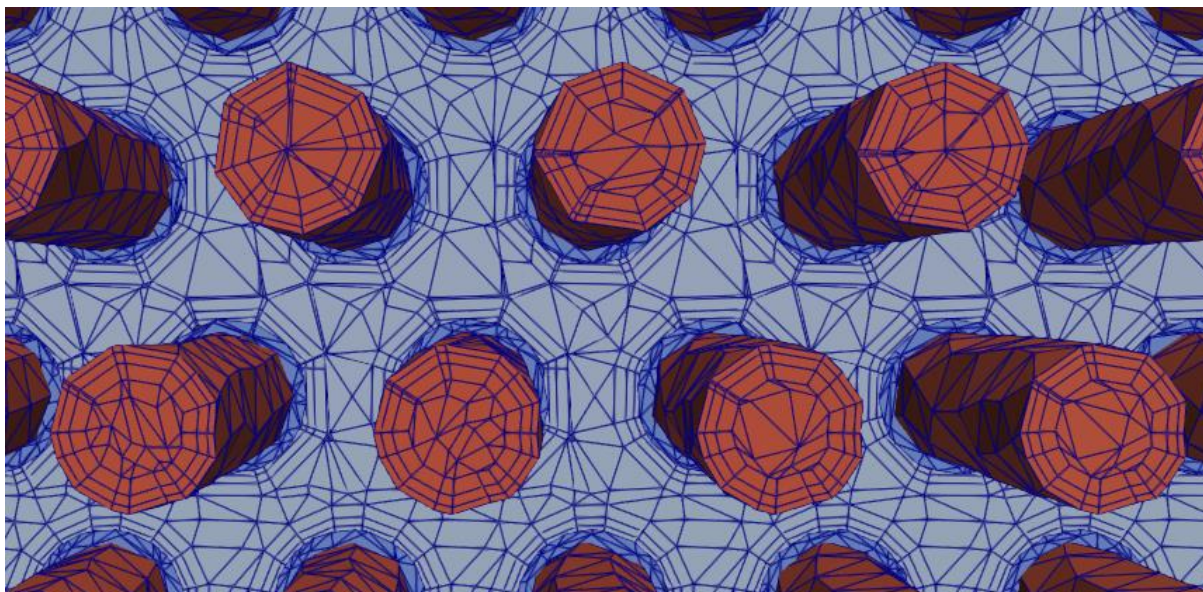


Figure 5.3 Simscale meshing, section view of the PHeX, showing boundary layers for both tube-side (blue) and shell-region (red).

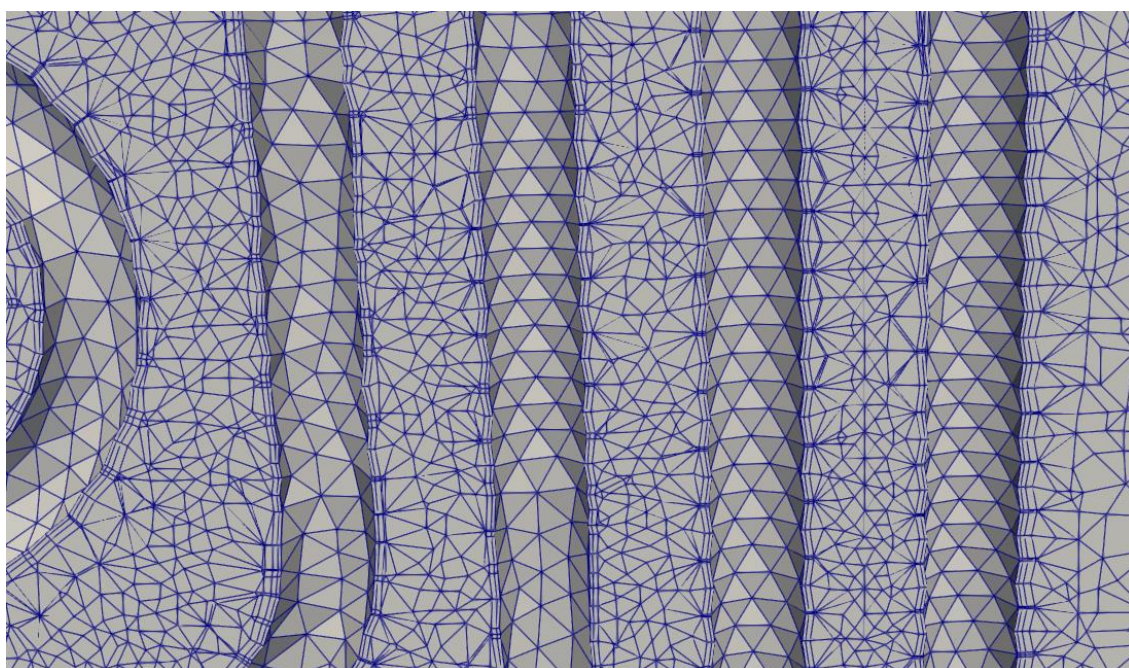


Figure 5.4 Simscale meshing, section view of the meshing of regions between PHeX tubes, showing boundary layers in the shell-side.

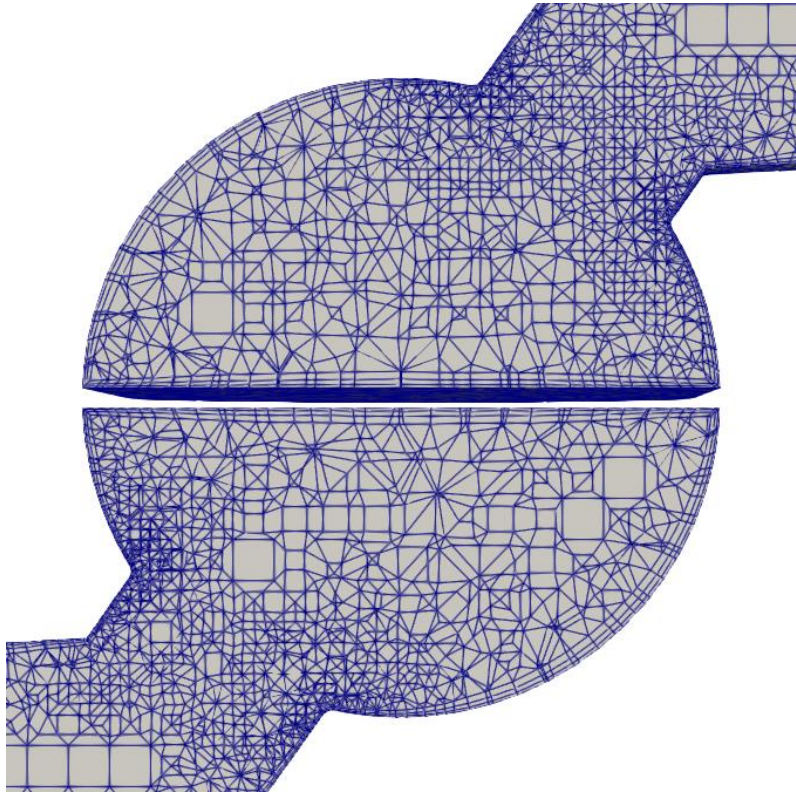


Figure 5.5 Simscale meshing of PHeX coolant bottom channel, with inlet (top right) and outlet (bottom left).

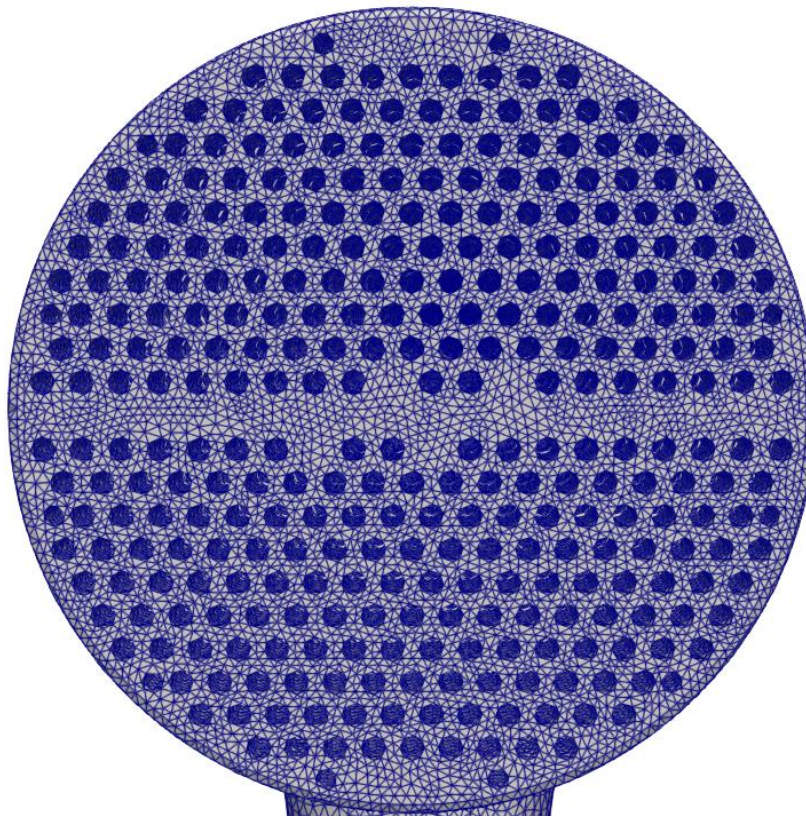


Figure 5.6 Simscale meshing of the tube sheet where all the tubes are attached in the PHeX.

5.1.2 Simscale mesh results: Radiator

Table 5.2 shows a quality breakdown for the radiator mesh produced by Simscale, followed by figures showing mesh for chosen regions. Images are produced with Paraview.

Table 5.2 Quality of Simscale radiator mesh.

Quality indicator	Max	Average
Non-orthogonality	84.7	23.8
Skewness	3.4	0.2
Aspect ratio	11.6	1.4
Total number of cells	Number of boundary layers included	
23,600,000	3	
		Overall quality
		0.39

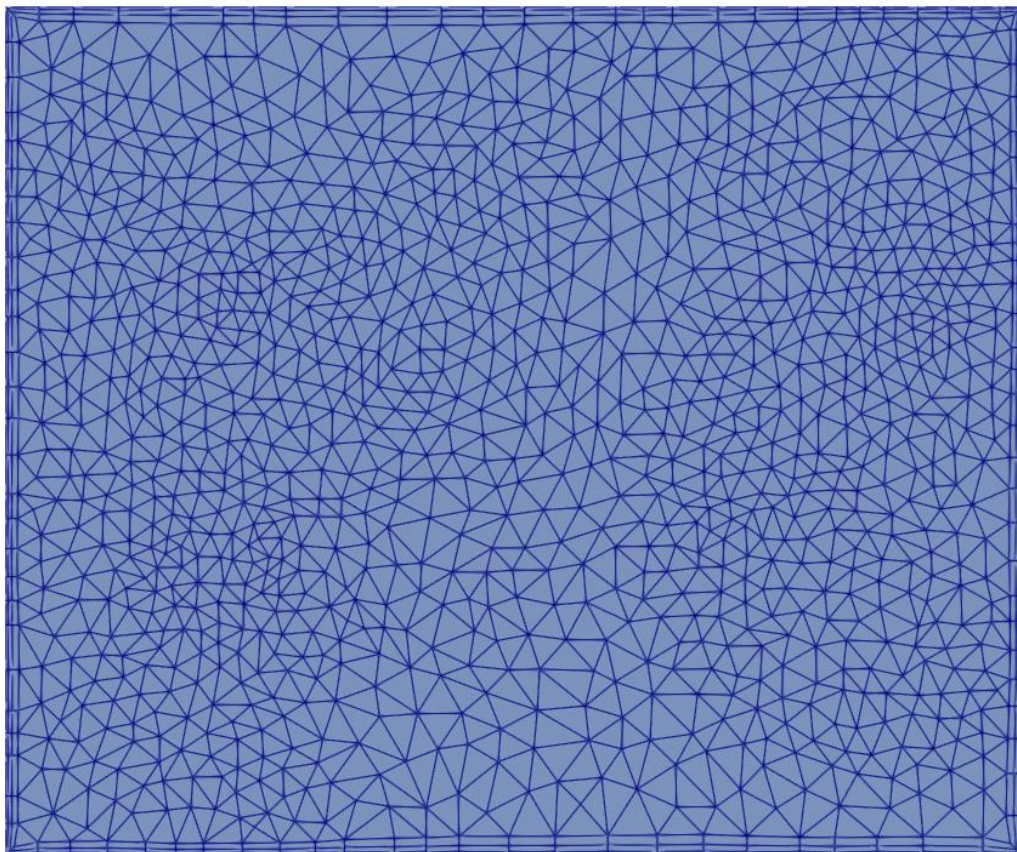


Figure 5.7 Simscale meshing of air inlet for the radiator, with boundary layers.

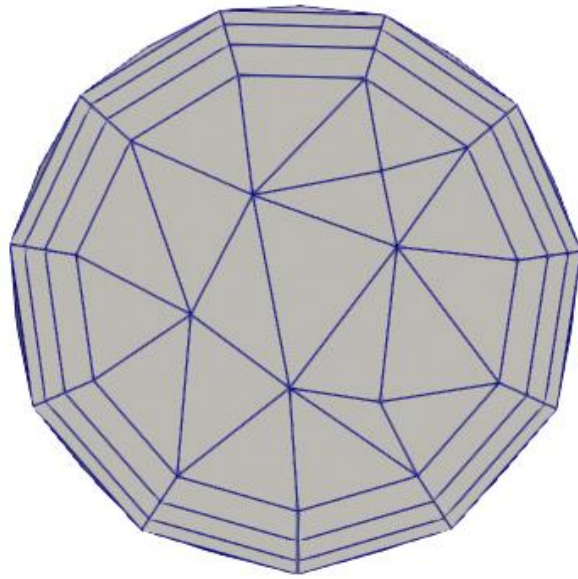
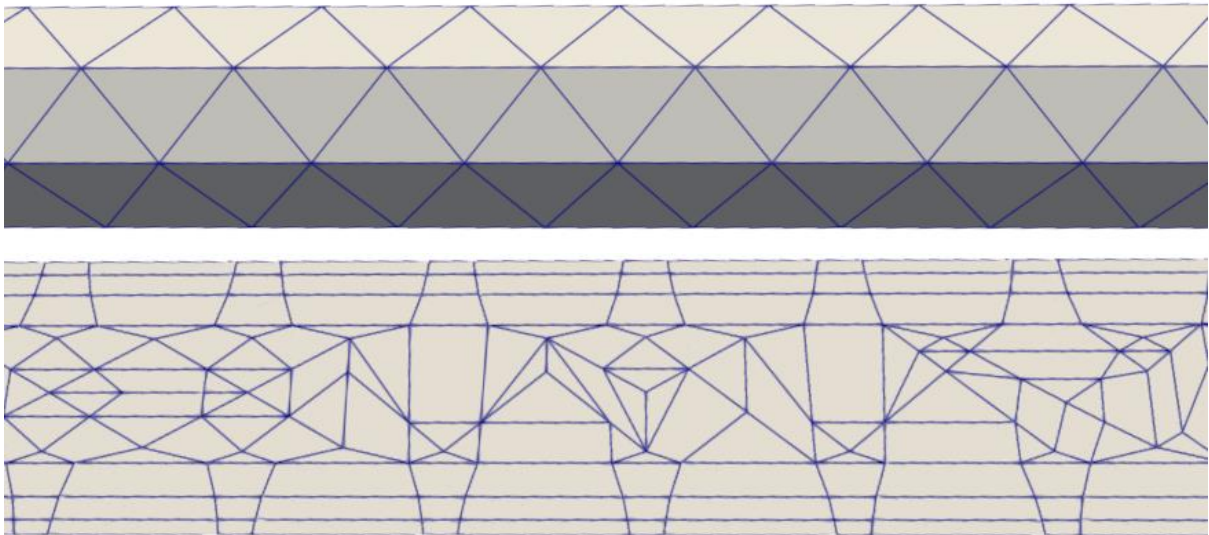


Figure 5.8 Simscales meshing of salt inlet for the radiator, with boundary layers.



*Figure 5.9 Simscales meshing of typical segment of radiator tube,
Top: Outside of tube,
Bottom: Inside of tube, showing boundary layers.*

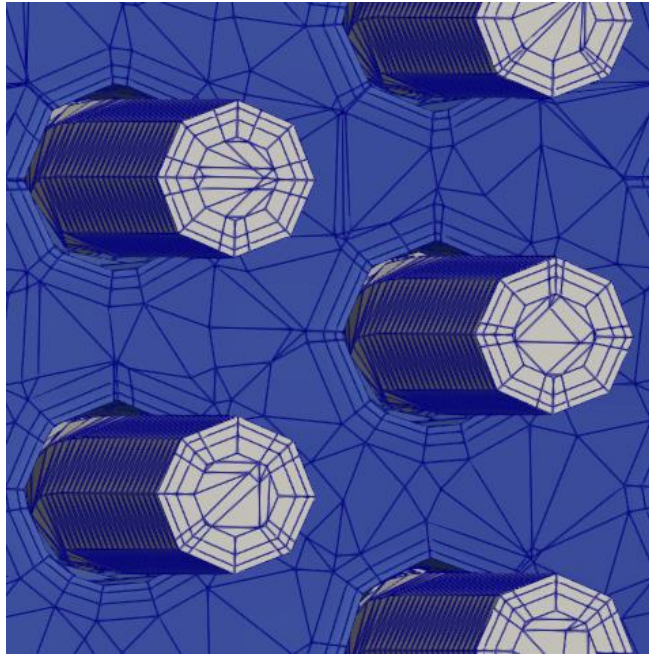


Figure 5.10 Simscape meshing of typical section of meshed radiator tube and surrounding shell, showing boundary layers in both regions.

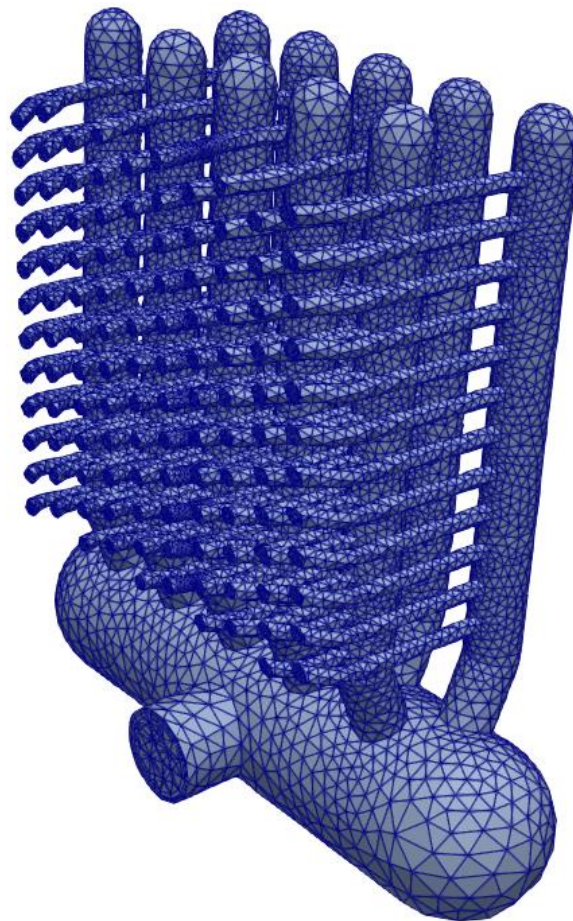


Figure 5.11 Simscape meshing of one of the main radiator headers with connected sub-headers and tubes.

5.2 Meshing with Salome

Salome does not have a built-in quality check for the meshes, so a python script produced by a Salome user has been used instead through Salome's script-editor. This script does not give information on non-orthogonality or an overall quality check. It was produced by Ludwig Wurstbrot and can be seen in Appendix IV.

5.2.1 Salome mesh results: PHeX

Table 5.5 shows a quality breakdown for the PHeX mesh produced by Salome, followed by figures showing mesh for chosen regions. Images are produced with Paraview and Salome.

Table 5.3 Quality of Salome PHeX mesh.

Quality indicator	Max	Average
Non-orthogonality	—	—
Skewness	84.1	7.5
Aspect ratio	11.54	1.07
Total number of cells	Number of boundary layers included	
59,950,946	0	
		Overall quality
		—

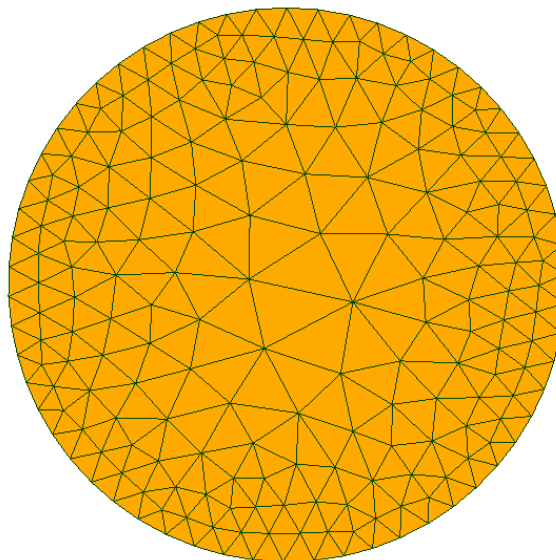
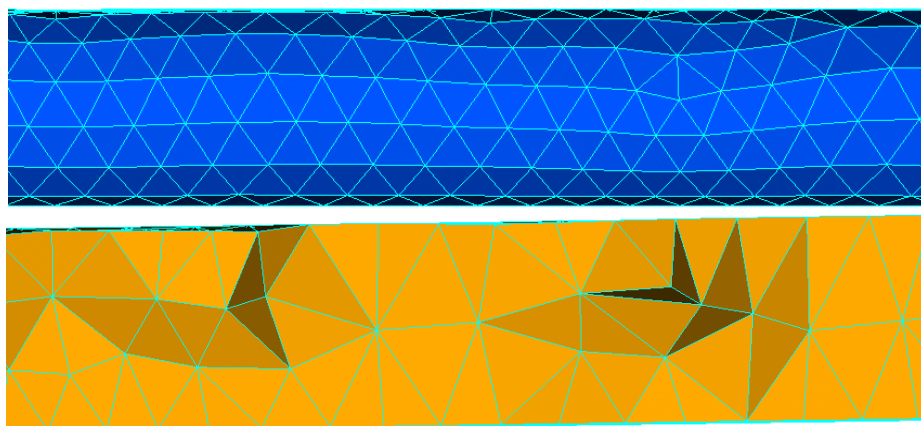


Figure 5.12 Salome meshing of typical in- and outlet of the PHeX.



*Figure 5.13 Salome meshing of a typical segment of the PHeX tube.
Top: Outside of tube,
Bottom: Inside of tube.*

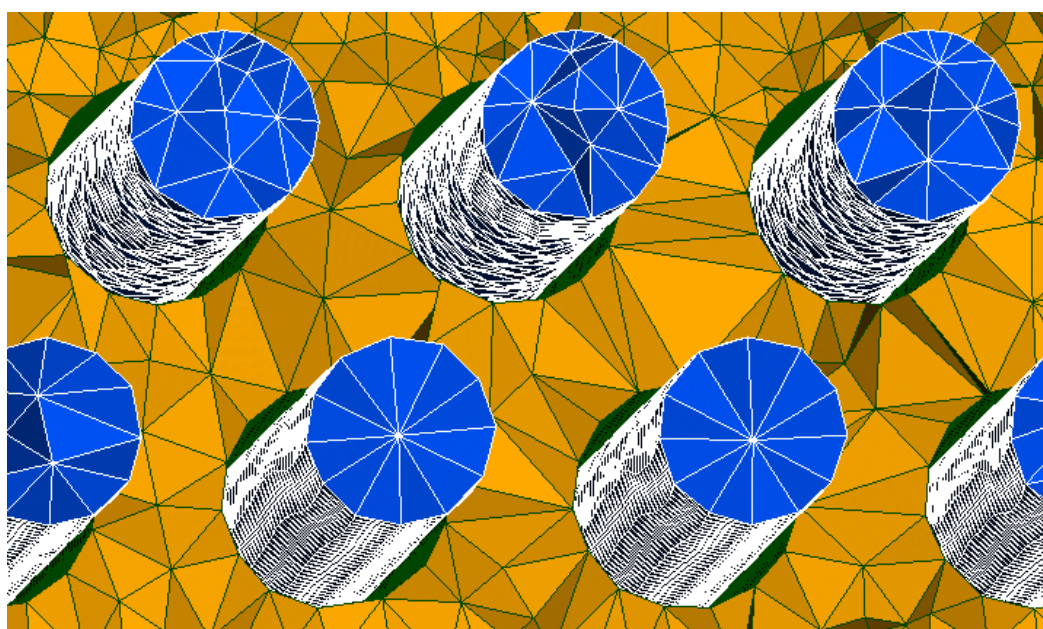


Figure 5.14 Salome meshing, section view of a typical meshing in-between tubes.

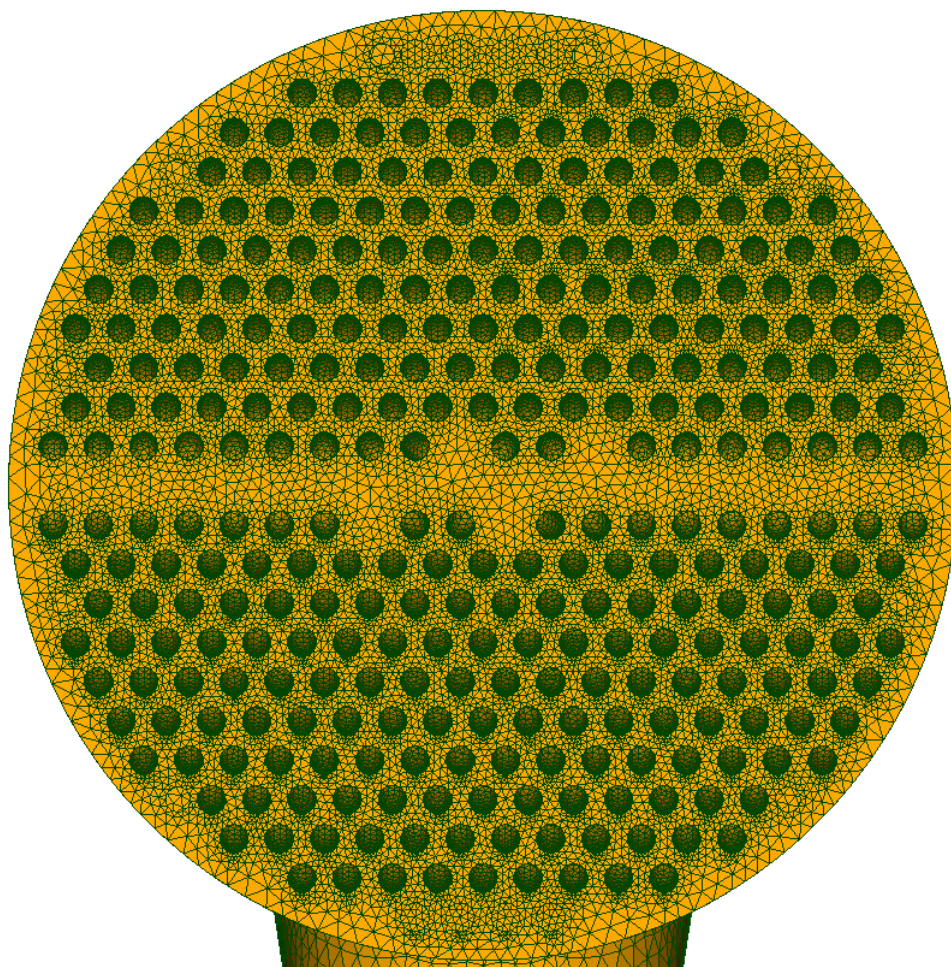


Figure 5.15 Salome meshing of the tube sheet, where all the tubes are attached in the PHeX.

5.2.2 Salome mesh results: Radiator

Table 5.4 Quality of Salome radiator mesh.

Quality indicator	Max	Average
Non-orthogonality	—	—
Skewness	66.9	8.1
Aspect ratio	3.2	1.07
Total number of cells	Number of boundary layers included	Overall quality
128,634,421	0	—

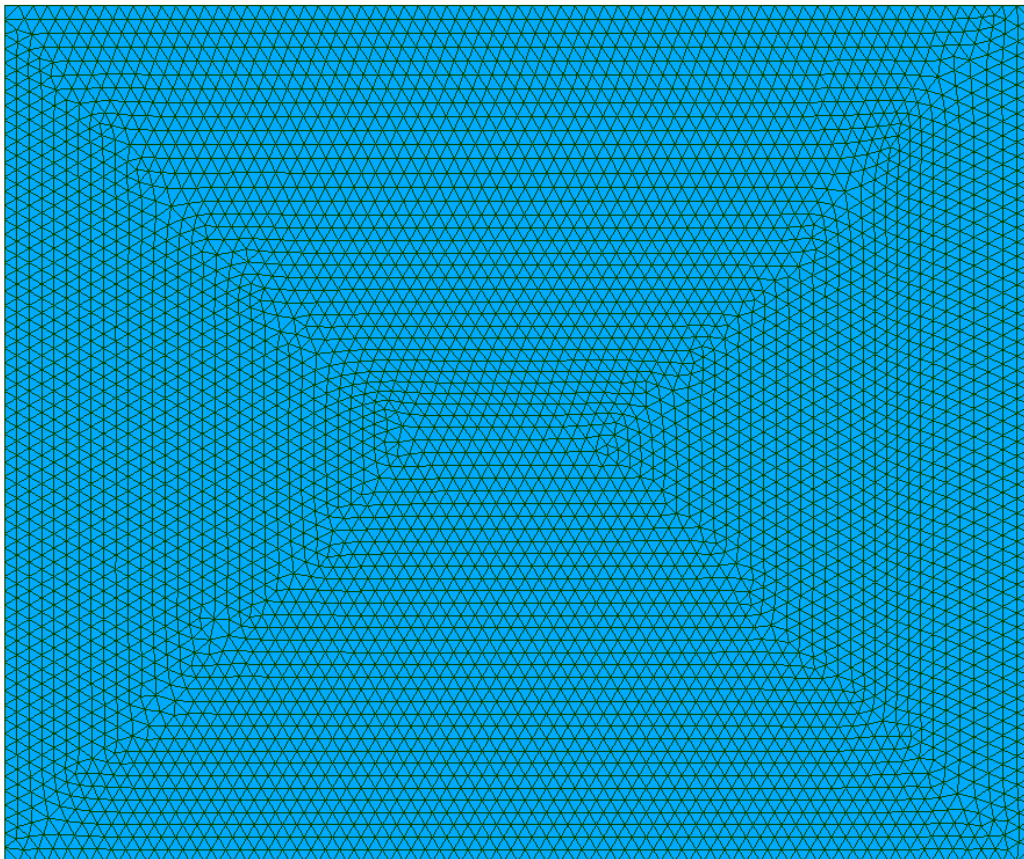


Figure 5.16 Salome mesh of radiator air inlet.

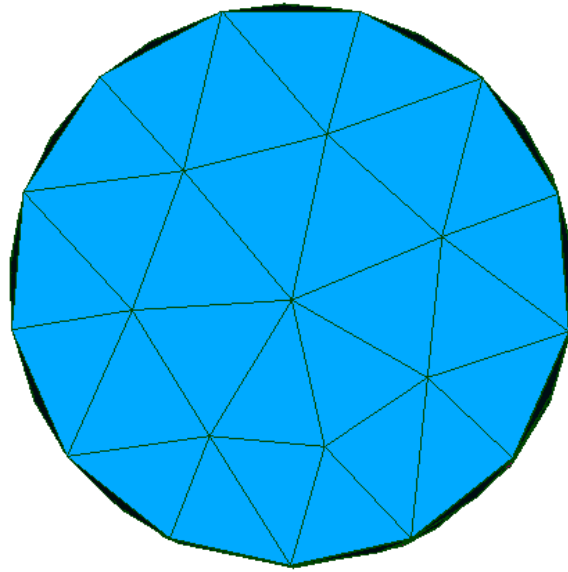


Figure 5.17 Salome mesh of radiator salt inlet.

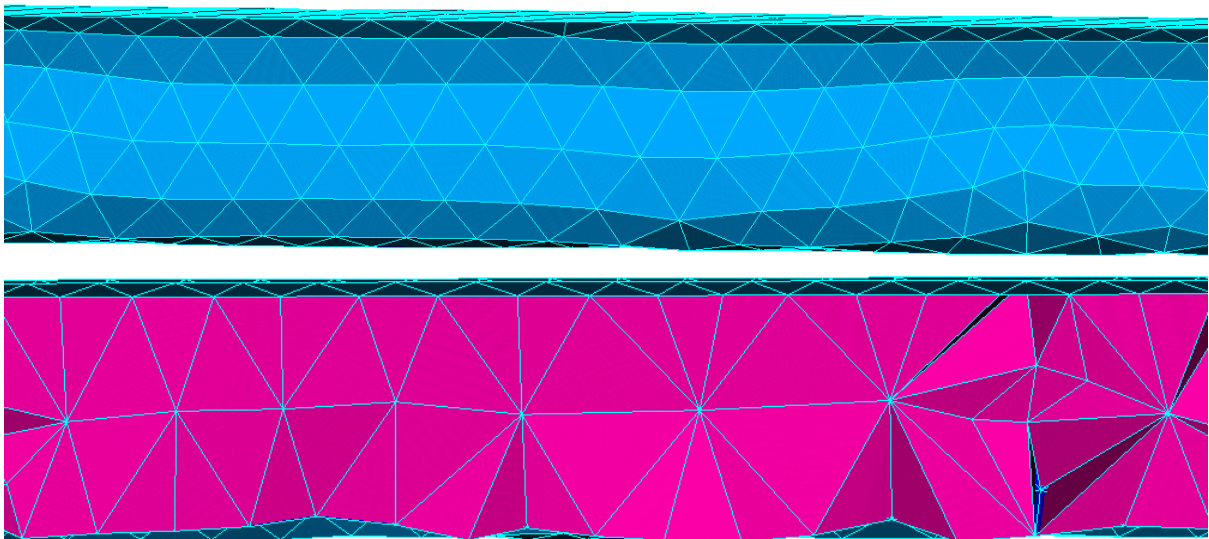


Figure 5.18 Salome mesh of radiator tubes.

Top: Outside of tubes.

Bottom: Inside of tubes.

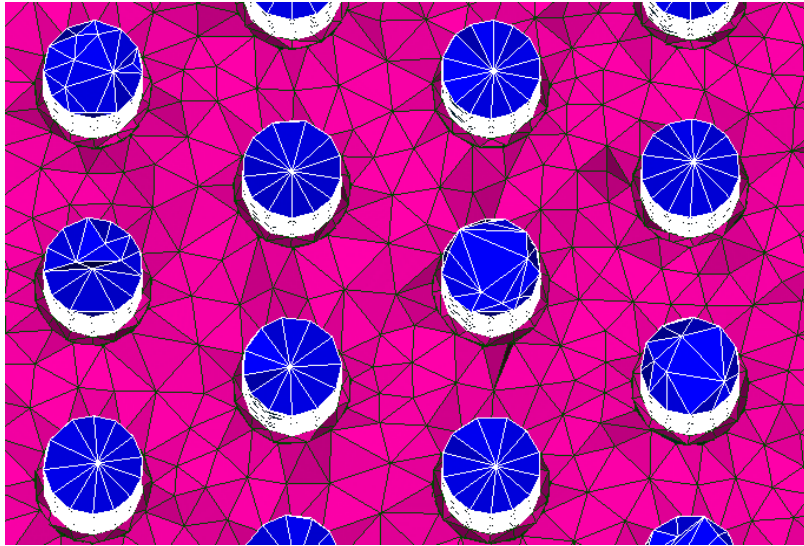


Figure 5.19 Section view of Salome mesh of air region in between tubes.

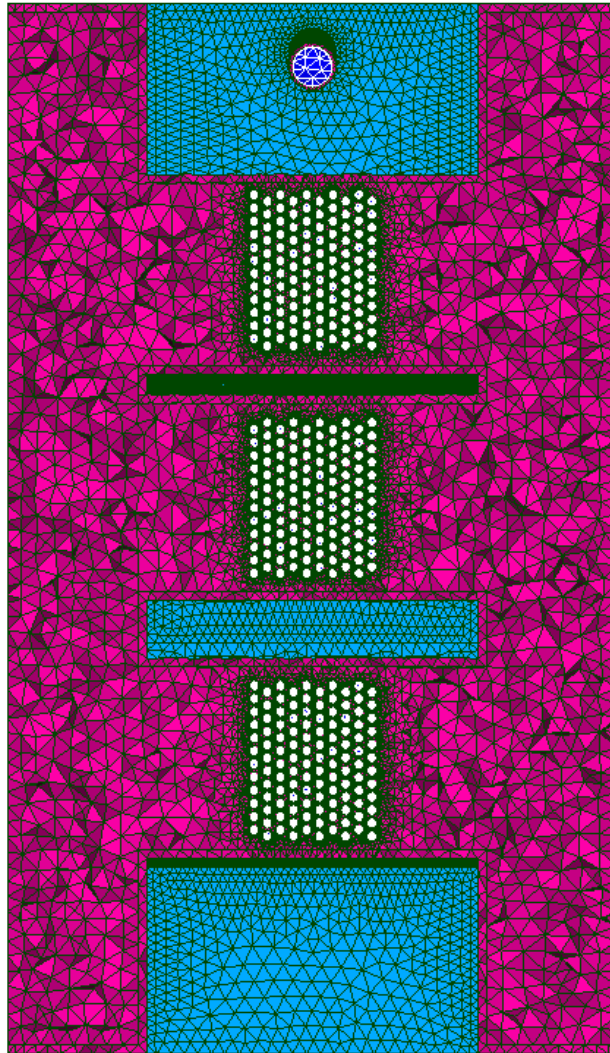


Figure 5.20 Section view of Salome mesh showing the entire radiator.

5.2.3 Salome mesh results: Heat exchanger test model

Table 5.5 Quality of Salome heat exchanger test model mesh.

Quality indicator		Max	Average
Non-orthogonality		—	—
Skewness		2.8	1.1
Aspect ratio		18.8	1.03
Total number of cells	Number of boundary layers included		Overall quality
631,161	3		—

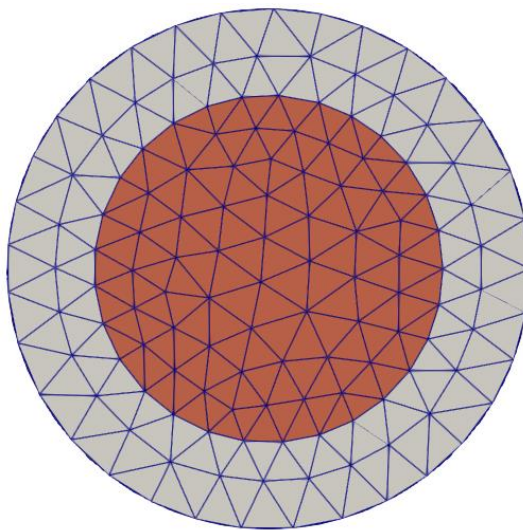


Figure 5.21 Salome meshing, showing typical inlet and outlet for the test model. Gray is the solid material.

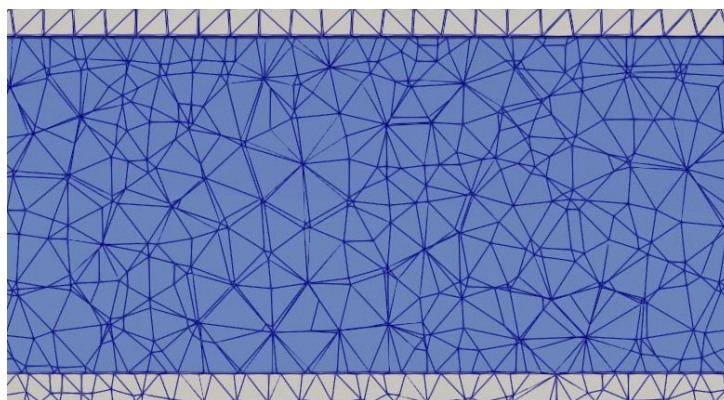


Figure 5.22 Salome meshing of typical tube section, showing inside of tube in test model. Gray is the solid material.

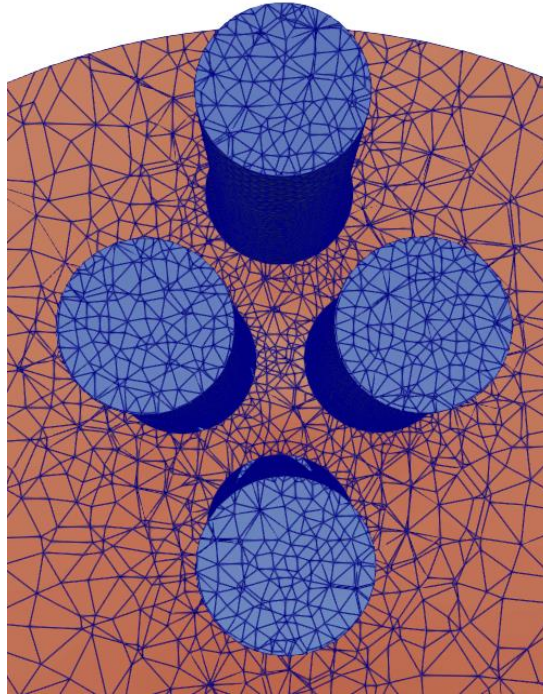


Figure 5.23 Salome meshing of typical section of meshed tube and surrounding shell of test model.

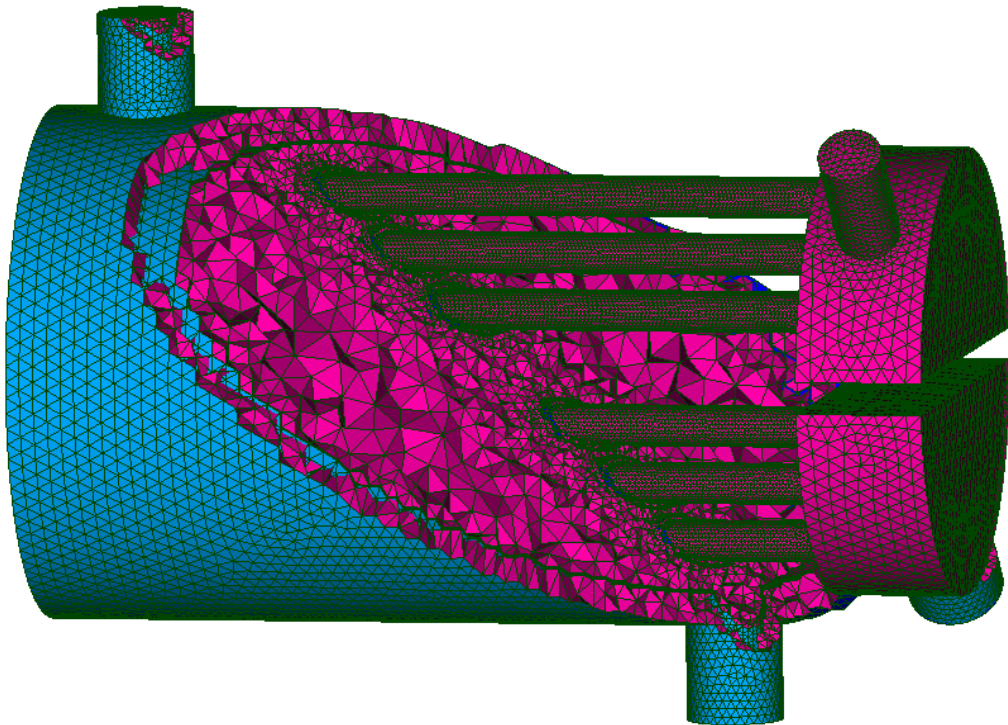


Figure 5.24 Salome meshing of heat exchanger test model, showing section view of shell-side with protruding tubes.

5.3 ideasUnvToFoam program

Figure 5.25 shows how overall cell count in the mesh corresponds to execution time of the program “ideasUnvToFoam”, which is a program that converts meshes from format .unv to .foam, hence its name.

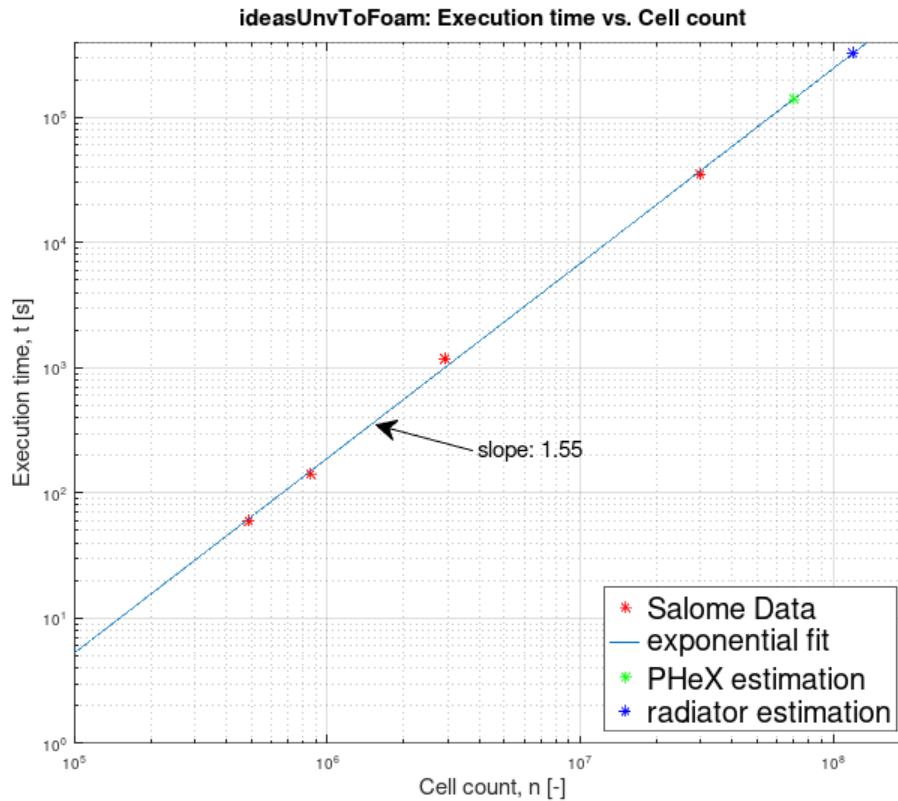


Figure 5.25 Log-log data fit for execution time of ideasUnvToFoam of meshes of different cell counts. Data fit onto equation of form: $t = An^b$, with an estimation of $b = 1.55$, and $A = e^{-16.25}$.

The data from Salome (red in Figure 5.25) comes from four different meshes of the ‘Heat exchanger test model’, meshed with $\sim 5e5$, $\sim 9e5$, $\sim 3e6$, $\sim 3e7$ cells, respectively. They were exported as .unv formats and then ran through the ideasUnvToFoam program successfully. Converting the axes to log-log, the slope of the line, i.e., the exponential fitting coefficient b , can be obtained and turned out to be $b = 1.55$.

These values are only applicable to models that have similar setup, i.e., groups defined on all the surfaces in a similar manner. The heat exchanger test model has 12 such groups defined on the mesh, and the same setup is present in the PHeX as well as in the radiator, since they are very similar multiregion cases. The mesh groups involve the three volume regions, inlets and outlets for

each fluid region, and interfaces between each region. Specific Salome case set up can be found in Appendix III.

By extending the data fit of the known mesh counts of the test model, with corresponding execution time, estimates for the time it would take for the bigger meshes of the PHeX ($\sim 7.5e7$ cells) and the radiator ($\sim 1.3e8$ cells) to run through ideasUnvToFoam can be obtained. These execution times are quite excessive according to the data fit and should be ~ 1.6 days for the PHeX and ~ 3.8 days for the radiator. However, when ideasUnvToFoam has been executed with these bigger meshes it has never finished, even when running continuously for > 6 days. This suggests that something is wrong in either the CAD-model, the mesh, the program itself, or the RAM-requirements when meshes of this size are used with this program.

Since Simscale has been able to run successful simulations of the same CAD-models, the problem most probably lies within the mesh or ideasUnvToFoam. What to do about this issue will be discussed under Future implications in Chapter 8.

5.4 snappyHexMesh

OpenFOAM’s inbuilt meshing tool “snappyHexMesh” has been suggested by many people as a solution to the meshing and conversion issue, but this has turned out to be difficult and computationally excessive. The computer used for this project was very powerful, with massive RAM capabilities (252 GB DDR6 RAM) and 56 cores, but this proved to not be enough when running snappyHexMesh for the full model, for many different settings and refinement levels. Figure 5.26 shows a screenshot just before the computer crashed, from the system-monitoring program “htop” (available on Linux) when the full model was run using snappyHexMesh. As seen in Figure 5.26, all cores were used, all RAM was used and all Swap memory was used, but this was still not sufficient, and the computer subsequently halted the program every time this was attempted. It might be possible to run with even more RAM available, but that defeats the purpose of having the findings and methods in this project being reproducible by others. Expecting users to have access to terabytes of RAM is completely unfeasible with current computer technology, and thus other solutions had to be found. Moore’s law will eventually solve issues like this.

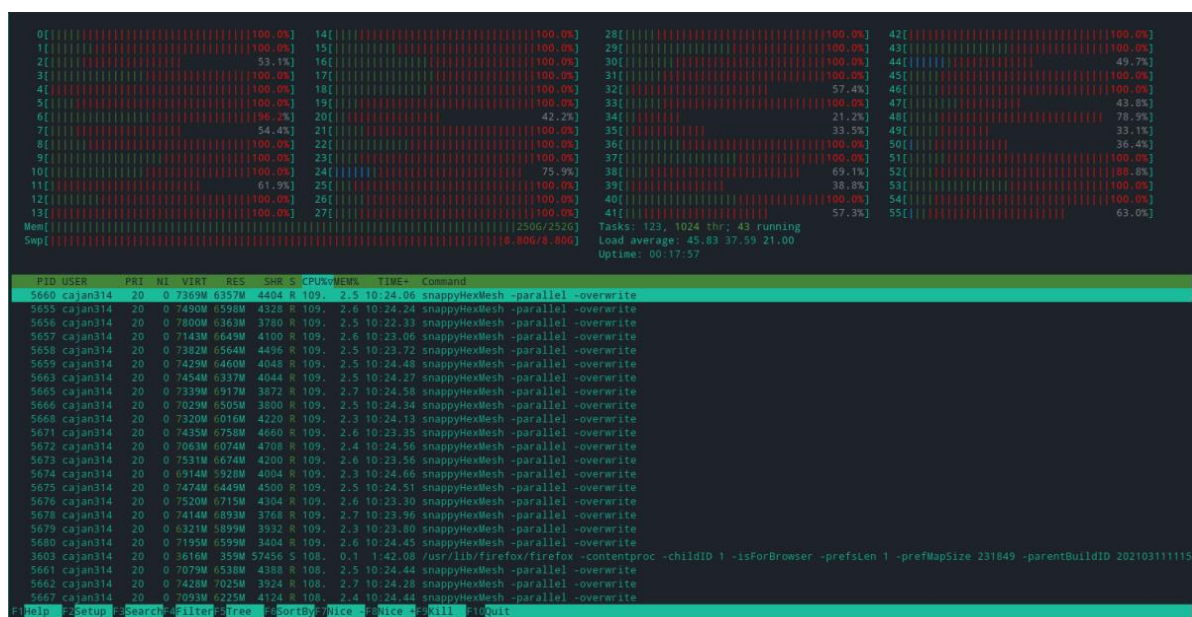


Figure 5.26 htop monitoring software showing system usage when running snappyHexMesh on the full PHeX model.

6 Simulation results and MSRE data

This chapter shows the results, both from the data gathered from the MSRE as well as the simulations conducted in this thesis. The MSRE results will be shown first since those data will be used for validation in the simulations. Tables of pressure drop, and temperature differences are provided, and some flow visualizations of the simulations will be shown for sanity checks, ensuring that the results are physically sound. The comparison between the MSRE data and the simulation data, as well as the accuracy of the data, will be discussed in Chapter 7.

6.1 Data from the MSRE

Since the MSRE was conducted in the U.S.A., all the measurements in all the reports are invariably imperial units. The Wolfram Alpha webpage has been used for all unit conversions to the SI system (Wolfram|Alpha).

Some of the data from the MSRE show up in various ORNL-reports as conflicting values. An effort has been made to provide the reader with the most accurate data, but this is not always possible since the documents often do not specify where the data has been gathered from, and instead simply states them in tables and figures. Measurements, estimations and calculations are mixed in the ORNL-documents available and references to the tests are still classified by the U.S. government. Table 6.1 contains all the operational data gathered from the reports at ORNL for the PHeX.

6.1.1 PHeX operational data

In Table 6.1, data from the operations of the MSRE PHeX is presented. Where conflicting values for certain parameters have been found, both are shown, and an indication of whether the data presented is known to be calculated or measured is shown when known.

Table 6.1 Results and salt parameters from the PHeX, installed and operated at ORNL in the MSRE.

Quantity	Unit	Shell-side		Tube-side		Source
		Inlet	Outlet	Inlet	Outlet	
Temperature	[C]	662.8 ⁽²⁾	635 ⁽²⁾	551.7 ⁽²⁾	593.3 ⁽²⁾	(ORNL-TM-2098, 1968)
Temperature difference	[C]	27.8		41.6		(ORNL-TM-2098, 1968)
Flow rate	[m ³ /s]	7.57e – 2 ⁽¹⁾		5.36e – 2 ⁽¹⁾		(ORNL-TM-2098, 1968)
Pressure drop	[kPa]	165.5		199.9		(ORNL-TM-2098, 1968)
		193.1 ⁽¹⁾		186.2 ⁽¹⁾		(ORNL-TM-0732, 1964)
Design pressure	[kPa difference to atm]	379.2 ⁽¹⁾		620.5 ⁽¹⁾		(ORNL-TM-2098, 1968)
Allowable working pressure	[kPa difference to atm]	517 ⁽¹⁾		861.8 ⁽¹⁾		(ORNL-TM-2098, 1968)
Overall heat transfer coefficient	[W/(m ² * K)]			3725 ⁽²⁾		(ORNL-TM-3039, 1973)
Effective heat transfer area	[m ²]			25.9 ⁽²⁾		(ORNL-TM-3002, 1970)

⁽¹⁾ Known to be calculated.

⁽²⁾ Known to be measured.

6.1.1.1 Water tests

In Figure 6.1, the relationship between flow rate and pressure loss for the PHeX is shown from a series of tests with water with varying flow rate, conducted at ORNL.

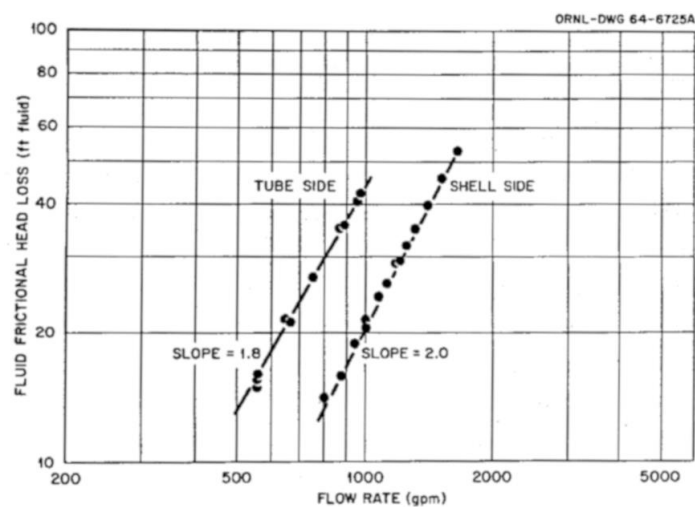


Figure 6.1 Relationship between flow rate and pressure drop for the PHeX. This test was conducted at ORNL with water (ORNL-TM-2098, 1968).

6.1.2 Radiator operational data

In Table 6.2, data from the MSRE radiator is shown. Conflicting values found in the documents are shown, and where known, an indication of whether the data is known to be calculated or measured is indicated.

Table 6.2 Results and parameters for the radiator, installed and operated at ORNL in the MSRE.

Quantity	Unit	Air-side		Salt-side		Source
		Inlet	Outlet	Inlet	Outlet	
Temperature	[C]	37.8 ⁽²⁾	148.9 ⁽²⁾	593.3 ⁽²⁾	551.7 ⁽²⁾	(ORNL-TM-0732, 1964)
Temperature difference	[C]	111.1		41.6		(ORNL-TM-0732, 1964)
Flow rate	[m ³ /s]	77.4 ⁽¹⁾		5.36e – 2 ⁽¹⁾		(ORNL-TM-0732, 1964)
		94.4 ⁽¹⁾		5.24e – 2 ⁽¹⁾		(ORNL-3708, 1964)
Pressure drop	[kPa]	2.9 ⁽¹⁾		44.8 ⁽¹⁾		(ORNL-TM-0732, 1964)
		2.5 ⁽¹⁾		136.5 ⁽¹⁾		(ORNL-3708, 1964)
Design pressure	[kPa difference to atm]	517.1 ⁽¹⁾				(ORNL-TM-2098, 1968)
Overall heat transfer coefficient	[W/(m ² * K)]	300.9 ⁽¹⁾				(ORNL-TM-0732, 1964)
		242.5 ⁽²⁾				(ORNL-TM-3002, 1970)
Effective heat transfer area	[m ²]	63.6 ⁽¹⁾				(ORNL-TM-0732, 1964)
		65.6 ⁽²⁾				(ORNL-3708, 1964)

⁽¹⁾ Known to be calculated.

⁽²⁾ Known to be measured

6.2 Results from simulations

6.2.1 Reynolds number (Re) analysis

For this study, the turbulence model $k - \omega SST$ was chosen. Heat exchangers in general are turbulent components, and so far in this report it has simply been asserted that a turbulence model is needed, with no further motivation. To motivate the choice of using a turbulence model (instead of a laminar model), a quick analysis of the size of the Reynolds number (Re) must be made. Recall the equation for calculating Re , namely:

$Re = \frac{UL}{\nu}$, where $\frac{1}{\nu} \approx 3e5$ for the salts in question, see Table 2.6. To justify the choice of a turbulence model, the Re should be larger than $4e3$ (Engineering Toolbox, 2004).

Thus, the only parameters that can change to minimize the Re are U and L . The smallest length scale in the models can be found within the diameters of the tubes (for the tube-side), or between the tubes (for the shell-side) where $L \approx 1e - 2\text{ m}$. With these parameters set, an estimate of U can be made for which the corresponding Re would be at least $4e3$.

$$4e3 > Re = \frac{UL}{\nu} = U * 3e3 \quad \text{Eq. 46}$$

Solving for U yields:

$$U < \frac{4}{3} \text{ m/s} \quad \text{Eq. 47}$$

This means that for the flow to have a substantially smaller Re than $4e3$, the velocity must be lower than $\frac{4}{3} \text{ m/s}$ in the smallest sections of these models.

Analysis in Paraview for completed runs shows velocities significantly larger than $\frac{4}{3} \text{ m/s}$ in the tube-side and velocities in the shell-side close to or above $\frac{4}{3} \text{ m/s}$ in most places, as shown in Figure 6.2.

The velocities and length scales are of similar magnitude in the radiator. This justifies the initial assertion of using a turbulence model.

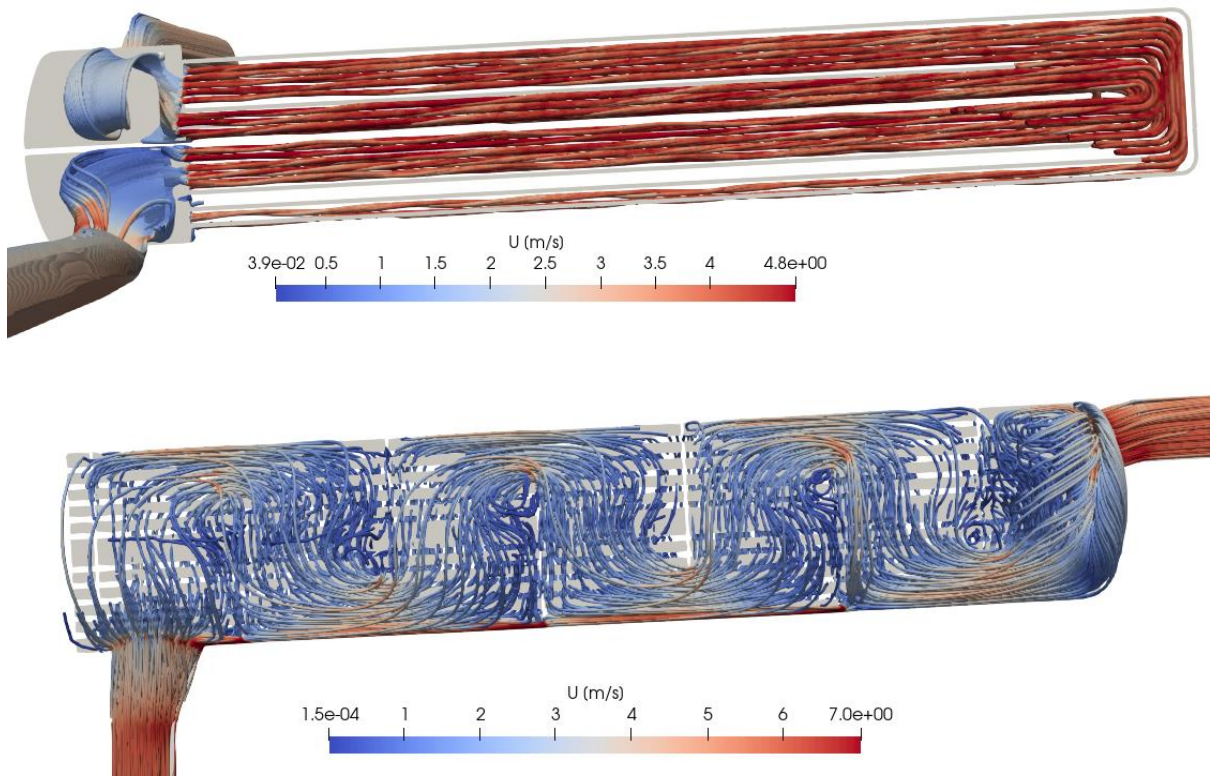


Figure 6.2 Velocity plot in a typical run of the PHeX, showing flow paths coloured as velocity as a Re number indicator.
Top: Tubes,
Bottom: Shell.

6.2.2 Simscale

In this section the simulation results from Simscale will be shown for both the PHeX and the radiator.

6.2.2.1 Simscale simulation results: PHeX

First the simulations for the PHeX are shown. Two types of simulations were conducted, water and salt. The water tests were initiated with standard water properties to validate against the water tests shown in Figure 6.1.

6.2.2.1.1 Water simulation

No exact flow rate- or pressure sensors can be present in the PHeX when it is operating with salt since the temperature, radiation and corrosion environment will destroy the sensors. Tests to correlate flow rate with pressure loss must therefore be done with water and be used as a rough estimate to the same correlation with molten salt. Figure 6.3 is to be compared with Figure 6.1. The meaningful data to extract are the slopes for how flow rate relates to pressure loss. From most of

the Simscale simulations, the pressure drop was consistently overpredicted by about a factor of 2 compared to the ORNL measurements in Figure 6.1.

The water simulations were run as $k - \omega$ SST turbulence models and were reproduced three times with different initial conditions for the flow rates; 800, 1000 and 1650 *gpm*, respectively (0.05, 0.063 and 0.1 m^3/s , respectively). Figure 6.1 was difficult to reproduce adequately, so the decision was made to keep this graph in imperial units to ease the comparison.

The initial conditions that Simscale uses to initiate the turbulent parameters in this simulation are:

$$k = 3.75e - 3 \text{ m}^2/\text{s}^2 \quad \text{Eq. 48}$$

$$\omega = 3.375 \text{ 1/s} \quad \text{Eq. 49}$$

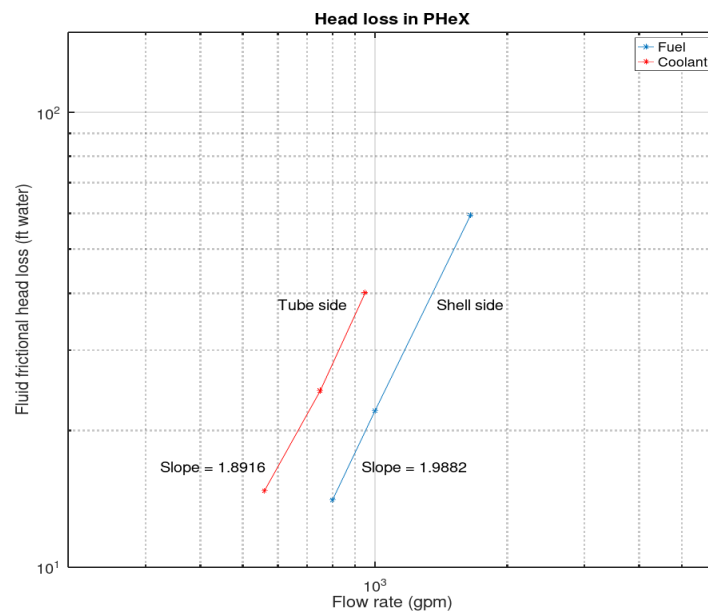


Figure 6.3 Simscale results with water parameters for pressure drop versus different flow rates. Data manipulated to fit MSRE data; all shell-side data points (blue curve) have been divided by 2 (see discussion in Chapter 7),
gpm: Gallon per minute,
ft water: Feet of water column.

6.2.2.1.2 Salt simulation

Many simulations were run from Simscale for the PHeX, with different turbulence models and runtimes. The major results are summarized in Table 6.3, from two runs of a $k - \varepsilon$ model with different run-times, and one run of a $k - \omega SST$ model.

Table 6.3 Temperature and pressure data for the PHeX, Simscale simulations.

Model & Runtime: [s]	Temperature [C]				Pressure [kPa]			
	Shell-side		Tube-side		Shell-side		Tube-side	
	Inlet	Outlet	Inlet	Outlet	Inlet	Outlet	Inlet	Outlet
$k - \varepsilon$, Runtime: 1e4	663	635	552	594	533	118	595	106
	Difference: 28		Difference: 42		Difference: 415		Difference: 489	
$k - \varepsilon$, Runtime: 1e5	663	635	552	592	549	105	572	105
	Difference: 28		Difference: 40		Difference: 444		Difference: 467	
$k - \omega SST$ Runtime: 8e4	663	635	552	590	550	105	572	105
	Difference: 28		Difference: 38		Difference: 445		Difference: 467	

Figure 6.4 shows the flow paths, coloured as temperature drop across the shell-side of the PHeX. This is primarily shown as a sanity check to make sure that simulation is working, and also as a reminder of how very complex the flow patterns are within this geometry. All these flow lines manoeuvre around 159 bent tubes as they criss-cross over and under the baffle-plates.

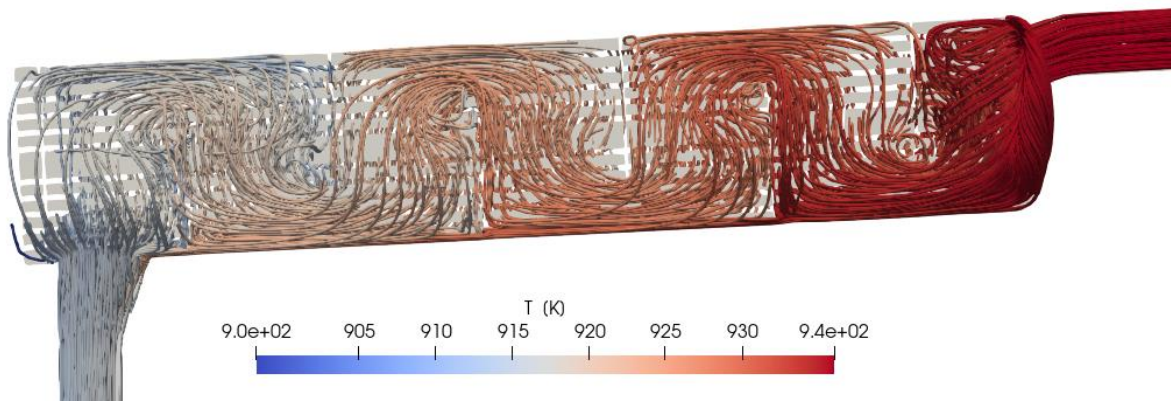


Figure 6.4 Flow paths of the salt in the shell-side, coloured with temperature.

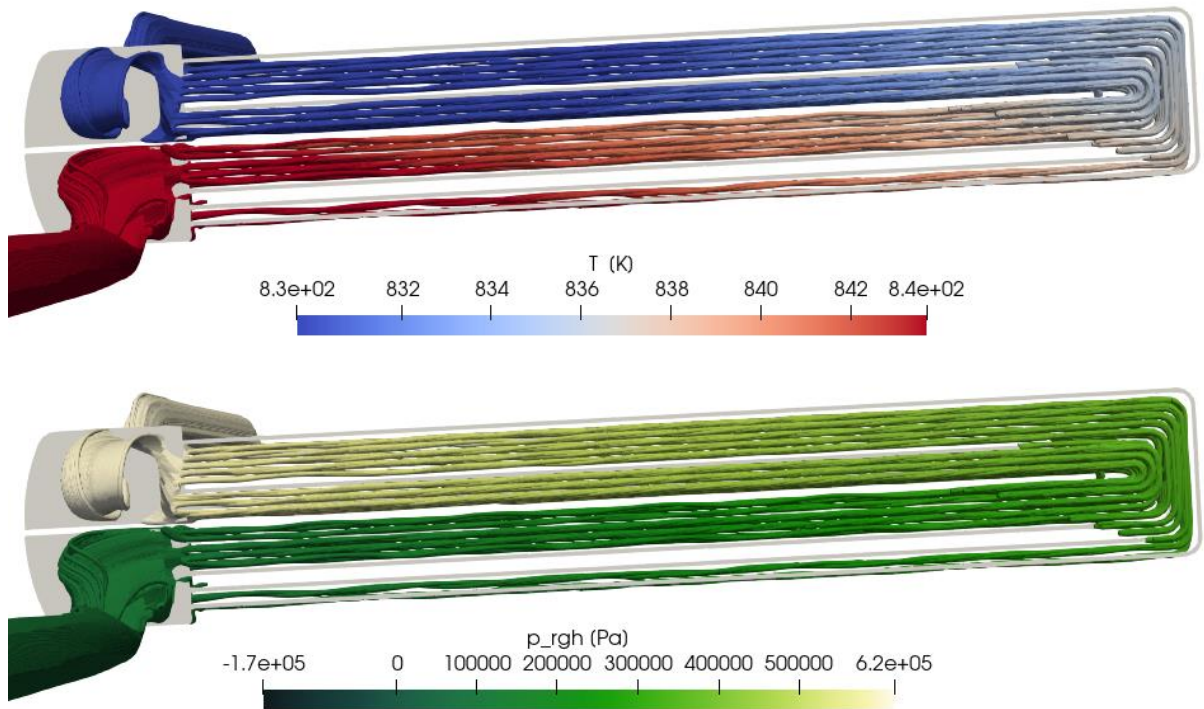


Figure 6.5 Flow paths of the salt in the tube-side, Top: Coloured as temperature, Bottom: Coloured as pressure.

Figure 6.5 shows the flow paths for the salt, coloured as temperature and pressure in the tube-side of the PHeX. A smooth gradient of each parameter is obtained over the entire region, showing the soundness of the physics involved. This also serves as a sanity check that the heat exchanger is performing as it should, i.e., cold salt entering and gradually being heated up until it exits, and pressure building up along the flow paths. Figure 6.5 also shows the very complex flow patterns that arise in the collecting volumes of the tube side channels. The high flow rate enters the channel and is then being pushed through all the tubes. This introduces a lot of turbulence as well as an excessive vorticity generation when going from a large volume to several small volumes with no gradient of flow in between.

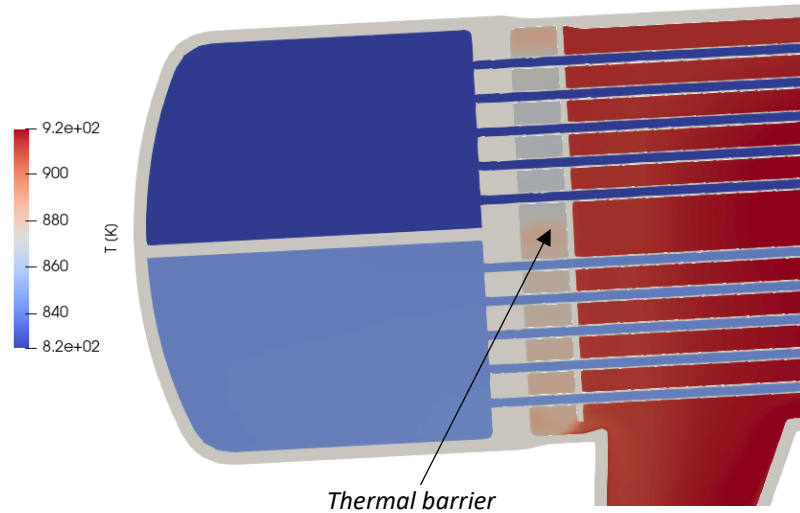


Figure 6.6 Thermal barrier in the shell-side, protecting the tube sheet from excessive thermal cycling.

In all the simulations for the PHeX, the temperature across the thermal barrier has looked very similar. In the colder region, the temperature lies in the range of 595 – 610 C, and in the warmer region just outside the thermal baffle plate the temperature lies in the range of 635 – 645 C. This temperature gradient is the intended purpose of the thermal barrier, trapping a stagnant salt flow which will be colder since it is in contact with the tube sheet which in turn is in contact with the coolant salt. In this way, excessive thermal cycling over the baffle plate can be reduced.

6.2.2.2 Simscale simulation results: Radiator

The radiator simulations never converged to a satisfying answer. Simulations always crashed or produced completely unphysical results, like the ones shown in Table 6.4. As can be seen in the temperature readings, both the air and the salt drop in temperature, which cannot happen. In the MSRE results, the air-side temperature increased by ~ 70 C.

Table 6.4 Temperature and pressure data for the radiator, Simscale simulations.

Model & Runtime: [s]	Temperature [C]				Pressure [kPa]			
	Air-side		Tube-side		Air-side		Tube-side	
	Inlet	Outlet	Inlet	Outlet	Inlet	Outlet	Inlet	Outlet
$k - \omega$ SST,	311	306	867	293	104	101	196	107
Runtime: 2.5e4	Difference: 5		Difference: 574		Difference: 3		Difference: 89	

Figure 6.7 and Figure 6.8 indicate that flow and streamlines are behaving somewhat accurately, but the data being computed is unusable and no further analysis on the data collected is deemed worthwhile.

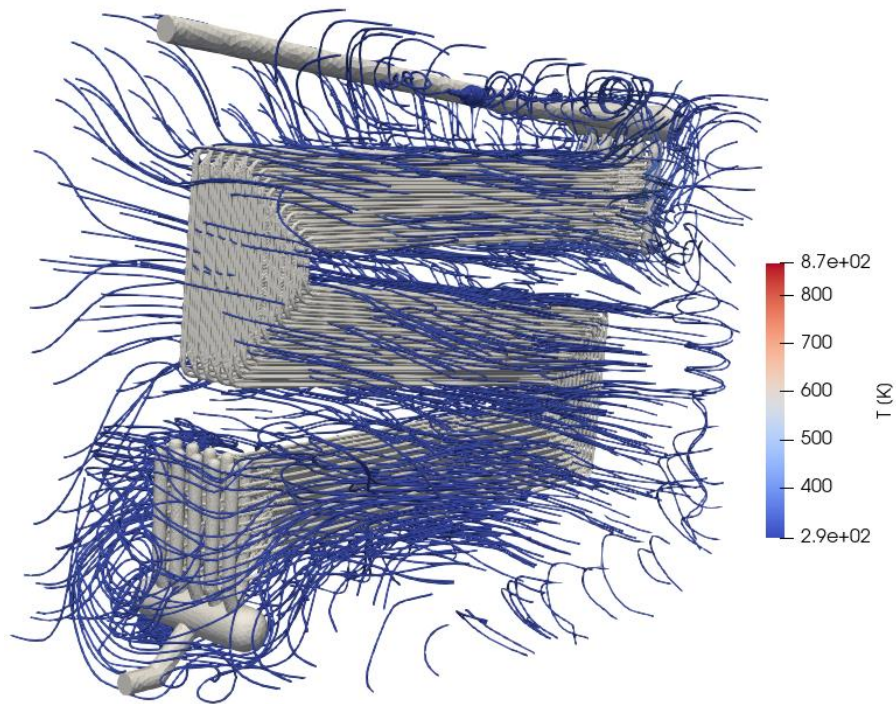


Figure 6.7 Flow paths of air across the radiator air-side, from left to right, coloured by temperature.

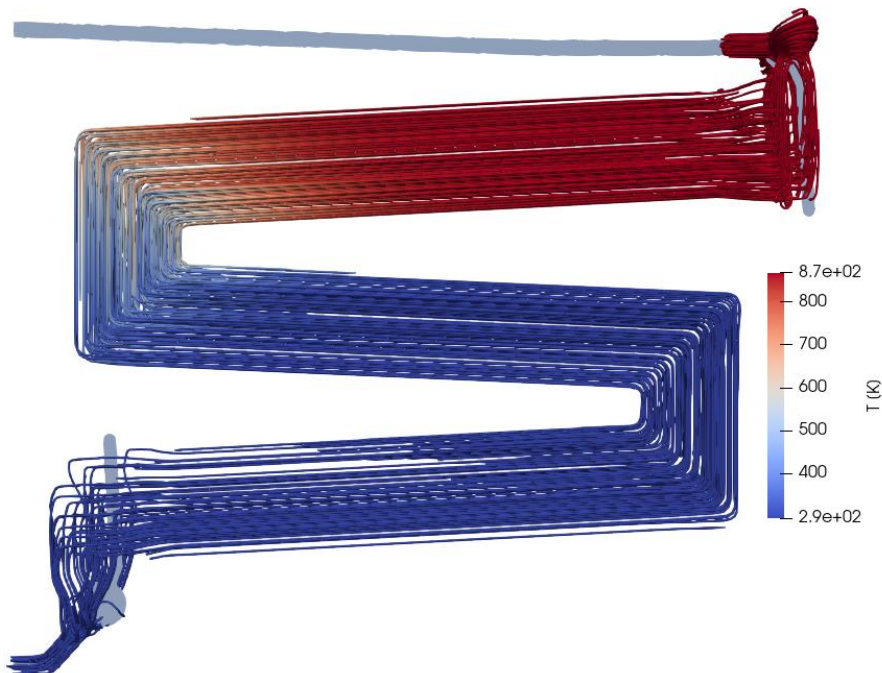


Figure 6.8 Flow paths of salt through tubes from top to bottom in the radiator, coloured by temperature.

6.2.3 OpenFOAM

6.2.3.1 Initial conditions for turbulence properties

Based on the data from the MSRE, estimates for the turbulent initial conditions for the salts can be made. These are used to start the simulations and will later converge to their true value. The speed and accuracy of this convergence is related to the magnitude of each initial condition.

The solver used in OpenFOAM is called ‘chtMultiRegionFoam’ and its turbulence parameters and estimation are shown in Table 6.5. The equations for the estimations can all be found in this reference (CFD-online, 2014). These estimations cannot be fully accurate from the start since they assume that the flow velocities and turbulent intensities are known, but all that is needed is a ballpark estimation to initiate the simulations.

Table 6.5 Estimates for initial values of turbulence coefficients for the OpenFOAM solver ‘chtMultiRegionFoam’

Parameter	Equation	Initial estimation
α_t	k_{th}/c_p	$7e - 4$
ε	$\frac{(3/2)^{3/2}}{L} [C_\mu^{1/4} I U_{ref}]^3$	$2.4e - 2$
k	$3/2 (I U_{ref})^2$	$6e - 2$
ν_t	Based on y^+	0.1
ω	$\sqrt{\frac{3}{2}} \frac{I U_{ref} }{C_\mu L}$	27

Rough estimations of reference velocity and length-scale.

$$|U_{ref}| = 1 \text{ m/s},$$

$$L = 0.1 \text{ m}.$$

6.2.3.2 OpenFOAM simulation results: PHeX

In Table 6.6, results from the OpenFOAM simulation can be found. Only one $k - \omega SST$ simulation could be run to completion. The simulation behaved physically sound and produced usable data.

Table 6.6 Temperature and pressure data for the PHeX, OpenFOAM simulation.

Model & Runtime: [s]	Temperature [C]				Pressure [kPa]			
	Shell-side		Tube-side		Shell-side		Tube-side	
	Inlet	Outlet	Inlet	Outlet	Inlet	Outlet	Inlet	Outlet
$k - \omega SST$ Runtime: 3.8e5	663	642	552	572	517	122	608	107
	Difference: 21		Difference: 20		Difference: 395		Difference: 501	

6.2.3.3 OpenFOAM simulation results: Radiator

No OpenFOAM simulation of the radiator was produced. See Chapter 7 for discussion.

7 Discussion

7.1 Comparison between simulations and MSRE data

The two important results to compare for this validation, for both the PHeX and the radiator, are the:

- Temperature difference for each inlet and outlet, respectively
- Pressure drops across each region

These results are presented as tables in each of the following sections.

7.1.1 PHeX data comparison

7.1.1.1 Water simulation comparison to MSRE data

From Figure 6.3 and Figure 6.1 the slopes of how flow rate and pressure drop relate in the PHeX are shown and compared in Table 7.1.

Table 7.1 Comparison of slopes of graphs in water simulation test vs. MSRE water test.

	MSRE water test		Simulation water test	
	Shell-side	Shell-side	Shell-side	Tube-side
Slope	2	1.8	1.99	1.89

The values from the MSRE show a near perfect match to the water simulations, which indicates that the physics is behaving realistically to changes in the model, even though the absolute pressure is overestimated in each simulation, which will be discussed in this chapter. This implies that the setup for these simulations can be used in future MSR technology development.

7.1.1.2 Salt simulation comparison to MSRE data

The data according to those found in the MSRE reports, mentioned in this chapter, for the PHeX are condensed in Table 7.2. The table shows the temperature differences and pressure drop between inlet and outlet for each region. Temperature differences are shown in absolute values.

Table 7.2 difference for temperature and pressure across the PHeX, MSRE results.

	Temperature [C]		Pressure drop [kPa]	
	Shell-side	Tube-side	Shell-side	Tube-side
MSRE difference	28 ⁽²⁾	41 ⁽²⁾	166 ⁽¹⁾	200 ⁽¹⁾

⁽¹⁾ Known to be calculated.

⁽²⁾ Known to be measured.

Table 7.3 Temperature and pressure comparison between simulations and MSRE data.

Platform	Model & Runtime: [s]	Indicators	Temperature [C]		Pressure [kPa]	
			Shell-side	Tube-side	Shell-side	Tube-side
Simscale	$k - \varepsilon$, Runtime: 1e4	Simulated difference	28	42	415	489
		Accuracy ratio (%)	100%	102.4%	250%	244.5%
	$k - \varepsilon$, Runtime: 1e5	Simulated difference	28	40	444	467
		Accuracy ratio (%)	100%	97.5%	267.4%	233.5%
	$k - \omega$ SST Runtime: 8e4	Simulated difference	28	38	445	467
		Accuracy ratio (%)	100%	92.7%	268%	233.5%
OpenFOAM	$k - \omega$ SST Runtime: 3.8e5	Simulated difference	21	20	395	501
		Accuracy ratio (%)	75%	48.8%	238%	250.5%

Difference (absolute value) is calculated as: $Inlet - Outlet$

Accuracy ratio (%) is calculated as: $Simulated\ difference / measured\ difference * 100\%$

100% indicate perfect match between expected value and simulation

7.1.1.3 Heat transfer coefficient

As a final comparison between the PHeX simulations and the MSRE data, the overall heat transfer coefficient is shown for the Simscale simulation using the $k - \omega$ SST model.

Table 7.4 Inlet- and outlet temperature definition for LMTD calculation.

		MSRE	Simscale simulation ($k - \omega$ SST)
$T1$	Inlet temperature, shell-side	663	663
$T2$	Outlet temperature, shell-side	635	635
$T3$	Inlet temperature, tube-side	552	552
$T4$	Outlet temperature, tube side	593	590

The $LMTD$ value is thus:

$$LMTD = \frac{\Delta T_1 - \Delta T_2}{\ln \frac{\Delta T_1}{\Delta T_2}} = \frac{(T1 - T4) - (T2 - T3)}{\ln \frac{T1 - T4}{T2 - T3}} \quad Eq. 50$$

$$LMTD_{MSRE} = 76.3$$

$$LMTD_{k-\omega SST} = 77.9$$

With the $LMTD$ defined, the overall heat transfer coefficient can be shown as:

$$k = \frac{\delta t \, m \, c_p}{LMTD \, A} \quad Eq. 51$$

with definitions according to those presented in Chapter 2. Making the analysis on the shell-side the following values are used for MSRE data and the Simscale $k - \omega$ SST simulation.

Table 7.5 Overall heat transfer coefficient parameters for the PHeX.

Quantity	MSRE	Simscale $k - \omega$ SST
δt	28	28
m	171.2	171.2
c_p	1982.4	1982.4
A	25.9	24.5
$LMTD$	76.3	77.9

Where m is the flow-rate in the shell-side multiplied by the density of the fuel salt.

Thus, the overall heat transfer coefficient can be shown for the Alfa Laval method of calculating introduced in Chapter 2, for the MSRE data compared to the simulated values, as well with ORNL's own reported heat transfer coefficient, shown in Chapter 6.

$$k_{MSRE} = 4808$$

$$k_{k-\omega SST} = 4979$$

$$k_{ORNL\ presented\ value} = 3725$$

The method ORNL used for calculating the overall heat transfer coefficient is shown in detail in (ORNL-TM-3002, 1970). The methods differ quite substantially and there is no clear comparison that can be made between them. A similar approach used at ORNL to calculate overall heat transfer coefficient for the simulations is possible but was not attempted here. For the Alfa Laval approach k_{MSRE} and $k_{k-\omega SST}$ differs by only 3.5%.

7.1.2 Radiator data comparison

The data according to those found in the MSRE reports (Table 6.2 in Chapter 6) for the radiator are condensed in Table 7.6. These are the temperature differences between inlet and outlet for each region and the pressure drop for each region for the radiator built and operated in the MSRE, and these values are to be compared with those from simulation.

Table 7.6 Expected difference for temperature and pressure across the radiator, MSRE results.

	Temperature [C]		Pressure drop [kPa]	
	Air-side	Salt-side	Air-side	Salt-side
MSRE Difference	111 ⁽²⁾	41.6 ⁽²⁾	200 ⁽¹⁾	166 ⁽¹⁾

⁽¹⁾: Known to be calculated.

⁽²⁾: Known to be measured.

Table 7.7 Temperature and pressure comparison between simulation and MSRE data

Platform	Model & Runtime: [s]	Indicators	Temperature [C]		Pressure [kPa]	
			Air-side	Salt-side	Air-side	Salt-side
Simscale	$k - \omega$ SST Runtime 2.5e4	Simulated difference	5	574	3	89
		Accuracy ratio (%)	5%	1380%	1.5%	54%

Difference (absolute value) is calculated as: $Inlet - Outlet$

Accuracy ratio (%) is calculated as: $Simulated\ difference/measured\ difference * 100\%$

100% indicate perfect match between expected value and simulation

By the time the radiator CAD model was finished, the core hours on Simscale were used up. To get a simulation running a Simscale user by the name of 'dschroeder' offered to use his core hours (dschroeder, 2019). However, this simulation produced unphysical values and cannot be used for validation. This Simscale simulation was run a couple of times, always producing similar, unphysical results with no convergence of the data.

There are many potential reasons for this, two of which are discussed here.

- 'Bad' cells

The most probable reason for these errors is the mesh. If bad (i.e., highly skewed, highly non-orthogonal etc.) cells exist within the mesh, the calculations over those cells will yield wrong results, which will seed errors into the solution, making the entire solution diverge.

- Inlet velocity profile development

Another problem that could cause a simulation to break like this is the development of the initial flow from the boundary of the air-side. In standard CFD-practice, usually what one does is to artificially lengthen the inlets (and outlets) by a couple of inlet-diameters, to allow for the flow to fully develop before it interacts with the region of interest. The inlet measurements for the radiator are ~ 3 by ~ 3.6 meters, which means that the artificial lengthening of the inlet would have to include meters of additional modelling. For a mesh containing $\sim 2.3e7$ mesh elements, this inclusion of an artificially lengthened inlet would produce an unreasonable number of mesh elements and was thus not attempted.

The OpenFOAM cases were run with many different parameter settings, wall functions, relaxation factors, initial conditions and boundary conditions. No combination thus far tested worked, and the simulation diverged within a couple of timesteps from initiation. With more experience in using OpenFOAM there is most probably a case set-up that will produce usable results to validate the findings of the MSRE.

7.2 Data accuracy

Here, the accuracy of the data from the MSRE and the data gathered from simulations are discussed.

7.2.1 Accuracy of simulated data

7.2.1.1 Temperature

As can be seen in Table 7.1, the relationship between increase in flow rate and pressure loss produced a great match, indicating that the relationship between these two parameters is computed accurately and realistically.

Table 7.3 shows that the temperature transfer nearly perfectly matched the data from the MSRE for the Simscale simulations of the PHeX. The temperature data from the MSRE are the most accurate available, since it is a comparatively easy measurement and the reports from ORNL specify numerous times that no issues were found with the thermocouples they used to measure temperature. Thus, the conjugate heat transfer (CHT) works well within Simscale for models and meshes of this size, and these data are deemed physical and usable.

The completed OpenFOAM simulations, however, underestimated the temperature transfer to quite a large degree. This suggests that something is wrong within the setup of the OpenFOAM case, most probably within the wall treatment, where the heat transfer occurs. There are a multitude of wall functions and wall treatment methods available in OpenFOAM, each with its own underlying mathematical modelling on how to treat the interphase between the fluid region and the solid region. Sensitivity to specific wall treatment factors within the OpenFOAM case structure, and more specifically with the $k - \omega$ SST setup, are most probably the greatest source of the errors for simulating the temperature transfer.

7.2.1.2 Pressure

As can be seen from Figure 6.3 and Table 7.3 there has been a consistent overestimation with a factor of about 2, for the simulated pressure drop in every simulation of the PHeXg, both for salt and water. There are two approaches on how to deal with this overestimation. Either:

- a) Something is wrong with the mathematical model and the pressure drop is not being adequately captured, or
- b) The pressure results from the MSRE are wrong.

It is quite a bold statement to propose that the people that built and operated the MSRE at ORNL would have had a consistent error of this magnitude throughout the otherwise successful operation

of the reactor, but it is still plausible. The pressure for both tube-side and shell-side are close to, or within the design pressure, and they both lie within the allowable working pressure stated in ORNL-TM-2098, shown in Table 6.1.

There are many sources of potential errors within any simulation, e.g., turbulence model, initial conditions, boundary conditions, mesh coarseness, boundary layers, convergence errors, truncation errors and many more (Celik, Karaismail, & Parsons, 2007). Each of these has to be analysed and a sensitivity analysis performed to see where the biggest source of the error might stem from and how to best perform a satisfactory simulation. Due to time limitations this could not be performed within the scope of this project.

Conversations with many experts in the field of CFD have confirmed that pressure is notoriously difficult to simulate, and especially using the $k - \omega SST$ model (Mårtensson, Karlsson, Tornblom, Stromer, & Andersson, 2021).

7.2.1.3 Temperature dependence

In reality there is a temperature dependence on both density and viscosity that is quite crucial for the neutronics in the fuel salt (i.e., negative temperature coefficients for passive reactor safety, where the salt expands as it heats up and thereby limits fission occurrences). For density, this effect is only important for the neutronics in the reactor core, thus for the purpose of this thesis, density variations have negligible impact on the final results and can be safely ignored.

Viscosity, however, has a more pronounced temperature dependence, according to Figure 7.1. In the PHeX the temperature interval for the salts lies between 820 – 930 K, which spans a ~40% difference in viscosity, as seen in Figure 7.1. This should have been modelled but was not considered in this project. Instead, the viscosity was treated as a constant.

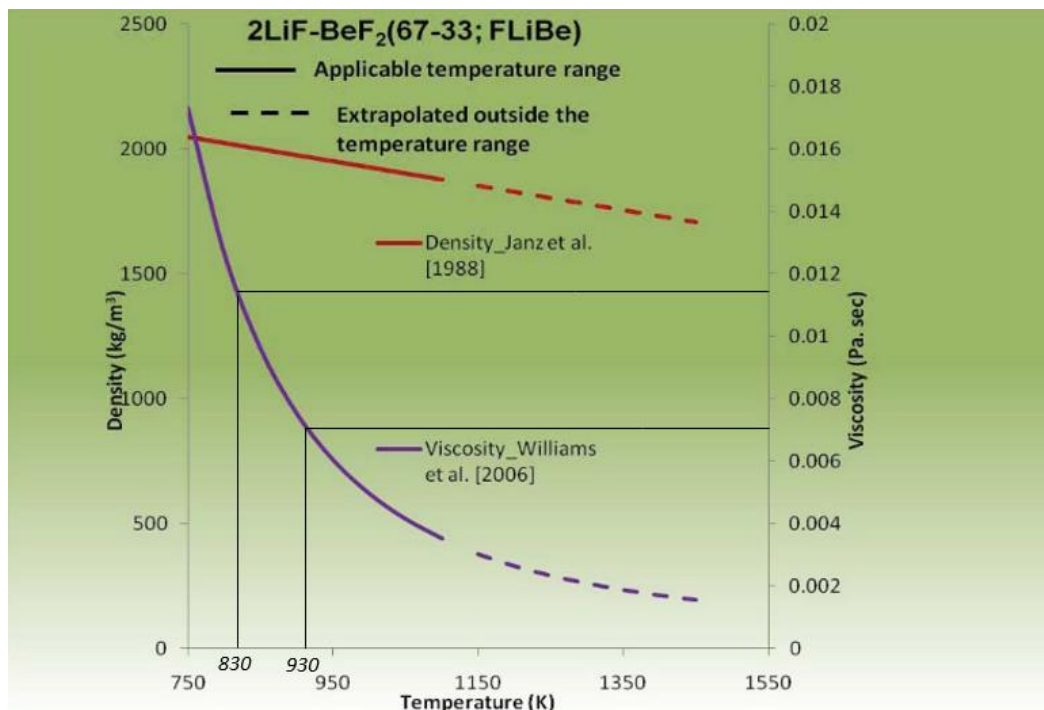


Figure 7.1 Density and viscosity variations over temperature for molten FLiBe salt (Sohal, Ebner, Sabharwall, & Sharpe, 2010).
Inserted lines show max- and min temperature of the salts in the PHeX.

In the energy equation, Eq. 10 in Chapter 2, there is a specific heat capacity for the salts in question. According to ORNL-4344 the specific heat of the salt is not temperature dependent and could thus be treated as a constant (ORNL-4344, 1969). There are always assumptions one can make to simplify any given model, and in the end, what is sought after for these large scale, steady state simulations are approximate values to give an estimation of the physical parameters of interest.

7.3 Accuracy of MSRE data

The MSRE operated successfully for 4 years. In Figure 7.2 a timeline of reactor power and the tests conducted is shown.

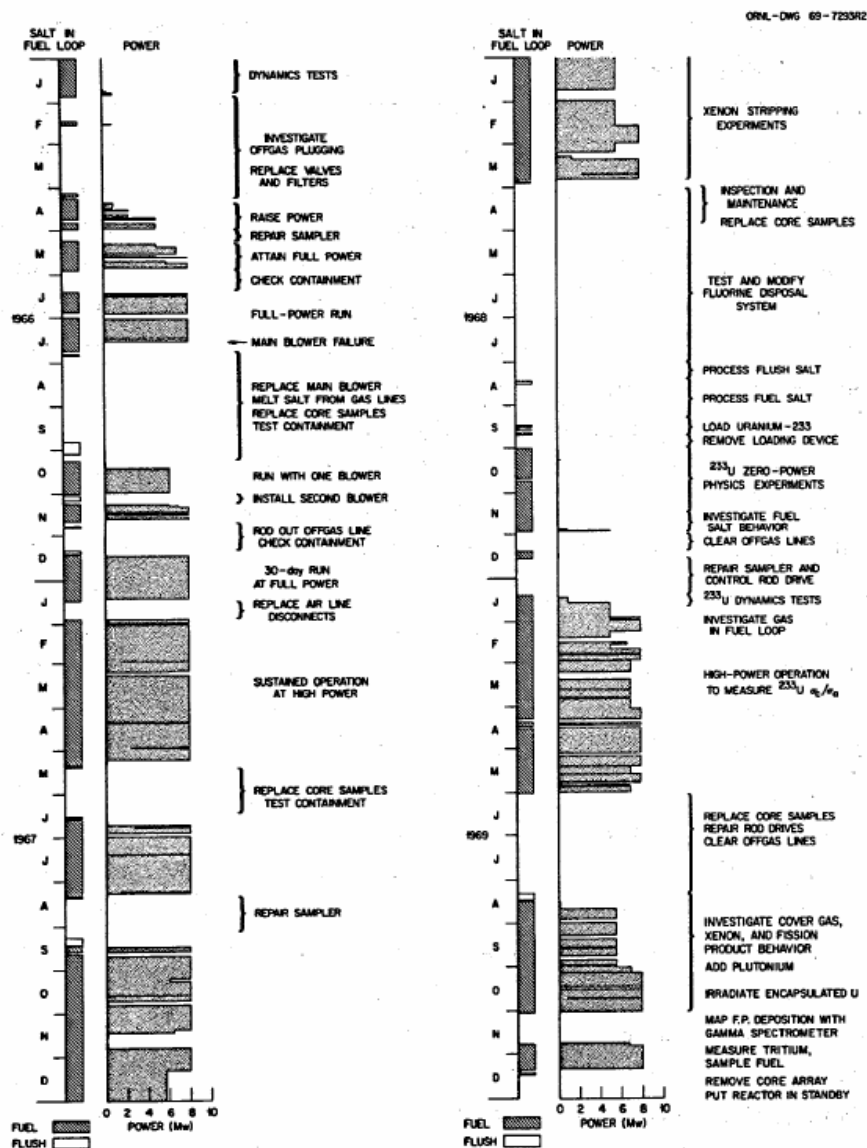


Figure 7.2 Timeline of reactor power and conducted tests (ORNL-TM-3039, 1973).

As can be seen from Figure 7.2, many tests were done at various reactor power levels over the 4 years of successful MSRE operation. However, since this research was performed in the midst of the cold war in the United States and financed by the U.S. government, all of the documents were initially classified. Most of the reports have been declassified since then, but test memos have not, and in these test memos exact procedures of testing and data gathering will be found. Not having

access to these data makes an exact comparison difficult. In many reports, such as ORNL-TM-2098, explicit references to test memos are being made, which would have aided this project greatly.

The declassified data that are presented by the team at ORNL are distributed over many documents, where it is often unclear what are measurements and what are calculations. For the coolant salt it is mentioned in several reports that a venturi-type flow meter was installed (ORNL-TM-3039, 1973), (ORNL-3419, 1963). However, the data from the flow meter and how it related to e.g., pressure measurements have not been found.

According to ORNL-TM-3039, no flow instrument was provided in the fuel salt. All the pressure data gathered for the fuel salt have been inferences or pure calculation estimates, never real measurements as far as the author of this thesis has found. In the document (ORNL-3303, 1971), it is stated that:

“In the MSRE molten-salt loops the pressures were determined indirectly by measuring the pressures in gas-purge or supply lines connected to gas spaces in the drain tanks and pump bowls.”

This is due to the harsh environment of radiation and highly corrosive salts at 600 C. Building flow meter apparatus and pressure sensors capable of withstanding this physical environment will be key in future development of MSR technology. Access to the pressure data in these supply lines and gas-purge lines have not been found in the available ORNL documents.

As mentioned in Chapter 1, the MSRE was initially designed to output 10 MW of power, but errors in calculations regarding the effectiveness of the PHeX capacity to remove heat from the salt limited the total reactor power output to 7.4 MW. In the document ORNL-4119 a discussion on methods of improving heat transfer were discussed as follows:

“A study was completed to determine whether the maximum power capability of the reactor could be raised by some convenient method. For normal operating conditions, an upper limit of 1210 F (655 C) has been placed on the reactor outlet temperature. This temperature was selected on the basis of thermal stress cycling and stress rupture life of the reactor system. The minimum coolant salt temperature in normal operation has been set at 1000 F (538 C), in order to reduce the probability of freezing the radiator in case salt flow is interrupted.

These two temperature limitations and the heat transfer capability of the main heat exchanger (PHeX) limit the reactor power to about 7.4 MW.

. . .

Other than replacement with a larger unit, the heat exchanger capability can be increased only by increasing the flow rates of the fuel and coolant systems. Increasing the temperature difference between the fuel and coolant system is undesirable because of adverse effects on the thermal-cycle and stress-rupture life of the reactor system.

. . .

In the radiator, increasing the salt flow has very little effect, since over 95% of the heat transfer resistance is on the air side of the tubes. There is no way to improve the radiator performance without major expense.

. . .

In conclusion, the difficulties in raising the power capability of the reactor far outweigh any advantages that could be gained from the relatively small power increase that can be reasonably achieved. Since the objectives of the MSRE can be met with the present heat removal system, no attempts to increase the power capability are planned."

(ORNL-4119, 1967)

7.3.1 Internal comments from personnel in MSRE

An internal document, labelled ORNL-CF-70-9-3, contains comments and critique about the MSRE made by 28 anonymous persons working at ORNL to aid future research into MSR technology (ORNL-CF-70-9-3, 1970). An excerpt of “reply E” in this document reads as follows:

Primary Fluid Flow Rate:

“The lack of a flow element in the primary loop has contributed much to analytical difficulties. Such a device could have added a great deal to our understanding of the system — it might even have helped resolve our current uncertainty in power level. The device in the coolant loop has demonstrated that such an installation need not compromise the integrity of the loop. A direct measure of primary flow should be strongly considered in the next reactor design.”

Pressure Indications:

“This may be one area in which the analytical needs could not be accurately predicted. However, we now know that a pressure-measuring device, with good high-frequency response, at some point in the liquid filled portion of the primary loop would have been a valuable asset in the studies of bubble effects and dynamic behaviour. If such devices are not currently available for molten-salt applications, it would probably be worth some development effort to get one (or more) for the next reactor.”

“Reply U” of the same document echoes similar concerns. This casts more doubt on the data from the ORNL documents, since these replies confirm that much of the data has been inferred or purely calculated, rather than measured.

7.3.2 Uncertainties in measurements

In the document ORNL-TM-2316, uncertainties in measurements for many parameters of a number of different salt compositions are shown. The compositions of interest for this thesis are presented as variations of the fuel salt used in the MSRE, denoted in ORNL-TM-2316 as $F1$ through $F4$, of which $F2$ is the closest to the MSRE fuel, as well as the coolant salt used in the MSRE. The uncertainties are shown in Table 7.8 (ORNL-TM-2316, 1968).

Table 7.8 Uncertainties in measured parameters of fuel and coolant salt of the MSRE

Quantity	Unit	Uncertainties			
		Fuel salt		Coolant salt	
Viscosity	$\left[\frac{kg}{m \cdot s}\right]$	$0.072 \exp\left(\frac{4370}{T}\right)$	25%	$0.116 \exp\left(\frac{3755}{T}\right)$	15%
Thermal conductivity	$\left[\frac{W}{cm \cdot C}\right]$	0.01	25%	0.01	10%
Heat capacity	$\left[\frac{cal.}{g \cdot C}\right]$	$0.39 + T * 12.7e - 5$	4%	$0.57 + T * 3.61e - 4$	3%
Density	$\left[\frac{g}{cm^3}\right]$	$3.153 - T * 5.8e - 4$	3%	$2.214 - T * 4.2e - 4$	2%
Vapor pressure*	[Torr]	$\log P = 8.0 - \frac{10\,000}{T}$	Factor 50	$\log P = 9.04 - \frac{10\,500}{T}$	Factor 10

*vapor pressure of salts used to infer pressure of the liquid

T is temperature measured in units of K

From the same document it is written that:

“Although the magnitudes of the uncertainties are . . . often disappointingly large, they should be taken seriously.”

These very large uncertainties in the thermophysical constants of the salts in question casts further doubt on the exactness of the values presented by the team at ORNL. Since then, improvements have been made on these values, but some still have a very large uncertainty do to the difficulty of measuring properties of these hot, corrosive substances (Sohal, Ebner, Sabharwall, & Sharpe, 2010).

7.4 Models

7.4.1 CAD-models

The CAD models of the PHeX and the radiator have all performed satisfactorily throughout the project. They were time consuming to create, but the attention to detail meant that very few modifications had to be made. These CAD models are the only highly detailed CAD models of these components that currently exist, and they are open to use for anyone, provided they cite this report. Links to models available for viewing and downloading are found within Appendix II.

After many hours of modelling, a few design choices have been identified that, if altered, may improve the performance of the physical system.

7.4.1.1 PHeX design suggestions

In the PHeX, the temperature in the outlet of the fuel was unevenly distributed and a consistent temperature gradient of about 15 C was found, as shown in Figure 7.3. Excessive thermal cycling during change in reactor power might give rise to an uneven thermal stress distribution and over time weaken the material. This may be solved by, for example introducing a branching structure to funnel the salt into and out of the tubes.

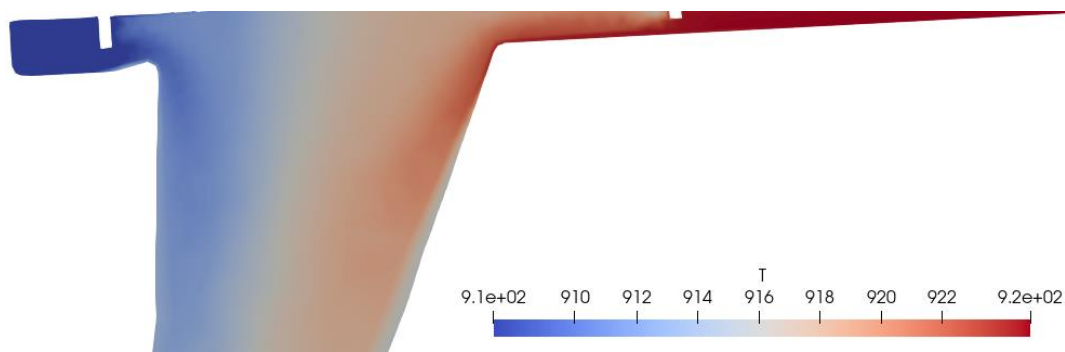


Figure 7.3 Temperature gradient in shell-side outlet of the PHeX.

There are many 90 degree bends present in the tube-side of the PHeX, one for each tube. When the fluid is flowing in from the tube-side inlet, it first collects in the tube head channel to be dispersed within the tubes. This transition, from the big open volume into small tubes gives rise to an excessive vorticity and therefore turbulence generation, as can be seen in Figure 7.4. Rethinking how the fluid enters the tubes in a smoother fashion, for example with a branching structure, may yield better heat exchanger performance.

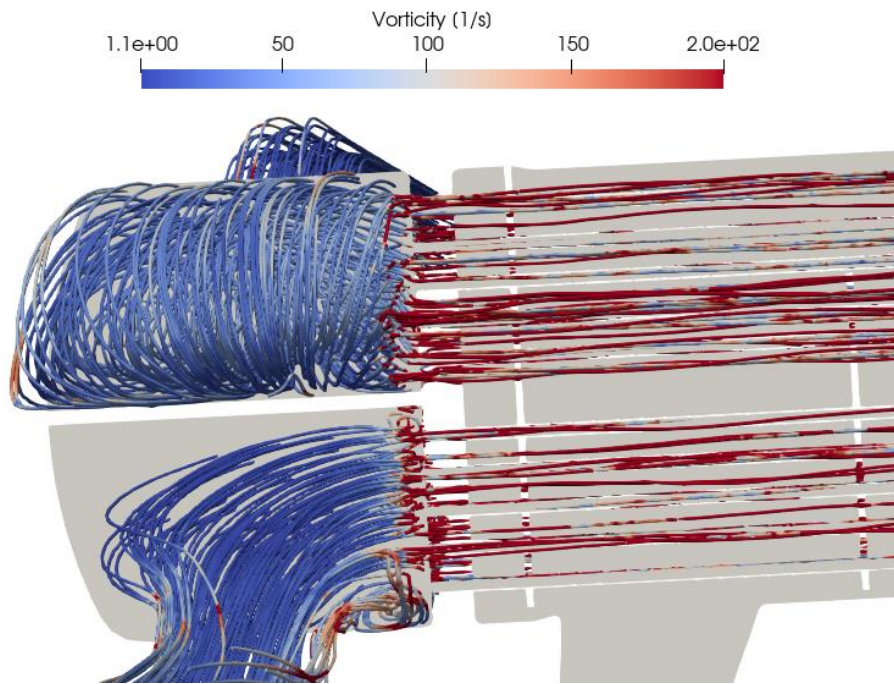


Figure 7.4 Flow paths in the PHeX tube-side, coloured as vorticity, indicating turbulence.

7.4.1.2 Radiator design suggestions

In the radiator tube-side there are many 90 degree bends in the main-header going into each of the sub-headers, as well as from the sub-headers to each tube, as shown in Figure 7.5. Every 90 degree bend in a fluid geometry introduces excessive vorticity and thus turbulence generation and should in general be avoided as much as possible. Rethinking how the salt gets funnelled into the tubes may improve the radiator performance. Using straightening vanes as those used in the reactor core, together with another method of getting the salt into the tubes, for example a branching structure, might reduce the vorticity and prevent unnecessary turbulence.

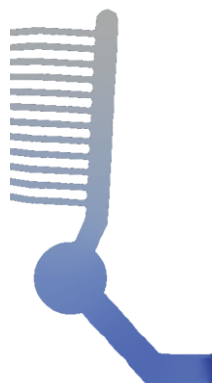


Figure 7.5 Outlet, main- and sub-header of radiator with connecting tubes.
Example of excessive use of 90 degree bends.

7.4.2 Validity of $k - \omega$ SST model

There are known sources of errors within the $k - \varepsilon$ model for adverse pressure gradients, which are present all over the PHeX and the radiator. This is why the $k - \omega$ SST model is used instead, to switch between $k - \omega$ and $k - \varepsilon$ based on distance to the wall. If this wall distance estimator locally gives the wrong results, for example based on a bad mesh, then the wrong model is used, and pressure data might diverge from the true value. For the OpenFOAM simulations performed in this thesis, the inbuilt utility 'meshWave' has been used to calculate the wall distance, and in the OpenFOAM-documentation this utility might not work as expected for highly non-orthogonal meshes (OpenFOAM, 2017). According to the mesh results in Chapter 5, the meshes in this thesis often have many cells with a fairly high non-orthogonal value, which might have led to bad wall distance estimations and thus poor performance of the $k - \omega$ SST model.

Test and validation cases performed by other researchers to show the efficacy of the $k - \omega$ SST model are often done on simple geometries, with a well-defined wall distance everywhere and few flow obstacles, making it difficult to know how well those results scale to more complex models. In the paper "Development and application of a cubic eddy-viscosity model of turbulence" Craft et. al. discusses flow situations where the $k - \omega$ SST model has limitations in its ability to predict flow parameters (Craft, Launder, & Suga, 1996). Drawings of geometries that might cause the $k - \omega$ SST model to misbehave are shown in Figure 7.6.

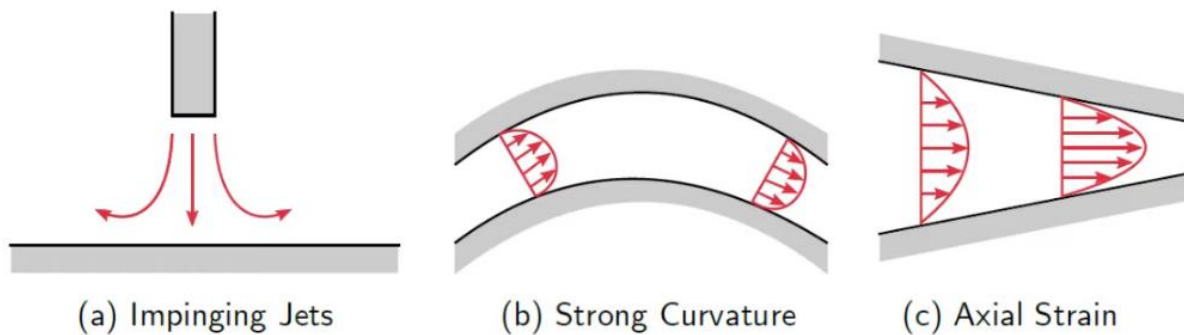


Figure 7.6 Geometry examples of limitations within the $k - \omega$ SST model.
Red arrows indicate velocity profiles or flow paths.

Case (a) in Figure 7.6 is present throughout the models of the PHeX and the radiator, for example in-between tubes and where the baffle plates impinge on the surrounding cylindrical shell.

Case (b) is present in every tube, especially the centremost ones, which have a small curve radius compared to the outermost tubes.

Case (c) is present most notably in the conical reducer in the fuel outlet of the PHeX, specifically installed to reduce pressure drop. Since the $k - \omega$ SST model used to simulate is known to give errors in flow situations like this, it might be the reason that the pressure was overestimated.

7.5 Experience with the software utilized

7.5.1 Onshape

Onshape has proved to be an excellent CAD platform and has been utilized in every model of this thesis. No other CAD-program was tried since Onshape performed well and was easy to share and edit between multiple partners, which has been invaluable for the feedback process of this thesis.

7.5.2 Simscale

Simscale performed well as long as it had available core hours, but models of this size, and especially for conjugate heat transfer simulations, require a lot of meshing- and solving-time. Thus, only about 10 simulations could be made, most of which were test cases and setups. For this purpose, however, Simscale was a great tool since the learning curve is very forgiving and a case can quickly be set up and simulated. For smaller models, this platform is highly recommended.

Simscale's meshing module (built on OpenFOAM) performed well but had very little user input, handling most meshing operations automatically in the background. The meshes produced had acceptable quality with a reasonable number of cells but by looking at the figures in Chapter 5 (Simscale section) it is clear that the meshing is quite rugged and uneven, especially in the tubes. For straight sections with jagged and non-parallel edges, e.g., Figure 5.3, this may impact the CFD-results.

7.5.3 Salome

Switching to Salome proved to be an easy workaround to produce good meshes with more control. The program is somewhat intuitive and with help from tutorials, forums and colleagues it took relatively little time to get proficient. Since Salome is designed for meshing it has more options than Simscale to create a mesh of good-enough quality, but it always produced meshes with significantly more cells than Simscale.

Salome had another drawback in that it could only be operated single core, which highly time consuming. This is a limitation in the meshing algorithms available in the free version of Salome.

There are multi-core meshing algorithms available with a license provided by Salome, but they are not free or open-source.

Another limitation in Salome is that it saves its project files in .HDF4 format, which is a quite old data format, which has a data limit of $< 2\text{ GB}$ per file. A completed mesh for the entire PHeX usually came out at $> 4\text{ GB}$, meaning that it could not be opened again once the Salome session was closed, and all the data were lost. All exporting and screen captures had to be done within the session. This was found out very late in the project and contributed to a lot of down-time. The version of Salome used for this thesis is Salome meca 2019 0.3_LGPL.

7.5.4 ideasUnvToFoam

This program proved to be quite the bottle neck. For smaller models it has worked perfectly fine, converting Salome's .unv formats to the .foam format used by OpenFOAM. Initially, these results gave great hope that this part of the toolchain would provide no further problems. However, for larger models it has halted partway through execution every time without any error messages. Troubleshooting this program has not been easy, but the code sections where it seems most likely to halt were identified. Nothing could be done with this information, however, since it was outside of the scope of this project to perfect a mesh-conversion algorithm. Each region of the PHeX was exported and converted separately to see if one of the regions was the source of the halting. Two of the regions (the shell and the solid part) never finished the conversion, and this problem remains unresolved.

7.5.5 OpenFOAM

OpenFOAM is a C++ environment, and a very powerful CFD-tool with great customizable capacity to fit the users' needs. It allows for users to construct their own executables to solve coupled problems and introduce governing equations as they are needed. It is however quite difficult to understand fully, since most internal objects and data types are defined in layers in the OpenFOAM structure. Following online tutorials and spending time in the terminal is a must for anyone using OpenFOAM. Getting started is quite easy after the initial learning curve, but it quickly became apparent that it is difficult to set up an accurate case for a more complex scenario. OpenFOAM's error message system is very useful and makes troubleshooting a relatively easy, although time consuming, endeavour. The documentation of OpenFOAM is completely open, and everything is accessible, but to fully understand what is going on behind the scenes the user needs a solid understanding of coding in

C++. Thanks to its open-source nature it will most probably continue to be a very important tool for the CFD-community going forward.

Downloading a casefile of a completed simulation from Simscale, one gets access to its mesh and underlying OpenFOAM case structure. It is possible to use these files for OpenFOAM simulations by going through the error-messages one-by-one when trying to execute. It takes time, and the simulations run with this method have so far only been done with a single core, since the multi-core setup requires more work. This is most probably doable, but due to time constraints the problem has been put aside for future work. The version of OpenFOAM used in this thesis was OpenFOAM V8.

7.5.6 Paraview

Paraview has performed well and been stable throughout the entire project. It has been an indispensable tool for analysing these huge datasets after completed mesh and simulation. It is easy to learn and to extract meaningful data in colourful plots, which has been a rewarding part of this project. Its branching structure is powerful and intuitive to work with.

Paraview has a lot of functionality, and it can be daunting when being subjected to all its capabilities, but for each project only a few of the tools are really necessary which simplifies the work a lot.

The version of Paraview used in this thesis was Paraview 5.8.1.

7.5.7 Atom

Atom is a powerful and easy to use text- and source-code editor. Since all the documents available from the MSRE have been subjected through an Optical Character Recognition (OCR) program, all the documents are searchable, which have been an indispensable tool throughout this project. The OCR of the ORNL documents has been done by the supervisor for this project, Aslak Stubsgaard. Similar information is generally spread out over many ORNL documents, which makes a powerful file-searching-program a must-have for a project like this.

8 Conclusions and future projects

8.1 Conclusions

8.1.1 Revisiting the problem formulation

The purpose of this thesis was to study whether existing, open-source programs could be used for a full CFD-analysis of MSRE heat exchangers. To validate the accuracy of the CFD-results, data gathered from the MSRE have been used, and the validity of that data have been discussed in Chapter 7.

CAD-, mesh-, simulation- and post-processing software have been identified and tested, and a toolchain has been found that performs well for the intended purpose, even though problems were faced for the bigger models. Anyone can download or register to use the programs outlined in this thesis, and the hope is that the work presented here can serve as a starting point for future work on these and other components within the MSRE and surrounding MSR technology.

8.1.2 CAD

Highly detailed and accurate CAD-models of the PHeX and radiator within the MSRE were created in Onshape with the aid of technical drawings found in the ORNL reports, and these models are available online to be used in future projects, see Appendix II. Within each model case in Onshape, the necessary technical drawings are included. Model creation and documents used to produce the models have been shown in detail in Chapter 4.

8.1.3 Mesh

The models of the PHeX and radiator have been meshed, using free and open software. The meshing process for Salome, which is outlined in Appendix III, had to be developed for big, multiregion cases like these, and it has performed well, albeit slowly since the mesh-algorithms available from Salome only operate in single core. The simulation results indicate faults that most probably are related to faults in the mesh. To produce a mesh without these faults (i.e., limiting bounds on skewness, non-orthogonality and aspect ratio, among other measures), a much more thorough mesh creation has to be undertaken.

The meshes produced by Simscale seem to be more robust, with good balance between resolution and overall mesh elements, but there is limited user input to affect the final mesh.

8.1.4 Simulations

The simulations were time consuming to run and had to be iterated many times to find a solution that converged. When a solution did converge, however, the results were physically sound and usable, and the heat transfer prediction from the Simscale simulations was found to be very close to the ORNL data from the MSRE. However, pressure data have differed quite substantially from the values reported for the MSRE, and an effort in explaining this discrepancy has been made. One possibility, argued for in Chapter 7, is that the MSRE pressure data were incorrect and the PHeX operated with a much higher pressure drop than what was estimated by the team at ORNL. The PHeX was designed by the team at ORNL to function over a large pressure range, which provided necessary safety margins for operation.

Being able to accurately solve conjugate heat transfer (CHT) of a turbulence model in a complex flow space such as the PHeX shows the efficacy of Simscale.

For OpenFOAM, the data gathered in this report show convergence and can provide useful data for a CHT in MSR components. More work is needed within the case set up to provide a simulation that more accurately predicts the pressure drop, and confidence is high that this is possible. Pressure is widely known in the CFD-community to be the most challenging parameter to correctly predict, which this thesis confirms.

8.2 Future implications and projects

There are many potential future projects that can use the findings in this thesis as a branching point. Due to time-limitations and know-how, many aspects could not be finished within the specified time frame. This is inevitable in a master's thesis, and this section is dedicated to listing possible future projects relevant for the MSRE, MSRs in general and heat exchangers.

8.2.1 Radiator simulations

Since no simulation of the radiator worked, a project undertaking a more comprehensive study into simulating this component needs to be undertaken. The CAD-drawing of the radiator is a good branching-off point, and the first suggestion is to lengthen the inlets and outlets of the model in order for the simulation to have a well-developed inlet flow before the tube-sections are approached. To properly mesh and simulate this structure within reasonable time requires a lot of computing power, so access to some form of large data cluster is most probably needed to proceed.

8.2.2 Comparative studies

8.2.2.1 Turbulence models

The turbulence model utilized in this thesis has been the 2-equation, $k - \omega$ SST formulation of the RANS equations. This is just one of many turbulence models, and a study in sensitivity to different turbulence models would be a great aid in advancing our knowledge in how to properly perform CFD on large and complex MSR components like the ones studied in this thesis.

Turbulence models recommended by the author to test are the:

- Spalart-Allmaras (S-A, algebraic model)
- Intermittency transitional (3-equation model)
- $k - k_l - \omega$ model (3-equation model)

The CFD-Online web site presents a comprehensive list of turbulence models and their applications (CFD-online, 2021), and a report produced by the Chalmers university in Gothenburg, Sweden further expands on these models (Davidson, 2018).

There is also a potential for direct numerical simulation (DNS) on small components and regions to study more closely how molten salt behaves as a fluid. A fluid with such a high density, but with a

viscosity comparable to water, might have very different small-scale behaviours and new turbulence models might be necessary. This is potentially a rich avenue to explore.

8.2.2.2 Other heat exchangers

Since the 1960s many new heat exchanger-concepts have been developed. At the time of the MSRE, the shell-and-tube heat exchanger was the best heat exchanger available. Today, there exists plate heat exchangers, printed circuit heat exchangers, spiral heat exchangers, and many other variants throughout industry (Annaratone, 2010).

Future projects looking into different heat exchangers for molten salt, ranking them for total heat transfer, pressure loss, amount of material, cost, and any other relevant metric is going to be useful for companies and industries looking to develop MSRs in the future.

8.2.2.3 Energy generation to demonstrate MSR feasibility

Since MSRs and other Generation IV nuclear reactors are still in their naissance, there is a substantial knowledge gap within the general public of the immense utility this technology could bring to society at large. Projects looking into detailed, easily understood comparisons between different energy sources with the focus of comparing them to MSRs will be very valuable in convincing the public and stakeholders that this technology needs to be further developed. Factors such as total power generation per year, land usage, material requirements, costs, deaths per GWh produced and many other metrics should be included to give a comprehensive comparison between the power generation methods available. Special emphasis should be placed on current nuclear waste burn-up capabilities of Gen IV reactors in general, and MSRs in particular.

8.2.3 Accessibility

8.2.3.1 Declassification of test memo-data from ORNL

Many reports, articles, and all test-memos and other documents from the MSRE are still classified by the U.S. government. Getting access to these documents would help immensely going forward with MSR technology, since the MSRE, to this day, is the only functioning MSR that has been built and successfully operated. How these documents would get declassified is still the issue, and a project looking into this would be of great help to the development of MSR technology.

8.2.3.2 Developing MSR-archive

The data available from the MSRE need to be organized in an intelligent and open way. Currently there are libraries online where anyone can download an immense number of documents which have already been OCR'd (Optical Character Recognition), but other programs, like Atom used in this thesis, must be used to be able to search the documents efficiently. Many of the OCR'd documents are also corrupted, since they are quite old and have often been subjected to multiple copying which degrades the readability of OCR programs.

The most comprehensive library is the one created by the supervisor and advisor for this thesis, Aslak Stubsgaard (CTO of Copenhagen Atomics). Using this library and creating an accessible web platform, where illustrations and documents can be shown and easily navigated between, is something that could streamline research of the MSRE and MSR technology in general. A software and/or graphic design project, looking into data gathering and presentation of the MSRE findings is needed.

8.2.3.3 Further toolchain development

For large projects like this it is necessary to have a well-functioning toolchain that works and is scalable. The toolchain developed and used in this thesis have some flaws, especially the difficulty of getting a mesh that OpenFOAM can handle. A continued effort into developing an open-source toolchain to work with big models for large CFD simulations is necessary to keep developing the findings of this thesis, keeping the information open and accessible.

One such effort is updating the ideasUnvToFoam program for mesh conversions between .unv and .foam formats, the major bottle-neck encountered in this project.

8.3 Freedom and the necessity of open-source

This project has been an exercise in finding and developing a working toolchain with open-source programs for the entire CFD-process of CAD drawing, meshing, simulation and post processing.

Many problems that arose are most probably solved within bigger and more complete CFD-suites (e.g., ANSYS or COMSOL), but those platforms are often tangled within legal agreements and restrictions on access and further development of the underlying code, preventing openness and development by outside parties. This halts the development unnecessarily and prevents researchers from collaborating if they do not share these platforms.

Software is developing faster than anything else, and the necessity of keeping it open and usable is crucial so as to not fragment our societies. As software changes, industry and researchers must change too, to include new progress in their work, as well as finding new ways and methods to broaden their work cross-disciplinary. By continuing the work on MSR technology in the spirit of open-source, collaborations worldwide will accelerate our knowledge and bring this marvellous technology into existence.

The push for open-source within the software world of today echoes the movement of spreading and opening up the scientific method during the renaissance era. More recently, the world-renowned Danish physicist Niels Bohr, one of the founders of quantum mechanics and modern physics, had a strong world view of open scientific discussion and the importance of free collaboration. In 1985, E. Rüdinger wrote an article titled “The open world of Niels Bohr” in which he describes how Bohr helped transform the discipline of physics into an international collaboration between researchers (Rüdinger, 1985).

The Free Software Foundation has identified 4 freedoms pertaining to open-source, and these are included here as they reflect the values of the author (Free Software Foundation, n.d.). Open-source will become more and more necessary as we move forward in a cross-disciplinary, software dominated world.

- **Freedom 0:** The freedom to run the program, for any purpose.
- **Freedom 1:** The freedom to study how the program works and adapt it to your needs.
 - Access to the source code is a precondition for this.
- **Freedom 2:** The freedom to redistribute copies so you can help your neighbour.
- **Freedom 3:** The freedom to improve the program, and release your improvements to the public, so that the whole community benefits.
 - Access to the source code is a precondition for this.

"As our society grows more dependent on computers, the software we run is of critical importance to securing the future of a free society. Free software is about having control over the technology we use in our homes, schools and businesses, where computers work for our individual and communal benefit."

- Free Software Foundation

"Free learning resources, like free software, is a matter of freedom, not price. It's about bringing the principles of free software to general knowledge and educational materials. Knowledge should be usable and accessible to all without restrictions and should not be treated as property."

- Free Software Foundation

APPENDIX I

9 Appendix I: Tensor notation

For mathematical expressions including tensors, the convention that is used in this thesis is the Einstein notation. Index most commonly used are i, j, k, l , each in the range 1, 2, 3 or x, y, z . For a double index, as in Figure 9.1, the first index specifies the face perpendicular to the direction indicated, and the second index specifies the direction on that face. In Figure 9.1, τ_{xy} is therefore a vector starting at the face perpendicular to the x direction, stretching out in y direction as indicated by the arrow.

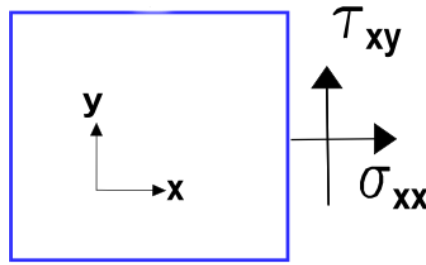


Figure 9.1 Double index convention of tensors.

When the same indices are used twice in one term, summation is implied, i.e.:

$$\frac{\partial U_i}{\partial x_i} = \sum_{i=1}^3 \frac{\partial U_i}{\partial x_i} = \frac{\partial U_1}{\partial x_1} + \frac{\partial U_2}{\partial x_2} + \frac{\partial U_3}{\partial x_3} = \frac{\partial u}{\partial x} + \frac{\partial v}{\partial y} + \frac{\partial w}{\partial z} = \Delta \cdot U \quad \text{Eq. 52}$$

This is a very powerful notation, capable of compressing complex mathematical notation and relations in just a couple of symbols. A term like $\varepsilon = \mu \frac{\partial u'_i}{\partial x_j} \frac{\partial u'_i}{\partial x_j}$ actually represents 9 terms when carrying out the summation implied by the Einstein Notation.

A special symbol used commonly in tensor notation is the Kronecker delta, which is an analogue of the identity matrix in vector notation and is shown in Eq. 48:

$$\delta_{ij} = \begin{cases} 1 & \text{if } i = j \\ 0 & \text{otherwise} \end{cases} = \begin{bmatrix} 1 & 0 & 0 \\ 0 & 1 & 0 \\ 0 & 0 & 1 \end{bmatrix} = I \quad \text{Eq. 53}$$

The resources in the reference should be sufficient for anyone that wants to understand more about tensors (McGinty, 2012).

APPENDIX II

10 Appendix II: Models and case set-up access

10.1 Simscale:

PHeX simulation:

<https://www.simscale.com/projects/MalcolmAkner/phex - final version/>

Radiator simulation:

https://www.simscale.com/projects/MalcolmAkner/msre_radiator_public/

10.2 Onshape:

PHeX CAD model:

<https://cad.onshape.com/documents/03be2f510296a2e264886390/w/8cfbca3b7b9682dd4e53a998/e/54728fd981a1b4f5594c73d6>

Radiator CAD model:

<https://cad.onshape.com/documents/bf944323ed6a82e05924078c/w/2a25d73c5a3a66824d2d5fbd/e/a83d5535602a053216fedff4>

Heat exchanger test model CAD model:

<https://cad.onshape.com/documents/a980c75870e8a4ed0c795c1a/w/b249e008bd8bef88c11864b0/e/ec1282d2e6b1d75420971759>

APPENDIX III

11 Appendix III: Salome set up and mesh guide

Salome geometry operations and meshing procedure for arbitrary complex geometry of multiple regions

All the commands that are in Salome are highlighted with **bold font** for clarity of what the user should interact with in Salome.

This scheme will work for Salome imports to OpenFOAM with models created in Onshape but should be translatable to any CAD software that can export to .step format.

One thing to note with Salome is that it seems to always scale down the model by a factor of 1000 upon import. This is only relevant during the meshing steps when parameters are set, which are usually specified in *mm*, but it can be a little inconsistent. I always recommend checking the size of the final mesh, which can be easily done in for example Paraview (a program every OpenFOAM user should have).

When working in Salome, it is helpful to always highlight the **Interaction style switch** to be able to use left mouse button to rotate the model (icon of a mouse, under my cursor, in image):

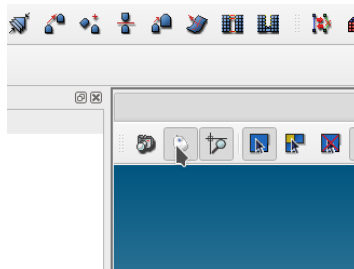


Figure 11.1 Interaction style switch in Salome, to activate model control by mouse movement.

To mesh a surface of arbitrary complexity for multi-region CFD-treatment (CHT of a shell-and-tube U-tube heat exchanger, named "FullKSHeX" for this case) do the following steps:

- Create your model in the CAD-program of your choice (Onshape for this case)
- Define all the regions in the CAD-program (solid, shell, tube for this case)
NOTE: Entire model should be *fully* defined with these regions and nothing else
- Export each region separately as a .STEP file
- Open Salome and enter the **Geometry** module
- **Import** all three regions to Salome
- **Partition** all the three regions into one compound and name them accordingly (FullKSHeX for this case)
- **Explode** the compound into **Solids** and rename the solids to their appropriate names (3 regions to rename in this step: 'solid', 'shell', 'tube' for this case)

- Right click each region and click **Create group** and select **Faces** (icon of plane) using the scheme outlined below. Remember to name all the groups according to a name convention that you will later use in OpenFOAM:
 - 'solid':
 - external:
Main shape is 'solid'. Click all the external faces (while holding Ctrl + shift for multiple selection), i.e., the faces that only have an interface to the outside. This is the only step requiring multiple selections from the model itself. When done, hit **Hide selected** to see that you have selected all the correct faces. If correct, hit **Add** and **Apply**. If any face is missing, simply click that face and hit **Add** until all the correct faces are selected.
 - solid_to_shell:
Main shape is 'solid', then hit **Only Sub-shapes of the second shape**, hit the box that becomes highlighted and click on 'shell' in the **Object browser**. Hit **Select all**, **Add** and **Apply**.
 - solid_to_tube:
 Same procedure as previous, but the second shape is now 'tube'.
 - 'shell':
 - inletShell:
Main shape is now 'shell'. Identify the inlet face for the shell in the model, hit **Add**, click **Apply**.
 - outletShell:
 Same procedure as inletShell but select the outlet.
 - shell_to_solid:
Select all, then in the **Object browser**, expand the shell group and while holding Ctrl select only the inletShell and outletShell that's just been created. Hit **Remove** in the **Create group** window and **Apply**.
 - 'tube':
 - inletTube:
Main shape is now 'tube'. Same as for shell but with tube inlet
 - outletTube:
 Same as above but with tube outlet
 - tube_to_solid:
 Same procedure as for shell_to_solid, i.e., **Select all** and **Remove** inletTube and outletTube in the **Object browser**.

After all these steps your **Object browser** should look like this (ignore "wallShell" and "wallTube", they are not needed):

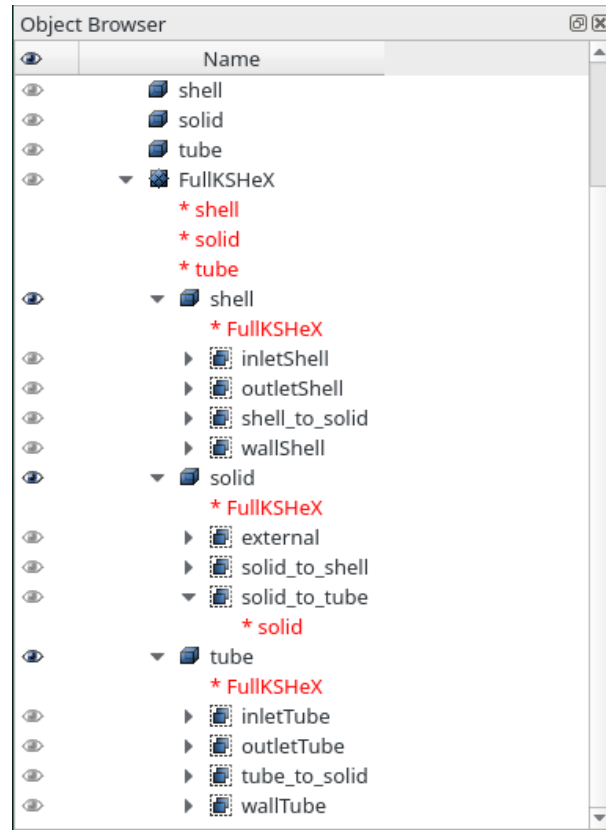


Figure 11.2 *Object browser* after all groups on geometry have been created.

Now let us get to meshing

- Go to the **Meshing** module
- Go to **Mesh** at the top menu bar and hit **Create mesh**
- For the **Geometry**, click the box and click the full partitioned model (named “FullKSHex” in this case, the compound in the **Object browser** that is the parent to all the things created thus far)
- Navigate to the **2D** tab (we are only creating a surface mesh at this step) and hit the **Algorithm** drop-down menu, select **NETGEN 1D-2D**
- Click the icon to the left of **Hypothesis** that looks like a gear and click **NETGEN 2D Parameters**. These parameters can be edited by clicking the triangle icon next to the gear icon.
- Hit **Apply and close**, and then right click the mesh in the **Object browser** and hit **Compute**.

This is just a surface mesh so far; we are going to create the rest of the mesh by making sub-meshes on all the relevant regions. The mesh should be 2D over the entire region. If it is too coarse, go back and edit the parameters by right clicking the mesh just created in the **Object browser** and hit **Edit mesh**. Navigate to the **2D** tab and hit the gear with a triangle. Edit the values, hit **Apply and close** and then **Compute** the mesh again from the **Object browser**.

Next, we will be creating the groups of faces and groups of volumes that will show up in the **Mesh** drop-down menu in the **Object browser**. These groups of faces and volumes will also show up as named in your OpenFOAM project, so remember to follow the name convention that OpenFOAM sets up or define your own name convention; just be consistent! The naming-scheme used in this guide is part of a case that has been used successfully in a multiregion CHT.

- Make sure you are in the meshing module, right click the 2D mesh just created and hit **Create group**.
- In **Elements type** hit **Face**.
- In **Group type** hit **Group on geometry**, then click the box that appears beneath and select each group in the **Object browser** previously created in the **Geometry** module.
- **Name** all the groups with the appropriate names just by using Ctrl + C, Ctrl + V. For example, “inletShell” should look like this:

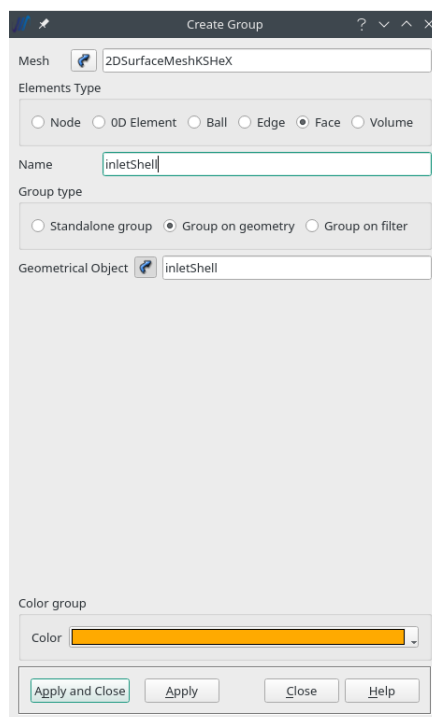


Figure 11.3 Mesh group creation, inletShell as example.

- Do this for all the groups of Faces.
- For the volumes, select **Volume** in the **elements type** and click each of the three volume regions (shell, solid and tube for this case)

When done with this, your **object browser** should look like this (again, ignore “wallShell” and “wallTube”):

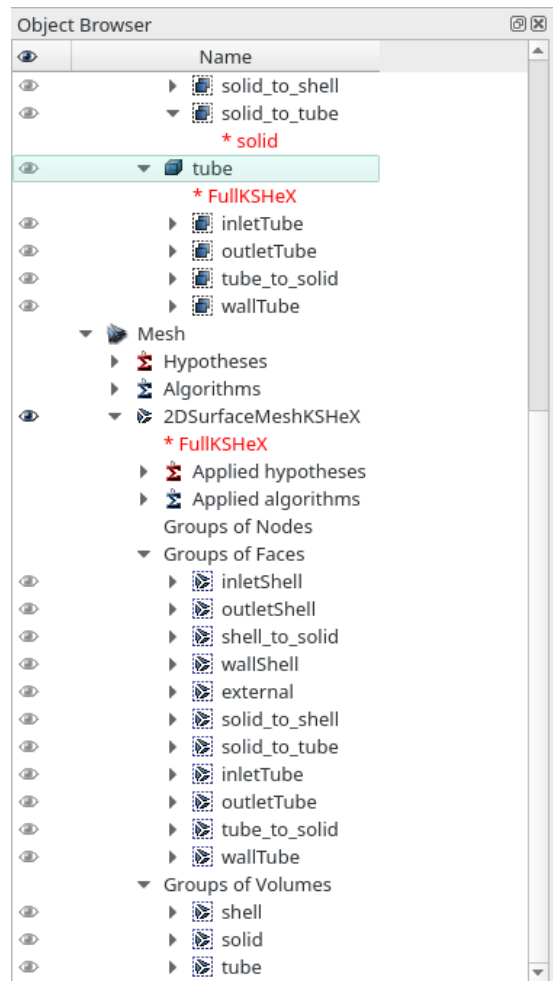


Figure 11.4 Groups of faces and groups of volumes in the **Object browser**.

Now we are creating the **Sub-meshes** which will be 3D, based on the 2D surface mesh so that all the elements fit together. We are going to end up with a main 2D mesh and 3 sub-meshes which all are 3D.

- Make sure you are still in the meshing module
- Right click your main mesh (the 2D surface mesh) in the **Object browser** and click **Create sub-mesh**. **Mesh** should be the 2D surface mesh and in the **Geometry** box you want to select each region from the **Object browser** under the geometry section. I usually start with the solid since that is where the thinnest parts are located for my model.
- For **Mesh type** I usually go with **Tetrahedral**. You want to stay in the **3D** tab and click the **Algorithm** drop-down menu. Select **NETGEN 3D**, and then for **Hypothesis** you hit the gear next to the drop-down menu and select **NETGEN 3D Parameters**. Edit the parameters as you see fit. They will be based on the 2D mesh, which will have to be quite fine. After you have specified your parameters, the dialogue box should look like this now:

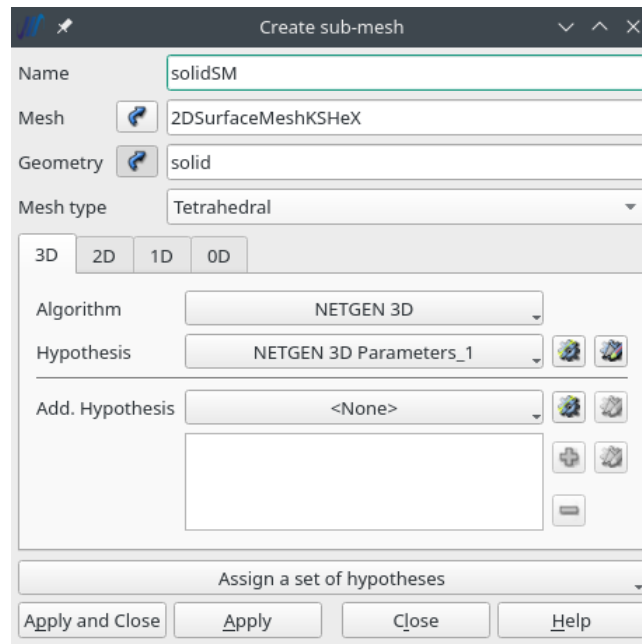


Figure 11.5 Sub-mesh creation.

- Hit **Apply** and then right click the newly created sub-mesh in the **Object browser** and hit **Compute**. If this step does not work, you need to refine the 2D surface mesh since it will act as a bound on how large or small the 3D elements will be. At this step, my model looks like this:

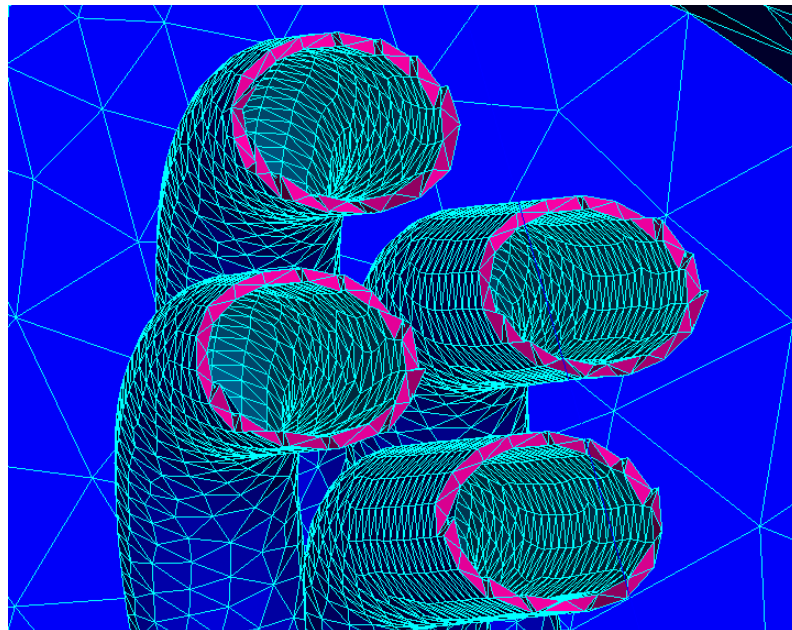


Figure 11.6 Section view of sub-mesh computed for the solid region.

Blue elements are my 2D surface mesh, pink elements are my newly defined sub-mesh for the solid. So far, the thickness of these tubes together with the mesh parameters only allows for one cell. This might have to be refined, which means that the 2D mesh needs to be refined first. This process is very

iterative, and you want to go back and forth editing the parameters until it looks fine for the purposes of your simulation.

To get a clipping, just right click anywhere at the model while in the meshing module, hit **Clipping** then **New** then **Absolute** and then **Apply and close**. This creates a slanted section view through the entire model. You can of course change the clipping plane to be in whatever orientation/location you want.

- Right click the main 2D surface mesh and hit **Create sub-mesh**. Click the box next to **Geometry** and click the shell from **Object browser** under the **Geometry** section
- Apply the same steps as for the solid parts with **NETGEN 3D** and input your relevant parameters
- Hit **Apply and close** and **Compute** the newly created sub-mesh. If it looks good, we can proceed with the boundary layers
- Right click the sub-mesh for the shell and click on the little gear icon next to the **Add. Hypothesis** drop down menu. Click **Viscous layers** and a new dialogue box appears.
- Specify **Total thickness** (in m), **Number of layers** (I usually go for 3) and **Stretch factor** (I usually go for 1.2).
- Identify the relevant inlets and outlets (for this case the inletShell and outletShell previously defined in the geometry section in the **Object browser**). Click them and hit **Add** and then **Apply and close**.
- **Recompute** this sub-mesh (which should now have a yellow warning-triangle in the **Object browser** since you have changed the parameters of the sub-mesh). Inspect the results and see that the boundary layers were added in the correct places and that the thickness looks fine.
- Do the same for the last region (in this case tube)
- With boundary layers for the tube and the shell side my meshing looks like this, zoomed in on one of the tubes:

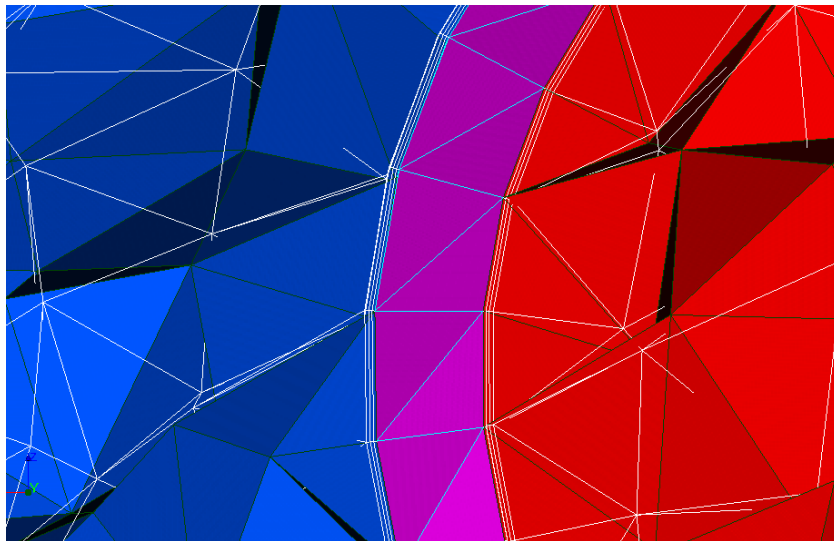


Figure 11.7 Section view of meshed boundary layers in test model.

If everything looks satisfactory, then right click the main mesh (not the sub-meshes) in the **Object Browser** and hit **export** and select UNV format. All the other sub-meshes are children underneath the main mesh, so we only have to export one file from Salome.

- In OpenFOAM there is a command called “ideasUNVtoFoam” which converts the mesh to a format OpenFOAM can understand. The names you’ve defined in Salome should all be in OpenFOAM.

To change the colours of the regions, just click the sub-mesh you want to edit in the **Object browser** and right click anywhere on the model view. Click **Properties** and in the dialogue box that pops up you can edit all the colours.

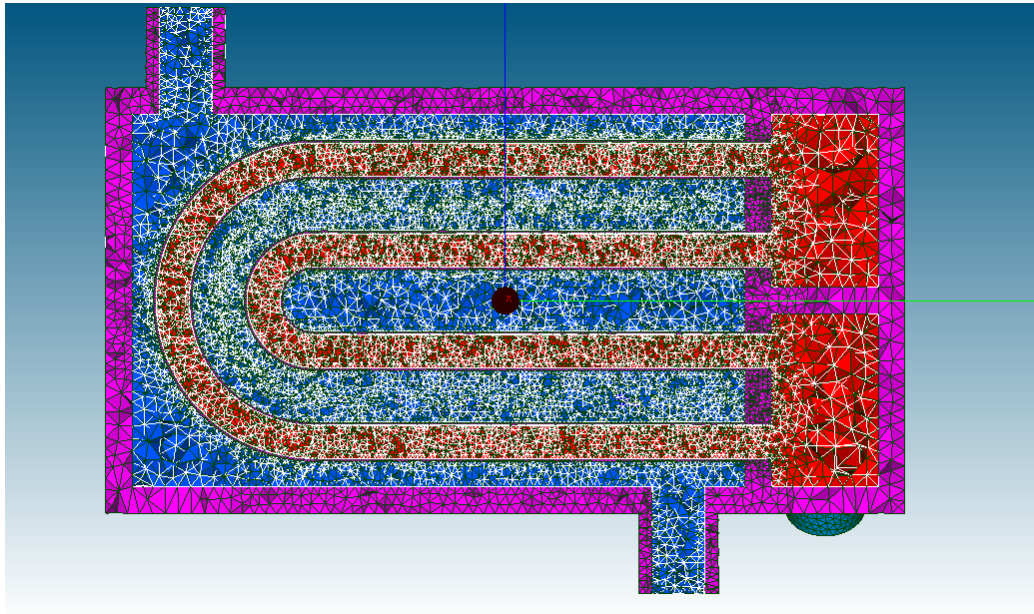


Figure 11.8 Section view of test model, fully meshed with the procedures outlined in this appendix.

APPENDIX IV

12 Appendix IV: Code

12.1 Salome script - mesh quality

Open Salome and run this script to do a mesh quality check. The script checks max and average quantities of skewness and aspect ratio. Code produced by Salome user 'Ludwig Wurstbrot'. Code compatible with Salome_meca 2019.0.3_LGPL.

```
import salome
import SMESH, SALOMEDS
from salome.smesh import smeshBuilder

salome.salome_init()
smeshObj = smeshBuilder.New(salome.myStudy)
unvMesh=smeshObj.CreateMeshesFromUNV(r'/directory_of_your_unv_file.unv')

faces = unvMesh.GetElementsByType(SMESH.FACE)
aspectRatios = []
skews=[]
nonortho=[]
qualityControl=[]

# aspect Ratio
for face in faces:
    aspectRatios.append(unvMesh.GetAspectRatio(face))

ratioSum = 0
for ratio in aspectRatios:
    ratioSum += ratio
averageAspectRatio = ratioSum / len(aspectRatios)
maxAspectRatio = max(aspectRatios)

qualityControl.append(['average aspect ratio',averageAspectRatio])
qualityControl.append(['maximum aspect ratio',maxAspectRatio])

# Skewness
for face in faces:
    skews.append(unvMesh.GetSkew(face))

skewSum=0
for skew in skews:
    skewSum += skew
averageSkew = skewSum / len(skews)
maxSkew = max(skews)

qualityControl.append(['average skew',averageSkew])
qualityControl.append(['maximum skew',maxSkew])

# Non-orthogonality
for face in faces:
    skews.append(unvMesh.GetSkew(face))
```

```

skewSum=0
for skew in skews:
    skewSum += skew
averageSkew = skewSum / len(skews)
maxSkew = max(skews)

qualityControl.append(['average skew',averageSkew])
qualityControl.append(['maximum skew',maxSkew])

print(qualityControl)

```

12.2 Octave scripts

The scripts run in Octave have been produced by the author of this thesis.

12.2.1 ideasUnvToFoam - cell count vs execution time for meshes of different size

```

clc, clear all, close all
%% ideasUnvToFoam: execution time vs. cell count

%% Data
% Four models: small, medium, mediumlarge and large
% Template: name = [time, cells];
small    = [59.496, 489853];
medium   = [2*60+21.983, 858823];
mediumLarge = [19*60+38.950, 2919528];
large    = [583*60+48.750, 29861708];
PHeX     = 70e6; % cell count of Primary Heat Exchanger
radiator = 120e6; % cell count of radiator
time     = [small(1), medium(1), mediumLarge(1), large(1)];
cells    = [small(2), medium(2), mediumLarge(2), large(2)];

%% Fitting
p = polyfit(log(cells), log(time), 1);
x1 = 0:100:2e8;
y1 = exp(p(2))*x1.^p(1);
PHeXTime = exp(p(2))*PHeX.^p(1)
radiatorTime = exp(p(2))*radiator.^p(1)
%% Plot
fontsize = 15;
figure
loglog(cells, time, 'r*');
hold on
grid on
loglog(x1, y1);
plot(PHeX, PHeXTime, '*g');
plot(radiator, radiatorTime, '*b');
title('ideasUnvToFoam: Execution time vs. Cell count', 'fontsize', fontsize);
ylabel('Execution time, t [s]', 'fontsize', fontsize);
xlabel('Cell count, n [-]', 'fontsize', fontsize);
xlim([1e5, 2e8]);
ylim([1, 4e5]);
legend('Salome Data', 'exponential fit', 'PHeX estimation', 'radiator estimation', ...
'location', 'southeast', 'fontsize', 20);
annotation('textarrow', [0.5 0.41], [0.45 0.48], 'string', ['slope: ', num2str(floor(p(1)*100)/100)], 'fontsize', fontsize)

radiatorTimeInDays = radiatorTime/(60*60*24);

```

```
PHeXTimeInDays = PHeXTime/(60*60*24);
```

12.2.2 Water tests for the primary heat exchanger

```
clc, clear all, close all;
```

```
%% Conversion factors
```

```
conv1 = 15850; % m³/s -> gpm
```

```
conv2 = 3.345526e-4; % kPa -> feet fluid (water)
```

```
% Flow rate data (m³/s)
```

```
fuelin = [0.05047, 0.06309, 0.1041];
```

```
coolantin = [0.03533, 0.04732, 0.05994];
```

```
% Fluid head loss (Pa) <-- Simscape
```

```
fuelout = [8.4e4, 1.32e5, 3.55e5];
```

```
coolantout = [4.4e4, 7.3e4, 1.2e5];
```

```
% Converting data
```

```
% Flow rate
```

```
fuelin = fuelin*conv1;
```

```
coolantin = coolantin*conv1;
```

```
% Pressure drop
```

```
coolantout = coolantout*conv2;
```

```
fuelout = fuelout*conv2;
```

```
% Extracting coefficients
```

```
coefficientsFuel = polyfit(log(fuelin),log(fuelout),1);
```

```
coefficientsCoolant = polyfit(log(coolantin),log(coolantout),1);
```

```
slopeFuel = coefficientsFuel(1);
```

```
slopeCoolant = coefficientsCoolant(1);
```

```
% Plotting data
```

```
loglog(fuelin,fuelout/2,"-*",coolantin,coolantout,"-r");
```

```
grid on;
```

```
axis([200,6000,10,150]);
```

```
title("Head loss in PHeX");
```

```
xlabel("Flow rate (gpm)");
```

```
ylabel("Fluid frictional head loss (ft water)");
```

```
legend("Fuel","Coolant");
```

```
h=get(gcf, "currentaxes");
```

```
set(h, "fontsize", 20, "linewidth", 2);
```

```
ta1 = annotation("textbox", [48 .25 .1 .2], "string", ["Slope = ", num2str(slopeFuel)], "fontsize", 20, "linestyle", "none");
```

```
ta2 = annotation("textbox", [24 .25 .1 .2], "string", ["Slope = ", num2str(slopeCoolant)], "fontsize", 20, "linestyle", "none");
```

```
ta3 = annotation("textbox", [57 .5 .1 .2], "string", "Shell side", "fontsize", 20, "linestyle", "none");
```

```
ta4 = annotation("textbox", [38 .5 .1 .2], "string", "Tube side", "fontsize", 20, "linestyle", "none");
```

13 References

- Ahrens, J., Geveci, B., & Law, C. (2005). *ParaView: An End-User Tool for Large-Data Visualization*, *Visualization handbook*. Elsevier. doi:10.1016/B978-012387582-2/50038-1
- Alfa Laval. (2004). *Plate heat exchanger calculation method*. Alfa Laval. Retrieved from Alfalaval.com: <https://www.alfalaval.com/globalassets/documents/local/united-states/hvac/the-theory-behind-heat-transfer.pdf>
- Alter, S. J. (2004). Structured Grid Quality Measure for Simulated Hypersonic Flows. *42nd AIAA Aerospace Sciences Meeting and*. 42. Virginia: NASA. doi:10.2514/6.2004-612
- AMS. (2012, 04 25). *Kolmogorov Microscale*. Retrieved from American meteorological society: https://glossary.ametsoc.org/wiki/Kolmogorov_microscale
- Anderson, J. D. (2009). *Computational Fluid Dynamics* (3rd ed.). Berlin: Springer-Verlag. Retrieved 03 17, 2021, from <https://www.eng.auburn.edu/~tplacek/courses/fluidsreview-1.pdf>
- Annaratone, D. (2010). *Handbook for Heat Exchangers and Tube Banks design* (1 ed.). Springer-Verlag Berlin Heidelberg. doi:10.1007/978-3-642-13309-1
- ANSYS. (2008). Reporting Mesh Statistics. In *ANSYS user guide*. ANSYS. Retrieved from <https://romeo.univ-reims.fr/documents/fluvent/tgrid/ug/chp15.pdf>
- ANSYS. (2009, January 29). *afs.enea*. Retrieved from Mesh Quality: <https://www.afs.enea.it/project/neptunius/docs/fluvent/html/ug/node167.htm>
- Atomic Energy Commission . (1959). *Report of the fluid fuel reactors task force*. United States Atomic Energy Commission . Atomic Energy Commission. Retrieved 03 11, 2021, from <https://digital.library.unt.edu/ark:/67531/metadc784245/>
- Banihani, E., & Assad, M. E. (2018, February). Boundary-Layer Theory of Fluid Flow past a Flat-Plate: Numerical Solution using MATLAB. *International Journal of Computer Applications*, 180(18). doi:10.5120/ijca2018916374
- Best, R., & Burke, P. J. (2018, July 1). Adoption of solar and wind energy: The roles of carbon pricing and aggregate policy support. *Energy Policy*, 404-417. doi:<https://doi.org/10.1016/j.enpol.2018.03.050>
- Bettis, E. S., Schroeder, R. W., Cristy, G. A., Savage, H. W., Affel, R. G., & Hemphill, L. F. (1957, June 18). The Aircraft Reactor Experiment-Design and Construction. *Nuclear science and engineering*(2), pp. 804-825. doi:10.13182/NSE57-A35495
- Brennen , C. E. (2006, June 10). *An Internet book on fluid dynamics - Reynolds stresses*. Retrieved from brennen.caltech: <http://brennen.caltech.edu/fluidbook/basicfluidynamics/turbulence/reynoldsstresses.pdf>
- Brocchini, M. (2013). *A reasoned overview on Boussinesq-type models: the interplay between physics, mathematics and numerics*. The royal society. Ancona, Italy: Royal society publishing. doi:10.1098/rspa.2013.0496
- Buongiorno, J., Corradini, M., Parsons, J., & Petti, D. (2019). *The Future of Nuclear Energy in a Carbon-Constrained World*. Massachusetts Institute of Technology, Department of Nuclear Science and Engineering. Institute of Electrical and Electronics Engineers (IEEE). Retrieved 02 06, 2021, from <https://dspace.mit.edu/handle/1721.1/126750>
- Carbon Brief Ltd. (2020, March 26). *Mapped: The world's coal power plants*. Retrieved 02 06, 2021, from <https://www.carbonbrief.org/mapped-worlds-coal-power-plants>
- Celik, I., Karaismail, E., & Parsons, D. (2007). A Reliable Error Estimation Technique for CFD Applications. *Computational Uncertainty in military vehicle design*, 32.1-32.20. Retrieved from <https://www.sto.nato.int/publications/STO%20Meeting%20Proceedings/RTO-MP-AVT-147/MP-AVT-147-32.pdf>

- CFD-Online. (2011, March 08). *CFD-Online*. Retrieved from Wilcox's k-omega model: https://www.cfd-online.com/Wiki/Wilcox%27s_k-omega_model
- CFD-Online. (2014, December 16). *Standard K-epsilon model*. Retrieved from cfd-online: https://www.cfd-online.com/Wiki/Standard_k-epsilon_model
- CFD-online. (2014, January 14). *Turbulence free-stream boundary conditions*. Retrieved from CFD-online: https://www.cfd-online.com/Wiki/Turbulence_free-stream_boundary_conditions
- CFD-Online. (2021, January 03). *CFD-Online*. Retrieved from Boussinesq eddy viscosity assumption: https://www.cfd-online.com/Wiki/Boussinesq_eddy_viscosity_assumption
- CFD-online. (2021, February 19). *Turbulence modelling*. Retrieved from cfd-online: https://www.cfd-online.com/Wiki/Turbulence_modeling
- Colebrook, C. F., & White, C. M. (1937). *Experiments with Fluid Friction in Roughened Pipes*. London: Imperial College, London. Retrieved from <https://royalsocietypublishing.org/doi/pdf/10.1098/rspa.1937.0150>
- Coleman, N. (2010). *A Derivation of the Navier-Stokes Equations*. Mathematics Exchange. Retrieved 03 17, 2021, from <https://cardinalsolar.bsu.edu/handle/123456789/202368>
- Courant, R., Friedrichs, K., & Lewy, H. (196, March). On the Partial Difference Equations of Mathematical Physics. *IBM Journal of Research and Development*, 11(2), 215-234. doi:10.1147/rd.112.0215
- Craft, T. J., Launder, B. E., & Suga, K. (1996). Development and application of a cubic eddy-viscosity model of turbulence. *International Journal of Heat and Fluid Flow*, 17(2). doi:10.1016/0142-727X(95)00079-6
- Davidson, L. (2018). *An introduction to turbulence models*. Chalmers University of Technology, Department of thermo- and fluid dynamics. Gothenburg: Chalmers. Retrieved from http://www.tfd.chalmers.se/~lada/postscript_files/kompendum_turb.pdf
- Dayman, K. J., Biegalski, S., & Haas, D. (2014, 01). Determination of Short-Lived Fission Product Yields with Gamma Spectrometry. *Journal of Radioanalytical and Nuclear Chemistry*. doi:10.1007/s10967-015-3993-9
- Defraeye, T., Blocken, B., & Carmeliet, J. (2011). An adjusted temperature wall function for turbulent forced convective heat transfer for bluff bodies in the atmospheric boundary layer. *Building and Environment*, 46(11), 2130-2141. doi:10.1016/j.buildenv.2011.04.013
- Driest, E. R. (1956). *On Turbulent Flow Near a Wall*. North America Aviation, inc. doi:10.2514/8.3713
- dschroeder. (2019). *Simscale*. Retrieved from https://www.simscale.com/users/dschroeder/#_ga=2.201818385.166409318.1616415308-902599676.1613662336#viewMode=thumbView&sortBy=project_popular
- Durmayaz, A., & Yavuz, H. (2001, 05). Exergy analysis of a pressurized-water reactor nuclear-power plant. *Applied Energy*, 69, 39-57. doi:10.1016/S0306-2619(00)00071-4
- Eaton, J. W. (2002). *GNU Octave Manual*. Network Theory Limited. Retrieved from <https://www.gnu.org/software/octave/>
- Electricitymap. (2021, 02). *Electricitymap*. Retrieved from <https://www.electricitymap.org/map>
- Electricitymap.org. (2021). *Electricitymap*. (E. Holms, Producer) Retrieved from Electricitymap.org: <https://www.electricitymap.org/map>
- Energy.gov. (2021, 01 22). *Energy.gov*. Retrieved 02 13, 2021, from How does a nuclear reactor work?: <https://www.energy.gov/ne/articles/nuclear-101-how-does-nuclear-reactor-work>
- Engineering Toolbox. (2004). *Laminar, transitional or turbulent flow*. Retrieved from engineeringtoolbox.com: https://www.engineeringtoolbox.com/laminar-transitional-turbulent-flow-d_577.html

- Free Software Foundation. (n.d.). *Free learning resources*. Retrieved from sarata: <https://mirrors.sarata.com/>
- George, W. K. (2013). *Lectures in turbulence for the 21st century*. Gothenburg: Chalmers. Retrieved from <http://citeseerx.ist.psu.edu/viewdoc/download?doi=10.1.1.454.2548&rep=rep1&type=pdf>
- Gonçalves, L. C., Maiorino, J. R., Monteiro, D. B., & Rossi, P. C. (2019). A REVIEW OF THORIUM UTILIZATION IN MOLTEN SALT REACTORS: CONCEPTS, TECHNOLOGY AND CALCULATION METHODOLOGIES. *International Nuclear Atlantic Conference*. Santos. Retrieved 03 11, 2021, from https://www.researchgate.net/publication/336826108_A_REVIEW_OF_THORIUM_UTILIZATION_IN_MOLTEN_SALT_REACTORS_CONCEPTS_TECHNOLOGY_AND_CALCULATION_METHODOLOGIES
- Greenshields, C. J. (2015, 05 21). OpenFOAM user guide. *OpenFOAM the open source CFD toolbox*. Retrieved from OpenFOAM.com: http://www.thevisualroom.com/_files/UserGuide.pdf
- GUS. (2019, November). Energy statistics in 2017 and 2018. *Energy statistics*. Retrieved 02 06, 2021, from <https://stat.gov.pl/en/topics/environment-energy/energy/energy-statistics-in-2017-and-2018,4,14.html>
- Haubenreich, P. N., & Engel, J. R. (1970). MSRE experience. *Nuclear applications and technology*, 8(2). doi:10.13182/NT8-2-118
- Hazra, S. (2020, December 03). *Literature review - RANS derivation analysis*. Retrieved 03 17, 2021, from skill-lync: <https://skill-lync.com/projects/week-8-literature-review-rans-derivation-and-analysis-34>
- Henningson, D. S., & Berggren, M. (2005). *Fluid dynamics: theory and computation*. KTH, Department of Mechanics and the department of Numerical Analysis and Computer Science (NADA). Stockholm: KTH. Retrieved from <https://windharvest.com/wp-content/uploads/2017/03/Fluid-Dynamics-Theory-and-Computation-Dan-S.-Henningson-Martin-Berggren-24-August-2005.pdf>
- Hess, J. L., & Smith, A. M. (1967). *Calculation of potential flow about arbitrary bodies*. Long Beach, California: Elsevier Ltd. doi:[https://doi.org/10.1016/0376-0421\(67\)90003-6](https://doi.org/10.1016/0376-0421(67)90003-6)
- IAEA. (2007). *Fissile material management strategies for sustainable nuclear energy*. Austria: International Atomic Energy Agency. Retrieved 02 06, 2021, from https://www-pub.iaea.org/MTCD/publications/PDF/P1288_web.pdf
- IAEA. (2016). *Climate change and nuclear power 2016*. Vienna: IAEA. Retrieved 02 06, 2021, from <https://www-pub.iaea.org/MTCD/Publications/PDF/CCANP16web-86692468.pdf>
- IAEA. (2017). *International Status and Prospects for Nuclear Power 2017*. IAEA. Retrieved 02 06, 2021, from https://www.iaea.org/sites/default/files/gc/gc61inf-8_en.pdf
- IAEA. (2020, January 01). *Preliminary Nuclear Power Facts and Figures for 2019*. (S. Krikorian, Editor) Retrieved 02 06, 2021, from iaea: <https://www.iaea.org/newscenter/news/preliminary-nuclear-power-facts-and-figures-for-2019>
- IEA. (2020, August). *iea*. Retrieved from <https://www.iea.org/reports/key-world-energy-statistics-2020>
- Iowa State University. (2016). *Stress and strain*. (I. S. University, Producer) Retrieved 03 17, 2021, from nde-ed: <https://www.nde-ed.org/Physics/Materials/Mechanical/StressStrain.xhtml>
- Jackson, J. D., & Launder, B. (2006). *Osborne Reynolds and the Publication of His Papers on Turbulent Flow*. University of Manchester. Manchester: Annual Review of Fluid Mechanics. doi:10.1146/annurev.fluid.39.050905.110241
- Jasak, H. (1996). *Error Analysis and Estimation for the Finite Volume Method With Applications to Fluid Flows*. Imperial College of science, technology and medicine, Mechanical engineering. London: Imperial College. Retrieved from https://www.researchgate.net/publication/230605842_Error_Analysis_and_Estimation_for_the_Finite_Volume_Method_With_Applications_to_Fluid_Flows
- Jones, W. P., & Launder, B. E. (1972, February). The prediction of laminarization with a two-equation model of turbulence. *International Journal of Heat and Mass Transfer*, 15(2), 301-314. doi:10.1016/0017-9310(72)90076-2

- Launder, B. E., & Sharma, B. I. (1974, November). Application of the energy-dissipation model of turbulence to the calculation of flow near a spinning disc. *Letters in Heat and Mass Transfer*, 1(2), 131-137. doi:10.1016/0094-4548(74)90150-7
- Lecce, F. D. (2018). *Neutronic and thermal-hydraulic simulations for Molten Salt Fast Reactor safety assessment*. Creative Commons Attribution. Retrieved 03 19, 2021, from <https://webthesis.biblio.polito.it/7831/1/tesi.pdf>
- Liu, F. (2017). *A Thorough Description Of How Wall function are implemented in OpenFOAM*. Chalmers university. Gothenburg: Chalmers. Retrieved from http://www.tfd.chalmers.se/~hani/kurser/OS_CFD_2016/FangqingLiu/openfoamFinal.pdf
- MacPherson , H. G. (1985). *The Molten Salt Reactor Adventure*. Nuclear Science and Engineering. doi:<https://doi.org/10.13182/NSE90-374>
- Manzano-Agugliaro, F., Alcayde, A., Montoya, F. G., Zapata-Sierra, A., & Gil, C. (2013). *Scientific production of renewable energies worldwide: An overview*. Almería: Pergamon. doi:<https://doi.org/10.1016/j.rser.2012.10.020>
- Mårtensson, G., Karlsson, G., Tornblom, O., Stromer, F., & Andersson, R. (2021, 03). Conversations with experts in CFD. Sweden.
- McCoy, H. E. (1969, 01 01). The inor-8 story. *Oak Ridge Nat. Lab., No. 2*(Rev. 3), 35-48. doi:OSTI: 4766202
- McGinty, B. (2012, February). *Tensor Notation (Basics)*. Retrieved from [continuummechanics.org: http://www.continuummechanics.org/tensornotationbasic.html](http://www.continuummechanics.org/tensornotationbasic.html)
- Menter, F. R. (1992). *Improved two equation k-omega turbulence models for aerodynamic flows*. NASA, Ames Research Center. NASA. Retrieved 03 19, 2021, from <https://ntrs.nasa.gov/api/citations/19930013620/downloads/19930013620.pdf?attachment=true>
- Menter, F. R. (1994, August). Two-equation eddy-viscosity turbulence models for engineering applications . *AIAA*, 32(8). doi:10.2514/3.12149
- Menter, F., Kuntz, M., & Langtry, R. B. (2003, January). Ten years of industrial experience with the SST turbulence model. *Heat and Mass Transfer*, 4. Retrieved from https://www.researchgate.net/publication/228742295_Ten_years_of_industrial_experience_with_the_SST_turbulence_model
- Mittal, S. (2000, July 21). On the performance of high aspect ratio elements for incompressible flows. *Computer Methods in Applied Mechanics and Engineering*, 188(1-3), 269-287. doi:10.1016/S0045-7825(99)00152-8
- Modir-Khazeni, S. M., & Trelles, J. (2015). Towards a Comprehensive Modelling and Simulation Approach for Turbulent Nonequilibrium Plasma Flows. *International symposium of plasma chemistry*. Antwerp: University of Massachusetts. Retrieved from https://www.researchgate.net/publication/275351834_Towards_a_Comprehensive_Modelling_and_Simulation_Approach_for_Turbulent_Nonequilibrium_Plasma_Flows
- Mohanty , S., & Arora, R. (2020, June). CFD Analysis of a Shell and Tube Heat Exchanger with Single Segmental Baffles. *International Journal of Automotive and Mechanical Engineering* , 17, 7890-7901. doi:10.15282/ijame.17.2.2020.08.0589
- Moin, P., & Mahesh, K. (1998, January). DNS: A tool in turbulence research. *annual review of fluid mechanisc*, 30, pp. 539-578.
- Murad, J. (2018, May). *What is y+ (yplus)?* Retrieved 03 20, 2021, from [Simscale: https://www.simscale.com/forum/t/what-is-y-plus/82394](https://www.simscale.com/forum/t/what-is-y-plus/82394)
- NASA. (2020, August 28). NASA Turbulent Flat Plate Validation Benchmark using TCFD. NASA. Retrieved from <https://turbmodels.larc.nasa.gov/flatplate.html>

- Nuclear-Power. (2021). *Reynolds number for pipe flow*. Retrieved 03 17, 2021, from Nuclear-Power: <https://www.nuclear-power.net/nuclear-engineering/fluid-dynamics/reynolds-number/reynolds-number-for-pipe-flow/>
- Oak Ridge National Laboratory. (2017, November 7). Overview of fuel and coolant salt chemistry and thermal hydraulics. Oak Ridge: ORNL. Retrieved from <https://www.nrc.gov/docs/ML1733/ML17331B115.pdf>
- Okui, S., & Sekimoto, H. (2009). Research and development of software for visualizing nuclear reactor and neutronics analysis. *ICAPP*. doi:10.13140/2.1.3077.1207
- Onshape. (2014). Onshape incorporated. Retrieved from <https://www.onshape.com/en/>
- OpenFOAM. (2004). *OpenFOAM documentation*. Retrieved 03 17, 2021, from openfoam: <https://www.openfoam.com/documentation/>
- OpenFOAM. (2006). *ideasUnvToFoam*. Retrieved from OpenFOAM.com: <https://www.openfoam.com/documentation/guides/latest/man/ideasUnvToFoam.html>
- OpenFOAM. (2011). OpenFOAM.org. Retrieved from <https://openfoam.org/>
- OpenFOAM. (2017). *Mesh-wave wall distance*. Retrieved from OpenFOAM.com: <https://www.openfoam.com/documentation/guides/latest/doc/guide-schemes-wall-distance-meshwave.html>
- OpenFOAMwiki. (2006). *ChtMultiRegionFoam*. Retrieved from openfoamwiki: <https://openfoamwiki.net/index.php/ChtMultiRegionFoam>
- ORNL-2465. (1960). *Termination report for construction of the ART facility*. Oak Ridge: Oak Ridge National Laboratory. Retrieved 03 12, 2021, from <https://www.google.com/search?q=ORNL+2465&ie=utf-8&oe=utf-8&aq=t>
- ORNL-3014. (1960). *Molten salt reactor program quarterly progress report for period ending july 31, 1960*. Oak Ridge: Oak Ridge National Laboratory. Retrieved 03 17, 2021, from <https://moltensalt.org/references/static/downloads/pdf/ORNL-3014.pdf>
- ORNL-3122. (1961). *Molten salt reactor program progress report from August 1, 1960 to February 28, 1961*. Oak Ridge National Laboratory. Oak Ridge: ORNL. Retrieved from <http://thmfgrcs.homestead.com/ORNL-3122.pdf>
- ORNL-3122. (1971). *Molten salt reactor program semiannual progress report for period ending february 28, 1971*. Oak Ridge: Oak Ridge National Laboratory. Retrieved 03 17, 2021, from <https://www.osti.gov/servlets/purl/4743040>
- ORNL-3215. (1961). *Molten salt reactor program progress report, for period from March 1 to August 31, 1961*. Oak Ridge National Laboratory. Oak Ridge: ORNL. Retrieved from <http://www.thmfgrcs.com/ORNL-3215.pdf>
- ORNL-3303. (1971). *Further development of instrumentation and controls development needed for the Molten Salt Breeder Reactor (MSBR)*. Oak Ridge National Laboratory. Oak Ridge: ORNL. Retrieved from <https://energyfromthorium.com/pdf/ORNL-TM-3303.pdf>
- ORNL-3369. (1962). *Molten salt reactor program semiannual progress report for period ending August 31, 1962*. Oak Ridge National Laboratory. Oak Ridge: ORNL. Retrieved from <https://moltensalt.org/references/static/downloads/pdf/ORNL-3369.pdf>
- ORNL-3419. (1963). *Molten salt reactor program, semiannual progress report for period ending January 3, 1963*. Oak Ridge National Laboratory. Oak Ridge: ORNL. doi:10.2172/4692918
- ORNL-3500. (1963). *Fabrication of the heat exchanger tube bundle for the MSRE*. Oak Ridge National Laboratory. Oak Ridge: ORNL. Retrieved from <https://github.com/openmsr/msr-archive/blob/master/docs/ORNL-3500.pdf>
- ORNL-3708. (1964). *MSRE reactor program semiannual report for period ending july 31, 1964*. Oak Ridge: Oak Ridge National Laboratory. Retrieved 03 17, 2021, from <https://technicalreports.ornl.gov/1964/3445600500358.pdf>

- ORNL-4037. (1967). *Molten salt reactor program semiannual progress report for period ending August 31, 1966*. Oak Ridge National Laboratory. Oak Ridge: ORNL. Retrieved from <https://moltensalt.org/references/static/downloads/pdf/ORNL-4037.pdf>
- ORNL-4119. (1967). *Molten-salt reactor program, semiannual progress report for period ending february 28, 1967*. Oak Ridge: ORNL. Retrieved from <https://moltensalt.org/references/static/downloads/pdf/ORNL-4119.pdf>
- ORNL-4344. (1969). *Molten salt reactor program semiannual progress report for period ending August 31, 1968*. Oak Ridge National Laboratory. Oak Ridge: ORNL. Retrieved from <https://moltensalt.org/references/static/downloads/pdf/ORNL-4344.pdf>
- ORNL-CF-60-11-108. (1960). *ORNL-CF-60-11-108 MSRE Radiator design*. Oak Ridge: Oak Ridge National Laboratory. Retrieved 03 17, 2021
- ORNL-CF-70-9-3. (1970). *Critique of the MSRE: A collection of comments submitted by persons associated with the reactor*. Oak Ridge National Laboratory. Oak Ridge: ORNL.
- ORNL-TM-0728. (1965). *MSRE design and operations report, Part I: Description of reactor design*. Reactor Division. Oak Ridge: Oak Ridge National Laboratory. Retrieved 03 11, 2021, from <http://moltensalt.org/references/static/downloads/pdf/ORNL-TM-0728.pdf>
- ORNL-TM-0732. (1964). *MSRE design and operations report, part V, reactor safety analysis report*. Oak Ridge National Laboratory. Oak Ridge: ORNL. Retrieved from <https://moltensalt.org/references/static/downloads/pdf/ORNL-TM-0732.pdf>
- ORNL-TM-1023. (1965). *Tube plugging in the MSRE*. Oak Ridge: Oak Ridge National Laboratory. Retrieved 03 17, 2021, from <https://www.osti.gov/biblio/4639028>
- ORNL-TM-2098. (1968). *TUBE VIBRATION IN MSRE PRIMARY HEAT EXCHANGER*. Oak Ridge: Oak Ridge National Laboratory. Retrieved 03 17, 2021, from <https://www.osti.gov/biblio/4553122-tube-vibration-msre-primary-heat-exchanger>
- ORNL-TM-2316. (1968). *Physical properties of Molten-salt reactor fuel, coolant and flush salts*. Oak Ridge: ORNL. Retrieved from <https://moltensalt.org/references/static/downloads/pdf/ORNL-TM-2316.pdf>
- ORNL-TM-3002. (1970). *Reactor power measurement and heat transfer performance in the MSRE*. Oak Ridge National Laboratory. Oak Ridge: ORNL. Retrieved from <https://moltensalt.org/references/static/downloads/pdf/ORNL-TM-3002.pdf>
- ORNL-TM-3039. (1973). *MSRE systems and components performance*. Oak Ridge: Oak Ridge National Laboratory (ORNL). Retrieved 03 12, 2021, from <https://moltensalt.org/references/static/downloads/pdf/ORNL-TM-3039.pdf>
- ORNL-TM-3151. (1972). *A study of fission products in the MSRE by gamma spectroscopy*. Oak Ridge National Laboratory. Oak Ridge: ORNL. Retrieved from <https://moltensalt.org/references/static/downloads/pdf/ORNL-TM-3151.pdf>
- ORNL-TM-3229. (1970). *Fluid dynamic studies of the molten salt reactor experiment (MSRE) core*. Oak Ridge: Oak Ridge National Laboratory. doi:Reference number: 2007942
- ORNL-TM-4174. (1972). *Postirradiation examination of materials from the MSRE*. Oak Ridge National Laboratory. Oak Ridge: ORNL. Retrieved from <https://moltensalt.org/references/static/downloads/pdf/ORNL-TM-4174.pdf>
- Pal, E., Kumar, I., Joshi, J. B., & Maheshwari, N. K. (2016, April 02). CFD simulations of shell-side flow in a shell-and-tube type heat exchanger with and without baffles. *Chemical Engineering Science*, 143, 314-340. doi:10.1016/j.ces.2016.01.011
- Paraview. (2005). *Paraview*. (National Technology & Engineering Solutions of Sandia, Kitware Inc.) Retrieved from Paraview: <https://www.paraview.org/>
- Petrock, S. (2017, August 8). *Is This a Good FEA Mesh?* Retrieved from Solidworks: <https://blogs.solidworks.com/tech/2017/08/good-fea-mesh-heres-answer-yes-no-need-know-meshing-infographic.html>

- Piomelli, U. (1999, May). LES: Achievements and challenges. *Progress in aerospace sciences*, 35(4), pp. 335-362. doi:[https://doi.org/10.1016/S0376-0421\(98\)00014-1](https://doi.org/10.1016/S0376-0421(98)00014-1)
- Pope, S. B. (2000). *Turbulent Flows*. Cambridge, USA: Cambridge University Press. doi:<https://doi.org/10.1017/CBO9780511840531>
- Powers, J. J. (2019). *First-ever MSR benchmark published, based on ORNL's past and present research*. Retrieved 03 12, 2021, from Oak Ridge National Laboratory: <https://www.ornl.gov/molten-salt-reactor/measurements>
- Purcell, E. M. (1976). *Life at Low Reynolds Number*. Harvard University, Lyman laboratory, Cambridge . Retrieved 03 17, 2021, from https://www2.gwu.edu/~phy21bio/Reading/Purcell_life_at_low_reynolds_number.pdf
- Richardson, L. F. (1922). *Weather Prediction by Numerical Process*. Cambridge: Cambridge university press. doi: <https://doi.org/10.1002/qj.49704820311>
- Ritchie, H. (2020, February 10). *What are the safest and cleanest sources of energy?* Retrieved from ourworldindata.org: <https://ourworldindata.org/safest-sources-of-energy>
- Rosenthal, M. W., Kasten, P. R., & Briggs, R. B. (1969). *Molten salt reactors - History, status, and potential*. Oak Ridge National Laboratory. Oak Ridge.: Oak Ridge National Laboratory. doi:10.13182/NT70-A28619
- Rüdinger, E. (1985). The Open world of Niels Bohr. *Impact of science on society*, 23-25. Retrieved from <https://unesdoc.unesco.org/ark:/48223/pf0000063643>
- Salome. (2001). Salome-meca. Retrieved from <https://www.code-aster.org/V2/spip.php?article146>
- Sheehan, G. (1957). *Chicago Pile-1*. Retrieved 02 06, 2021, from <https://kids.britannica.com/students/assembly/view/177393>
- Shen, D., Fraton, M., Aufiero, M., & Bidaud, A. V. (2018). ZERO-POWER CRITICALITY BENCHMARK EVALUATION OF THE MOLTEN SALT REACTOR EXPERIMENT. *PHYSOR 2018, Reactor Physics paving the way towards more efficient systems*. Cancun, Mexico. Retrieved 03 12, 2021, from https://www.researchgate.net/publication/325333833_ZERO-POWER_CRITICALITY_BENCHMARK_EVALUATION_OF_THE_MOLTEN_SALT_REACTOR_EXPERIMENT
- Simscale. (2013). Simscale . Retrieved from <https://www.simscale.com/>
- Simscale. (2020, October 23). *Simscale*. Retrieved 03 17, 2021, from K-omega and K-omega SST: <https://www.simscale.com/docs/simulation-setup/global-settings/k-omega-sst/>
- Sohal, M. S., Ebner, M. A., Sabharwal, P., & Sharpe, P. (2010). *Engineering Database of Liquid Salt Thermophysical and Thermochemical Properties*. Idaho National Laboratory. Idaho: INL. doi:10.2172/980801
- Spalding, D. B., & Launder, B. E. (1974, March). THE NUMERICAL COMPUTATION OF TURBULENT FLOWS. *Computer Methods in Applied Mechanics and Engineering*, 269-289. doi:[https://doi.org/10.1016/0045-7825\(74\)90029-2](https://doi.org/10.1016/0045-7825(74)90029-2)
- Sreenivasan, K. R. (1999). Fluid Turbulence. *Reviews of modern physics*, 71(2). Retrieved 03 17, 2021, from https://pdfs.semanticscholar.org/2b1c/a9a00e46cdf5dd87428cf21939ddc1393f83.pdf?_ga=2.165036031.1530064255.1605805665-1892300395.1603203579
- TEMA. (2007). *Standards of the tubular exchanger manufacturers association* (9 ed.). USA: TEMA. Retrieved from https://www.academia.edu/34947218/TEMA_9TH_EDITION
- Thorium Energy Alliance. (2020, 06). *MSRE heat exchanger tubes*. Retrieved 03 17, 2021, from thorium energy alliance: <https://thoriumenergyalliance.com/resource/msre-heat-exchanger-tubes/>
- Thorium Energy Alliance. (2020, 06). *MSRE radiator*. Retrieved from thorium energy alliance: <https://thoriumenergyalliance.com/resource/msre-radiator/>

- U.S. Department of Energy. (1982). *The first reactor*. Office of the Executive Secretary. Washington: U.S. Department of Energy. Retrieved 02 06, 2021, from <https://www.energy.gov/sites/prod/files/The%20First%20Reactor.pdf>
- Vasconcelos, V., Santos, A., Campolina, D., Theler, G., & Pereira, C. (2018, May). Coupled unstructured fine-mesh neutronics and thermal-hydraulics methodology using open software: A proof-of-concept. *Annals of Nuclear Energy*, 115, 173-185. doi:10.1016/j.anucene.2018.01.021
- Waltar, E. A., Todd, R. D., & Tsvetkov, V. P. (2012). *Fast Spectrum Reactors* (1 ed.). Springer US. doi:10.1007/978-1-4419-9572-8
- Weller, H. G., Tabor, G., Jasak, H., & Fureby, C. (1998, November). A Tensorial Approach to Computational Continuum Mechanics Using Object Orientated Techniques. *Computers in Physics*, 12(6), 620-631. doi:10.1063/1.168744
- Wimshurst, A. (2021, February 24). *Youtube*. Retrieved from Fluid Mechanics 101: https://www.youtube.com/watch?v=SVYXNICeNWA&ab_channel=FluidMechanics101
- Wolfram|Alpha. (n.d.). Wolfram Alpha. Wolfram Alpha LLC. Retrieved from <https://www.wolframalpha.com/>
- World Nuclear Association. (2020, November). *Nuclear Power in the world today*. Retrieved 02 06, 2021, from World-nuclear: <https://www.world-nuclear.org/information-library/current-and-future-generation/nuclear-power-in-the-world-today.aspx>
- World-Nuclear. (2020, 11). *Nuclear Power Reactors*. Retrieved 02 13, 2021, from World-Nuclear: <https://www.world-nuclear.org/information-library/nuclear-fuel-cycle/nuclear-power-reactors/nuclear-power-reactors.aspx>
- World-Nuclear. (2021, January). *Nuclear Power in France*. Retrieved 02 06, 2021, from world-nuclear: <https://www.world-nuclear.org/information-library/country-profiles/countries-a-f/france.aspx>
- World-nuclear. (2021, 02 01). *Nuclear Powered Ships*. Retrieved 03 11, 2021, from World-nuclear: <https://www.world-nuclear.org/information-library/non-power-nuclear-applications/transport/nuclear-powered-ships.aspx>
- Zuck, D. (1971, 12 01). Osborn Reynolds, 1842-1912, and the flow of fluids through tubes. *British Journal of Anaesthesia*, 43(12), 1175-1182. doi:10.1093/bja/43.12.1175